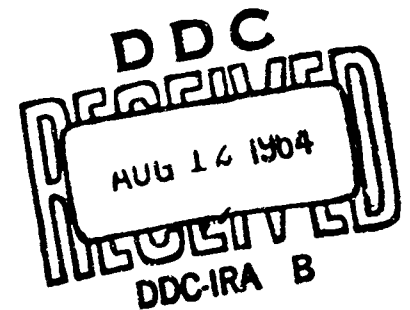


605 393 THE
ANTENNA
LABORATORY

COPY	2	OF	3	215
HARD COPY				\$. 6.00
MICROFICHE				\$. 1.25

AD RESEARCH ACTIVITIES in ---

Automatic Controls Antennas Echo Area Studies
Microwave Circuits Astronautics E M Field Theory
Terrain Investigations Radomes Systems Analysis
Wave Propagation Submillimeter Applications



Proceedings of the OSU-RTD Symposium
on
Electromagnetic Windows

2-4 June 1964

Vol. V

Department of ELECTRICAL ENGINEERING



THE OHIO STATE UNIVERSITY
RESEARCH FOUNDATION
Columbus, Ohio

**Best
Available
Copy**

**CLEARINGHOUSE FOR FEDERAL SCIENTIFIC AND TECHNICAL INFORMATION CFSTI
DOCUMENT MANAGEMENT BRANCH 410.11**

LIMITATIONS IN REPRODUCTION QUALITY

ACCESSION #

- ☒ 1. WE REGRET THAT LEGIBILITY OF THIS DOCUMENT IS IN PART UNSATISFACTORY. REPRODUCTION HAS BEEN MADE FROM BEST AVAILABLE COPY.
- ☐ 2. A PORTION OF THE ORIGINAL DOCUMENT CONTAINS FINE DETAIL WHICH MAY MAKE READING OF PHOTOCOPY DIFFICULT.
- ☐ 3. THE ORIGINAL DOCUMENT CONTAINS COLOR, BUT DISTRIBUTION COPIES ARE AVAILABLE IN BLACK-AND-WHITE REPRODUCTION ONLY.
- ☐ 4. THE INITIAL DISTRIBUTION COPIES CONTAIN COLOR WHICH WILL BE SHOWN IN BLACK-AND-WHITE WHEN IT IS NECESSARY TO REPRINT.
- ☐ 5. LIMITED SUPPLY ON HAND: WHEN EXHAUSTED, DOCUMENT WILL BE AVAILABLE IN MICROFICHE ONLY.
- ☐ 6. LIMITED SUPPLY ON HAND: WHEN EXHAUSTED DOCUMENT WILL NOT BE AVAILABLE.
- ☐ 7. DOCUMENT IS AVAILABLE IN MICROFICHE ONLY.
- ☐ 8. DOCUMENT AVAILABLE ON LOAN FROM CFSTI (TT DOCUMENTS ONLY).
- ☐ 9.

PROCESSOR:

Proceedings of the OSU-RTD Symposium
on
Electromagnetic Windows

2-4 June 1964

Vol. V
Papers Submitted for the Proceedings Only

The publication of this report does not constitute approval by either The Ohio State University or the United States Air Force of the findings contained herein. It is published only for the fruitful exchange and stimulation of ideas.

FOREWORD

The papers presented in this report were submitted for the Seventh Symposium on Electromagnetic Windows held at The Ohio State University, Columbus, Ohio, 2, 3, and 4 June 1964. They were compiled by Alan I. Slonim of The Ohio State University under Air Force Contract AF 33(615)-1081 administered by The Research and Technology Division, Air Force Systems Command, Wright-Patterson Air Force Base, Ohio with Richard A. Ireland serving as Task Engineer.

The proceedings are published in five volumes as follows:

Vol. I

Session I - Objectives and New Techniques

Session II - Materials for High Temperature Applications

Vol. II

Session III - Electrical Design

Session IV - Structural Design for Large Radomes

Vol. III

Session V - Fabrication and Testing of Airborne Radomes

Session VI - Hypersonic Environment

Vols. IV and V

Oral papers received too late for inclusion in Vols. I, II, and III.
Papers submitted for the proceedings only.

Vol. V
CONTENTS

PAPERS SUBMITTED FOR THE PROCEEDINGS ONLY

- A. Electrical Design and Performance Evaluation of Dual-Frequency Radome Test Panels, E. Donald Wegner, N.D. LoBue
- B. Transmission Characteristics of Ground Based Radomes, J. D'Agostino, F. Rouffy
- C. Radome Thermal Design for a Mach 4 Missile, R.P. Suess, L.B. Weckesser
- D. Radome Materials Research at Rutgers University, E.J. Smoke, C.F. Bersch
- E. Comments on the Synthesis of Longitudinally Inhomogeneous Plasma-Dielectric Media, Martin C. Blyseth
- F. Quality Control and Non-Destructive Testing of Dielectric Components Using the Microwave Thickness Gauge, J.D. Leonard, G.T. Stropki
- G. Dual Frequency Radome Feasibility, Grant M. Randall, Donald F. Zemke
- H. Large Air Supported Radomes for Satellite Communications Ground Station, Walter W. Bird
- I. Effects of Aperture Obstructions and Radome Finishes Upon Radome Electrical Characteristics, J.R. Rogers
- J. Measurements of Dynamic Collimation Error, D.L. Loyet, J.R. Maurer
- K. A Technique for Electrical Evaluation of Electromagnetic Window and Radome Shapes, Forrest L. Coling

ELECTRICAL DESIGN AND PERFORMANCE EVALUATION OF DUAL-FREQUENCY RADOME TEST PANELS

by

E. Donald Wegner, N. D. LoBue

**North American Aviation, Inc.
Los Angeles, California**

INTRODUCTION

The primary objective of this paper is to present dual-frequency (X-band and K_a -band) radome design criteria and to show how these criteria are used to obtain dual-frequency radome panel designs. A second objective is to outline our method for calculating the theoretical power transmission and insertion phase delay performance curves. Also, a test panel fabrication and laboratory test program are described.

Dual frequency radar operation is being considered for applications in high performance air vehicles to a larger and larger extent as multi-purpose vehicles are required. In order for this type of radar system to be successful, good radome electrical performance must be achieved for the frequencies employed. The radome development work described in this paper was conducted by the Los Angeles Division of North American Aviation, Inc, to fulfill this need. Initial work was refined in conjunction with the development of dual frequency radar systems by the Autonetics Division of North American Aviation, Inc.

SPECIFICATIONS

At the beginning of this program of obtaining design and laboratory test data on the feasibility of the dual-frequency radome concept, electrical performance specifications were established to meet the requirements of the dual-frequency radars. The X-band frequency requirements are listed in Table I, and the K_a -band frequency radome requirements are listed in Table II.

MATERIALS CONFIGURATION

Two types of low-loss, high-temperature dielectric materials were selected for this investigation and used in the fabrication of the test panels. The candidate materials were designated Type I, "E" glass fabric preimpregnated with 38 (± 2) percent Dow Corning DC-2106 silicone resin (used in panels No. 1 and 3), and Type II, General Electric quartz fabric preimpregnated with 38

(± 2) percent Dow Corning DC-2106 resin (used in panel No. 2). Waveguide size samples were cut from the test panels, and dielectric constant and loss tangent measurements were made at room temperature in the laboratory.

ELECTRICAL DESIGN

The radome wall design equations for plain dielectric sheets and dielectric-reactive array design configurations have been programmed on the IBM-7094 data processing computer system. The calculated power transmission coefficient and insertion phase delay data for dual-frequency operations were determined with the use of this computer program.

Dual-frequency measurements were made for power transmission and insertion phase delay on the fabricated radome test panels. These measurements were conducted for both perpendicular and parallel polarization in a

Table I

X-BAND FREQUENCY RADOME REQUIREMENTS

Antenna Look Angle in Radome	T ² Power Transmission (Percent)	BDE, Beam Deflection Error (Milliradians)
± 15 deg in azimuth, -15 deg to +10 deg in elevation	85 (avg) 80 (min)	3.0
All look angles outside ± 15 deg cone	90 (avg)	6.3

T² Design objective: 90-percent (average) over-all

Table II

K_a-BAND FREQUENCY RADOME REQUIREMENTS

Antenna Look Angle in Radome	T ² Power Transmission (Percent)	BDE, Beam Deflection Error (Milliradians)
±40 deg in azimuth -15 deg to +10 deg in elevation	60 (avg) 55 (min)	6.3
All look angles outside of the above	60 (avg) 55 (min)	12.3

T² Design objective: 70-percent (average) over-all

laboratory microwave interferometer. At the beginning of this program, it was decided to design, fabricate, and test three different radome panels that appeared to have the desired material and electrical qualities for good dual-frequency operation. The first panel configuration was designed with the Type I material. This material was chosen since it yields a low loss value and dielectric constant and maintains good structural properties. The second panel was developed with the Type II material. This material was selected for its very low loss tangent and dielectric properties. Also, this material maintains constant dielectric properties over a wide temperature range. However, the structural properties of this material are not as good as the Type I material. It was felt that the reactive wall concept would be of value for dual-frequency radome panel design. Therefore, the third panel was developed around this concept using the Type I material configuration.

A complete description and discussion of these three panels along with a fourth panel design (reactive wall, not fabricated) follows:

Panel No. 1

This panel was manufactured by the hand lay-up, press molding technique. The material used in the construction of this panel was a 181 style "E" glass fabric, preimpregnated with 38 (± 2) percent Dow Corning DC-2106

f_x (X-BAND)	f_k (K-BAND)
8715 MC	34860 MC

FREQUENCY RATIO = 4:1

----- MEASURED DATA
————— CALCULATED DATA

PANEL NO. 1
TYPE I MATERIAL
DIELECTRIC = 3.87
LOSS TANGENT = 0.007
THICKNESS = 0.371 IN.

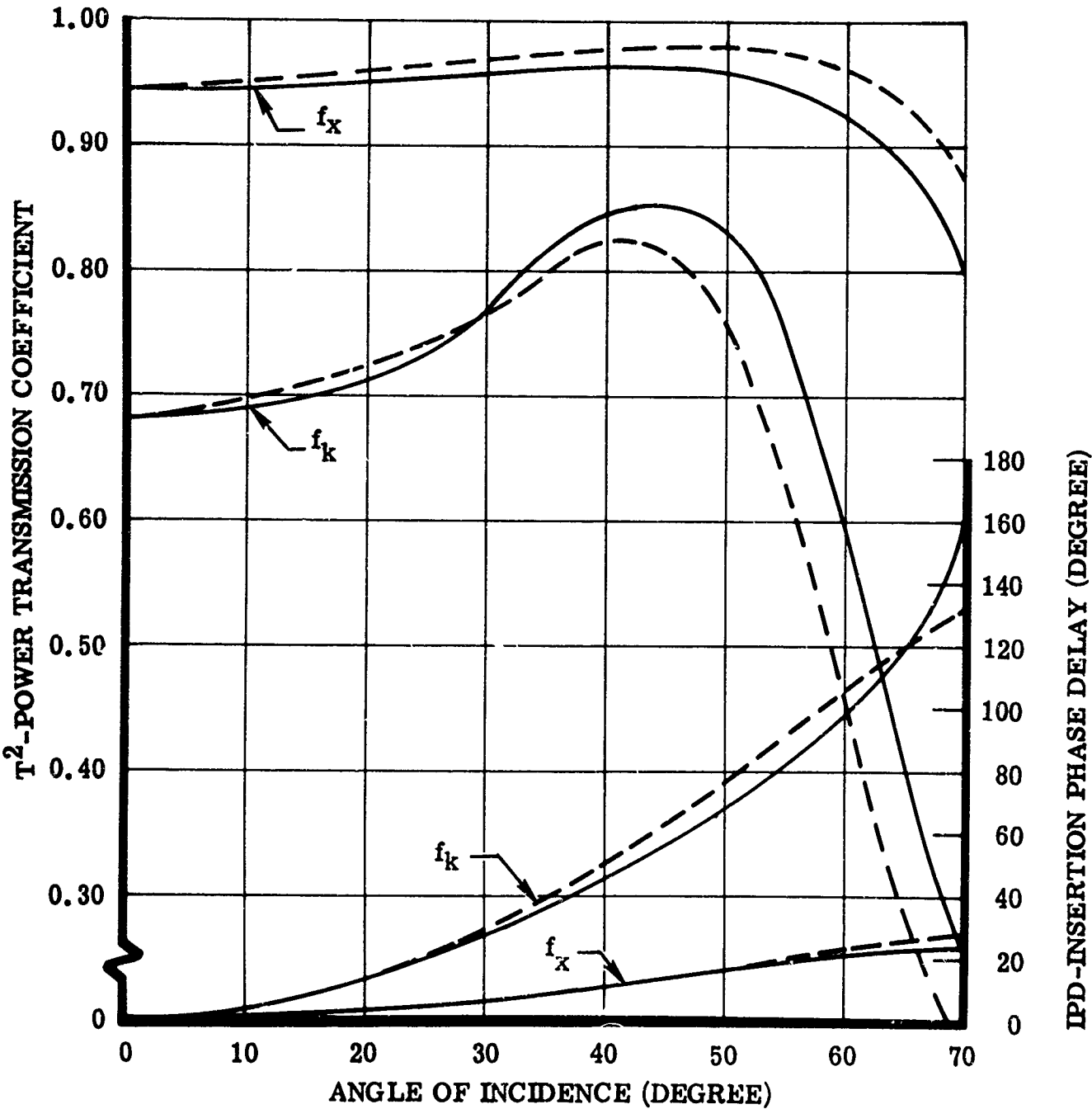


Fig. 1 Power transmission and IPD versus angle of incidence for perpendicular polarization.

f_x (X-BAND)	f_k (K-BAND)
8715 MC	34860 MC

FREQUENCY RATIO = 4:1

PANEL NO. 1
TYPE I MATERIAL
DIELECTRIC = 3.87
LOSS TANGENT = 0.007
THICKNESS = 0.371 IN.

--- MEASURED DATA
— CALCULATED DATA

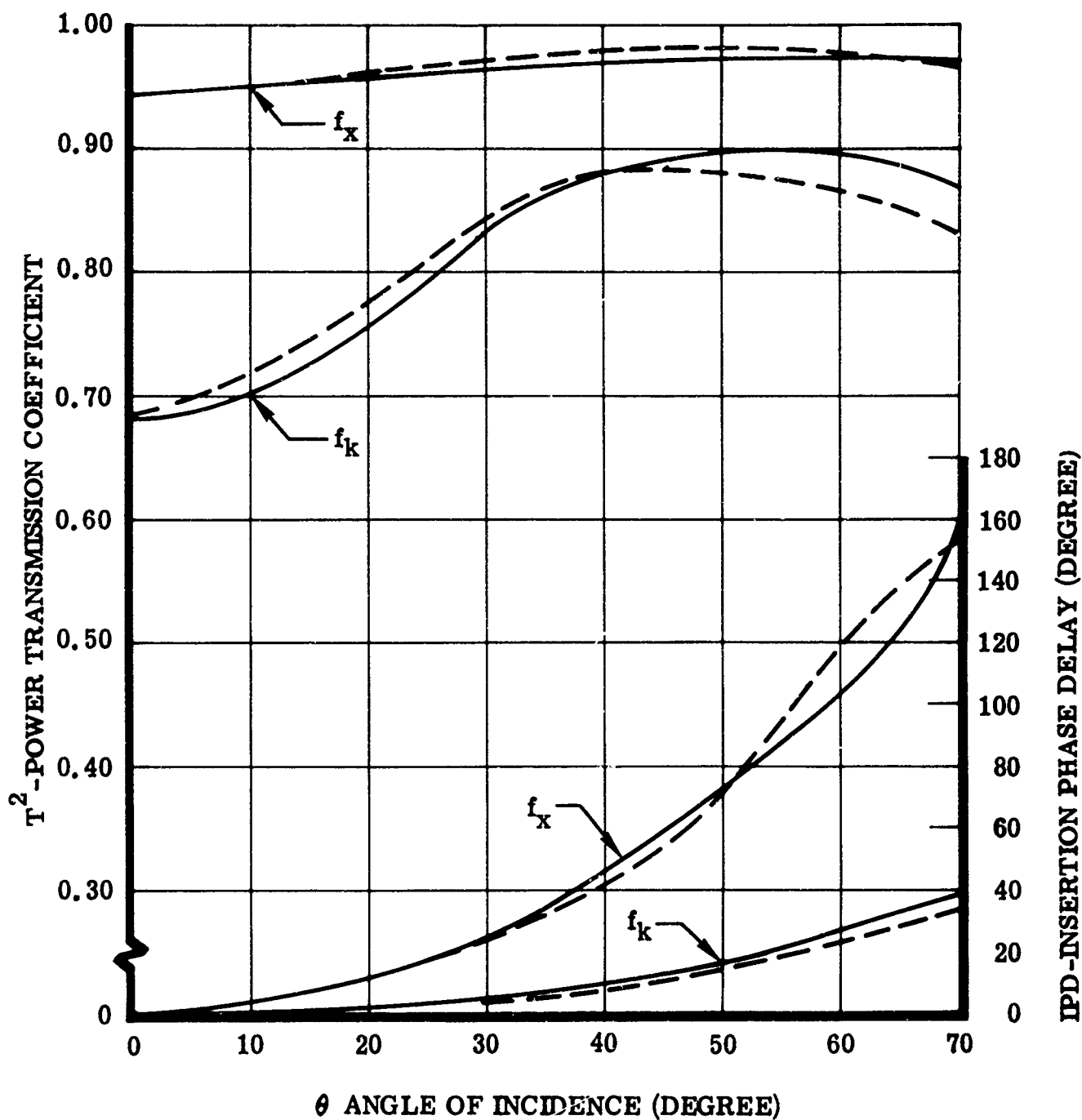


Fig. 2 Power transmission and IPD versus angle of incidence for parallel polarization.

silicone resin. This panel has a measured dielectric constant of 3.87 and a loss tangent of 0.007. The optimized wall thickness of 0.371 inch was designed for dual-frequency operation at 8715 mc and 34860 mc (4 to 1 frequency ratio). For this design, the calculated and measured power transmission and insertion phase delay (IPD) curves are shown in figure 1 for perpendicular polarization and in figure 2 for parallel polarization. The curves for the X-band frequency show good power transmission with low IPD values for incident angles from 0 to 70 degrees and for both polarizations. The transmission curves for K_a-band drop off rapidly at the higher incident angles for perpendicular polarization and increase for the parallel case. For all data given in this paper, there is generally good agreement between calculated and measured results.

Because of the experimental test error and panel fabrication tolerance, perfect agreement between calculated and test data was not obtained.

Panel No. 2

Panel No. 2 was manufactured in the same manner as panel No. 1 except using a General Electric quartz fabric preimpregnated with 38-(± 2) percent DC-2106 silicone resin (Type II material). An optimum wall thickness of 0.448 (± 0.002) inch was calculated, based on a dielectric constant of $E = 3.13$ and a loss tangent of 0.0036. Machining was again required to hold the wall-thickness tolerances for the panel. The calculated and measured power transmission and insertion phase delay curves are shown in figure 3 for perpendicular polarization and in figure 4 for parallel polarization. The X-band transmission correlation of the calculated and measured data is within 3 percent, and the K_a-band is within 4.5 percent through 60 degrees incidence angles. This data is felt to be good correlation, considering that power transmission is through a fourth order radome wall at the K_a-band frequency.

Panel No. 3

This panel was designed as a solid laminate panel with imbedded reactive disk arrays, manufactured in two stages by the press molding technique, using 181 style "E" glass fabric preimpregnated with 38 (± 2) percent DC-2106 silicone resin. The center section of the panel was laminated, postcured, machined, and smooth-sanded to a thickness of 0.311 (± 0.001) inch. Silver reactive elements were then painted on both surfaces by a silk-screen process and cured. This stage of panel development is shown in the photograph in figure 5. Additional pieces of cloth were laminated on each side and the panel was again press molded and postcured. The panel was then machined to a thickness of 0.380 (± 0.002) inch. The complete dimensions, electrical

f_x (X-BAND)	f_k (K-BAND)
8715 MC	34860 MC

FREQUENCY RATIO = 4:1

--- MEASURED DATA
— CALCULATED DATA

PANEL NO. 2
TYPE II MATERIAL
DIELECTRIC = 3.13
LOSS TANGENT = 0.0036
THICKNESS = 0.448

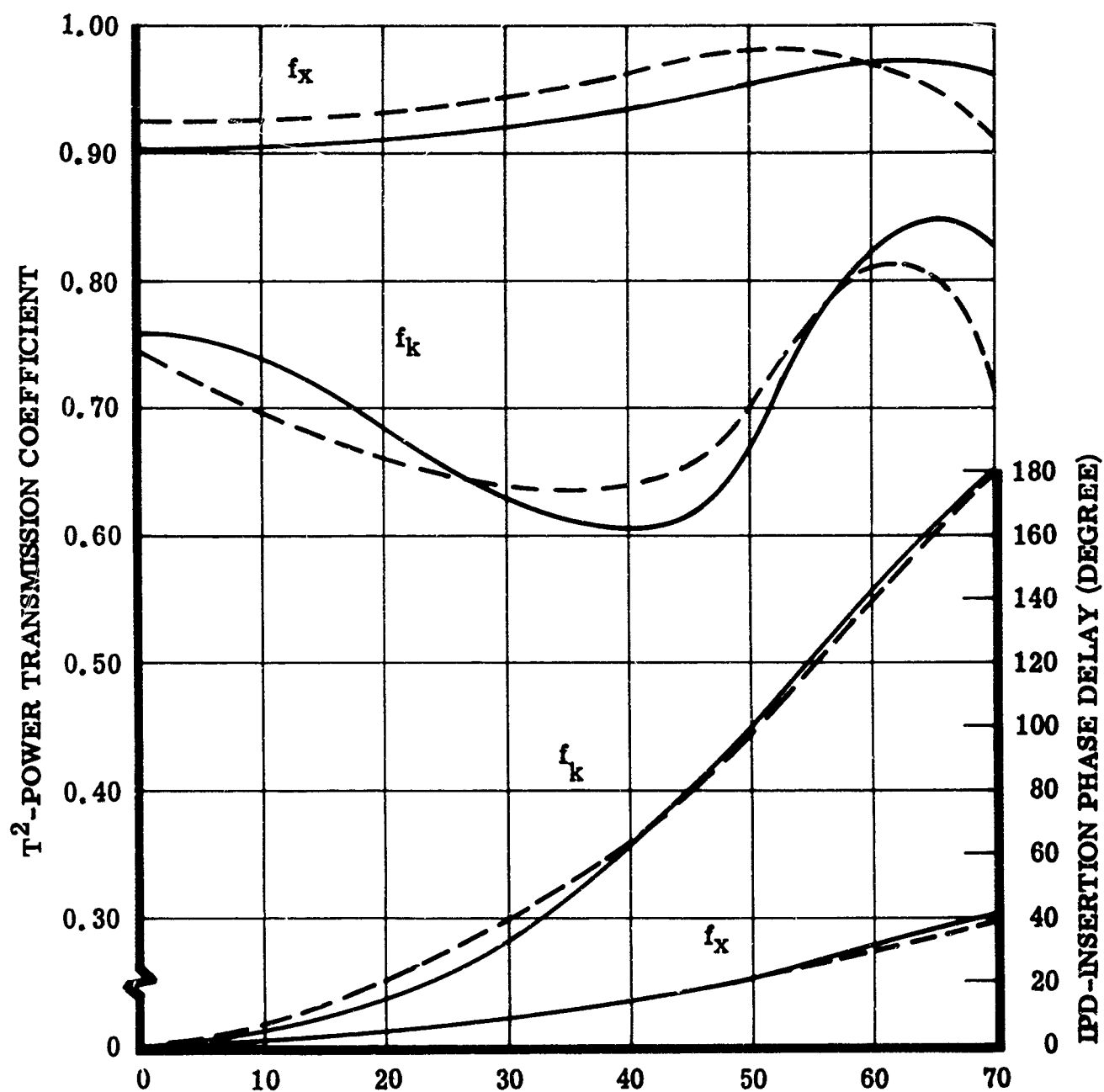


Fig. 3 Power transmission and IPD versus angle of incidence for perpendicular polarization.

f_x (X-BAND)	f_k (K-BAND)
8715 MC	34860 MC

FREQUENCY RATIO = 4:1

PANEL NO. 2
TYPE II MATERIAL
DIELECTRIC 3.13
LOSS TANGENT = 0.0036
THICKNESS = 0.448

--- MEASURED DATA
— CALCULATED DATA

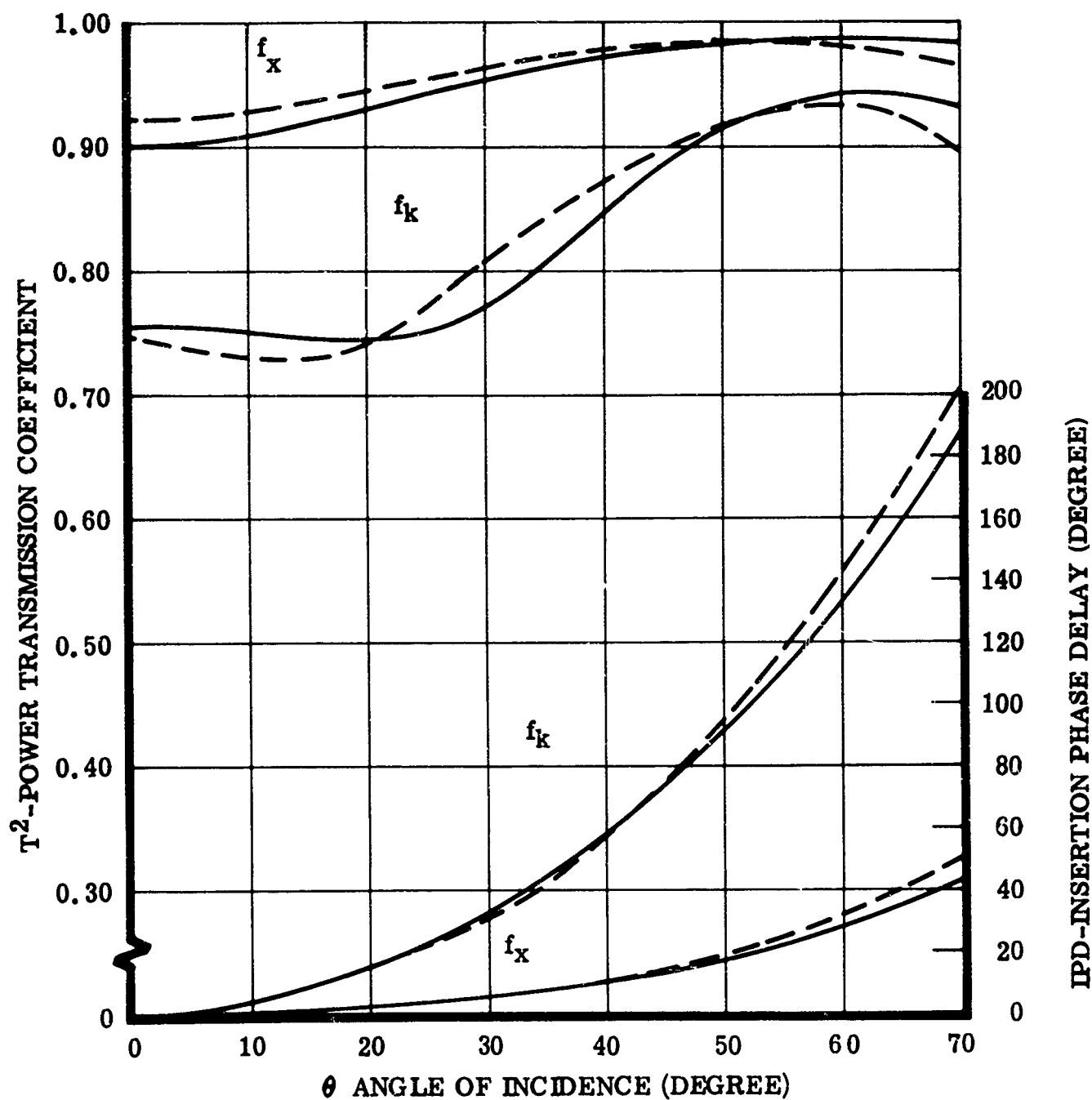
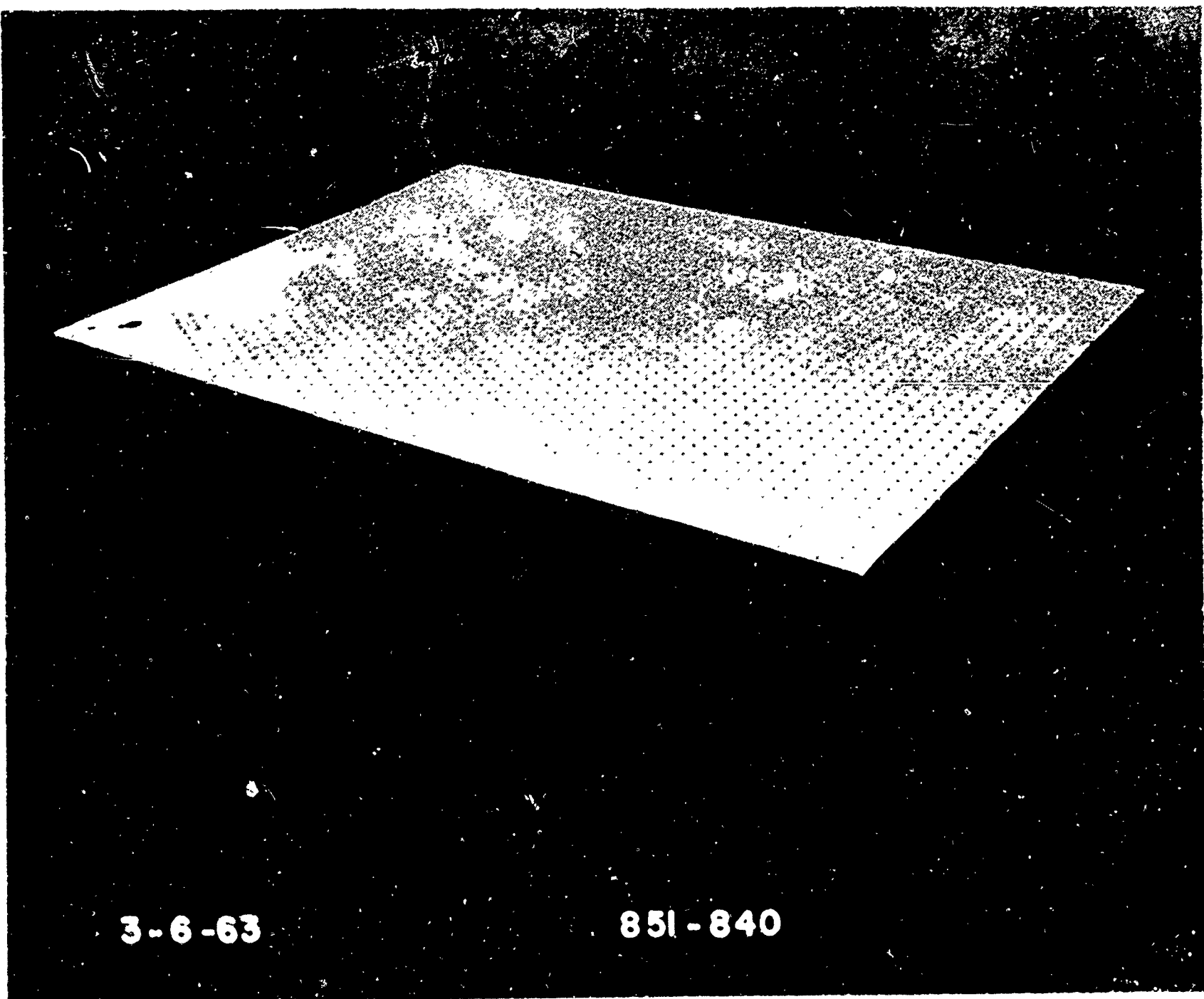


Fig. 4 Power transmission and IPD versus angle of incidence for parallel polarization.

Fig. 5 Reactive wall panel showing (silver)
capacitive discs.



properties, and design data of the reactive wall (panel No. 3) are given in Table III. This panel was also designed for a 4 to 1 frequency ratio (8715 mc and 34860 mc). The calculated and measured power transmission coefficient and insertion phase delay curves are shown in figure 6 for perpendicular polarization and in figure 7 for parallel polarization. The curves for the X-band frequency show that the transmission is above 90 percent for incident angles out to 68 degrees with a maximum IPD of 43 degrees at a 70-degree incident angle. The transmission curves for K_a-band frequency decrease to a minimum of 54 percent at 25 degrees incident angle and then increase to 75.5 percent at 55 degrees for the perpendicular case. For the parallel case, the K_a-band transmission increases from 59 percent at 0 degrees to 84.5 percent at 55 degrees incident angle. In comparing figures 1 and 2 with figures 6 and 7, the following is noted. For X-band, the reactive wall design yields a small increase in transmission at the higher incident angles and decreases the transmission in the lower incident region. For K_a-band, at perpendicular

Table III

DIMENSIONS AND DESIGN CONFIGURATION FOR REACTIVE WALL
(PANEL NO. 2)

Material - "E" glass and silicone DC-2106	Type I
Dielectric constant	3.95
Loss tangent	0.007
Thickness of wall	0.380 in.
Type of reactive array	Metal disk
Number of reactive arrays	2
Diameter of disks	0.125 in.
Center-to-center spacing of disks	0.9375 in.
Distance of array to dielectric surface	0.035 in.

Table IV

DIMENSIONS AND DESIGN CONFIGURATION FOR REACTIVE WALL
(3.7:1 FREQUENCY RATIO)

Material - quartz and silicone DC-2106	Type II
Dielectric constant	3.22
Loss tangent	0.004
Thickness of wall	0.446 in.
Type of reactive array	Metal disk

f_x (X-BAND)	f_k (K-BAND)
8715 MC	34860 MC

FREQUENCY RATIO = 4:1

PANEL NO. 3 (REACTIVE)
 REACTIVE - TABLE
 TYPE I MATERIAL
 DIELECTRIC = 3.95
 LOSS TANGENT = 0.007
 THICKNESS = 0.380

--- MEASURED DATA
 — CALCULATED DATA

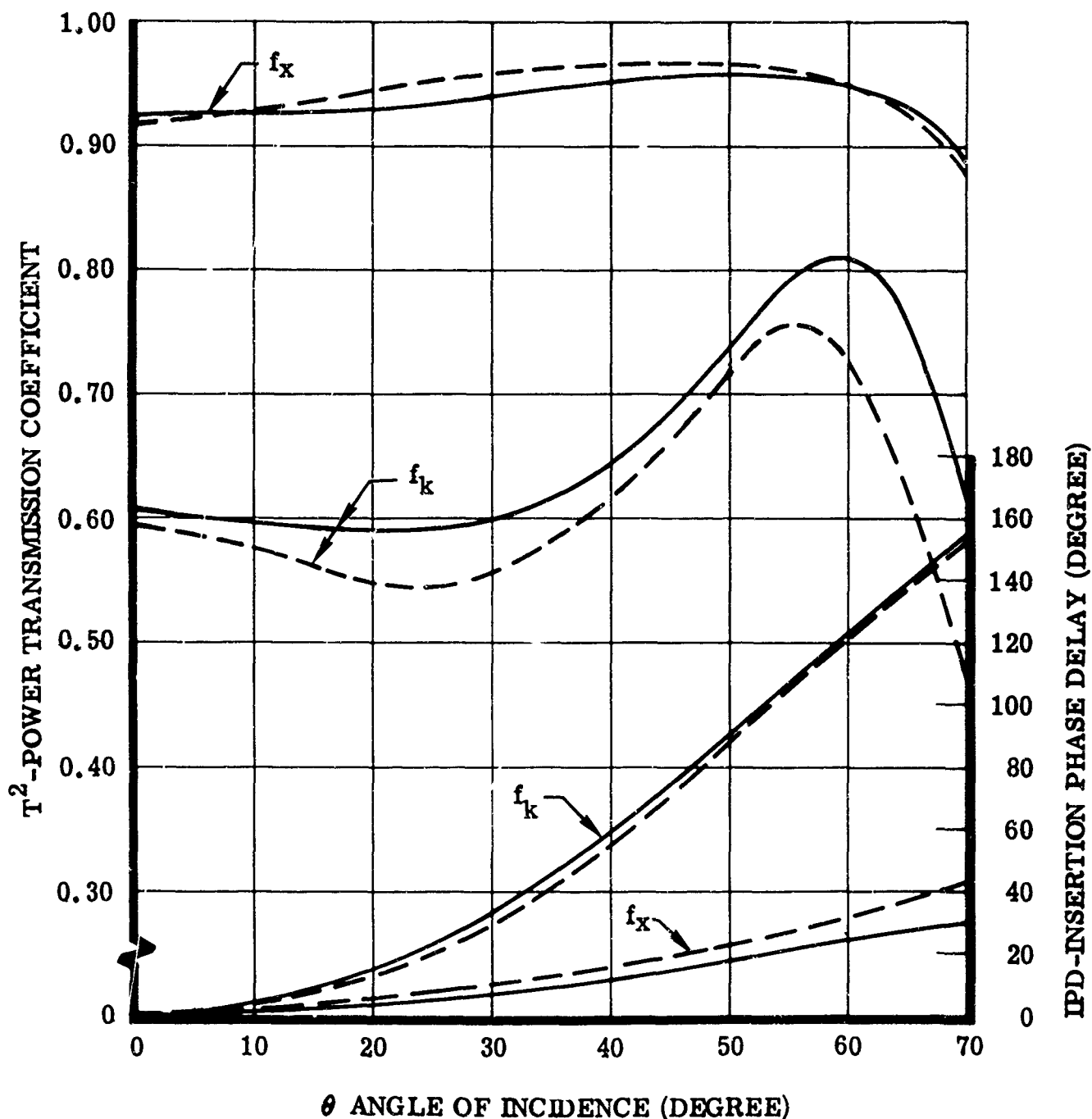


Fig. 6 Power transmission and IPD versus angle of incidence for perpendicular polarization.

f_x (X-BAND)	f_k (K-BAND)
8715 MC	34860 MC

FREQUENCY RATIO 4:1

--- MEASURED DATA
 ——— CALCULATED DATA

PANEL NO. 3 (REACTIVE)
 REACTIVE - TABLE
 TYPE I MATERIAL
 DIELECTRIC = 3.95
 LOSS TANGENT = 0.007
 THICKNESS = 0.380

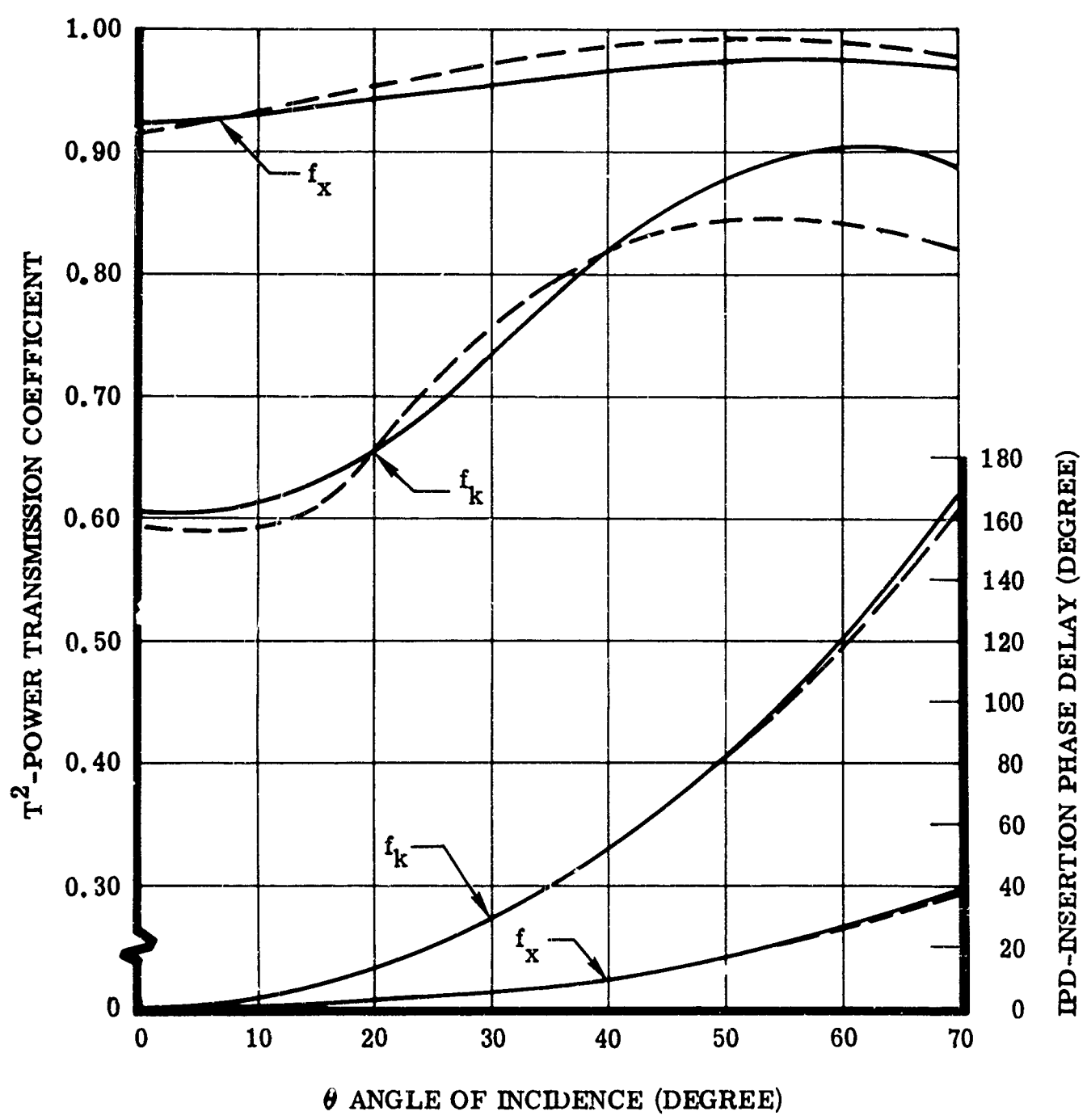


Fig. 7 Power transmission and IPD versus angle of incidence for parallel polarization.

Table IV

DIMENSIONS AND DESIGN CONFIGURATION FOR REACTIVE WALL
(3.7:1 FREQUENCY RATIO) (CONT)

Number of reactive arrays	2
Diameter of disks	0.125 in.
Center-to-center spacing of disks	0.500 in.
Distance of array to dielectric surface	0.023 in.

polarization, the reactive wall yields an improvement in transmission at the higher incident angles, but decreases the transmission at lower incident angles. It is concluded that, when operating at a 4 to 1 frequency ratio, the reactive wall design will not significantly improve the over-all electrical performance of the panel and thus does not justify the extra design and fabrication cost. The reason for this is that, at the 4 to 1 frequency ratio (only), the plain dielectric panel wall thickness is designed to yield the best average impedance match over the given range of incidence angles for a half-wave and fourth order wall. Therefore, this average impedance match generally cannot be improved upon with the use of reactive elements.

REACTIVE WALL DESIGN

Based on analytical development, it was concluded that the reactive wall design will improve power transmission to a marked degree when the operating frequencies are not even multiples. Therefore, the frequencies chosen for the data shown in figures 8 and 9 are 3.7 to 1 rather than the 4 to 1 frequency ratio. With all dielectric parameters remaining constant (for a Type II material), the performance curves in figures 8 and 9 show a significant improvement in power transmission coefficient of the reactive wall as compared to the nonreactive wall for the given angles of incidence and for both perpendicular and parallel polarization and at X-band and K_a-band frequencies. Also, these figures show an improvement in the insertion phase delay values (reduction) at the higher angles of incidence. The complete dimensions, electrical properties, and design data used in this study are given in Table IV.

REACTIVE WALL FORMULATIONS

At the start of this program, it was felt that the reactive wall concept could be used to improve the electromagnetic performance of the plain radome

f_x (X-BAND)	f_k (K-BAND)
9375 MC	35000 MC

FREQUENCY RATIO = 3.7:1

REACTIVE - TABLE TYPE II MATERIAL DIELECTRIC = 3.22 LOSS TANGENT = 0.004 THICKNESS = 0.446
--

--- REACTIVE WALL
 ——— NONREACTIVE WALL

CALCULATED DATA

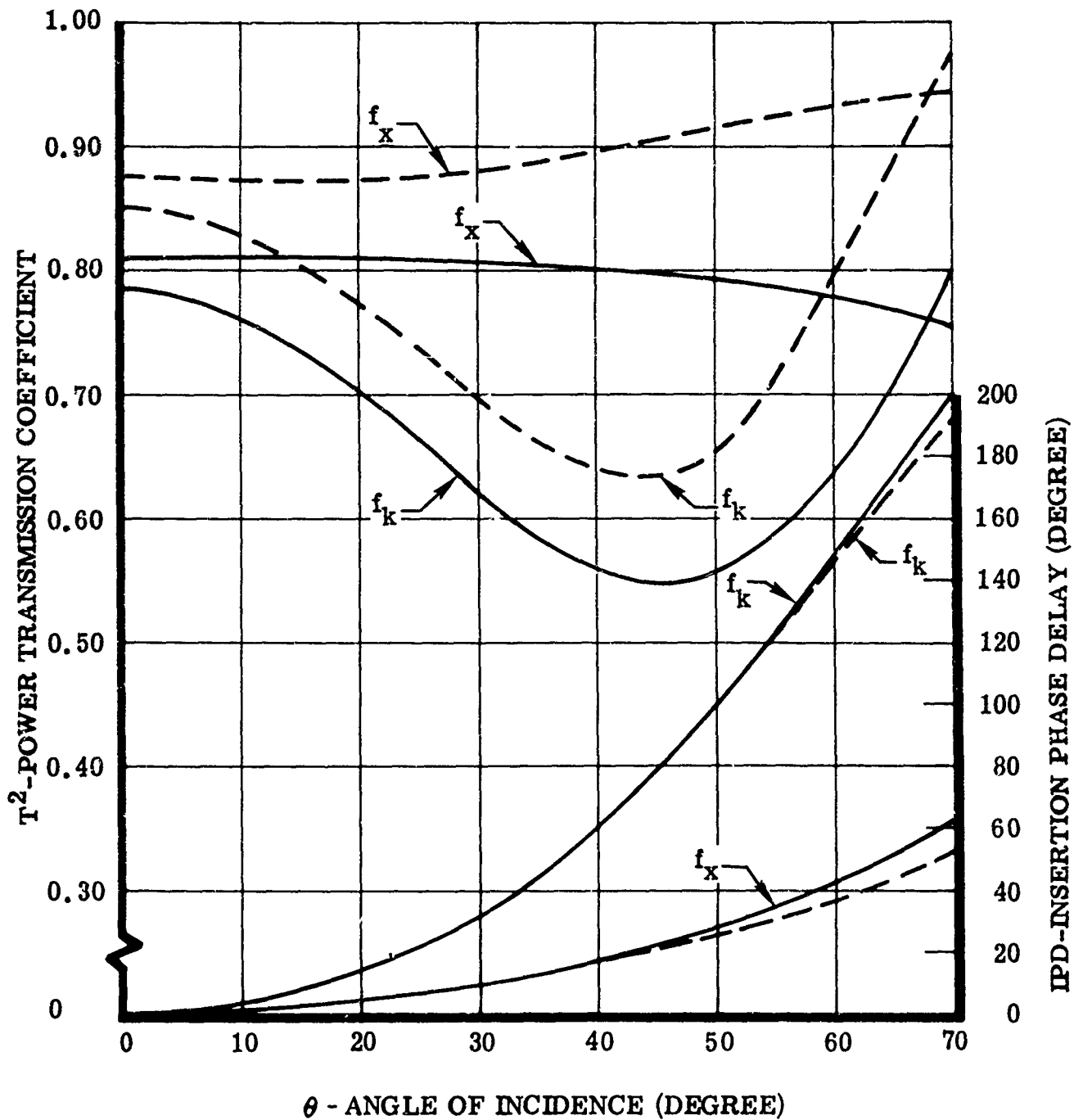


Fig. 8 Power transmission and IPD versus angle of incidence for perpendicular polarization.

f_x (X-BAND)	f_k (K _a -BAND)
9375 MC	35000 MC

FREQUENCY RATIO = 3.7:1

REACTIVE - TABLE TYPE II MATERIAL DIELECTRIC = 3.22 LOSS TANGENT 0.004 THICKNESS = 0.446
--

--- REACTIVE WALL
 ——— NONREACTIVE WALL

CALCULATED DATA

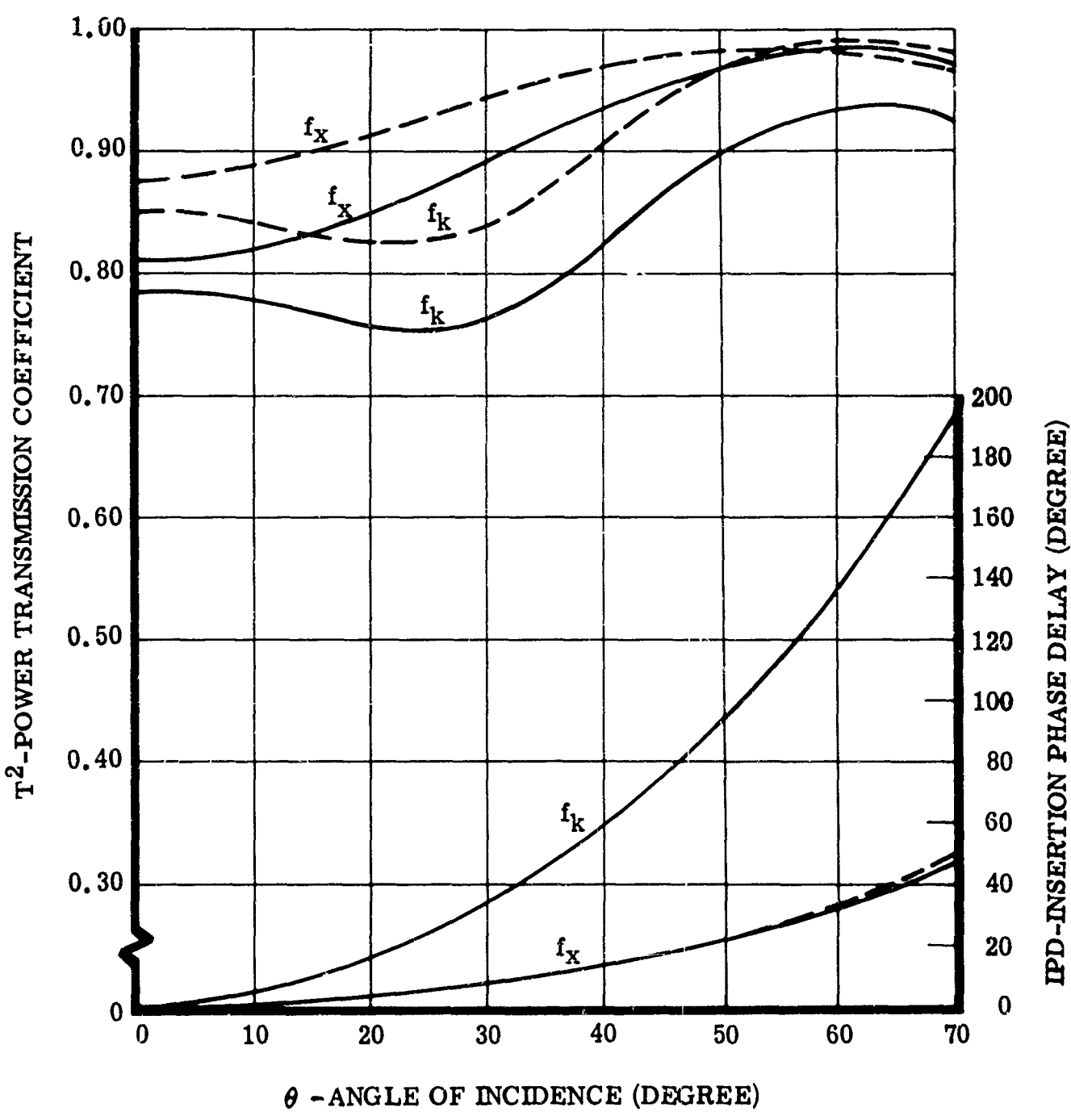


Fig. 9 Power transmission and IPD versus angle of incidence for parallel polarization.

panel designs and, therefore, an investigation into the suitability of this concept for dual-frequency radome design was conducted. Because of the uncommon use of reactive wall equations in radome design, the following formulations used in our analyses are given for reference.

POWER TRANSMISSION COEFFICIENT AND INSERTION PHASE DELAY OF A CAPACITIVE DISK TYPE REACTIVE WALL RADOME

Formulation

The power transmission coefficient and insertion phase delay of a reactive wall type radome with two capacitive disk arrays may be calculated from its equivalent circuit. A convenient method for performing these calculations is the well-known general-circuit-parameter technique where the ABCD matrix represents a section of a transmission line (Reference 1).

Applying the transmission line analogy, the general circuit parameters, ABCD of a radome wall loaded with two arrays of capacitive elements are found from the matrix product of Eq. (1).

$$\begin{aligned}
 \begin{bmatrix} A & B \\ C & D \end{bmatrix} &= \begin{bmatrix} \cosh \gamma_s l_{s1} & \frac{\sinh \gamma_s l_{s1}}{Y_s} \\ Y_s \sinh \gamma_s l_{s1} & \cosh \gamma_s l_{s1} \end{bmatrix} \begin{bmatrix} 1 & 0 \\ \pm jB_1 & 1 \end{bmatrix} \\
 (1) \quad &\begin{bmatrix} \cosh \gamma_s l_{s2} & \frac{\sinh \gamma_s l_{s2}}{Y_s} \\ Y_s \sinh \gamma_s l_{s2} & \cosh \gamma_s l_{s2} \end{bmatrix} \begin{bmatrix} \cosh 2 \gamma_c l_{c3} & \frac{\sinh 2 \gamma_c l_{c3}}{Y_c} \\ Y_c \sinh 2 \gamma_c l_{c3} & \cosh 2 \gamma_c l_{c3} \end{bmatrix} \\
 &\begin{bmatrix} \cosh \gamma_s l_{s4} & \frac{\sinh \gamma_s l_{s4}}{Y_s} \\ Y_s \sinh \gamma_s l_{s4} & \cosh \gamma_s l_{s4} \end{bmatrix} \begin{bmatrix} 1 & 0 \\ \pm jB_2 & 1 \end{bmatrix} \\
 &\begin{bmatrix} \cosh \gamma_s l_{s5} & \frac{\sinh \gamma_s l_{s5}}{Y_s} \\ Y_s \sinh \gamma_s l_{s5} & \cosh \gamma_s l_{s5} \end{bmatrix}
 \end{aligned}$$

The effective power transmission coefficient, T_e^2 , and the effective insertion phase delay θ_e , are calculated using Eq. (2) through (7), respectively:

$$(2) \quad T_{\perp, 11}^2 = \frac{4}{\left| A + BY_{1\perp, 11} + \frac{C}{Y_{1\perp, 11}} + D \right|^2}$$

$$(3) \quad T_{\perp, 11}^1 = \text{ARC TAN} \frac{\text{Im} \left(A + BY_{1\perp, 11} + \frac{C}{Y_{1\perp, 11}} + D \right)}{\text{Re} \left(A + BY_{1\perp, 11} + \frac{C}{Y_{1\perp, 11}} + D \right)}$$

$$(4) \quad T_e^2 = (T_{\perp} \sin^2 \delta)^2 + (T_{11} \cos^2 \delta)^2 + 2 T_{\perp} T_{11} \sin^2 \theta \cos^2 \delta \cos \Delta$$

$$(5) \quad \Delta = \left| T_{\perp}^1 - T_{11}^1 \right|$$

$$(6) \quad T_e^1 = T_{\perp}^1 - \text{ARC SIN} \left(\frac{T_{11} \cos^2 \delta \sin \Delta}{T_e} \right)$$

$$(7) \quad \theta_e = T_e^1 - \frac{2 \pi \cos \theta}{\lambda} \left(\ell_{s1} + \ell_{s2} + \ell_{c3} + \ell_{s4} + \ell_{s5} \right)$$

where:

θ = Angle of incidence measured in free space between the incident ray and the normal to the radome surface

λ = Wave length in free space

δ = Polarization angle of the \vec{E} -vector

Y_1	=	Characteristic admittance of free space
γ	=	Propagation constant of the skin material
B_s	=	Susceptance of the capacitive disk array
l_{s1}, l_{s5}	=	Thickness from outer surface of skin material to center of reactive array
l_{s2}, l_{s4}	=	Thickness from center of reactive array to inner surface of skin material
l_{c3}	=	Thickness of core material (not used)
Y_s	=	Characteristic admittance of the skin material
Y_c	=	Characteristic admittance of the core material (not used)
\perp	=	Perpendicular polarization
11	=	Parallel polarization

CALCULATED RADOME PERFORMANCE

For the final phase of this program, an analytical study was made of the actual power transmission and beam deflection error performance of a typical streamline ogive-shaped radome shown in figure 10, for X-band and K_a -band operation. This analysis was conducted with an IBM-7094 radome computer program in use at NAA. Both the radome and antenna aperture system were simulated on the computer and the radome power transmission and beam deflection error were calculated for a given range of antenna lock positions in the radome. The Type II material wall chosen for this study, and the radome wall thickness was optimized at 0.392 inch. The radome power transmission and beam deflection errors are plotted for azimuth look angles from 0 to 40 degrees, the elevation angle being held fixed at 0, 5, 10, and 15 degrees. Both the error horizontal (boresight) and vertical (crosstalk) to the plane of scan are graphed as separate curves. The curves in figure 11 show that the minimum transmission at X-band is 94.5 percent through the nose region of the radome and, at K_a -band, the minimum is 59 percent in the same region. Average power transmission at X-band and K_a -bands was approximately 96 percent and 74 percent, respectively. The curves in figure 12 and 13 show that the maximum beam deflection error is less than 2.2 milliradians for X-band and K_a -band over the complete range of antenna scan angles.

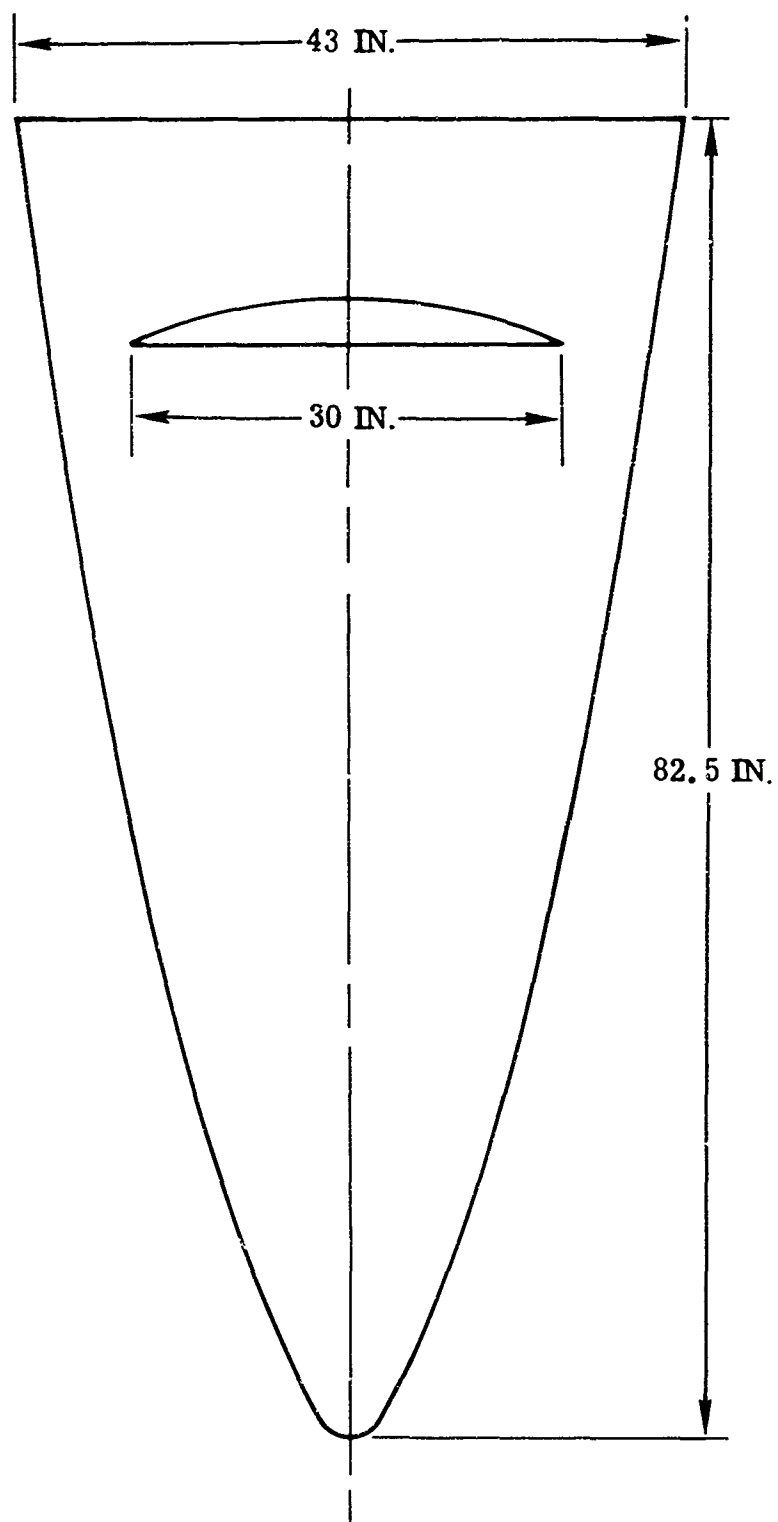


Fig. 10 Ogive-shaped radome.

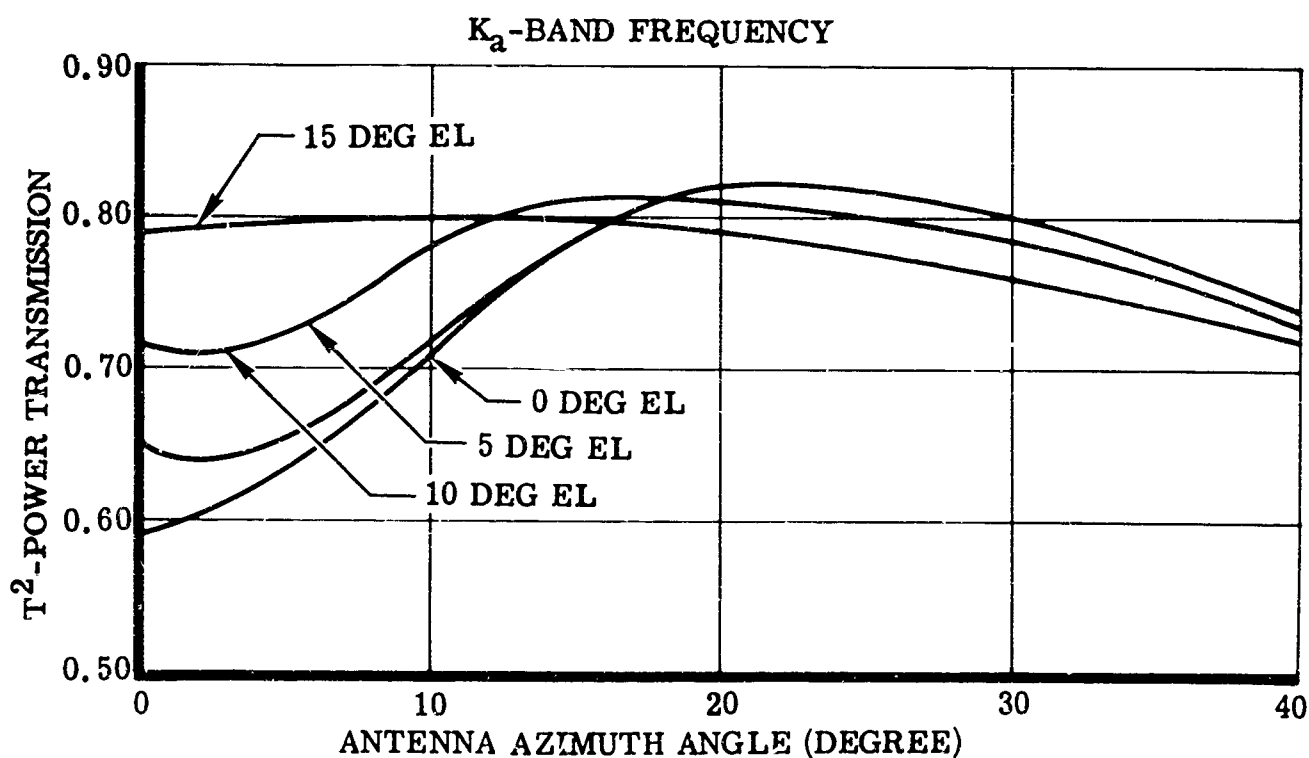
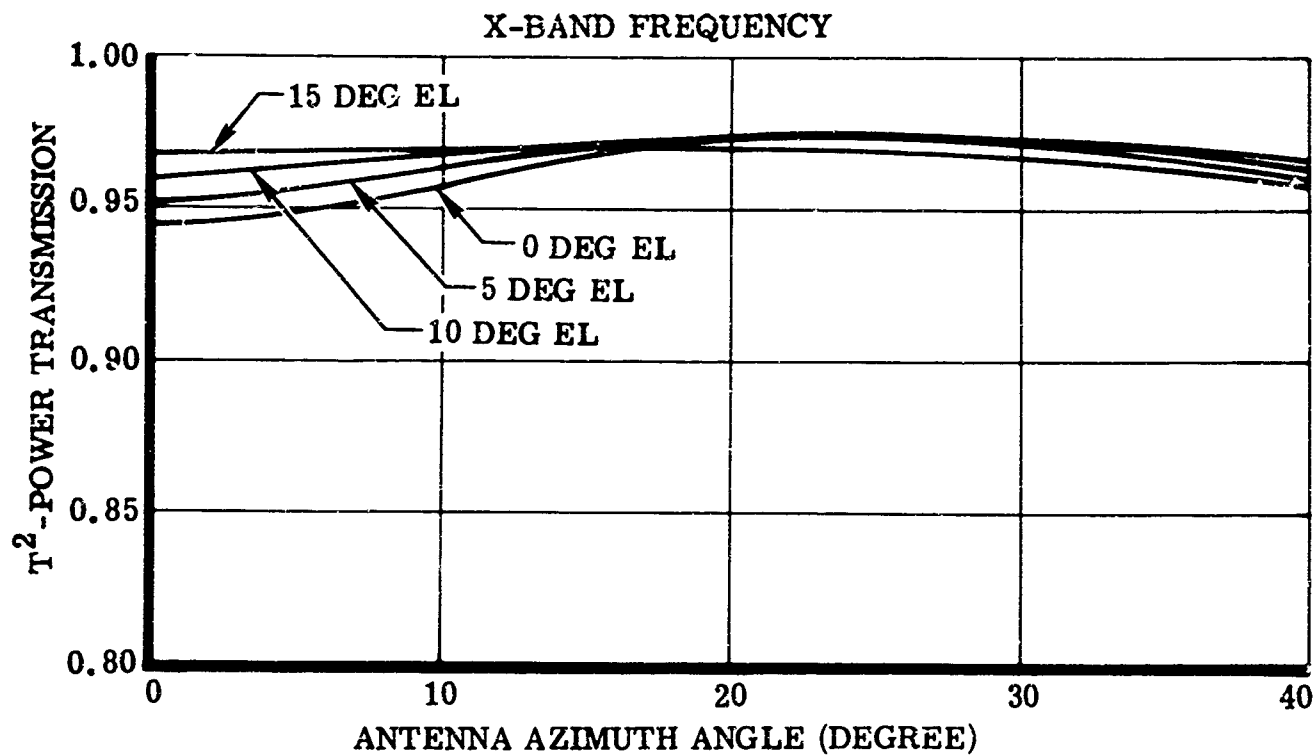


Fig. 11 Radome power transmission coefficient for Type II material.

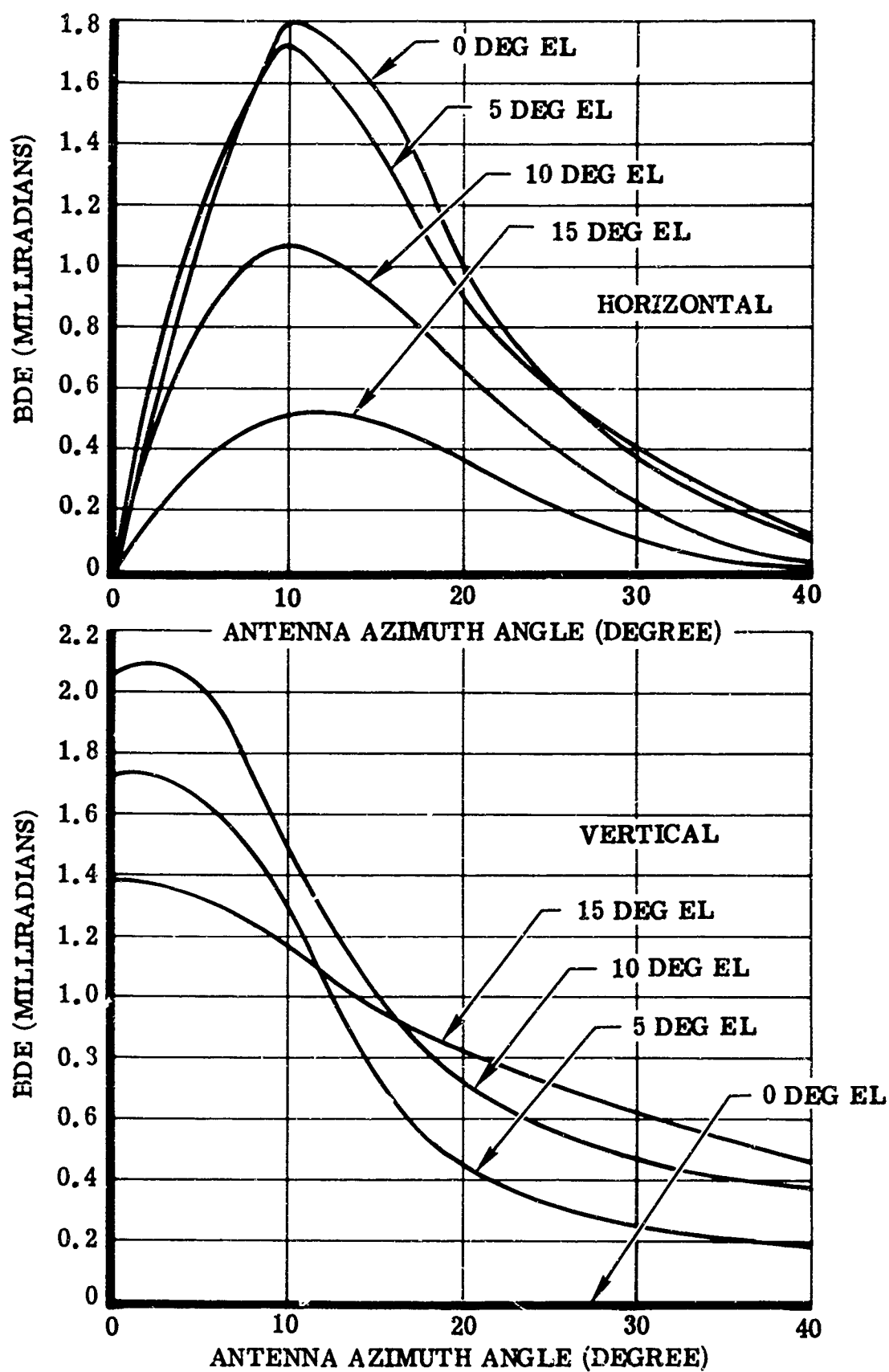


Fig. 12 Radome beam deflection error for X-band frequency, Type II material

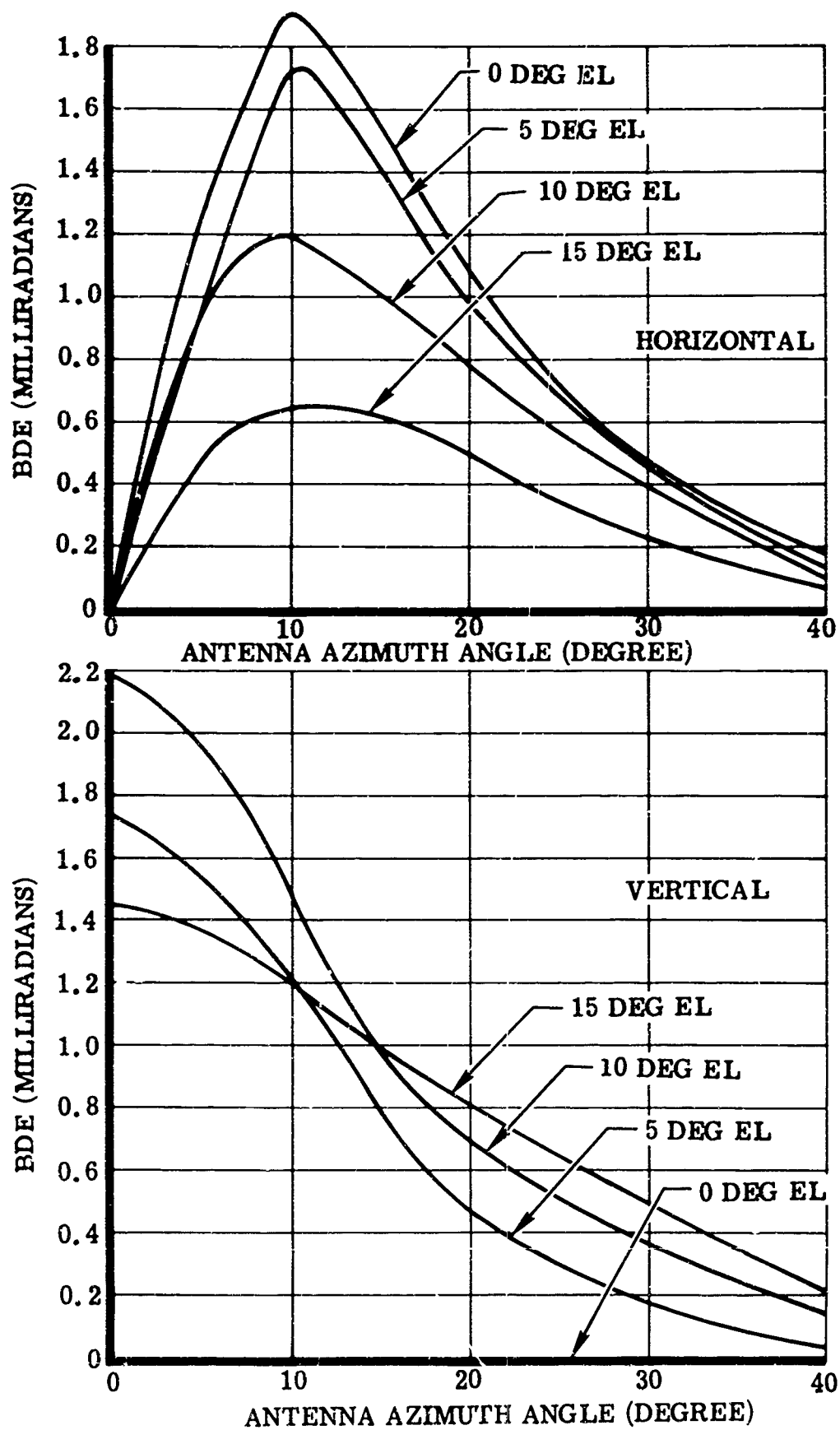


Fig. 13 Radome beam deflection error for K_a -band frequency, Type II material.

These radome performance results are well within the specification requirements listed in Tables I and II.

CONCLUSIONS

The results obtained by an analytical design and laboratory test program for electrical performance of dual-frequency, solid laminate radome test panels supports the feasibility of designing and constructing a workable dual-frequency radome of either Type I or Type II radome material. An analytical study and evaluation of the reactive wall concept for dual-frequency radome design indicated that the power transmission coefficient will be improved to a marked degree when the operating frequencies are not even multiples. Therefore, the advisability of using a reactive wall design will depend on radar operating frequency ratio required for a given application.

ACKNOWLEDGEMENT

The authors wish to express their thanks to J. Bowers for his assistance in this program.

REFERENCE

1. Robinson, L. A. and Jones, E. M. T., "Research and Development on the Electrical Properties of Metal Inclusions for Radomes," WADC Report 57-658, May 1958

TRANSMISSION CHARACTERISTICS OF GROUND BASED RADOMES

by

J. D'Agostino

F. Rouffy

Radiation Division
Sperry Gyroscope Company
Division of Sperry Rand Corporation
Great Neck, New York

I. INTRODUCTION

Since the onset of large ground based radars, the quest for a suitable weather protection has been initiated by various government and civilian agencies. These investigations have resulted in the use of three basic types of radomes: the air inflated, dielectric, and metal space frame radome (MSFR) configurations. The choice of the type of radome that will optimize the electrical and mechanical properties of the radar is often a very difficult task for not only must the designer be knowledgeable in the electrical and mechanical properties and tradeoffs associated with them, but must weigh the economics of the initial and operating costs.

It is therefore the purpose of this paper to summarize the fundamental electrical characteristics of the three basic types of radomes and to condense the electrical design parameters to a series of performance curves. The transmission characteristics are treated from the broad frequency band aspect; where optimum performance is required at a particular frequency, additional investigation is required.

II. AIR INFLATED RADOMES

Single wall and dual wall air inflated radomes such as shown in Figs. 1 and 2 offer the most expedient protection for transportable or semi-permanent radar system installations. ^{1,2}

Transmission losses for these air inflated radomes are a function of the thickness, dielectric constant, and loss tangent of the radome material as well as the radar system's frequency band. These losses, due to both absorption and reflection, are generally

negligible at low frequencies and increase rapidly above the point at which the radome becomes electrically thicker than $\lambda/32$, where λ is the free space wavelength.

For illustration of transmission loss effects, hypalon coated dacron (loss tangent = 0.038; dielectric constant = 3.0) is regarded as typical of the many materials both mechanically and electrically suitable for air inflated radome usage. Absorption and reflection losses for this material, as calculated from standard reference formulas, ^{3,4} are plotted in Fig. 3. This data is representative of the various electrical properties used in the construction of air inflated radomes.

The combination of absorption and reflection losses related to transmission efficiency for the single wall air inflated hypalon coated dacron radome is shown in Fig. 4. The high frequency behavior of air inflated radomes is predominantly influenced by reflection losses up to the frequencies at which the radomes appear electrically reflection free (half wavelength thick). Beyond this point the exponential increase of absorption losses predominate in determining radome transmission efficiency. For frequencies above 10,000 megacycles, narrow band operation may be achieved for half wavelength thick radomes.

The hypalon coated dacron material transmission loss calculations assumed normal incidence. For any particular antenna/radome combination, more detail calculations are required for investigations of elliptical polarization losses and transmission losses vs. variable polarization and variable angle of incidence.

The general set of curves in Figs. 5 and 6 give the losses through a solid dielectric wall radome. The total percent transmission efficiency is the product of the reflection loss efficiency times the dielectric loss efficiency. It is again apparent that the dielectric losses keep increasing with frequency. The upper limit of broad frequency band operation is noted from the reflection loss efficiency curves where the thickness is less than $\lambda/32$ for dielectric materials having values of dielectric constants approximately equal to 4.

The operation of a dual wall radome is the same as a single wall radome except that the two walls must be taken into account in determining the total loss. In most cases dual wall radomes use thinner skins than an equivalent single wall radome and the losses are generally only slightly higher than for the single wall radome. For

example the AN/TPS-34 50 foot diameter radome (Fig. 2) uses .015 inch thick inside wall with a .020 inch thick outside wall. A fifty foot single wall radome will in general have a 0.040 inch wall. The dual wall has additional losses where the air cells are joined to form an integral unit. The metallic fastener and dacron catenary lines also add some additional loss. In general, the losses for a dual wall radome will not exceed twice the losses of a single wall radome for frequencies where the skin thickness is less than $\lambda/32$.

The advantages of a dual wall radome far exceed the additional losses when the need for this type of radome is required. They are listed below:

- a) No air lock needed for entering the radome.
- b) Whole sections may be deflated for replacement or movement of large equipment into the dome without complete deflation. (see Fig. 7)
- c) Radome has a 4 hour stand time after loss of power.

Special single wall radomes are used to minimize boresight errors. The radome shown in Fig. 8 was used for the AN/SPG-56 fire control and missile tracker. Boresight accuracy was very critical so all seams were kept symmetrical about the reflector's vertical axis and the radome/antenna combination as a unit rotated in azimuth.

III. DIELECTRIC STRUCTURE RADOMES

Solid foam and flanged shell radomes, dielectric space frame radomes and honeycomb sandwich radomes are included in the category of dielectric structure radomes.

Analyses of the electrical transmission characteristics of solid foam and flanged shell radomes are similar to those for air inflated radomes and as such are not detailed here. Performance data for various specific designs is available from the sources listed in the MIT Radome Bibliography. ⁵

Analysis of dielectric space frame radomes are in general similar to those made in the next section for metal space frame radomes. For performance data of specific dielectric space frame radomes and information concerning exceptions to the general similarities between dielectric and metal space frames, reference is again made to the sources listed in the MIT Radome Bibliography.

The 140-foot BEMEWS radome shown in Fig. 9 illustrates the design features of honeycomb sandwich radomes. This particular radome is made up of 1646 internally bolted panels. A cross sectional view of each panel reveals a light-weight low dielectric craft paper core bonded in the fashion of a honeycomb; the core itself is bonded together by two thin fiberglass skins, hence the name honeycomb sandwich.

The transmission characteristics of honeycomb sandwiches are calculated by standard formulas.⁶ For example, the transmission characteristics of a honeycomb sandwich with a 6-inch core and 1/8-inch skin are shown in Fig. 10. The frequency response curve, calculated for normal incidence only, reveals the multiple half wave-length cyclic reflections that occur at the dielectric interfaces. The envelope of decreasing transmission efficiency for increasing frequency is based on absorption effects. In addition to the information in figure 10 the envelope of maximum reflection losses for a honeycomb sandwich design may be estimated by use of a universal type curve, such as in Fig. 5, which relates reflection losses to the electrical thickness of a lossless dielectric material.

In order to estimate the envelope of maximum reflection losses for the honeycomb sandwich shown in Fig. 10, only the total skin thickness (1/4 inch) is considered; for this type approximation core material reflections are considered negligible. Again, like the single wall radome, a good approximation to the maximum loss will be the product of the dielectric loss efficiency times the reflection loss efficiency.

A more exact analysis, justified only for a particular design, must include the effects of variable polarization over the angles of incidence and frequency bandwidth of interest. The exact analysis must also determine scattering losses due to the metallic panel interlocks; such a suitable analysis utilizing the "induced current ratio" is presented in various Ohio State University reports.⁷

IV. METAL SPACE FRAME RADOMES

An investigation of the feasibility of using metal space frame radomes (MSFRs), an answer to the problem of providing broad band, large diameter ground based radomes was reported by Lincoln Laboratories, M. I. T. in early 1957.⁸ The MSFR concept was regarded as practical on the basis of the transmission properties of a structural framework in which the separation between members is

of the order of a few wavelengths. For radar system usage, the development of spherical space frame radome design criteria emphasized mutual satisfaction of mechanical and electrical functional requirements. Mechanically, the frameworks are designed to accept environmental loading and to incorporate installation economy through the use of as many duplicate structural members as possible. Electrically, the metal frameworks are designed to present as minimal an aperture blockage as possible with either a random or regular polarization sensitive member alignment which is consistent with minimal boresight shift effects.

A. Spherical Geometry Relations

The geometrical configurations of MSFRs are related to the basic polyhedra which are inscribable on a spherical surface. These polyhedra fall into two categories: ⁹

1. "Platonic" Solids - These solids have regular faces (equal congruent sides) and vertices which are regular (equiangular) polyhedral angles. The five "Platonic" solids are:

1. Tetrahedron	4 faces
2. Hexahedron (cube)	6 faces
3. Octahedron	8 faces
4. Dodecahedron	12 faces
5. Icosahedron	20 faces

2. "Archimedian" Solids - These semi-regular solids have regular faces, but not all of the same kind, and vertex figures which are congruent but not regular. Two of the 15 possible "Archimedian" solids, the icosidodecahedron and the snub dodecahedron, were initially investigated for metal space frame usage but later were de-emphasized in favor of the more expedient and practical development of spherical projections for two of "Platonic" solids, the Icosahedron and the Dodecahedron.

Three different types of presently operational metal space frame radomes are derived from spherical projections of the Icosahedron and the Dodecahedron. Each of these radomes is identified by the geometrical term which most suitably describes either the "Platonic" projection or the basic repetitive configuration with the "Platonic" projection. The two radome types derived from the

Icosahedron are identified here as the Trapezoidal Hexacontahedral and Icosahedral radomes. The third radome type, derived from the Dodecahedron, is identified as the Dodecahedral radome.

B. Radome Geometries in Current Use

1. Trapezoidal Hexacontahedral Radome - The latticework or rib orientation within any one of the repetitive regular triangular faces is shown in Fig. 11. The heavy dashed lines trisect this basic triangle into three smaller congruent trapezoidal sections each of which occupies $1/60$ of the total surface area, (thus the term "Trapezoidal Hexacontahedral").

The light dashed lines illustrate the manner in which adjoining trapezoidal sections form a complete surface. With the exception of common panels, each trapezoidal section is seen to be made up of two (left and right handed) Schwartz triangles. Schwartz triangles by definition are the spherical congruent triangles which by repeated reflection in their sides cover a spherical surface an integral number of times.

The rib orientation shown in Fig. 11 was made random, polarization insensitive, by breaking the regularity of the sides of the trapezoidal figures in such a way that the interconnecting framework is randomly oriented (no more than two ribs lie on the same great circle arc) yet is symmetrical about the common sides of the two Schwartz triangles which make up the trapezoid.

The Trapezoidal Hexacontahedral geometry is used in the CW-620/FPS-35 150-foot radome at Baker, Oregon, the AF/MIT Lincoln Labs Haystack Antenna System 150-foot radome at Tyngsborough, Mass., and the 110-foot radome at Ft. Greely, Alaska.

The manner in which the basic triangles are located on Trapezoidal Hexacontahedral CW-620/FPS-35 Radome is illustrated in Fig. 12. Five of the spherical triangles lie between the north pole and the region above the small circle which is the 60° latitude. Ten triangles occupy the region between the upper and lower 60° latitudes. The other five triangles lie in the lower polar region. The radome structural lattice or pattern as seen by an antenna during azimuth plane rotation is repeated five times, or every 72° .

2. Icosahedral Radome - The latticework within any one of the twenty regular faces of this radome is shown in Fig. 13. The centroid of the basic triangle is located in a common panel of three otherwise similar trapezoids which, in the same manner of Fig. 11, are made up of a pair of Schwartz triangles. The common center panel precludes use of term Trapezoidal Hexacontahedral, the description as Icosahedral geometry suffices.

The Icosahedral geometry is used in the 55-foot diameter Nike-Zeus TTR 2-psi Hardened Radome.

3. Dodecahedral Radome - The geometry of this radome is derived from the 12 faced dodecahedron. As shown in Fig. 14 each pentagonal face is subdivided into five congruent triangles. As for the other radome geometries, a random rib orientation was achieved. No symmetries exist in this geometry; however, the design economy is apparent as one visualizes the vertex of a repetitive triangle as being reflected about the centroid of the pentagonal faces of the Dodecahedron. The unit surface area of a repetitive triangle in the Dodecahedral radome is the same as the unit surface area in the trapezoidal sections of the other two radome designs.

The Dodecahedral geometry is used in the Nike-Zeus 110 ft. diameter radome at White Sands, New Mexico.

C. Insertion Loss Analysis

Insertion losses due to MSFRs are attributed to two sources: 1) the physical or geometrical blockage presented by the structural framework of the radome, and 2) low-frequency resonance effects at the radome hubs.

1. Physical Blockage - The empirically determined relation between physical blockage and transmission loss is plotted in Fig. 15. Proportionality factors of approximately 1.7:1 and 2:1 for random and regular geometries, respectively, are used to express physical blockage in percentage transmission loss. For the trapezoidal hexacontahedral geometry radomes, the physical blockage is approximately 6-1/2%; for the Icosahedral and Dodecahedral geometries the physical blockages are approximately 8% and 6% respectively. The minimum transmission loss for metal space frame radomes thus varies from approximately 10% to 16% or 0.5 db to 0.8 db; exact values for any particular radome depend upon design details.

2. Low-Frequency Resonance Effects - For frequencies lower than those at which the electrical wavelength is larger than the hub diameter, additional insertion losses are caused by resonance (electrical shadowing) between the closely spaced adjacent ribs at a hub junction. This condition is regarded as one in which the effective hub area becomes increasingly larger for progressively lower operational frequency (longer wavelength).

The physical blockage or structural area for the various MSFR designs consists of approximately 90% rib area and 10% hub area. Since the low-frequency resonance effects are in addition to the initial 10% contributing sources of transmission loss, the additional insertion losses due to the resonance effect are expected to be small for wavelength/hub diameter ratios less than 2:1. However, as the operational wavelength becomes several times larger than the hub diameter (or the mean spacing between rib centroids) the additional insertion losses increase rapidly so that the radome acts as a low frequency cut-off device. These effects are plotted Fig. 16 for the various radome geometries. The analysis leading to figure 16 is based on Rayleigh-type scattering from randomly oriented ribs and on the increased hub areas predicted by Fig. 17. In Fig. 17 hub areas are determined (without regard to polarization effects) from polygons each of whose sides are a quarter wavelength long and perpendicular to the center of the hub.

The information of Fig. 16 is translated into Fig. 18 to illustrate the calculated frequency response characteristics of the various geometries. For Fig. 18 a 150-ft diameter radome is used as the reference size.

The frequency response analysis is further extended in Fig. 19 to illustrate the relations between radome diameter and cut-off frequency ($\leq 80\%$ transmission) for the various radome geometries. The effects of scaling the various radome geometries can be anticipated from an inspection of Figs. 11, 13 and 14. A lower cutoff frequency will be associated with the relatively open Dodecahedral latticework of Fig. 14 than with the relatively smaller, closer spaced, Icosahedral latticework of Fig. 13.

Since an extensive engineering analysis for any particular design can be made only in terms of the peculiarities of the specific design, the information in Figs. 16-19 is intended for and presented only as a handbook type analysis of the frequency response characteristics of metal space frame radomes.

V. COMPARISON OF RADOME TYPES

A. Transmission Loss

Fig. 20 presents frequency response characteristics for the three major different types of radomes: the air inflated, honeycomb sandwich, and MSFR. A 100-foot diameter radome was chosen as a nominal size for comparison. The frequency response characteristics of the air inflated and honeycomb sandwich radomes are the same as previously shown in Figs. 4 and 8. For a constant cross-sectional dielectric thickness, the transmission loss vs. radome diameter relations are essentially constant; changes in transmission loss effects are primarily due to changes in material thickness as required for the structural integrity of various size of radome diameters. The transmission loss vs. diameter characteristics of MSFR as shown in Fig. 18 and 19 are a function of radome geometry. That is, the relative number of ribs per unit area and the mean number of ribs at the hub junctions determine the transmission loss vs. diameter relations. The air inflatable and honeycomb sandwich radomes exhibit the characteristics of a low pass filter; in contrast, metal space frame radomes exhibit high pass filter characteristics.

B. Sidelobe Level Changes

For the air inflated and honeycomb sandwich radomes, sidelobe level changes can be approximated by calculating the insert phase delay produced for a particular antenna/radome combination. The calculated insert phase information can then be used to determine the associated antenna aperture phase error, for which sidelobe level increases can be calculated.

The presence of metallic members randomly oriented in the radome structure also produces sidelobe level increases. These effects can be evaluated by an analysis which utilizes a "scattered energy level" to predict the envelope of maximum sidelobe level increases. This "scattered energy level" is determined by an examination of the flat portion (minimum loss bandwidth) of the MSFR frequency response characteristics as indicated in Fig. 18. The "scattered energy voltage levels" are added to the quantized antenna voltage pattern in order to determine the maximum sidelobe level increases for a given antenna to radome combination. This analysis is illustrated in Fig. 21; the angularly dependent "scattered energy level" established for the Trapezoidal Hexacontahedral radome geometry is added to the quantized pattern of a typical 50 to 55 wavelength

aperture antenna. The effects of metallic interlocks in honeycomb sandwich radomes and the ribs of MSFRs can be analyzed in the same manner; however, different weighing factors are used for each type of randomly oriented structure. The maximum value of the "scattered energy level" is determined from the energy level associated with the on-axis transmission loss. The difference, or weighting factors, between dielectric and MSFRs is in the type of loss associated with the on-axis transmission loss. The MSFR loss is essentially all scattered energy loss while the honeycomb sandwich or solid dielectric losses are composed of absorption and reflection losses; the scattered or reflected energy losses may be used to establish the peak values of the "scattered energy levels" for the various types of radomes.

C. Boresight Shift Effects

The insert phase relations previously discussed for air inflatable and honeycomb sandwich radomes sidelobe level changes also produce boresight shift errors. The magnitude of these errors depend upon the displacement between the antenna rotation axes and the geometric center of the radome, as well as the dielectric properties of the radome material. These errors are illustrated in Fig. 22 for a particular antenna to radome configuration in which the radome consists of a single dielectric layer. The boresight shift errors normally encountered in air inflatable radomes are similar to, but of a lower magnitude than, those illustrated in Fig. 22.

Reference to published performance data 8, 10 provides the following representative boresight shift information for honeycomb sandwich and metal space frame radomes:

- o Honeycomb Sandwich (140-ft. BEMEWS RADOME)
 Boresight Error 0.3 mils
 Boresight Error Rate 0.005 mils/mil
- o Trapezoidal Hexacontahedral Metal Space Frame Radome
 Boresight Error 0.65 mils (maximum)¹¹
 0.20 mils (average)¹¹
- o Icosahedral Metal Space Frame Radome
 Boresight Error 0.10 mils for 99% of
 measured values.
 0.15 mils maximum
- o Dodecahedral Metal Space Frame Radome
 Boresight Error 0.3 mils
 Boresight Error Rate 0.005 mils/mil

VI. Conclusion

Three basic types of radomes have been described in the previous test with corresponding transmission properties. For broadband operation there is a basic difference in the operation of the dielectric or metal space frame radomes. The air-inflated radomes and honeycomb radomes are good for low frequency operation and become poorer as the skin thickness exceed a half wavelength in electrical thickness. The metal space frame radome has a definite low frequency cutoff and becomes poorer with frequency when the membranes between the metal space frame structure exceeds a half wavelength in electrical thickness. The metal space frame radome, however, has the advantage in one respect that while the basic scattering losses are higher, they remain relatively constant with frequency, and the upper limit of the radome's operation, like the dielectric radomes, is the skin thickness. The skin thickness in MSFRs is not used structurally as in the dielectric radomes and therefore may be made much thinner to maintain the high frequency operation.

In general, the radome with the overall best electrical properties is the air inflated radome. For durability the dielectric (honeycomb sandwich or solid dielectric) radome is best suited for low frequency operation while the metal space frame radome is best suited for frequencies above its low frequency cutoff. There is obviously a crossover region where more than one type of radome may satisfy the electrical transmission requirements. The selection of a radome for crossover region operation thus progresses to a tradeoff study between the cost factors and mechanical (structural) requirements for each type of electrically acceptable radome.

VII. REFERENCES

1. Niechniedowicz, F. and Bird, W. "Dual Wall Radomes" Signal Vol. 15, No. 5, p. 40, January 1961.
2. Beal, C. S. , "Radomes for Ground USAF Equipment Phase I Air-Supported Radomes", November 1953, RADC Technical Report 53-6.
3. Cady, Karelitz and Turner, "Radar Scanners and Radomes," Vol. 26, p 261, MIT Rad. Lab. Series, McGraw-Hill Book Co. N. Y. , 1948.
4. Silver, S. , "Microwave Antenna Theory and Design", Vol. 12, p. 339, MIT Rad. Lab. Series, McGraw-Hill Book Co. , N. Y. , 1949.
5. Weinberger, J. and Orabona, J. F. , "Lincoln Laboratory 15th Reference Bibliography", MIT, January 30, 1963, AFESD-TDR-63-31, AD 401 159.
6. Jasik, H. , Editor, "Antenna Engineering Handbook", Chapter 32, McGraw-Hill Book Co. , N. Y. 1961.
7. Ohio State University Research Foundation Series 722, 722-1 to 722-17.
8. Quarterly Progress Reports, Division 7, Lincoln Laboratories, MIT, January 1957 to present, inclusive.
9. Encyclopedia Britannica, 1945 Edition, Vol. 20, p. 941 (Refer to: Solids, Geometric)
10. Curtis, R. B. and Vaccaro, J. , "Survey of Ground Radomes", Rome Air Development Center, May 1961, RADC-TR-61-52, AD 258 776.
11. Quarterly Progress Report, Division 7, Lincoln Laboratories, MIT, 15 July 1958 AFCRC-TN-58-1016, p. 37, AD 303131.



FIGURE 1
SINGLE WALL AIR
INFLATED RADOME

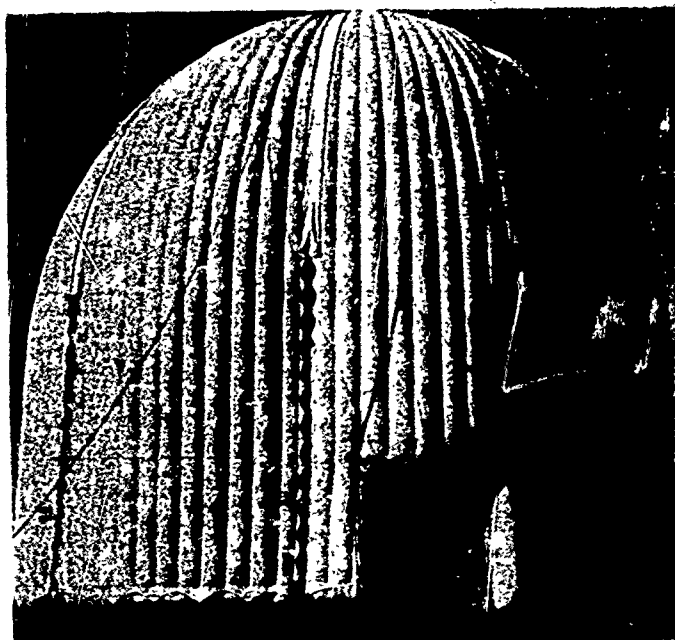


FIGURE 2
DUAL WALL AIR INFLATED RADOME

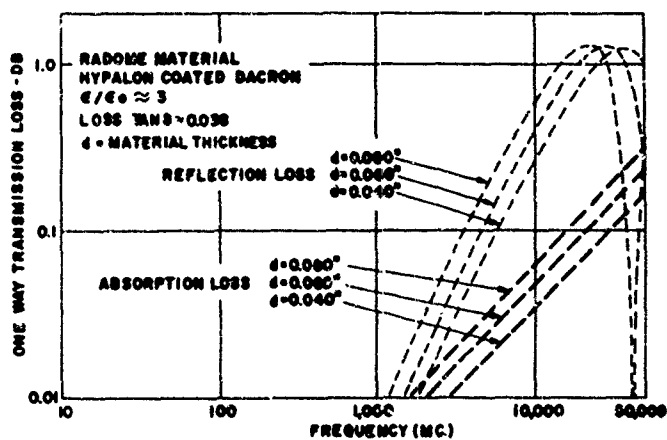


FIGURE 3. SINGLE WALL AIR INFLATED RADOME REFLECTION
AND ABSORPTION LOSSES

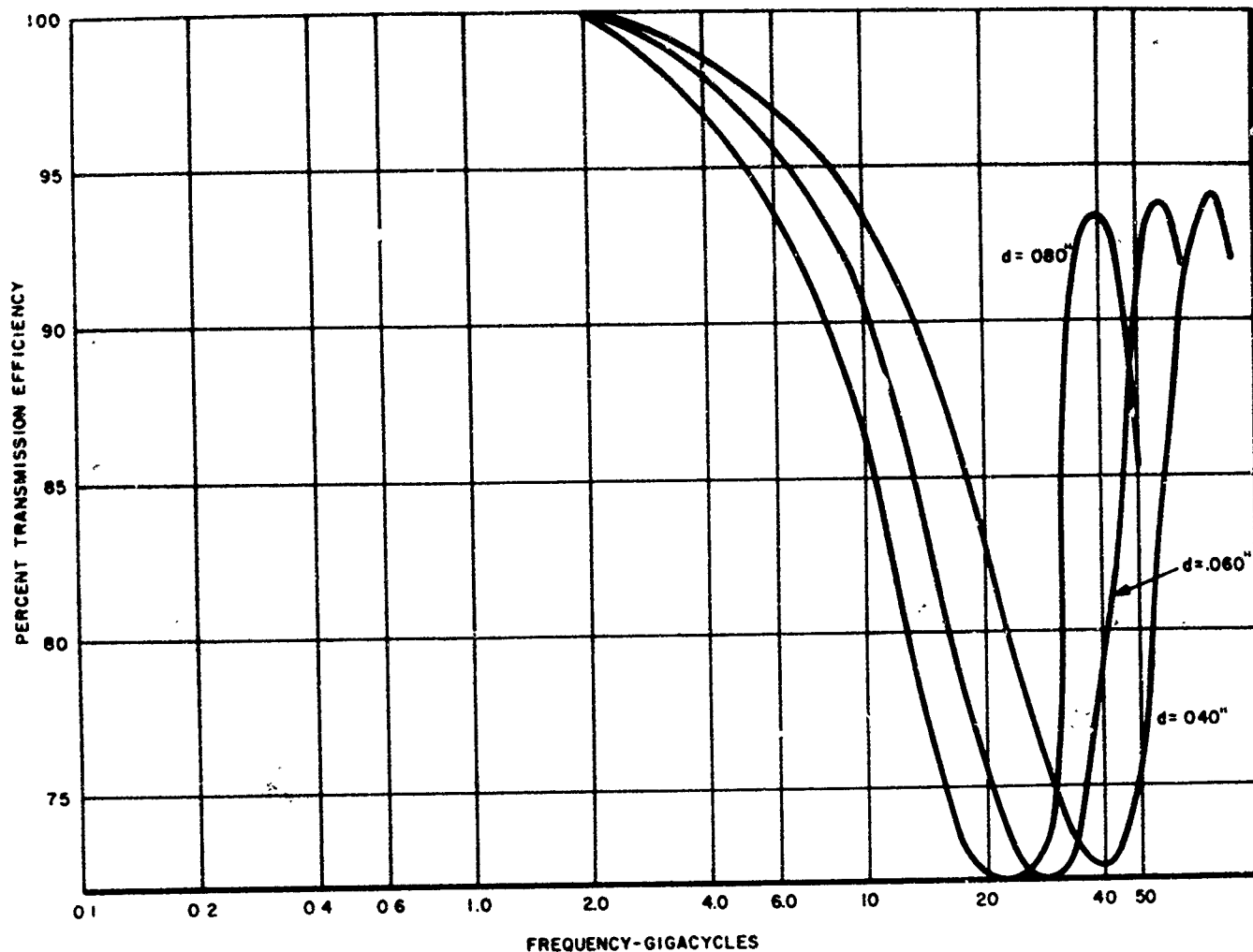


FIGURE 4
 PERCENT TRANSMISSION CHARACTERISTICS OF
 HYPALON COATED DACRON $\epsilon/\epsilon_0 \approx 3$
 LOSS $\tan \delta \approx .038$ d = MATERIAL THICKNESS
 SUM OF REFLECTION AND ABSORPTION LOSSES

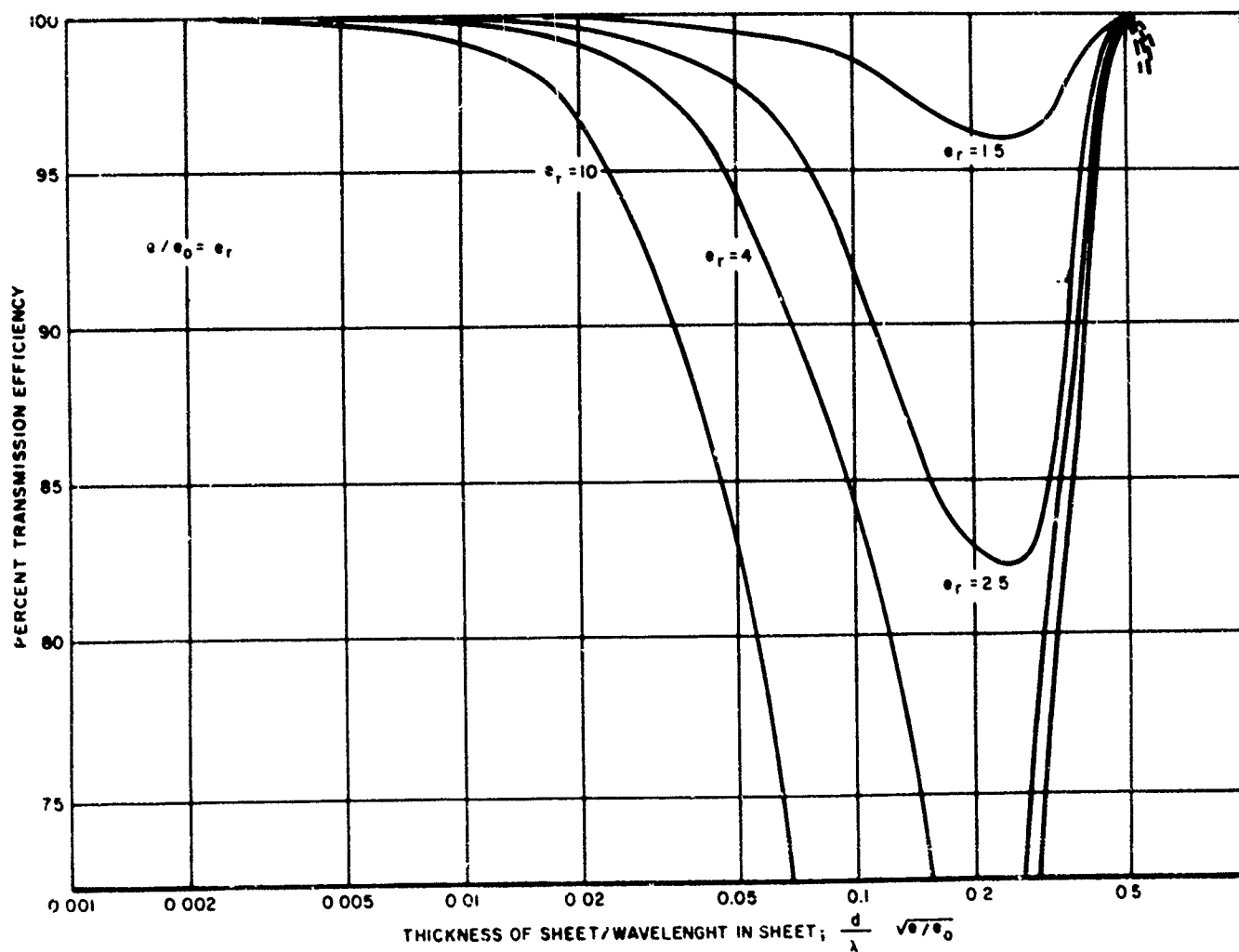


FIGURE 5

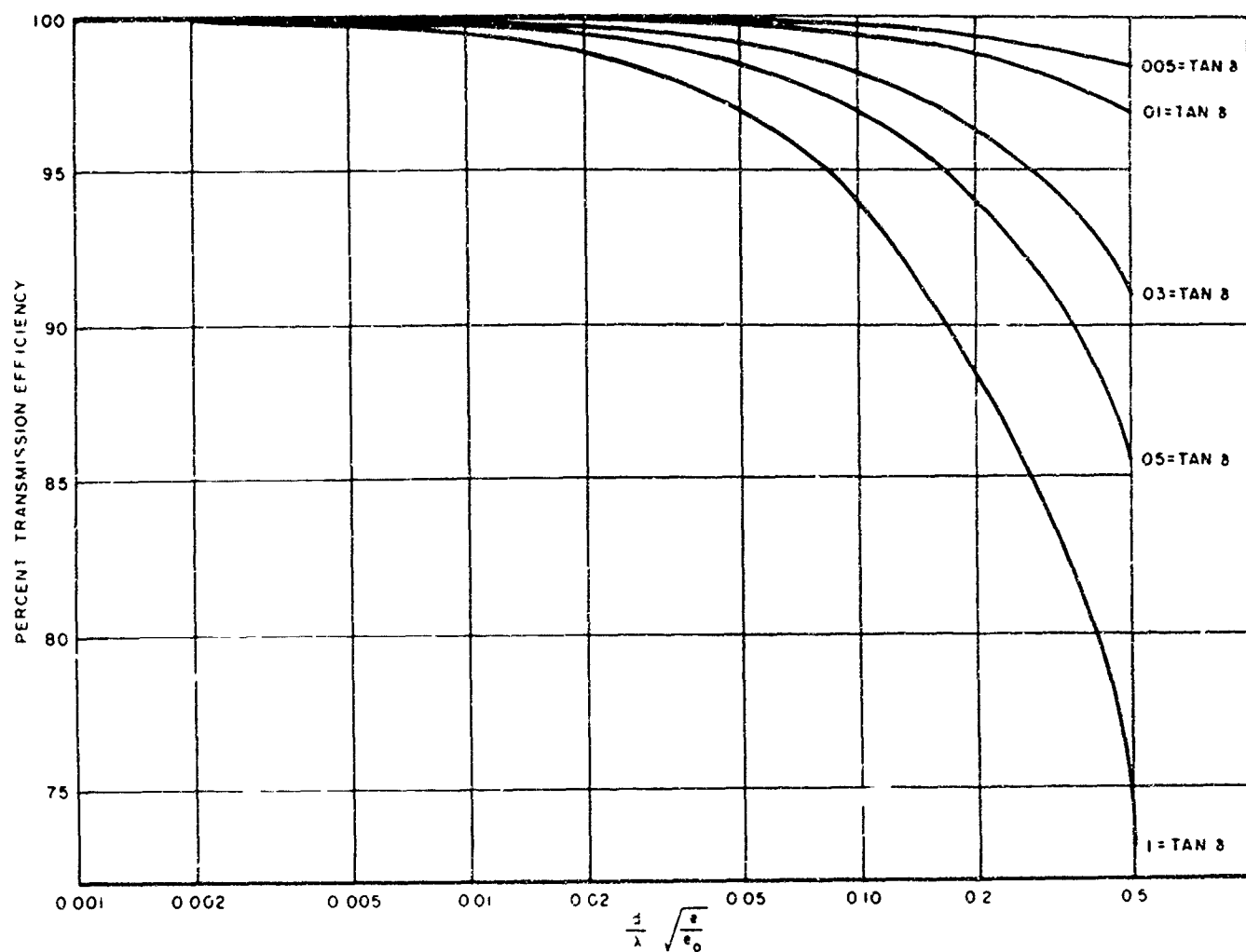


FIGURE 6
PERCENT TRANSMISSION CHARACTERISTICS
OF A SOLID DIELECTRIC SHEET
(ABSORPTION LOSSES-DIELECTRIC LOSSES)

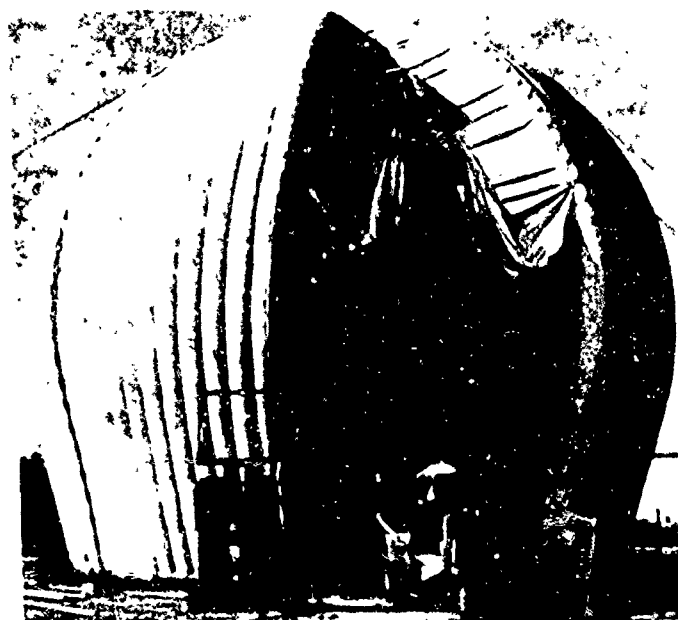


FIGURE 7
DUAL WALL AIR INFLATED RADOME
(SECTION OPENED)

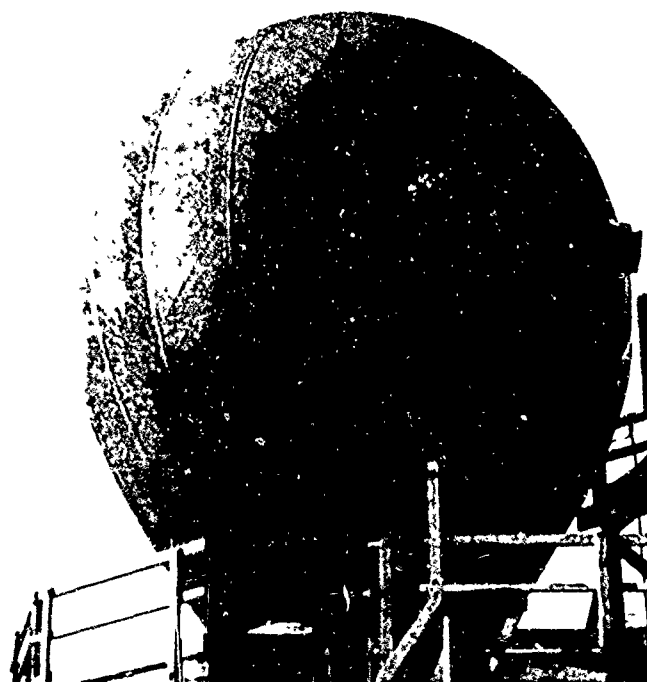


FIGURE 8
MINIMUM BORESIGHT ERROR RADOME

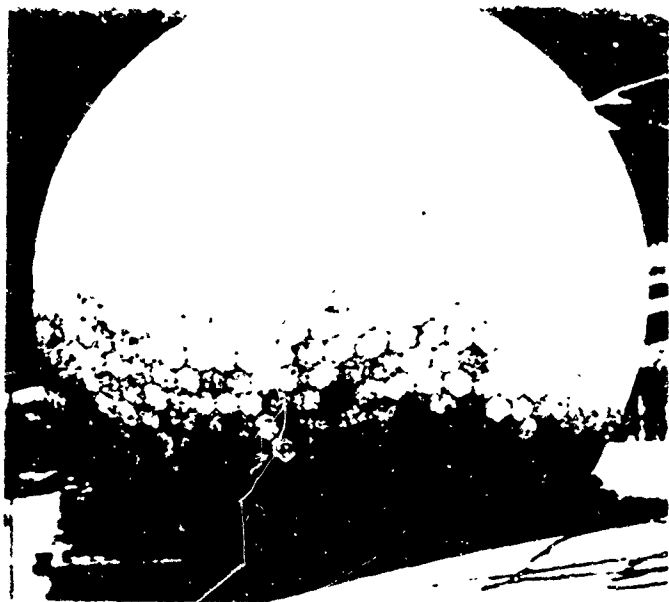


FIGURE 9
HONEYCOMB SANDWICH RADOME
BMEWS 140 FT.

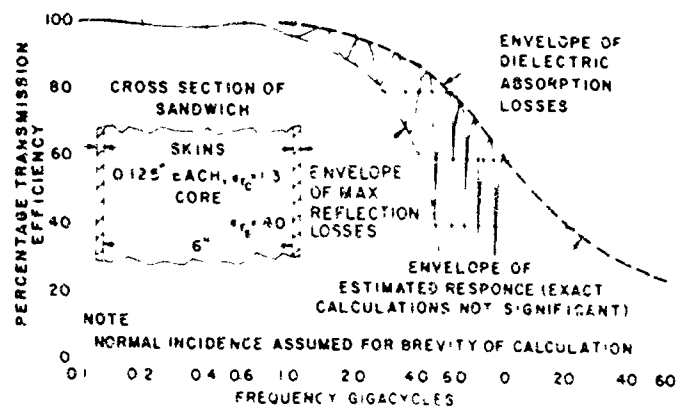


FIGURE 10 TRANSMISSION CHARACTERISTICS
FOR HONEYCOMB SANDWICH RADOME

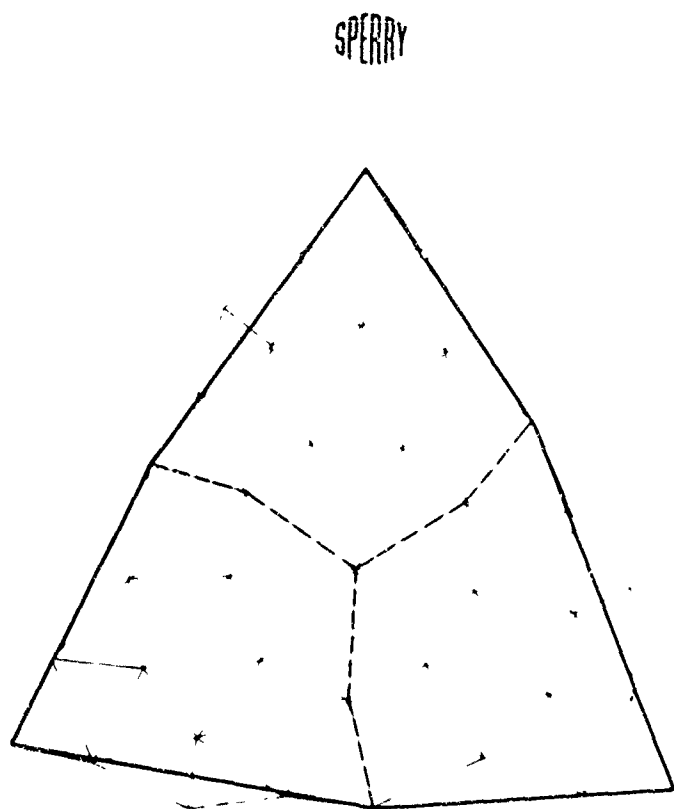


FIGURE 11 BASIC TRIANGLE TRAPEZOIDAL
HEXACONTAHEDRAL GEOMETRY



FIGURE 12
CW-62C/FPS-35 RADOME
SHOWING BASIC TRIANGLES

SPEARY

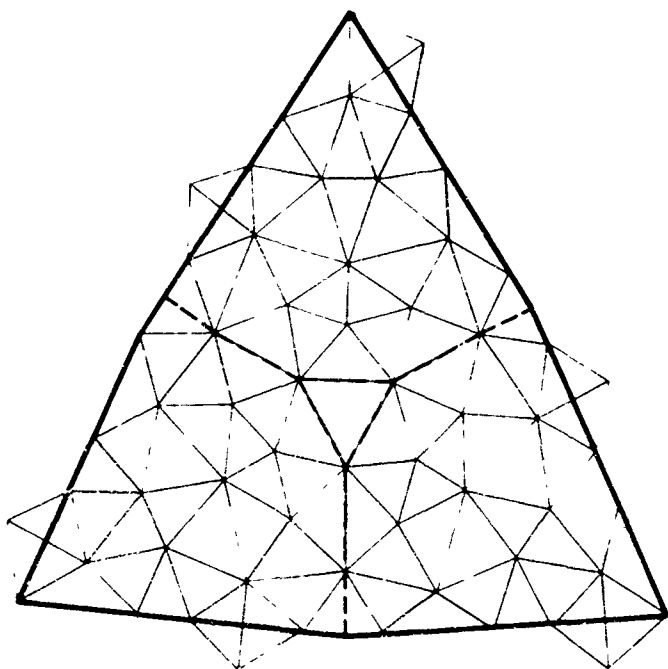


FIGURE 13. BASIC TRIANGLE ICOSAHEDRAL GEOMETRY

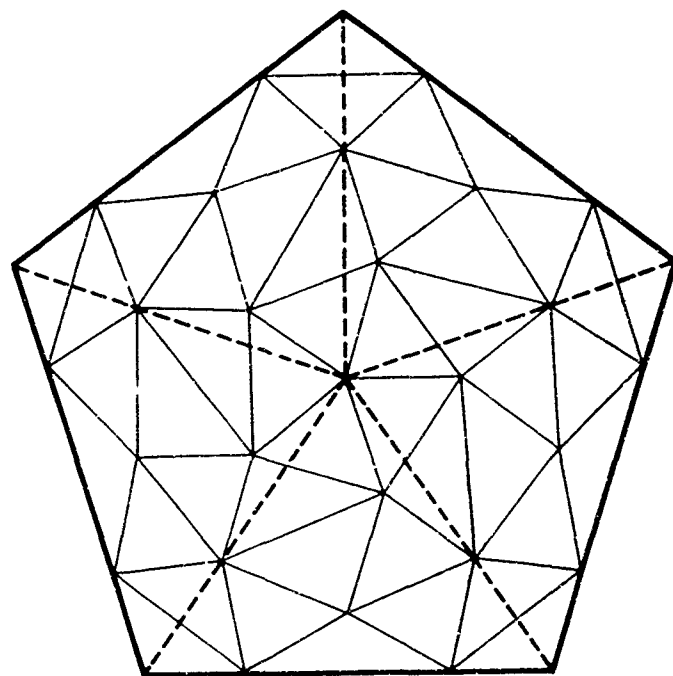


FIGURE 14. BASIC PENTAGON DODECAHEDRAL GEOMETRY

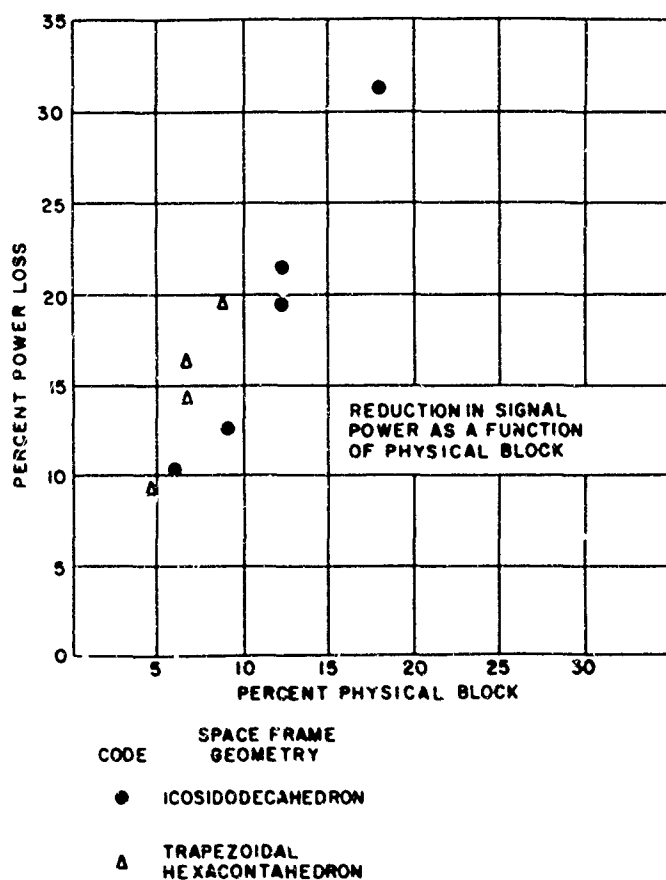


FIGURE 15. TRANSMISSION EFFICIENCY VS. PHYSICAL BLOCKAGE

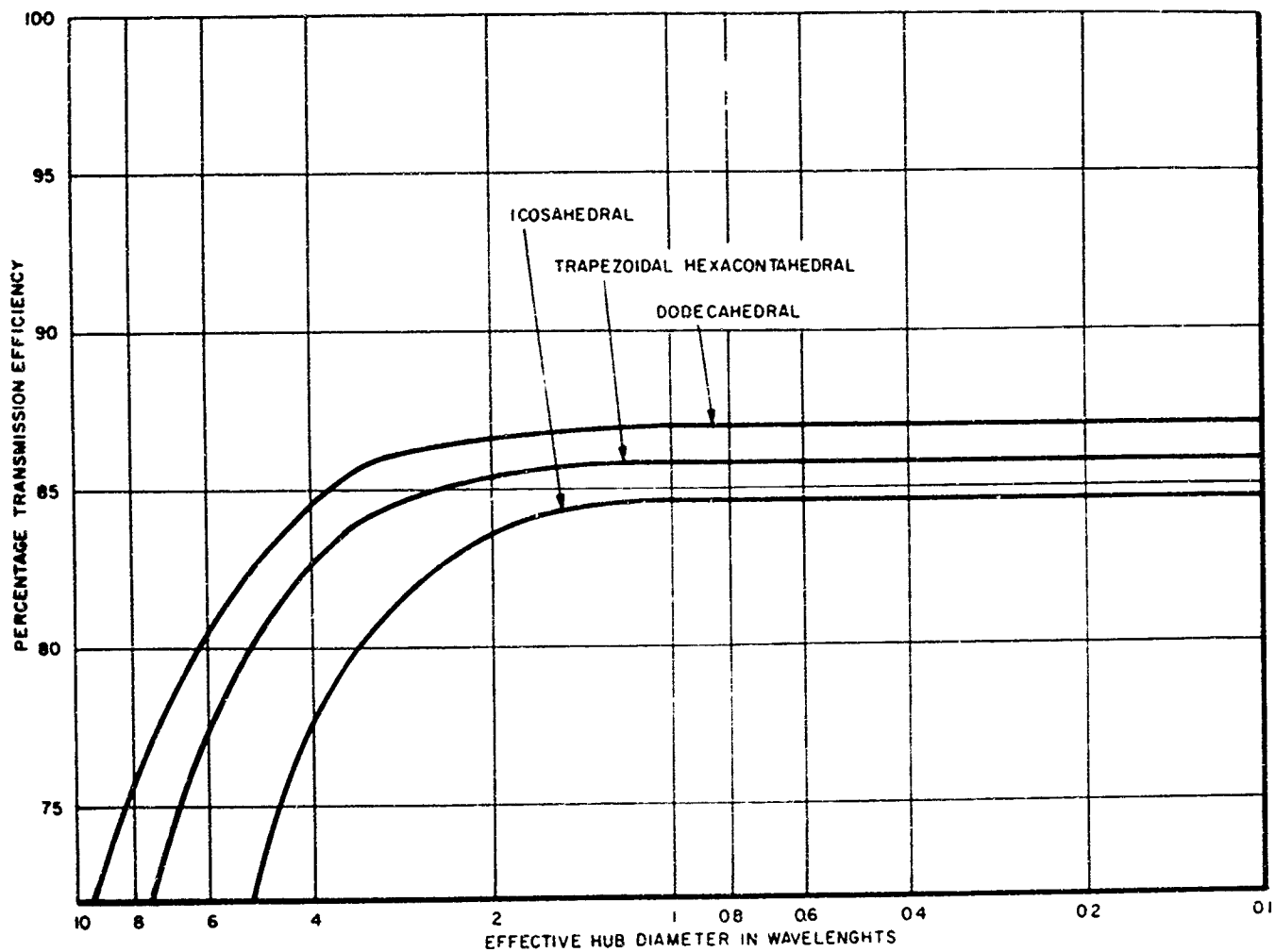


FIGURE 16
PERCENT TRANSMISSION VS. EFFECTIVE
HUB DIAMETER FOR VARIOUS MSFR GEOMETRIES
[PHYSICAL BLOCKAGE INCLUDED]
[PHYSICAL = HUBS + SPACE FRAME]

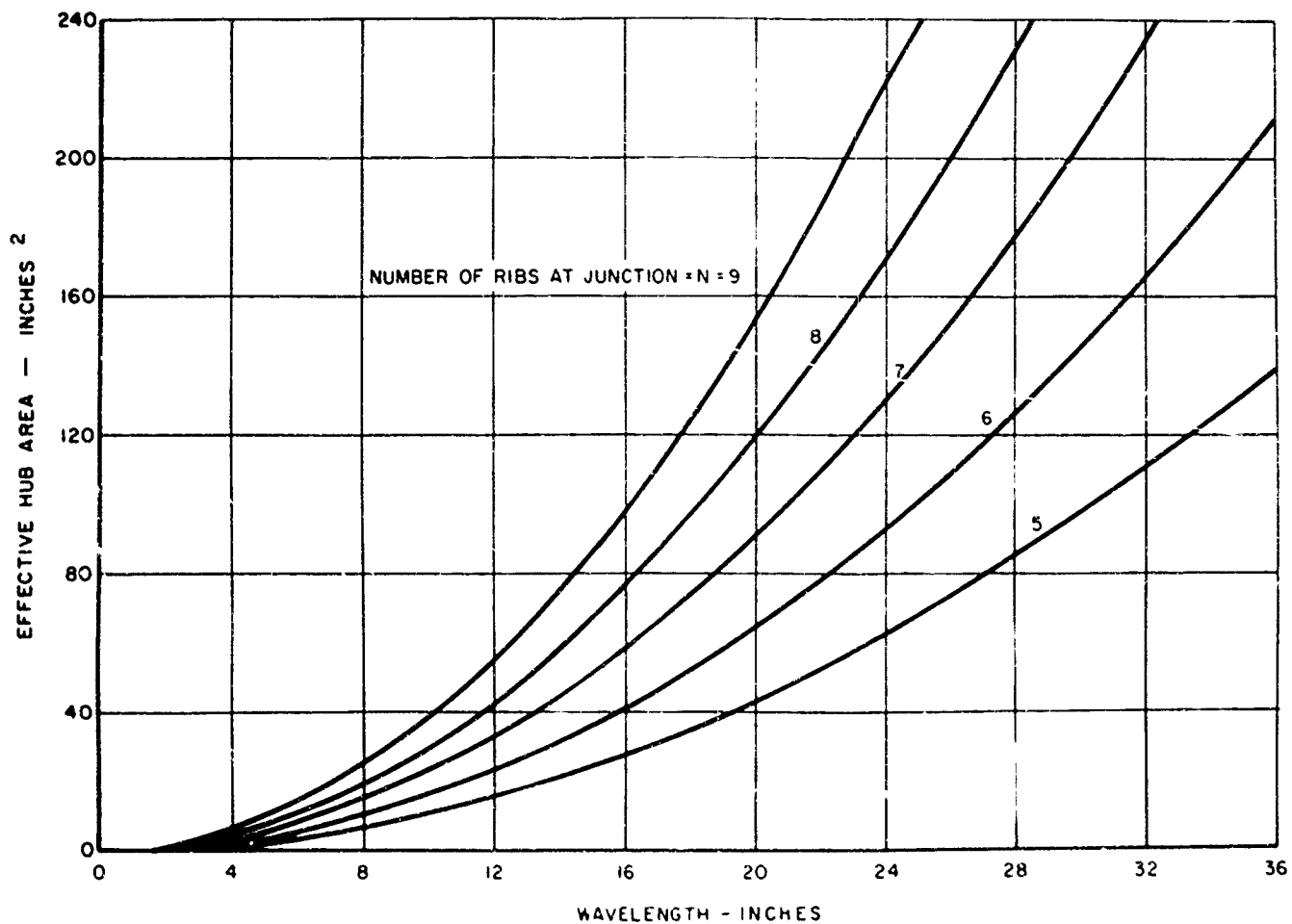


FIGURE 17 EFFECTIVE HUB AREA VS WAVELENGTH
VARIOUS HUB GEOMETRIES

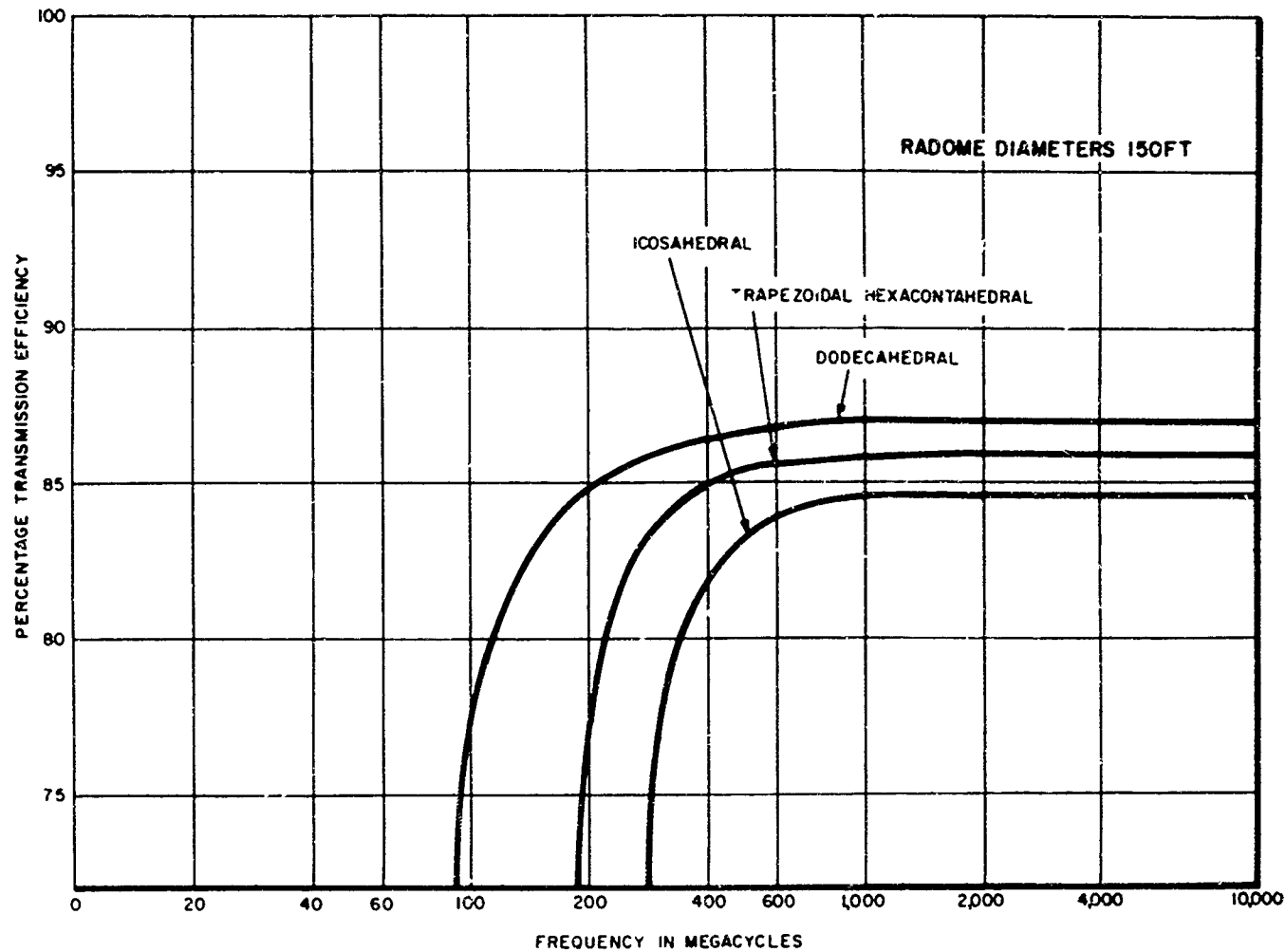


FIGURE 18
PERCENT TRANSMISSION EFFICIENCY VS. VARIOUS MSFR
GEOMETRIES

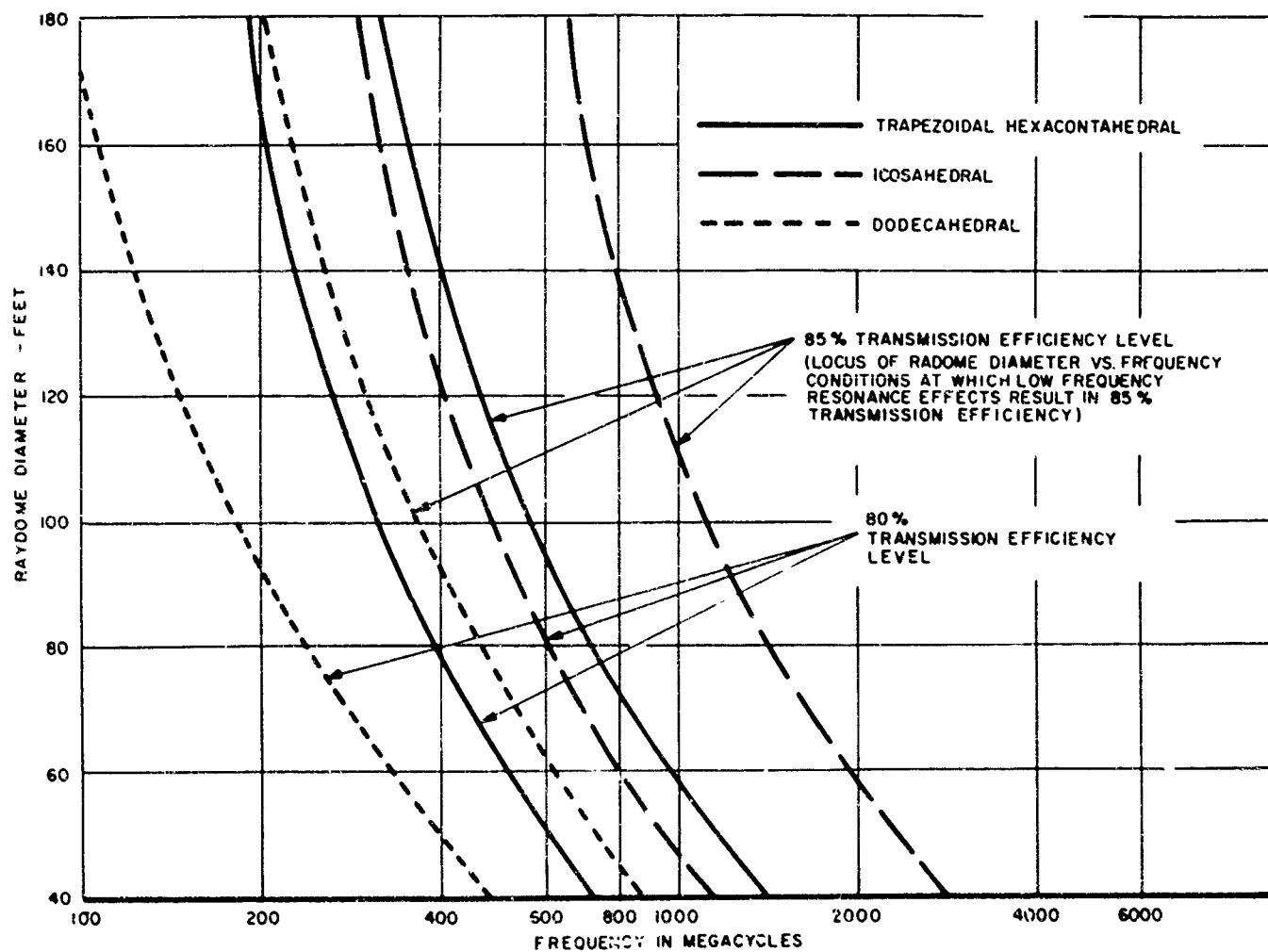


FIGURE 19
CUT-OFF CHARACTERISTICS OF MSFR
AS FUNCTION OF SIZE AND GEOMETRY

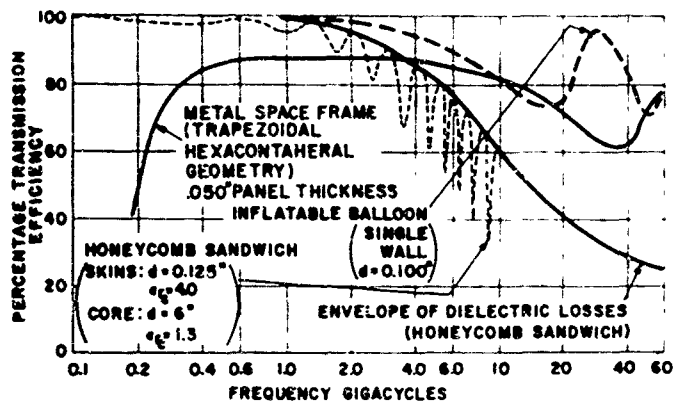


FIGURE 20. TRANSMISSION EFFICIENCY COMPARISON OF 100 FT. DIELECTRIC AND MSFRS

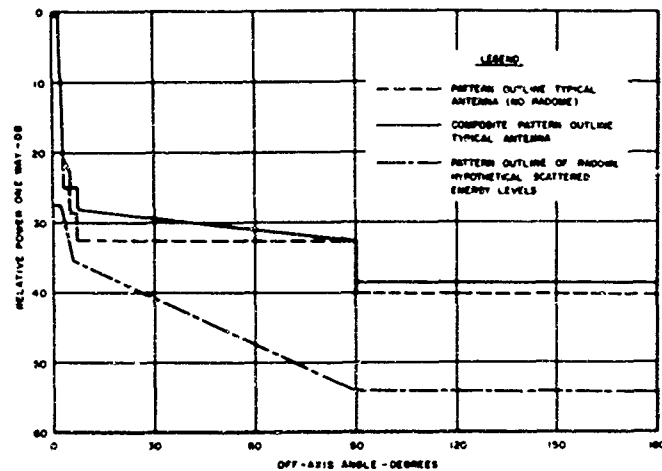


FIGURE 2. PREDICTED MAXIMUM SIDELOBE LEVEL OF MSFRS

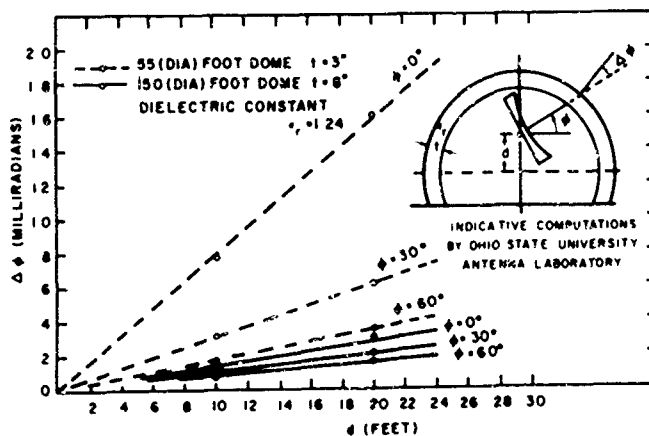


FIGURE 22. BORESIGHT SHIFT AS A FUNCTION OF OFF-AXIS ANTENNA POSITION IN IDEAL SPHERICAL THIN SHELL RADOME

RADOME THERMAL DESIGN FOR A MACH 4 MISSILE

R. P. Suess and L. B. Weckesser
Johns Hopkins University, Applied Physics Laboratory

Introduction

Previous favorable experience with Pyroceram as a radome material led to its choice in a design study for a new Mach 4 missile. Because the expected thermal environment would be more severe than any previously encountered by the material, a thorough temperature and stress analysis had to be made to insure the radome could withstand the flight thermal stresses.

Definition of Critical Thermal Environment

Before the temperature and stress analyses were performed, it was necessary to choose the one missile trajectory which would be the most thermally severe. Because this could not be done by inspection, a trajectory analysis was performed in which twenty-one representative trajectories, both ballistic and line of sight, were considered. Each of these trajectories was used to generate aerodynamic heating on several dummy geometries of varying thickness. The trajectory chosen as the one which would generate the maximum radome thermal stress was the one giving the highest rate of heat input; i.e., the one generating the steepest temperature-time slope. Two interesting results arose from the trajectory analysis:

1. The line of sight trajectories gave higher heating rates than the ballistic trajectories and it was noted that the launch angle did not influence the heating rate significantly.
2. The choice of the thermally severe trajectory was not affected by material thickness.

Figure 1 presents the Mach number and altitude history of the trajectory found most thermally severe. Note that the maximum Mach number of the trajectory is considerably below the design number (4.0) of the study. The trajectory analysis revealed that those trajectories which achieve a Mach number of 4.0 were not critical from a radome thermal stress viewpoint.

Radome Temperature and Stress Analysis

The radome shape (Von-Karman) and thickness were dictated by other than thermal considerations. However, thermal considerations did initiate an effort to determine if slightly blunting the radome would result in a reduction of the thermal stresses. Since the maximum stress capability of Pyroceram had never been firmly established and the new environment was more severe than any previously encountered, the fear existed that the material would be pushed near the limit of its thermal stress capability. Any means of reducing the thermal stresses was, therefore, felt worthy of examination.

Figure 2 is a sketch of the two radomes analyzed; one a standard Von-Karman shape and the other a Von-Karman blunted with a 1.35 inch radius. Only the extreme forward portion of each radome was analyzed since experience had shown that this area encompassed the region of maximum thermal stress.

Two-dimensional temperature analyses of both radomes were performed utilizing the IBM 7090 computer program described in Reference (1). The program is quite general in nature and can handle complicated three-dimensional geometric configurations involving heat transfer by radiation, conduction, and convection. The theory upon which the heat transfer calculations are based includes a modified Colburn reference enthalpy method for computing aerodynamic heating and a forward finite difference method for handling the differential equations of heat conduction. Radiation is computed using the Stefan-Boltzmann law.

Because radome-shaped bodies do not lend themselves to exact theoretical stress solutions, they must be analyzed assuming the stresses can be approximated by cylindrical or spherical shell theory. In these radome stress analyses, spherical theory was chosen since it yields more conservative (higher) numbers than does cylindrical theory. The stresses were hand computed using the temperature distributions generated from the heat transfer program described above.

The analyses on both the pointed and blunted radomes produced temperature variations over the surface such as are shown in Figure 3. It is obvious from Figure 3 that a sharp rise in temperature occurs at the transition point from laminar to turbulent flow on the shell portion of each radome. On both radomes the transition Reynold's Number was assumed to be 1.5×10^6 . On the pointed radome the maximum temperature (855°F) occurs at the stagnation point as would be expected. However, on the blunted radome the maximum temperature (705°F) occurs not at the stagnation point but at the transition point. Figure 3 was used as an aid to locate the points of maximum stress since these points can be expected to occur at locations where the highest heat input has generated the highest temperatures early in flight.

Because the maximum temperature on the blunted radome occurred at the transition point, it was expected that the maximum stress would also occur at that point. Figure 4 shows this to be true. The maximum stresses at the transition and stagnation points are 16,850 psi and 14,800 psi, respectively. These values are tensile stresses on the inside surface which are the most critical stresses.

Figure 3 showed that the maximum temperature on the shell portion (i.e., away from the stagnation point) of the pointed radome occurred at the transition point. Consequently, the maximum stress on the shell portion also occurred at that point. This stress was computed and is compared with the maximum stress on the blunted radome in Figure 5. As can be seen the stresses are nearly identical. The conclusion to be drawn from this figure is that on the shell portion of the pointed radome the tensile stresses are no more severe than those on the blunted radome. In this area little value is gained by blunting the radome.

However, by reference to Figure 6, it would seem that a substantial thermal stress advantage could be gained at the stagnation point by blunting

the radome. This impression is given by the fact that the blunted radome reaches a maximum stagnation point temperature of only 635°F in 7.5 seconds while the pointed radome reaches 855°F in just 5 seconds. In addition, Figure 7 shows the extreme temperature gradient which exists along the centerline of the pointed radome at 5 seconds. This gradient, though large, is such as to generate compressive thermal stresses on the outside surface which are far less critical than are tensile thermal stresses. However, the passing of time would see a progressive decrease of compressive thermal stresses on the outside surface and a build up of tensile stresses on the inside surface. It should be evident that the discussion of the pointed radome stagnation point region has thus far been confined to temperature results. The reason for this is that, due to the geometry of the area, no theoretical method (exact or approximate) is known to calculate the thermal stresses in the immediate region of the stagnation point.

Preliminary Experimental Compressive Stress Evaluation

In order to obtain an indication of whether the pointed radome could withstand the high compressive stresses at the stagnation point, a test was derived to determine what thermal environment would be necessary to cause a compressive stress failure at the point. Figure 8 is a schematic of the test apparatus used for this purpose. In this test, small samples of Pyroceram measuring 1/4" x 1/8" x 3" were plunged into a molten aluminum bath and placed in contact with the bottom of the container which was heated to the desired temperature. The sole purpose of the molten aluminum was to wet the surface of the samples and increase the thermal conductivity between the bottom of the container and the test sample. After each test, the specimens were examined under a 120 power microscope. No failure was noted at 1100°F or in subsequent tests at 2000°F.

In an effort to find what was needed to generate a compressive thermal stress failure, an oxy-acetylene torch was applied to the surface of a sample. The torch generated temperatures high enough to melt the material - that is, approximately 2500°F. After the test, cracking was noted indicating that a compressive thermal stress failure had occurred. There was some concern that the observed crack had occurred after the test during the rapid cool-down of the sample. This was disproved when the test was repeated on another sample which was slowly cooled after the test and a similar failure was noted. The conditions which caused this failure were obviously far more severe than can be expected in flight. For this reason a preliminary conclusion was drawn that no compressive thermal stress problem would exist with the pointed radome.

As a result of the theoretical and preliminary experimental work just described, pointed Pyroceram radomes were indicated in the Mach 4 missile study. Because of the complexity and the resultant uncertainty of the theoretical analyses, it was decided further to verify the theoretical conclusions by testing several radomes at the Ordnance Aerophysics Laboratory (OAL), Daingerfield, Texas.

Full Scale Wind Tunnel Tests

The first experiments showed that the radomes could comfortably withstand the maximum flight tensile thermal stresses which they might face (17,000 psi). Next it was decided to test three radomes to the limit of the facility in order to attempt to cause tensile thermal stress failures.

The testing procedure employed for the Pyroceram radomes was as follows. The radomes were held below the airstream until the tunnel conditions had stabilized as much as possible (this required 4 to 6 seconds); the radomes were then injected into the airstream (injection time 1/2 second) and remained there for 14 seconds which was one second after the computed time of peak thermal stress. The radomes were then withdrawn from the airstream. Just prior to a run the radomes were cooled to an initial temperature of +50°F or -10°F depending on the stress level sought. This cooling was accomplished with a CO₂ spray inside the radomes. In order to hold the radomes at these reduced temperatures, the radomes were wrapped in an asbestos cloth which blew off upon injection into the airstream. The radomes were tested at a Mach number of 2.44, a total pressure of 215 psi, and an average total temperature of approximately 1350°F.

On two of the three tests, good strain gage data was obtained. The results of these tests are shown in Figures 9 and 10. The tunnel flow conditions were essentially the same for both runs. The difference noted in maximum stress between the two runs is due to the difference in initial temperature.

Comparison of Wind Tunnel Data with Theory

Because the radomes were instrumented with strain gages, there was an opportunity to compare measured stresses with those theoretically computed. In order to make this comparison, theoretical predictions were made using the heat transfer computer program previously described. By this time the program had been amended so that it would compute stresses (based on cylindrical or spherical shell theory) in addition to temperatures. The theoretical results shown in Figures 9 and 10 were generated by this combined program and are for a location approximately two inches behind the stagnation point.

The experimental data from the first test is shown in Figure 9 compared with theoretical predictions based on cylindrical and spherical shell theory. The experimental and theoretical maximum stresses agree within 2 percent if cylindrical theory is used for the comparison and within 10 percent if spherical theory is used. In addition, the shape of the experimental and theoretical curves is quite similar. The agreement is excellent particularly since the analysis began with only the wind tunnel pressure and temperature-time histories and Mach number as inputs. The comparison from the second test is shown in Figure 10. The comparison between the theoretical and experimental maximum stresses is once again good, (2 percent or 11 percent depending on whether cylindrical or spherical theory is used). However, the shape of the theoretical curves differ somewhat from the experimental. The reason for this is unknown.

Since only a small amount of data was available for correlation, no firm conclusions can be drawn from the theoretical and experimental stress comparisons. However, from the work that has been done, it is obvious that cylindrical shell theory predicted the experimental stresses better than spherical shell theory.

Reference

- (1) APL/JHU CF-2954, "Numerical Approximations in Heat Transfer Problems and Usage of IBM 7090 Computer for Solutions", D. W. Fox, H. Shaw, Jr., and J. Jellinek, May 17, 1962.

THERMALLY SEVERE TRAJECTORY

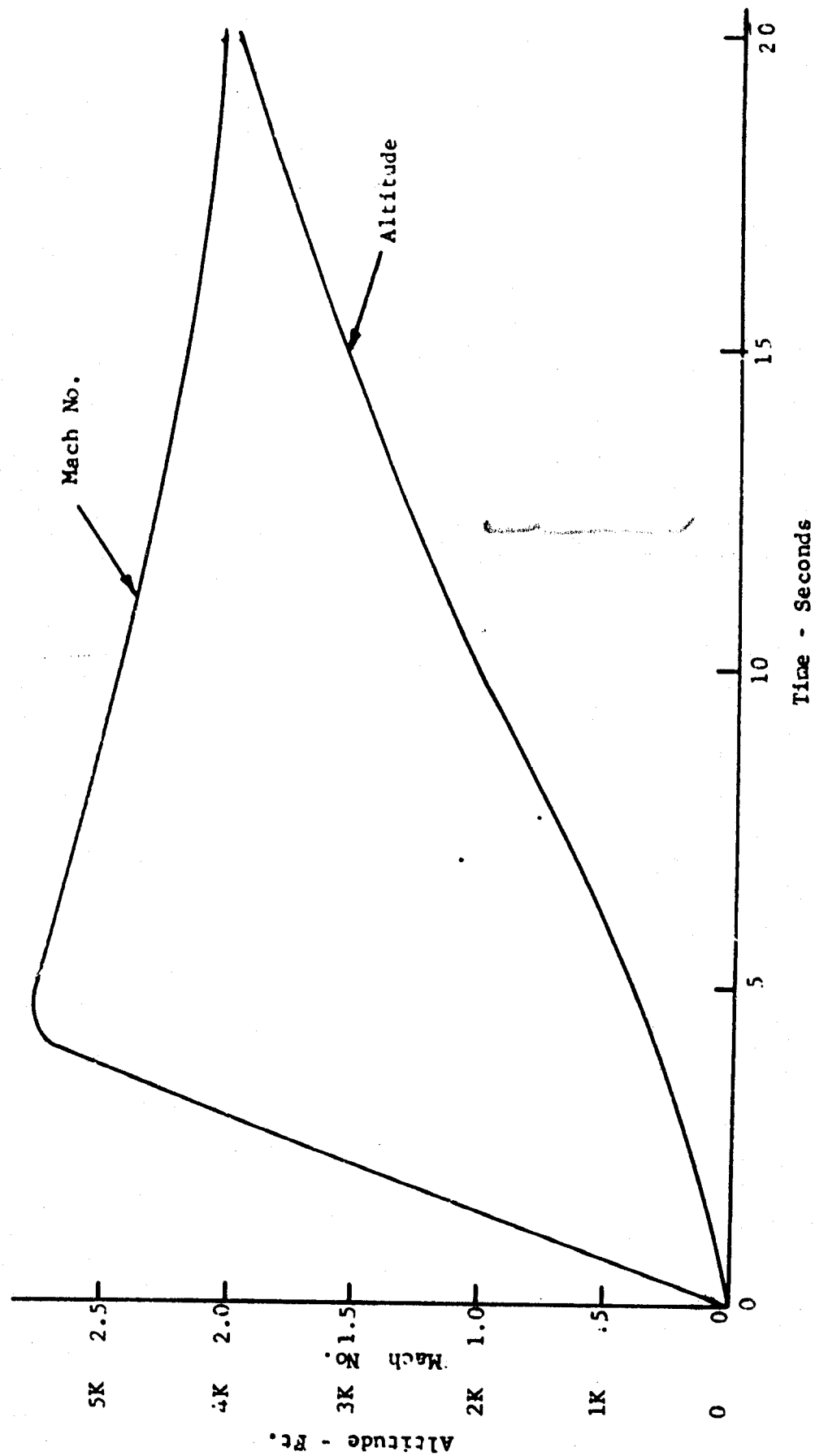


Figure 1

RADOME CROSS SECTION
(POINTED AND BLUNTED)

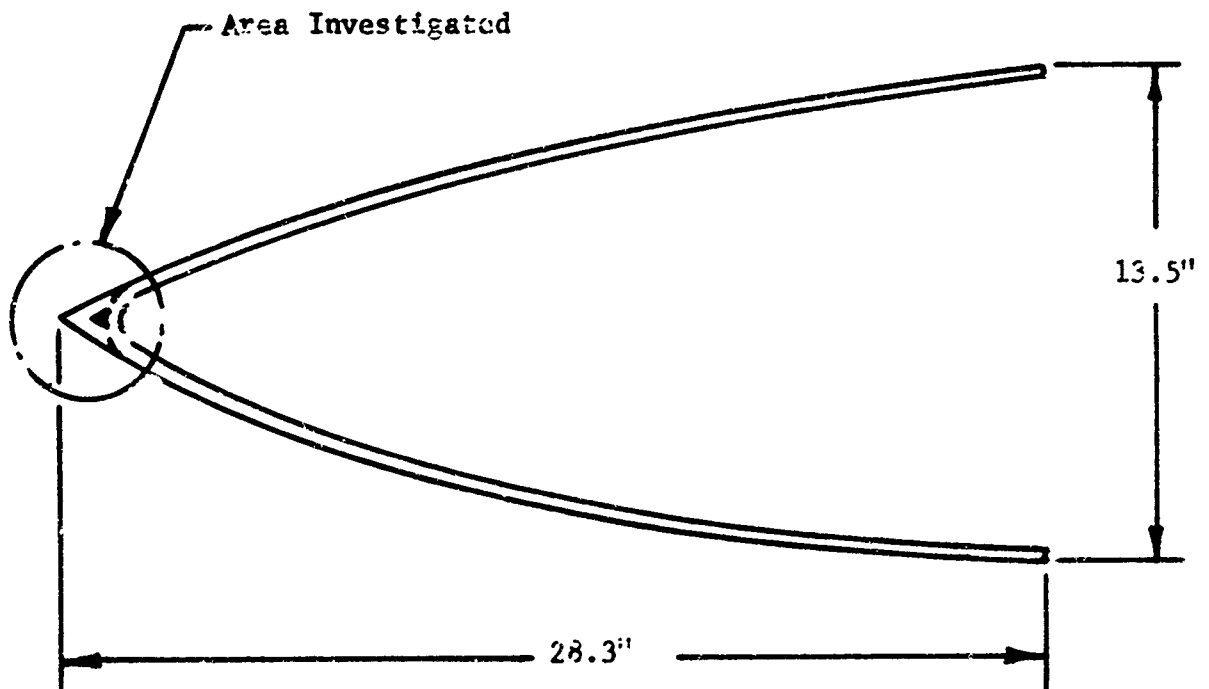


Figure 2

POINTED AND BLUNTED RADOMES
SURFACE TEMPERATURE VERSUS DISTANCE
FROM STAGNATION POINT

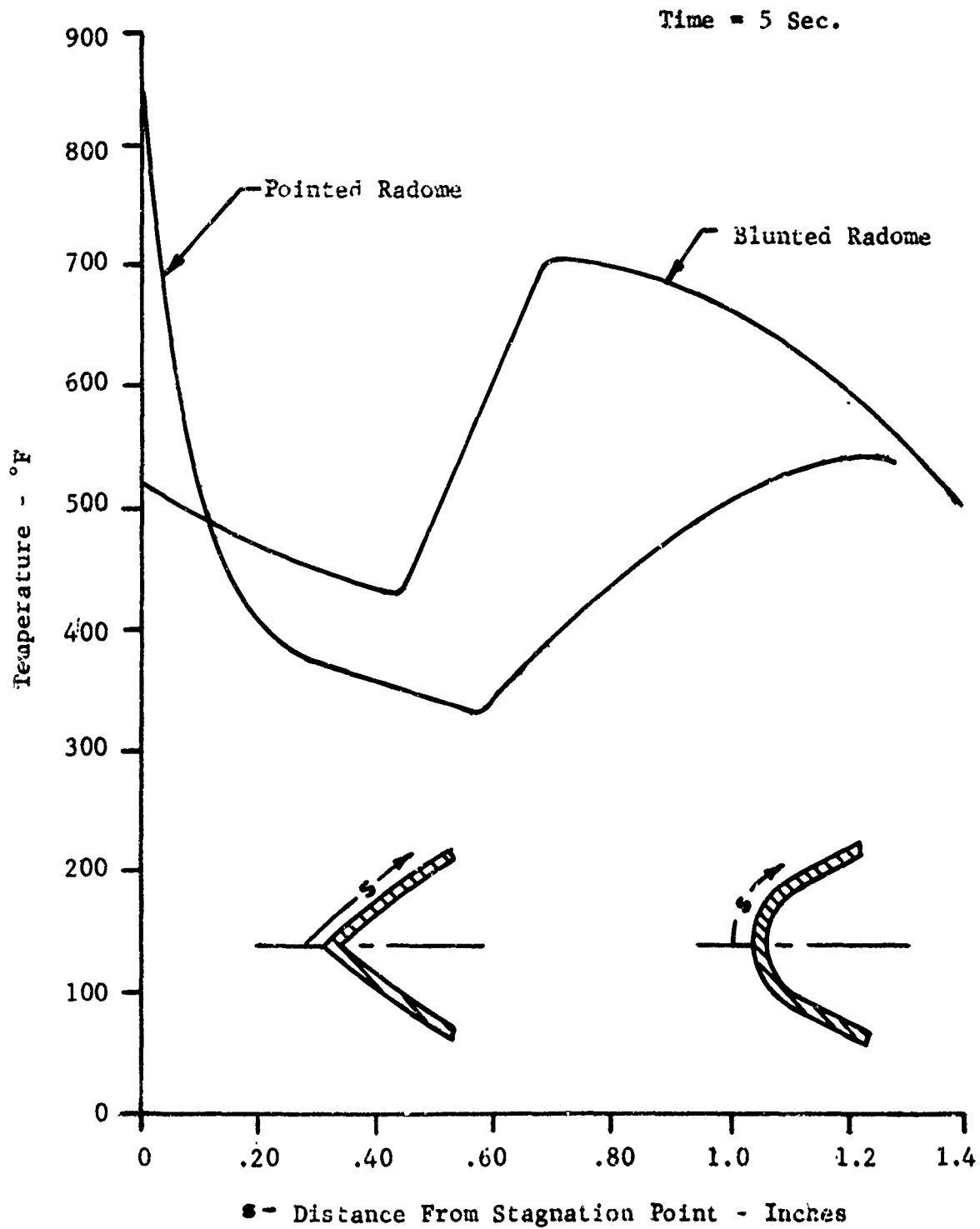


Figure 3

ELUNTED RADOME THERMAL STRESSES

(TENSILE)

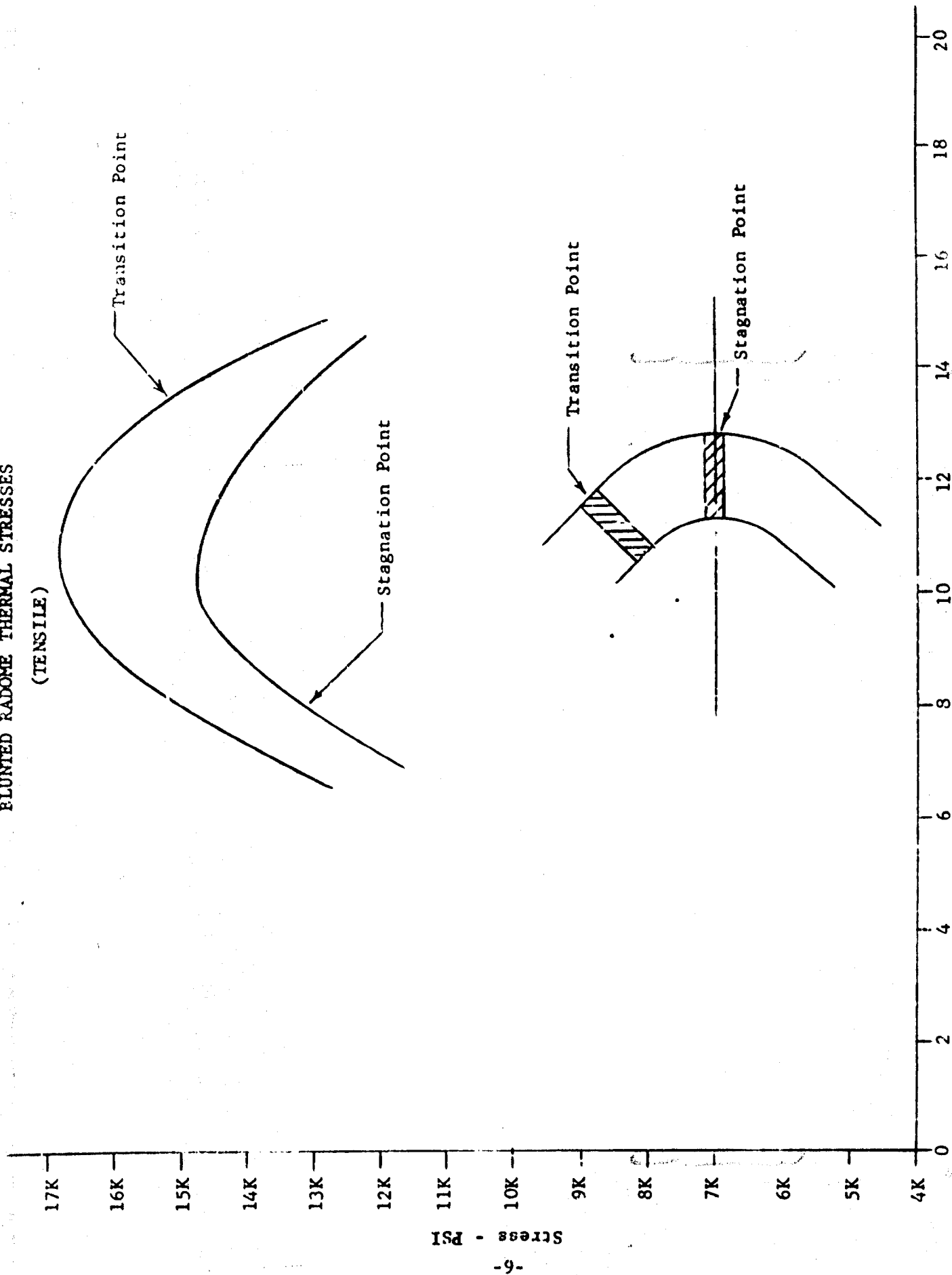
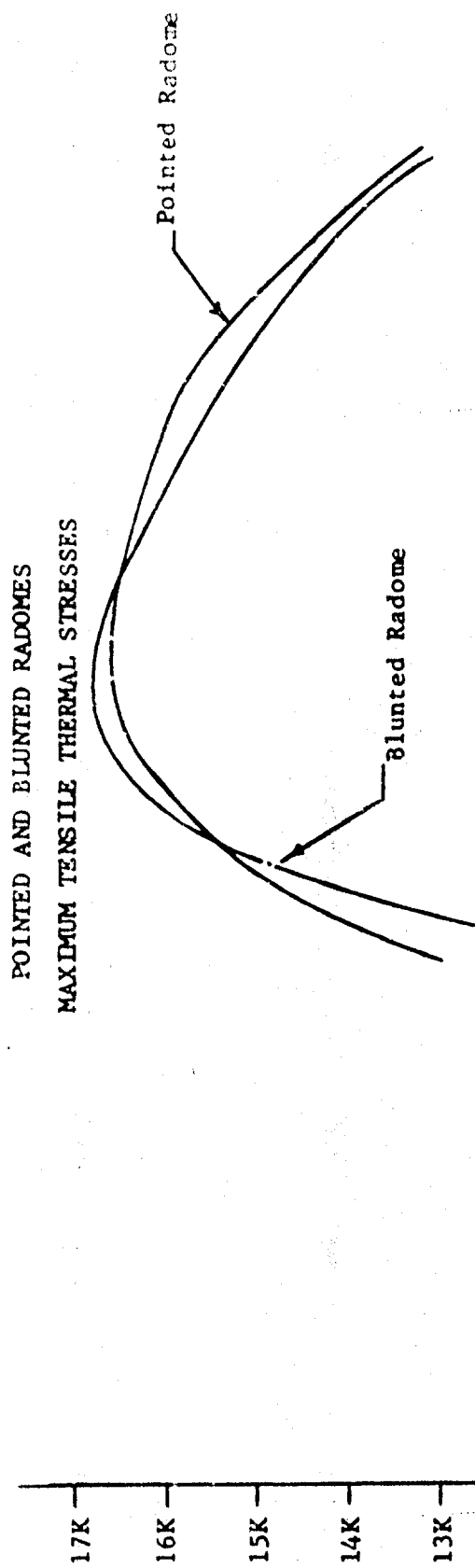


Figure 4

Time - Seconds



LOCATIONS OF MAXIMUM TENSILE THERMAL STRESSES
(TRANSITION POINTS)

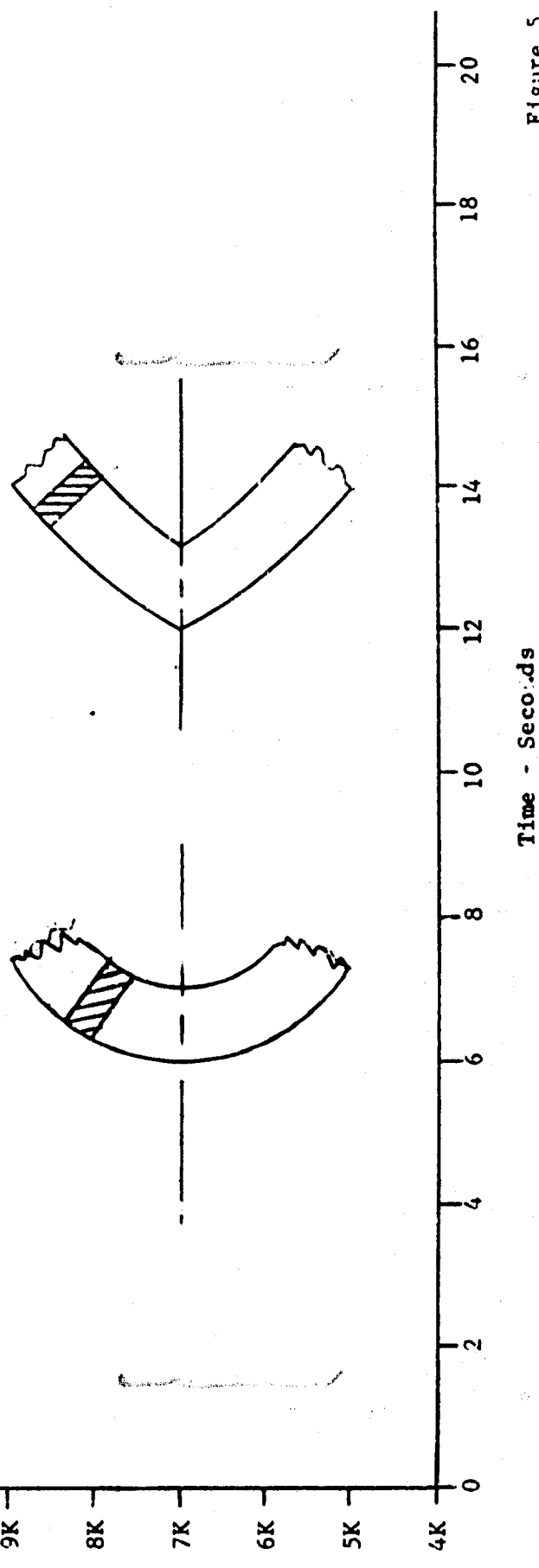
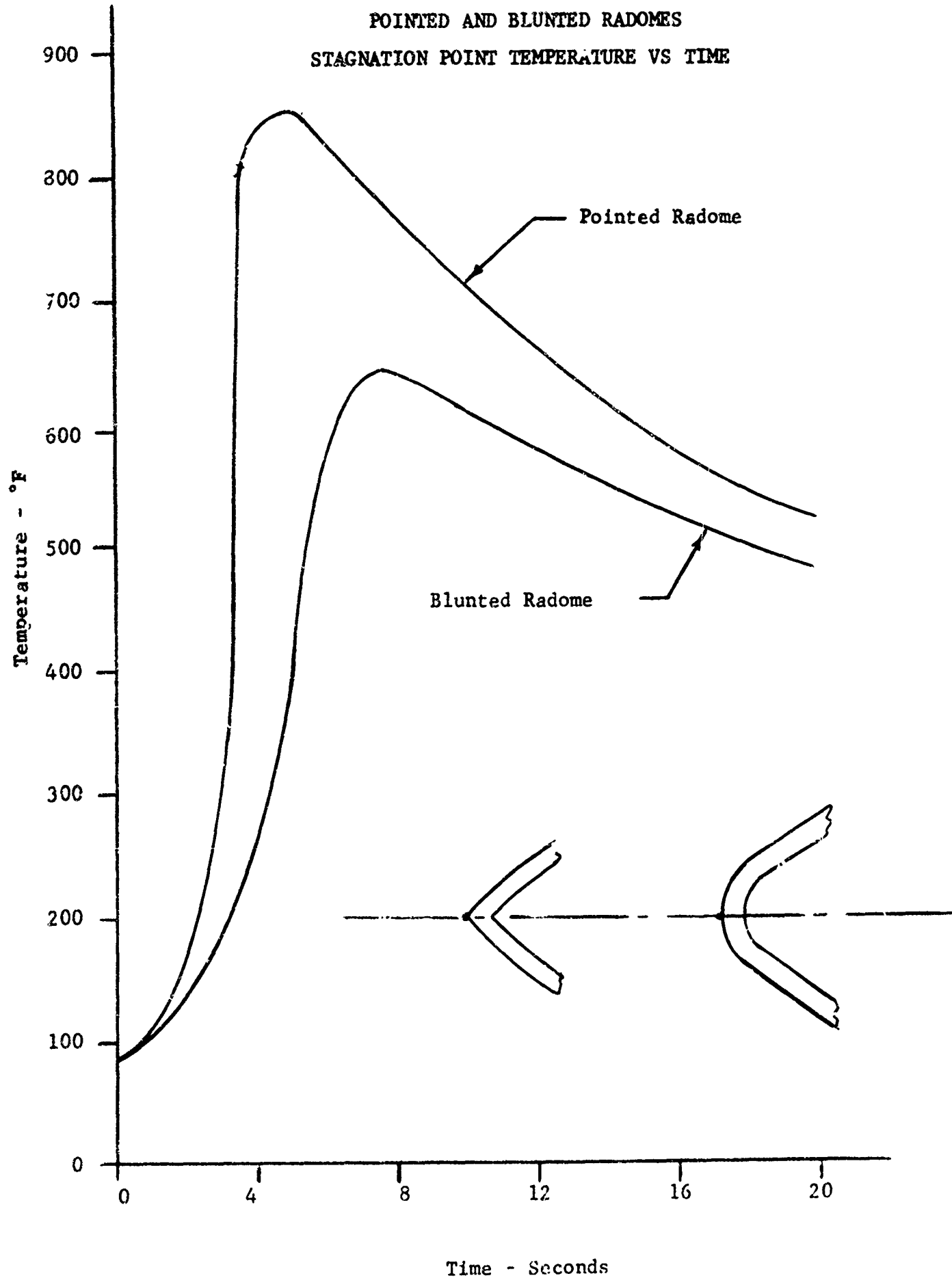
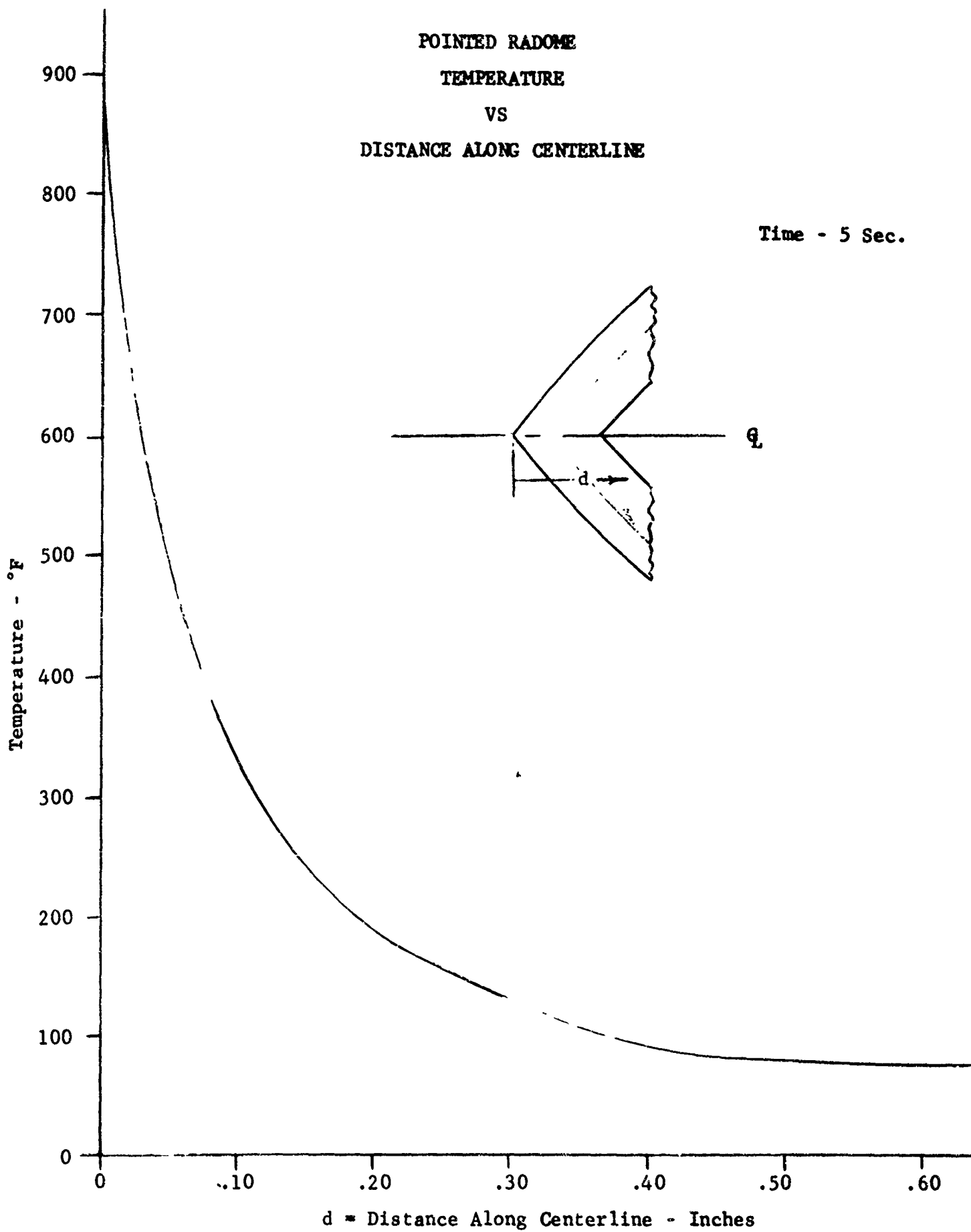


Figure 5



POINTED RADOME
TEMPERATURE
VS
DISTANCE ALONG CENTERLINE

Time - 5 Sec.



COMPRESSIVE THERMAL STRESS EVALUATION
OF PYROCERAM
TEST ARRANGEMENT

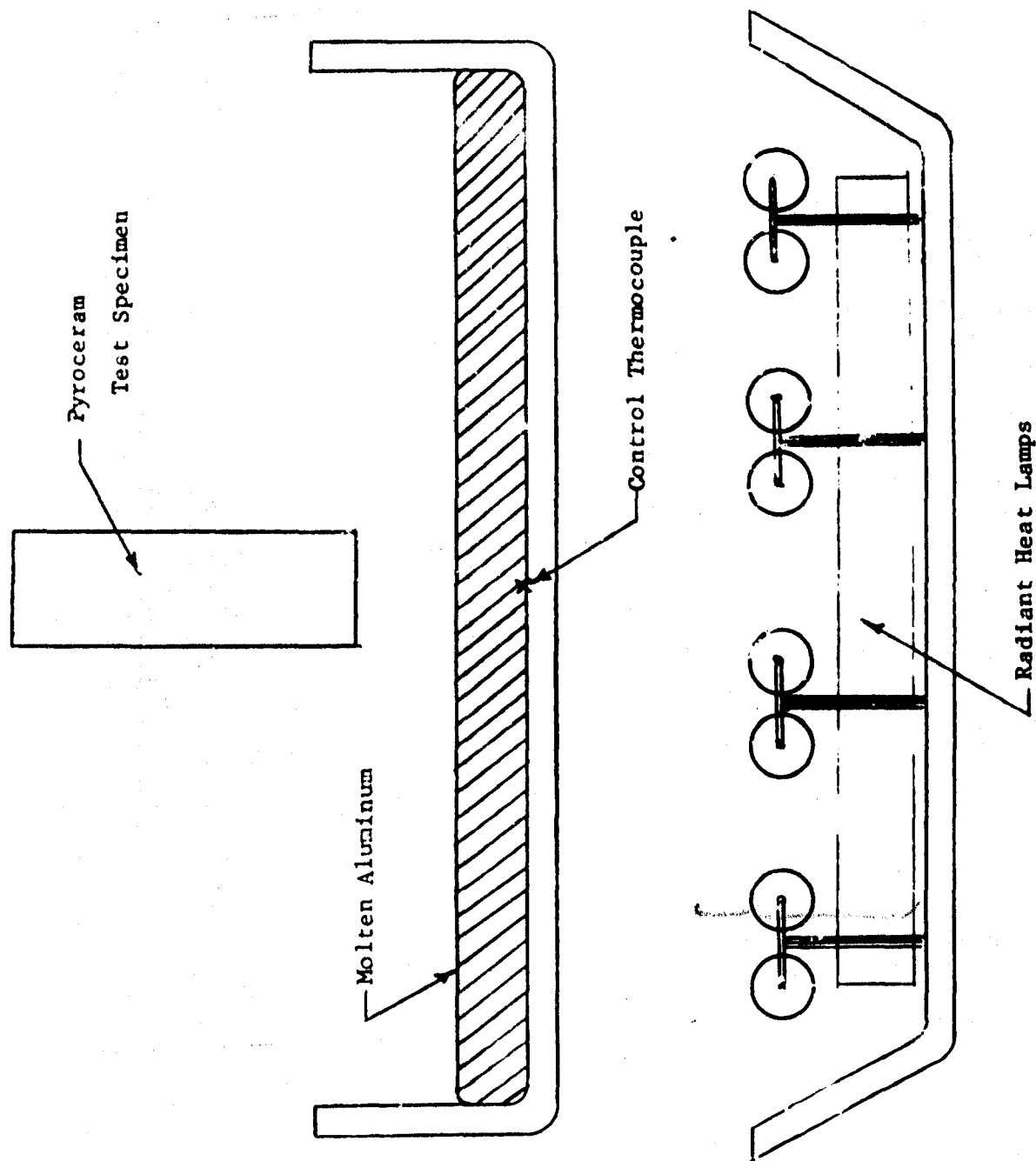


Figure 8

COMPARISON OF THEORETICAL AND EXPERIMENTAL
STRESSES

Test No. 1

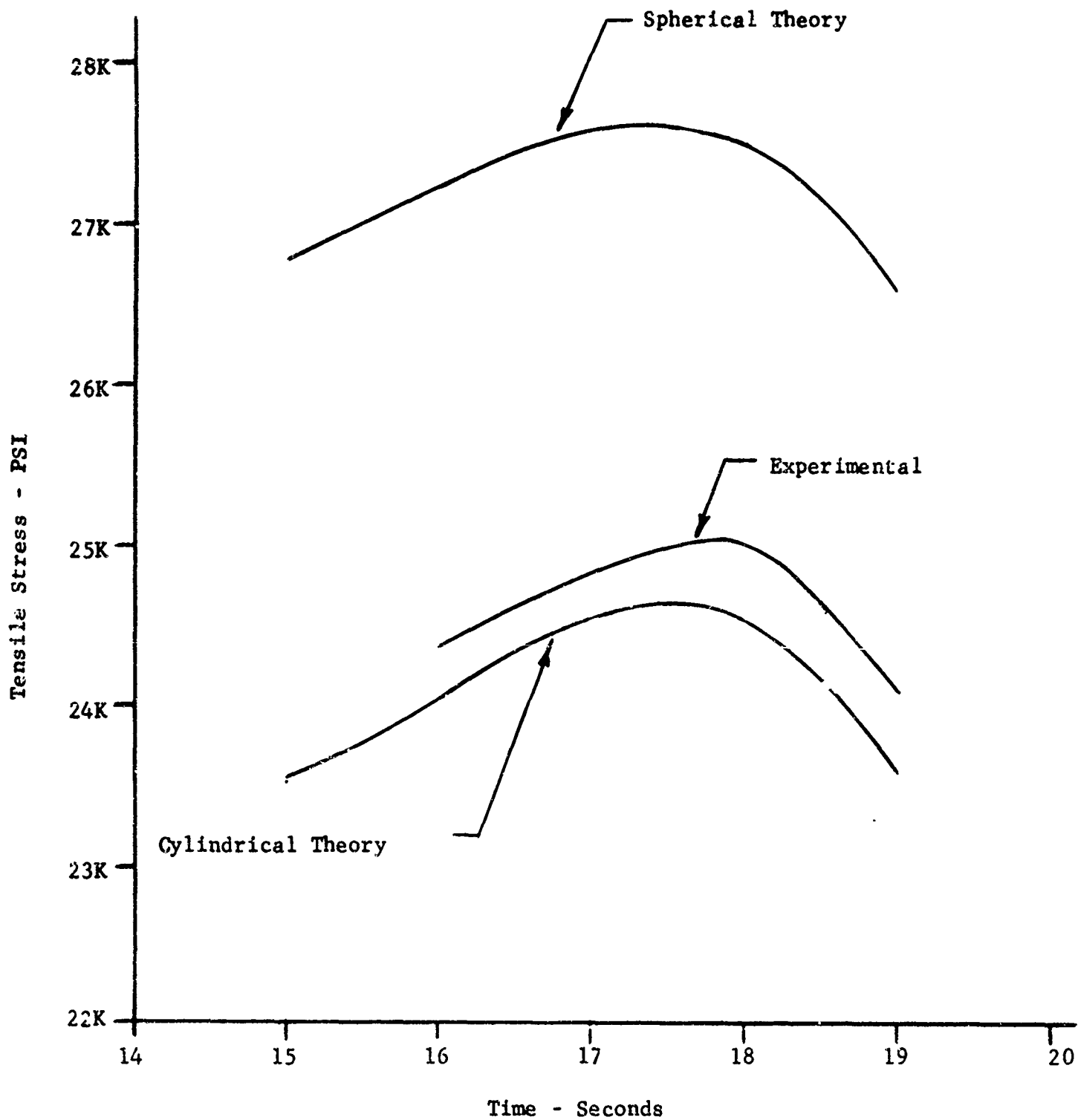


Figure 9

COMPARISON OF THEORETICAL AND EXPERIMENTAL STRESSES

Test No. 2

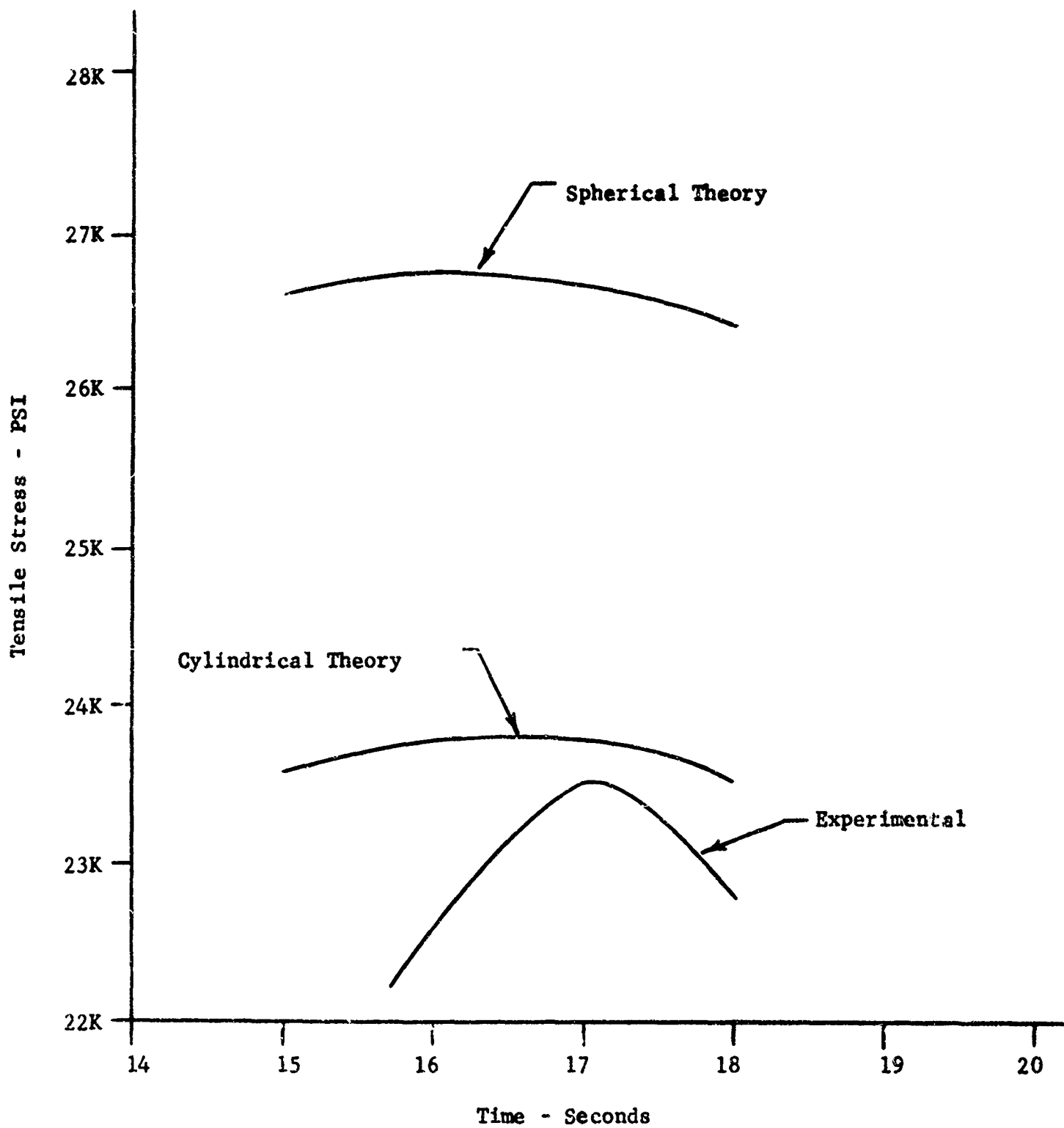


Figure 10

Introduction

Some years ago, on a Navy sponsored research program on ceramic radomes, a rather intensive examination of the micro-structure of certain type ceramics was undertaken. The void content was of particular interest. It was found that all the industrial impervious high alumina compositions (85 to 99% alumina) evaluated contained from 8 to 12% by volume of voids. It was further found some time later that this void volume, especially in larger specimens, was not uniform but varied over this range in a given specimen. This type of structure is not conducive to good radar transmission; a need to improve it led to the development of the "Prereacted Raw Materials" technique.

Prereacted Raw Materials Approach

In essence this technique uses the finished products of industry as raw material, which, after being reduced to a controlled particle size distribution, is fabricated and fired again. Figure 1 shows the effect of firing temperature on the bulk density of a typical high alumina body processed conventionally and by prereacted raw materials technique. Note the marked increase in bulk density, decrease in firing temperature and increase in firing range resulting by the application of this technique.

¹Rutgers, The State University, New Brunswick, N. J.

²Bureau of Naval Weapons, Department of the Navy, Washington 25, D. C.

The procedure by which this was accomplished is as follows: the complete composition was dry mixed in a muller type mixer with sufficient water and additives for extrusion into 1/8" diameter rods without de-airing. The rods were dried, broken into small lengths and fired to maturity. After firing they were wet ground in an alumina lined mill, containing alumina grinding media, to a controlled particle size distribution in which all particles are finer than 44 microns and approximately 15% are finer than 1 micron. Figure 2 shows this particle size distribution curve plus compositions and other pertinent data. Note that after the first firing the bulk density is only 88.5% of the true density of this composition. Radomes were fabricated by the drain slip casting method using only the prereacted composition, water and deflocculant. After drying the specimens were fired to the temperature noted in Figure 2. The bulk density was increased to 3.68 which is 99% of the true density of this composition. The true density is 3.71 as determined by the pycnometer method. Figure 3 demonstrates the effect of firing on the moisture absorption, bulk density and apparent density. Note that apparent density is the pycnometer density. Thus the prereacted raw materials technique results in: (1) grinding out the voids; (2) redistributing the compositional discontinuities; and, (3) supplying a particle size distribution conducive to high fired bulk density. Further this particle size distribution results in sufficient fines for a deflocculated system which makes it possible to make the radomes

by the slip casting procedure.

Slip casting has been utilized to fabricate ogive radomes with fired dimensions up to 16" base diameter by 50" high to the same high quality described above, namely 99% of true density. Some specimens weighed up to 125 lbs. The same prereacted raw material was fabricated isostatically at up to 45,000 psi with no improvement in quality over that attained by conventional slip casting.

Radar transmission was very good. Other engineering properties were at least as good as those attained by conventional methods and in most cases much better.

Studies To Reduce Firing Temperature

The advantages of the prereacted raw materials technique led to a Navy sponsored research program entitled "Development of Refractory Ceramics Which Can Be Processed Considerably Lower Than Their Maximum Use Temperature." Three temperatures ranges are being studied: 3000°F and above; 2600-3000°F and 1800-2600°F.

3000°F and Above

For the highest temperature range alumina was selected as the refractory phase for study. Considerable effort has been expended studying the sintering characteristics of this material; however the present objective is to determine the conditions, including lowest firing temperature, under which 99% of true density can be attained.

Three compositions were chosen for intensive study: Composition C is 100% alumina; Composition R is 99.75% Alumina, 0.25% magnesia; and, Composition CR is 98.0% Alumina and 2.0% magnesia. Both raw materials are 99.99% pure. The function of the magnesia is to minimize grain growth. The mechanism may be solid solution however this remains to be proven. The compositions were wet mixed and specimens fabricated by dry pressing. Air as a firing atmosphere is not conducive to attaining high percentage of true density. Considerable work is reported on firing in various atmospheres; however the conditions vary appreciably. Hydrogen, helium and vacuum were selected for study. The first two were chosen because they can diffuse quite readily. Further, hydrogen is an active gas and is a reducing agent which can produce defects; also, it may diffuse as H^0 , H^+ and possibly as H_2 . Helium is an inert gas and its small size and its high diffusion rate are its prime assets. Vacuum will reduce the gas pressure within the pores and maximize gas diffusion from the structure. All compositions were fired for 1, 3, 5 and 7 hours respectively at 1550, 1650, 1700 and 1750°C respectively. A special molybdenum resistance furnace was used for all fires.

Bulk density or percentage of true density is difficult to determine directly as the true density of those compositions containing magnesia is difficult to establish. Percent total porosity was measured instead and was determined by bulk density measurements and augmented petrographically in the lowest porosity

region.

Figure 4 shows the effect of firing time on percent total porosity of all three compositions fired in hydrogen, helium and vacuum over the time-temperature range discussed above. The objective is the lowest firing temperature at which 99% of true density, or, less than 1% porosity is attained. This is attained by firing in vacuum to 1550°C (2822°F) after a three hours soaking period with the CR composition (2% MgO), and after 7 hours with the R composition (1/4" MgO). It can also be obtained by firing in hydrogen to 1650°C (3000°F) after a 1 hour soaking period with either of the compositions containing magnesia. Further it can be realized by firing to the same temperature in helium but only after approximately a 4 hours soak. To approach true density or total porosity less than 0.1% it is necessary to fire to 1750°C in either vacuum or hydrogen. The R composition (1/4% MgO) attains this quality at one hour soak in either atmosphere. The CR composition (2% MgO) must be fired approximately 3 hours to reach this quality. The percent total pore volume of the pure alumina composition reaches a minimum of 1.9% at the highest temperature but only in a vacuum. The reason for this is the exaggerated grain growth exhibited by this composition. The magnesia included in the R and CR compositions acts as a grain growth inhibitor. Further it results in a higher sintering rate; the postulated reason is that it is due to solid solution with alumina creating a greater concentration of vacancies. Figure 5

shows that the maximum average crystal size developed in either of the magnesia containing compositions is 18 microns while that of the pure alumina at the highest temperature is 35 microns. Spinel formation is detected in both magnesia-containing compositions.

Thus the lowest temperature at which a nearly pure alumina composition can attain less than one percent total pore volume is 1550°C (2822°F). This is accomplished using 2% magnesia as a grain growth inhibitor and firing in a vacuum for 3 hours. At 1/4% magnesia this quality is reached only after seven hours soak. A hydrogen atmosphere necessitates an increase in firing temperature to 1650°C (3000°F) and soaking for 1 hour, while when firing in helium the soaking period must be increased to 4 hours; this holds for both magnesia containing compositions. The total pore volume of the pure alumina composition never gets below 1.9% even at the highest temperature and soaking periods.

2600-3000°F

The procedures adapted for the second temperature range, 2600-3000°F, utilized the prereacted raw materials technique. The objective was to determine the mechanisms which result in the long firing range and allow retention of the engineering properties well above the minimum maturing temperature. The high alumina portion of the $\text{MgO} \cdot \text{Al}_2\text{O}_3 \cdot \text{SiC}_2$ triaxial was studied from 72-96% alumina. The prereacted raw materials procedure described earlier was used with the exception that the calcined material was ground

to pass 325 mesh only, because the problems involved in attempting to duplicate the particle size distribution curve in Figure 2 were many and time consuming. The decreased control of the particle size distribution results in a lower bulk density than can be attained; however, a much improved quality over that attained by the conventional procedure resulted in all cases. Further the specimens were dry pressed rather than cast. Again, the problems of attaining a deflocculated system or casting slip were felt to be too time consuming.

Twenty compositions as noted in Figure 6 were weighed and dry mixed with sufficient water for extrusion into 1/8" diameter rods which were dried and calcined to 2000, 2600, 2700 and 2800°F respectively. These 80 batches were then ground to pass 325 mesh, pressed into 1-1/2 O.D. x 1/8" thick specimens and fired to 2600, 2700, 2800 and 2900°F respectively. Bulk density, moisture absorption, crystal phases, etc., were determined.

The compositions located on the alumina-silica binary are quite refractory and none mature within the temperature range under study. All other compositions attained 0.0% moisture absorption at 2700°F with the exception of composition #53 which attains it at 2600°F. In general the density tends to increase through the 2800°F fire. The improvement in quality is illustrated by a typical composition in this area which when fabricated normally and fired to 2800°F has a density of 2.79 and a moisture absorption of 9.0%. However when fabricated by the prereacted raw

materials method it has a density of 3.58 and a moisture absorption of 0.00%.

The presintering fire is primarily a phase formation process in which crystalline phases and glass are being formed. When this fire is 2600°F or higher the bulk density after the sintering or final fire is practically independent of the presintering firing temperature. In general those specimens made of 2000°F presintered material must be subjected to a higher sintering fire.

In the final or sintering fire the melting temperatures of the ternary compounds present, cordierite $2\text{MgO} \cdot 2\text{Al}_2\text{O}_3 \cdot 5\text{SiO}_2$ and/or sapphirine $4\text{MgO} \cdot 5\text{Al}_2\text{O}_3 \cdot 2\text{SiO}_2$, are exceeded (approximately 2650°F). These phases have incongruent melting temperatures, that is, they form a glass and a crystalline phase; the cordierite theoretically forms mullite and a glass while sapphirine forms spinel and a glass. These glasses combine with that resulting from the presintering fire to form the bond. This results in a 0.00% moisture absorption by 2700°F. The reason for the compositions having a long firing range is that mullite and spinel are dissolved, forming more alumina as determined by X-ray analysis, thus maintaining a changing glass composition of sufficient refractoriness and high viscosity to prevent slumping or overfiring. These are essentially non-equilibrium reactions taking place in a rather sluggish system.

An attempt was then made to determine whether these mechanisms were adaptable to other compositional systems. The high

alumina region of the $\text{CaO} \cdot \text{Al}_2\text{O}_3 \cdot \text{SiO}_2$ system was selected for study because: (1) calcia is a more potent flux than magnesia; (2) the ternary compounds in this system melt congruently; and (3) the calcium ion is quite similar to the magnesium ion. Four compositions were systematically selected at 90% alumina from one side to the other in the triaxial. They were fabricated conventionally and by prereacting in the same manner as the magnesia containing bodies.

In general the compositions made by prereacting mature at 2500°F which is 100° lower than, and at 10% higher density than those prepared conventionally. Further, they matured 200°F lower than those compositions containing magnesia. The firing range appears to be quite extensive. X-ray and petrographic studies show that the glass forms by congruent melting and that a higher glassy content is present than in the magnesia containing bodies. All compositions exhibited low transverse strength properties ranging from 11,500 to 20,800 psi; the value for a comparable magnesia containing body is 35,000 psi. The electrical properties varied appreciably and on the whole are poorer than comparable magnesia containing bodies. These poor properties appear to be due to the rather high glass content.

The prereacted raw materials approach definitely aids in increasing percentage of true density and results in decreasing the maturing temperature. The system in which incongruent melting took place along with the changing glass composition with

increasing temperature, resulted in superior engineering properties.

1800-2600°F

In the lowest temperature range, 1800-2600°F, the "devitrification" approach of the prereacted raw materials technique is being used. Here the complete composition is melted resulting in mixing on an atomic basis, and, on cooling in attaining a randomly oriented structure or glass. After fritting the composition is ground to a controlled particle size distribution and specimens of this "powdered glass" are pressed. During a subsequent fire a crystalline phase or phases devitrify and as the temperature is increased the composition matures to a body containing crystals bonded by a glass. This procedure results in structures which are 99% of their true density with marked improvements in physical and electrical properties.

The first crystalline phase selected for study was cordierite $2\text{MgO} \cdot 2\text{Al}_2\text{O}_3 \cdot 5\text{SiO}_2$. Its incongruent melting temperature is approximately 2625°F. Its important property is its low linear thermal expansion at approximately $2 \times 10^{-6}"/"/^\circ\text{C}$. Little information is available on the thermal expansion characteristic of the cordierite area of crystallization in the $\text{MgO} \cdot \text{Al}_2\text{O}_3 \cdot \text{SiO}_2$ system. The first objective was to systematically study this property and the firing characteristics of compositions in this area. Figure 7 shows the compositions studied.

In the compositional area of cordierite (Figure 7) the linear thermal expansion increases as the silica content with the cordierite compound exhibiting the lowest value. There is little change in this property with magnesia and alumina variations at any given silica content. The overall range is 1.3 to 6.5×10^{-6} . All compositions exhibit rather short firing ranges. To the present, composition 8 shows the most promise, with a firing range of about 50°C , resulting in 0.00% moisture absorption and a bulk density of 2.39 .

Summary

Navy sponsored research on ceramic radomes and radome materials has resulted in the "Prereacted Raw Materials" technique by which ceramics can be made quite readily to 99% of their true density which quality results in good radar transmission. This earlier work led to a research program entitled "Development of Refractory Ceramics That Can Be Processed At Temperatures Considerably Lower Than Their Maximum Use Temperature." Three temperature ranges are being studied.

The first range is 3000°F and above, and pure alumina is the principal crystalline phase under study. Magnesia was added in small percentages as a grain growth inhibitor. The effect of firing time and temperature in vacuum, helium and hydrogen atmospheres is being studied. The minimum conditions under which 99% of true density or 1% porosity can be attained are: firing temperature - 1550°C ; atmosphere - vacuum; soak time - 3 hours;

and grain growth inhibitor - 2% magnesia.

The second temperature range is 2600°-3000°F. The prereacted raw materials technique as applied to compositions in $\text{MgO} \cdot \text{Al}_2\text{O}_3 \cdot \text{SiO}_2$ system results in complete maturity at 2700°F and stability above 2900°F. High density was attained, however to reach 99% of true density, a controlled grinding of the prereacted material is necessary.

In the third temperature range, 1800-2600°F the "devitrification" approach to the prereacted raw materials technique is used. This necessitates the melting of the complete composition and thus the fabrication of a powdered glass. Cordierite is the crystalline phase presently under study.

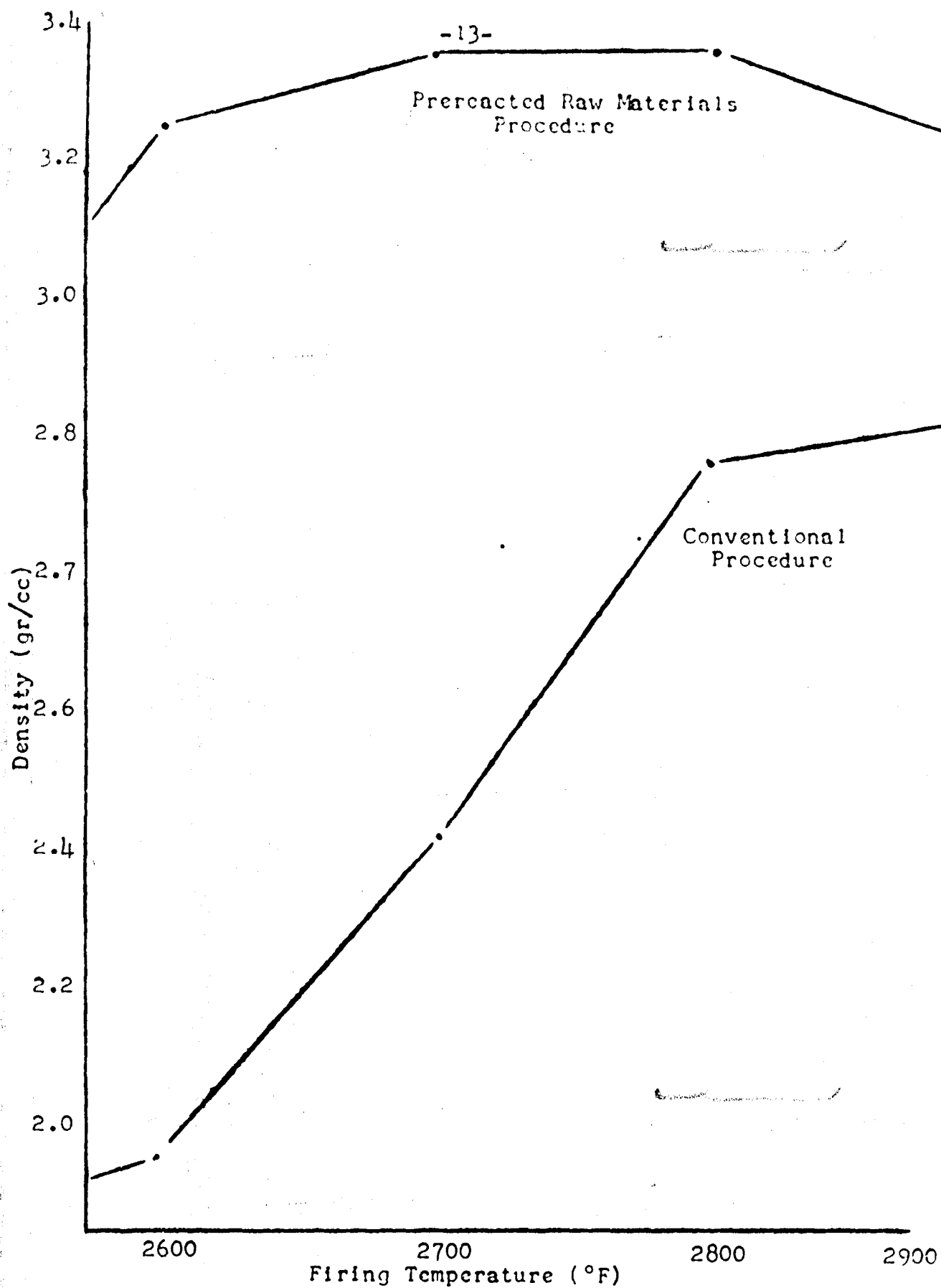
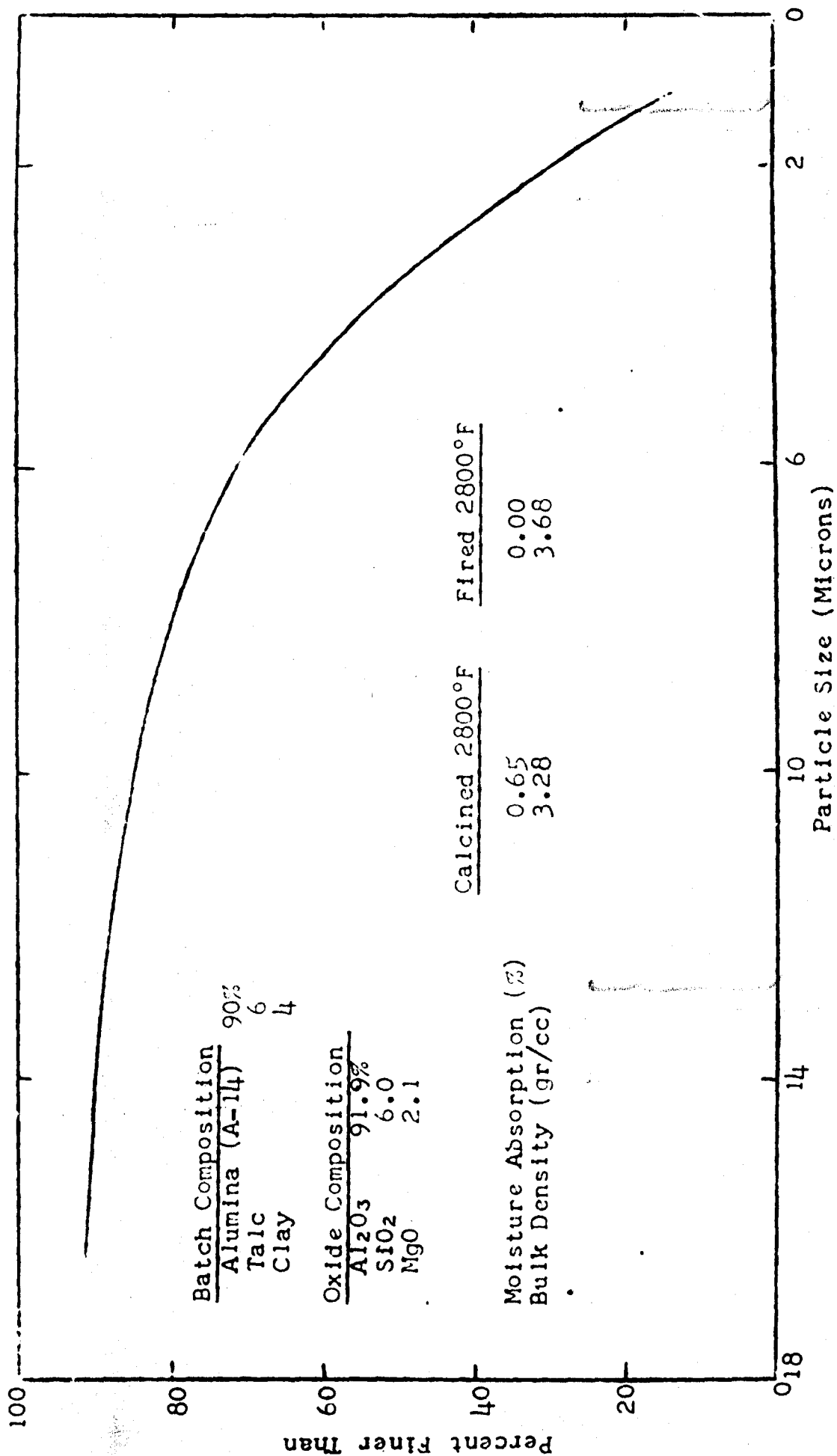


Figure 1 - Density vs Firing Temperature of Several Fabricating Procedures

Figure 2 - Data and Particle Size Distribution of Base Body



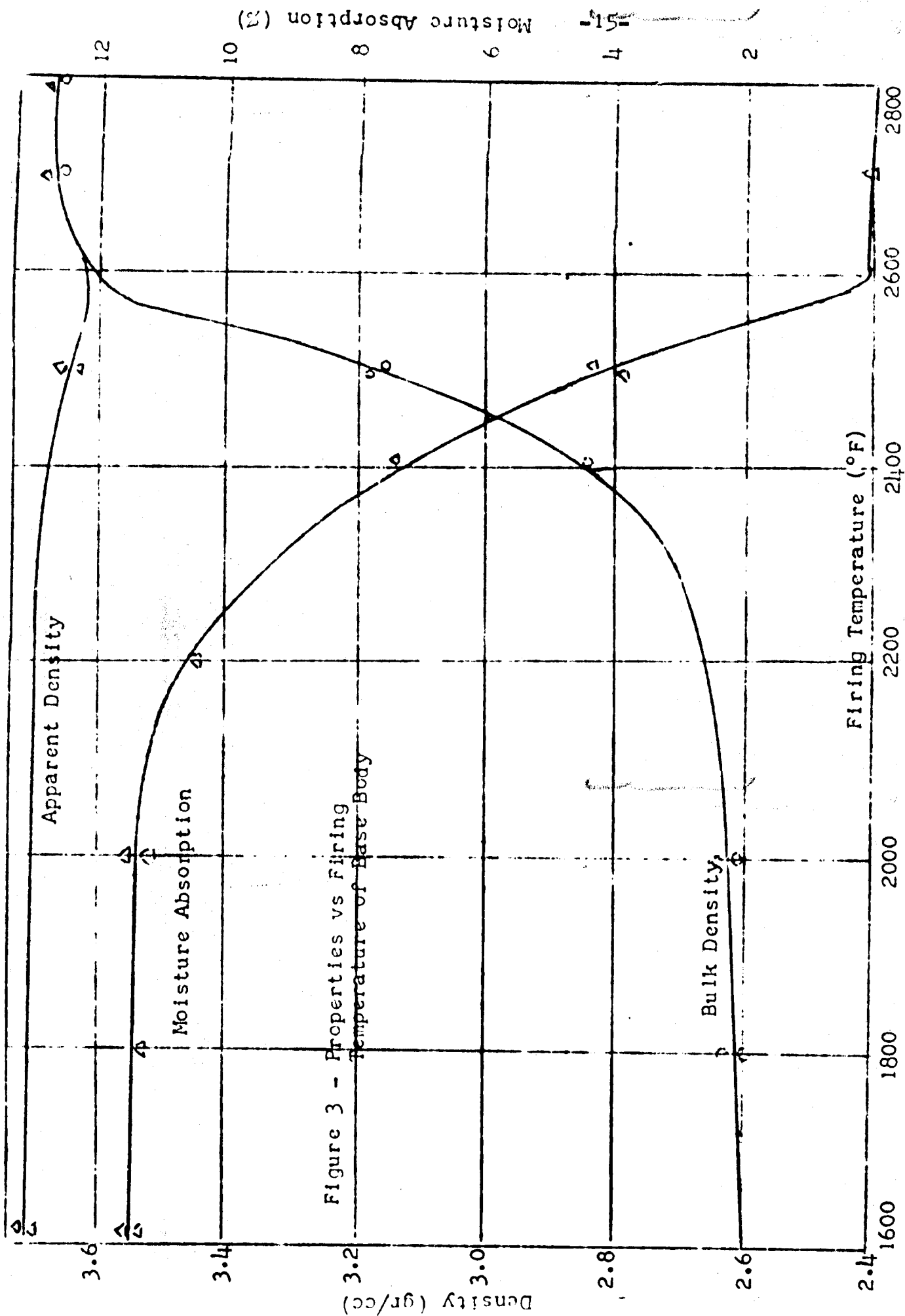


Figure 3 - Properties vs Firing Temperature of Base Body

Figure 4 - Percent Total Porosity vs Time in Hydrogen, Helium and Vacuum at Several Temperatures

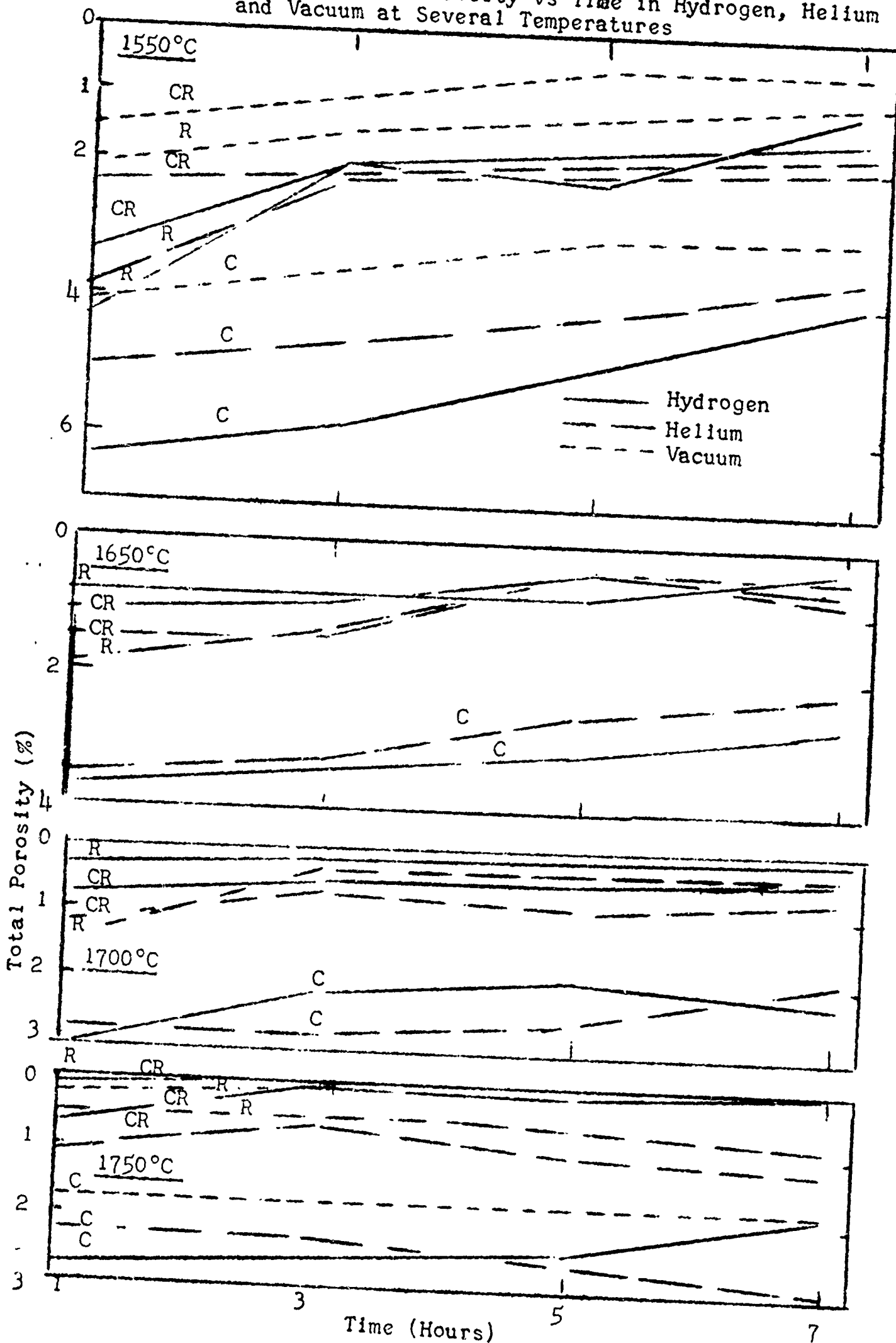
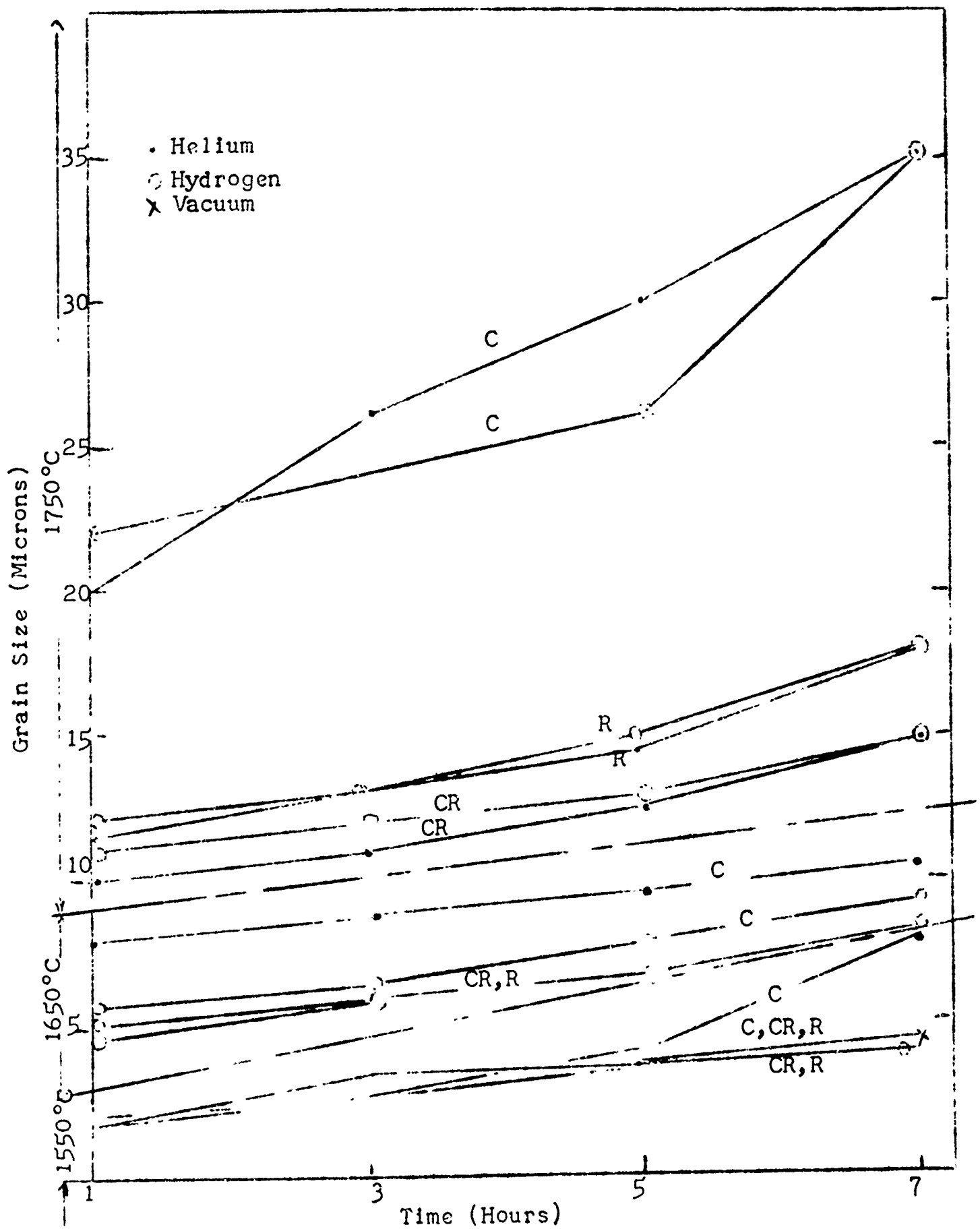


Figure 5 - Grain Size vs Firing Time at Several Temperatures and Atmospheres



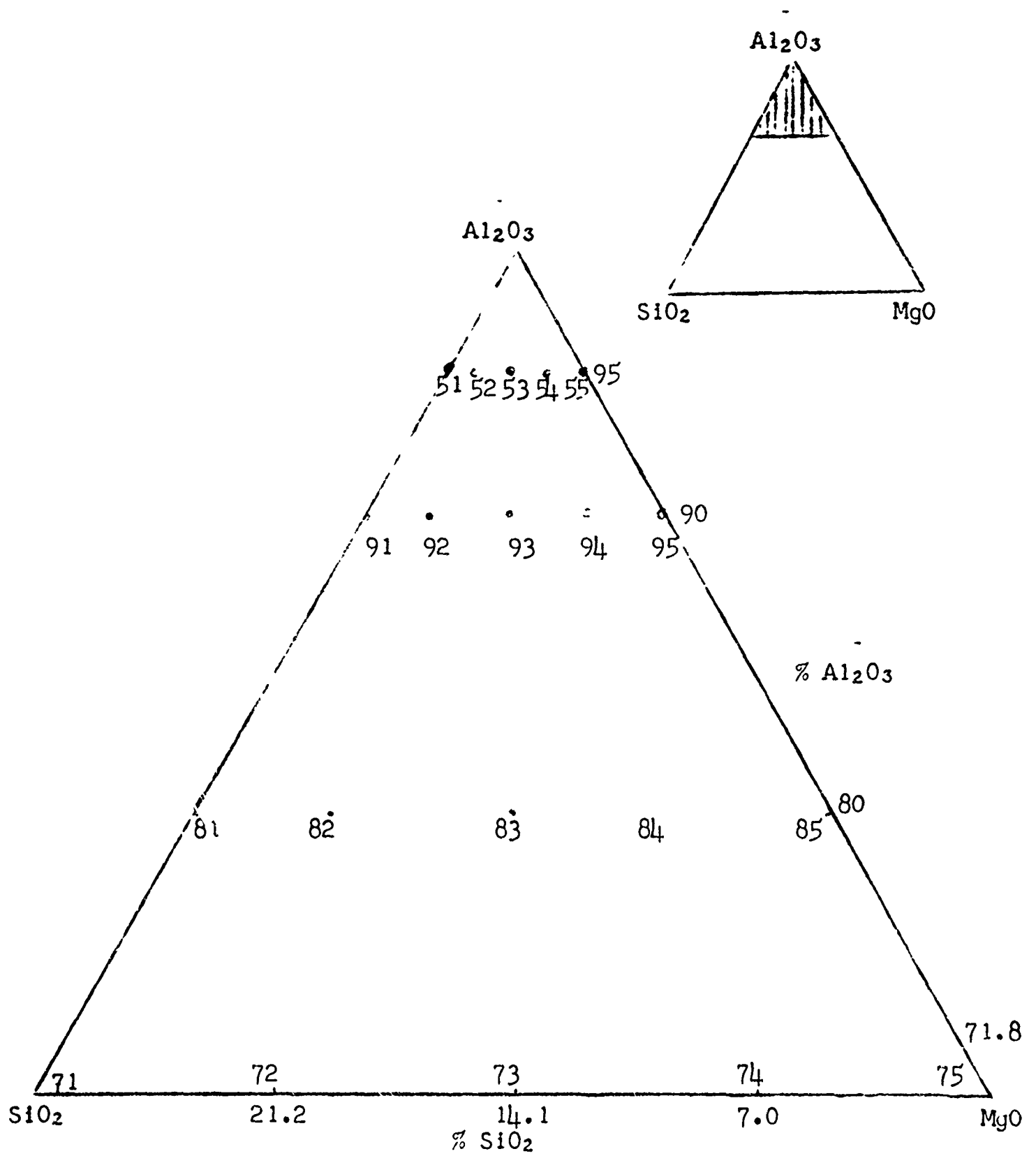


Figure 6 - Compositions Evaluated in MgO•Al₂O₃•SiO₂ System

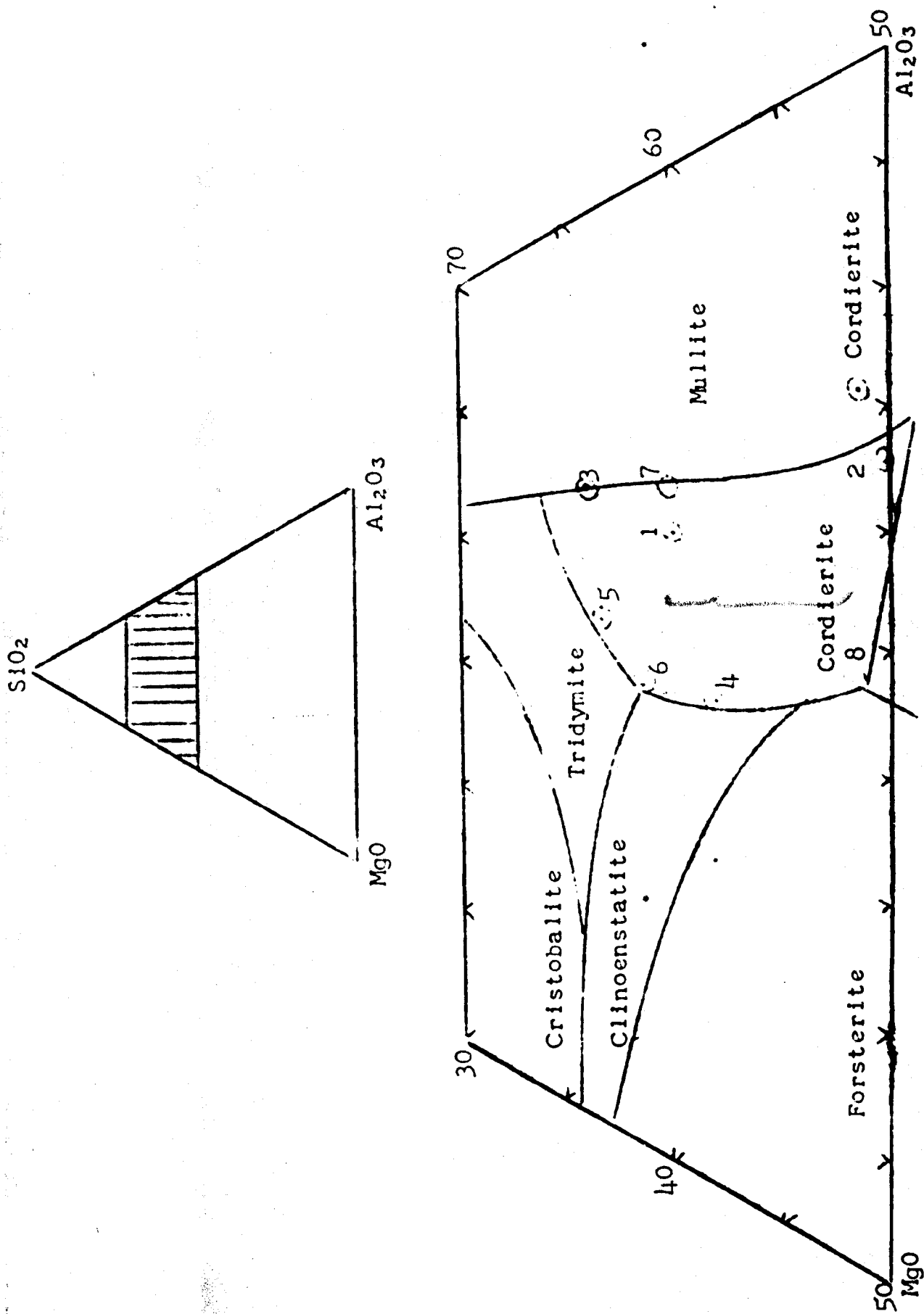


Figure 7 - Compositions Studied in $\text{MgO}-\text{Al}_2\text{O}_3-\text{SiO}_2$ System

COMMENTS ON THE SYNTHESIS OF LONGITUDINALLY INHOMOGENEOUS PLASMA-DIELECTRIC MEDIA

by

Martin C. Blyseth
Grumman Aircraft Engineering Corporation

I. INTRODUCTION:

The major aim of this paper is to demonstrate how the techniques of n-dimensional optimization have been combined with certain evaluation procedures to yield a technique for the synthesis of longitudinally inhomogeneous, plasma-dielectric media. There exist a number of relatively practical methods for evaluating the reflection and transmission coefficients of longitudinally inhomogeneous media for which distributions of dielectric constant and conductivity (or collision frequency and electron density for a plasma) can be specified analytically in terms of the optimization variables and thereby made compatible with the n-dimensional optimization technique. This paper will discuss the application for three media, namely:

1. a homogeneous multilayer using standard multilayer evaluation techniques,
2. an inhomogeneous multilayer composed of linear and quadratic variations using a matrix multiplication evaluation technique and,
3. a continuously defined inhomogeneous structure using iterative techniques.

The first method is essentially that presented by the author at the 1962 ASD-OSU Electromagnetic Window Symposium; however, an extension of the technique to the design of metal-backed multilayers will be shown and its applicability to the design of microwave absorbing materials discussed. The second method is presently of interest in the field of plasma diagnostics. The matrix evaluation technique is used for evaluation of inhomogeneous plasma-dielectric media where the variations in the parameters which define the media (i. e. , dielectric constant, conductivity, collision frequency or electron density) are approximated in a piecewise-continuous sense by linear and quadratically varying stratifications. Although limited here to the normal incidence evaluation of structures composed of dielectric regions and plasma regions, the general scheme considers the problem as that of synthesizing a cascaded two-port network and has been used to synthesize distributed and lumped parameter filters as well. For these reasons a greater emphasis will be placed on this method than on the other two methods.

The third method has at present apparently only one major application, the design and synthesis of continuous parameter microwave absorbers. The description of this method ties together the n-dimensional optimization technique and the iterative type solutions such as those exhibited by J. H. Richmond,⁹ C. T. Swift, and J. S. Evans¹⁵ and arrives at a procedure capable of synthesizing inhomogeneous plasma-dielectric media.

II. THE BASIC APPROACH

The basic philosophy of the n-dimensional optimization technique is to create a function of the design parameters, often referred to as the merit or quality function, which attains its maximum value when the required design characteristics are achieved. Once this is done one may call upon the well formulated n-dimensional optimization techniques of gradient projection^{10, 11} and dynamic programming.² Although the method of gradient projection often consumes more computer time during execution than the dynamic programming method, it always maintains the interrelatedness of the optimization variables during the optimization process and is therefore the essential method for true synthesis problems. To the knowledge of this author, the dynamic programming procedure has not as yet been applied to the design of multilayers and should provide an additional design technique.

Evaluation and synthesis techniques of this nature are inherently computer oriented and if sufficient generality is built into the basic optimization computer programs, a whole host of problems may be attacked without any reprogramming. To apply such techniques one must have 1) a means to evaluate the characteristics of the basic structure for the determination of the merit function and 2) a means to associate the parameters of the structure with the optimization variables. At Grumman we have chosen to separate these two operations into separate computer routines or subroutines. For the class of problems of interest here, a computational procedure performs a frequency or frequency - incidence angle study (which ever is appropriate), as is generally done, and compares the resultant characteristics with the desired characteristics (which are fed to the computer separately) to generate the desired merit function. The merit function most often used is an error function which is expressed below in terms of the overall scattering coefficients⁶ of the structure:

$$\epsilon = - \int_{\theta_1}^{\theta_2} \int_{f_1}^{f_2} \sum_{j=1}^3 W_j^2 | S_j - S_j' | W_j^1 df d\theta \quad 2.1$$

where S_j are the three scattering terms S_{11} , $S_{12}=S_{21}$ and S_{22} , and W_j^1 and W_j^2 are arbitrary weighting functions which may be functions of f and θ . The prime denotes the desired characteristics for a design problem or the measured values for a true synthesis problem. The scattering notation is maintained because it is a universal notation for multilayer media as well as for lumped and distributed parameter networks.

The operation of associating the parameters of the structure with the optimization variables will be discussed in the following sections and may be accomplished in a number of ways dependent upon the type of structure used. As a point of interest, if this entire operation is properly contained in a subroutine the amount of programming from problem to problem can be reduced to a few simple statements (e.g., $E(2) = X(3)$; interpreted as, the dielectric constant of the second layer is derived from the third optimization variable).

III. A. THE HOMOGENEOUS MULTILAYER

A multilayer structure comprised of cascaded homogeneous layers is used as an academically - exact model for radome walls and is often used as an approximation to continuously varying longitudinally inhomogeneous media. The reflection and transmission coefficients for arbitrary angles of incidence of the basic n-layer model can be calculated using either a concise computational formalism such as that of J. F. Carpenter ⁷ or a matrix multiplication procedure as illustrated by R. E. Collin. ⁸ In either case, the parameters are the dielectric constants, conductivities and thicknesses of the individual layers, any or all of which may be directly related to the optimization variables on a 1-to-1 basis as illustrated in reference 3. If the multilayer is to be used as an approximation, then the parameters under optimization will in general far outnumber the optimization variables (for practical reasons only), and will be described by "Grouping Functions." Examples of the use of "Grouping Functions" whereby a small number of optimization variables are used to assign the locations and feeding coefficients of hundreds of antenna elements will be fully described in reference 5.

Reference 3 contains a number of examples of optimized dielectric multilayers. However, to extend the technique to include metal backed dielectric multilayers is of decided importance in the field of radar absorbers. The reflection coefficients for such a structure may be obtained by simply modifying the last interface reflection coefficients in Carpenter's formulation, ⁷ namely let

$$r_{m-1,m} = \pm 1 = - r_{m,m-1} \quad 3.1$$

where the (+) sign is for parallel and the (-) sign for perpendicular polarization. If matrix notation is used, one merely terminates the overall scattering matrix with the proper reflection coefficient and calculates the overall input reflection coefficient using,

$$S_{in} = S_{11} + \frac{S_{12} S_{21} S_L}{1 - S_L S_{22}} \quad 3.2$$

$$\text{where } S_L = \pm 1.$$

Using this technique with the merit function in Section II it has been shown possible to design multilayer microwave absorbers having peak absorptive efficiency over several discrete frequency bands.

III. B. INHOMOGENEOUS MULTILAYERS

If inhomogeneous layers are cascaded as a multilayer it becomes possible to approximate arbitrarily inhomogeneous media in a piecewise-continuous manner (See Figure 1). In particular, for normal incidence or for perpendicular polarization and arbitrary incidence angles, there exist solutions (series type) for a number of variations. These solutions are applicable to the study of TE wave propagation in waveguides and, in the field of plasma diagnostics to a problem of general concern, the synthesis and evaluation of a contained plasma.

The analysis technique begins with the determination of the scattering and scattering transfer matrix for an inhomogeneous slab in terms of the linearly independent solutions to the pertinent wave equation namely $f(z)$ and $g(z)$.⁴ The scattering matrix for the normal incidence case is given by:

$$\begin{aligned} S_{21} &= 2\gamma_1 \left[g(d) f'(d) - g'(d) f(d) \right] \div \Delta \\ S_{12} &= 2\gamma_2 \left[g(0) f'(0) - g'(0) f(0) \right] \div \Delta \\ S_{11} &= \left[f(d) \left\{ \gamma_1 \gamma_2 g(0) + \gamma_2 g'(0) \right\} + f'(d) \left\{ g'(0) + \gamma_1 g(0) \right\} + \right. \\ &\quad \left. - g(d) \left\{ \gamma_1 \gamma_2 f(0) + \gamma_2 f'(0) \right\} - g'(d) \left\{ f'(0) + \gamma_1 f(0) \right\} \right] \div \Delta \\ S_{22} &= \left[f(d) \left\{ \gamma_1 \gamma_2 g(0) - \gamma_2 g'(0) \right\} + f'(d) \left\{ g'(0) - \gamma_1 g(0) \right\} + \right. \\ &\quad \left. - g(d) \left\{ \gamma_1 \gamma_2 f(0) - \gamma_2 f'(0) \right\} - g'(d) \left\{ f'(0) - \gamma_1 f(0) \right\} \right] \div \Delta \end{aligned} \quad 3.3$$

where

$$\begin{aligned} \Delta &= \left[f(d) \left\{ \gamma_1 \gamma_2 g(0) - \gamma_2 g'(0) \right\} + f'(d) \left\{ \gamma_1 g(0) - g'(0) \right\} + \right. \\ &\quad \left. - g(d) \left\{ \gamma_1 \gamma_2 f(0) - \gamma_2 f'(0) \right\} - g'(d) \left\{ \gamma_1 f(0) - f'(0) \right\} \right] \end{aligned}$$

From these expressions we can see that if $f(z)$ or $g(z)$ contain any arbitrary fixed constants as multipliers, (i.e., $af(z)$) then these may be discarded.

The scattering transfer matrix coefficients are then simply given by:

$$\begin{aligned} \tau_{11} &= \left(R_4 - \frac{R_1^2 - R_2^2}{R_3} \right) \div \Delta & \tau_{12} &= \frac{R_1 + R_2}{R_3} \\ \tau_{21} &= \frac{R_2 - R_1}{R_3} & \tau_{22} &= \frac{\Delta}{R_3} \end{aligned} \quad 3.4$$

where

$$\begin{aligned} R_1 &= \gamma_1 \gamma_2 \left\{ f(d) g(0) - g(d) f(0) \right\} + f'(d) g'(0) - g'(d) f'(0) \\ R_2 &= \gamma_2 \left\{ f'(d) g'(0) - g(d) f'(0) \right\} + \gamma_1 \left\{ f'(d) g(0) - g'(d) f(0) \right\} \end{aligned}$$

$$R_3 = 2\gamma_1 \left[g(d) f'(d) - g'(d) f(d) \right] \quad 3.5$$

$$R_4 = 2\gamma_2 \left[g(0) f'(0) - g'(0) f(0) \right]$$

where γ_1 and γ_2 are the propagation coefficients of the exterior boundary media at ports 1 and 2 respectively.

Once the coefficients for the individual matrices are determined, the total transfer matrix for the cascaded system is found by simple matrix multiplication. Since it is not necessary that the normalized scattering matrices be used, the only requirement is that the mating terminal planes have the same reference wave impedance.

The homogeneous media together with the linearly and quadratically varying media constitute the three basic structures considered. All these elements contain loss terms and, being free from the commonly invoked assumptions, exhibit realistic characteristics. For instance, the inclusion of a non-zero collision term eliminates the possibility of the plasma becoming non-propagating. These elements are really all that is necessary to provide a very accurate piecewise approximation of any prescribed inhomogeneous media.

For a class of linear inhomogeneities the field equation takes the form

$$\frac{d^2 E(z)}{dz^2} + (2\pi)^2 [P + Qz] E(z) = 0 \quad 3.6$$

which can be reduced to the Airy form.¹³ The generalized solutions and their derivatives are given by,

$$f^{(0)}_{(d)} = \left\{ 1 + \sum_{\ell=1}^{\infty} (-1)^{\ell} \left(\frac{2\pi}{3Q} \right)^{2\ell} \frac{D^{(0)}_{(d)}{}^{3\ell}}{\ell! \prod_{k=0}^{\ell-1} (k + 2/3)} \right\}$$

$$g^{(0)}_{(d)} = D^{(0)}_{(d)} Q^{-1} \left\{ 1 + \sum_{\ell=1}^{\infty} (-1)^{\ell} \left(\frac{2\pi}{3Q} \right)^{2\ell} \frac{D^{(0)}_{(d)}{}^{3\ell}}{\ell! (3\ell+1) \prod_{k=0}^{\ell-1} (k + 1/3)} \right\} \quad 3.7$$

$$f'^{(0)}_{(d)} = - \left[2\pi D^{(0)}_{(d)} \right]^2 Q^{-1} \left\{ \frac{1}{2} + \sum_{\ell=1}^{\infty} (-1)^{\ell} \left(\frac{2\pi}{3Q} \right)^{2\ell} \frac{D^{(0)}_{(d)}{}^{3\ell}}{\ell! (3\ell+2) \prod_{k=0}^{\ell-1} (k + 2/3)} \right\}$$

$$g'^{(0)}_{(d)} = \left\{ 1 + \sum_{\ell=1}^{\infty} (-1)^{\ell} \left(\frac{2\pi}{3Q} \right)^{2\ell} \frac{D^{(0)}_{(d)}{}^{3\ell}}{\ell! \prod_{k=0}^{\ell-1} (k + 1/3)} \right\}$$

where

$$D^{(0)}_{(d)} = \left[P + Qz \right] \Big|_{z = \begin{pmatrix} 0 \\ d \end{pmatrix}}$$

The expressions for P, Q and D are tabulated in Figure 2. For the linear variation, the series defined by the four summations in Equation 3.7 are absolutely convergent. However, for certain ranges of Q and D the series converge very slowly and the accumulative terms rise to large values which exceed the computer limits and in turn invalidate the particular computation. Since this computer deficiency does not necessarily coincide with the point at which the asymptotic, large argument expansions or approximations become valid, no asymptotic solutions were formulated. In lieu of this, the computational procedure is altered when the accuracy falters and a multilayer approximation is incorporated to calculate the coefficients. Experience has shown that when the multilayer approximation is used the results are comparable, providing the slope is $\ll 1$ or the number of layers per wavelength is large enough.^{1, 14}

A quadratic variation has application in regions having an initially zero slope. A number of quadratic variations can be put in the form

$$\frac{d^2 E(W)}{dW^2} + (2\pi)^2 \left[\bar{P} - \bar{Q} W^2 \right] E(W) = 0 \quad 3.8$$

The solutions for this equation are given by the Weber-Hermite polynomials and expressed here in terms of the confluent hypergeometric functions ${}_1F_1$.¹² The specific series used, ${}_1F_1$, is convergent for all values of a, b, and x both complex and real excluding $b = 0, -1, -2, \dots$, and is given by

$${}_1F_1 \left[a; b; x \right] = 1 + \sum_{n=1}^{\infty} \frac{\prod_{k=0}^{n-1} (a+k)}{\prod_{k=0}^{n-1} (b+k) n!} x^n$$

Utilizing the derivative properties of ${}_1F_1$, namely

$$\frac{d}{dz} \left\{ {}_1F_1 \left[a; b; x \right] \right\} = \frac{dx}{dz} \cdot \frac{a}{b} {}_1F_1 \left[a+1; b+1; x \right]$$

and the ability to discard arbitrary constants, the solutions to 3.8 and their derivatives become

$$f(z) = W e^{\frac{-\bar{D}W^2}{2}} {}_1F_1 \left[\frac{3}{4} - \pi^2 \frac{\bar{P}}{\bar{D}} ; \frac{3}{2} ; \bar{D}W^2 \right]$$

$$g(z) = e^{\frac{-\bar{D}W^2}{2}} {}_1F_1 \left[\frac{1}{4} - \pi^2 \frac{\bar{P}}{\bar{D}} ; \frac{1}{2} ; \bar{D}W^2 \right]$$

$$\begin{aligned}
f'(z) &= e^{\frac{-\bar{D}W^2}{2}} 2\bar{D}W^2 \left[\frac{1}{2} - \frac{2\pi^2\bar{P}}{3\bar{D}} \right] {}_1F_1 \left[\frac{7}{4} - \frac{\pi^2\bar{P}}{\bar{D}}; \frac{5}{2}; \bar{D}W^2 \right] + \\
&+ \left[1 - \bar{D}W^2 \right] {}_1F_1 \left[\frac{3}{4} - \pi^2 \frac{\bar{P}}{\bar{D}}; \frac{3}{2}; \bar{D}W^2 \right] \Bigg\} \\
g'(z) &= e^{\frac{-DW^2}{2}} \bar{D}W \left\{ \left[1 - (2\pi)^2 \frac{\bar{P}}{\bar{D}} \right] {}_1F_1 \left[\frac{5}{4} - \pi^2 \frac{\bar{P}}{\bar{D}}; \frac{3}{2}; \bar{D}W^2 \right] \right. \\
&\left. - {}_1F_1 \left[\frac{1}{4} - \pi^2 \frac{\bar{P}}{\bar{D}}; \frac{1}{2}; \bar{D}W^2 \right] \right\}
\end{aligned}$$

$$\text{where } \bar{D} = +2\pi\sqrt{\bar{Q}}$$

The reversed element (Case II) with a zero slope occurring at $z = d$ can be obtained by logically switching S_{11} and S_{22} or by redefining the variations. The variable W was introduced to unify these various configurations. Since $dW/dz = 1$ and $d^2W/dz^2 = 0$ for the transformations $W = z$ and $W = z - d$ a simple relation between the two cases exists. The coefficients for Equations 3.9 are tabulated in Figure 3.

In essence, it is the ability to approximate arbitrary distributions in a piecewise continuous manner which makes the evaluation technique compatible with the optimization process.

The synthesis process is initiated by choosing an initial estimate of the distribution. The distribution is then piecewise approximated by N elements (See Fig. 1). The $2N + 1$ optimization variables are ν_i and $\omega_{p,i}$ defined as the collision frequency of the i th layer and the plasma frequency at the junction of layer i and $i-1$. The only physical constraints imposed are that $0 \leq \nu_i < \infty$ and $0 \leq \omega_{p,i} < \infty$. For a dielectric media, the variables would be the dielectric constants and conductivities at the multilayer interfaces. A lossy, non-symmetrical, reciprocal structure such as this is defined by the three complex quantities S_{11} , $S_{12} = S_{21}$ and S_{22} .

For convenience, let these quantities be denoted by S_j when measured and S'_j when calculated such that if the estimated structure is the actual structure, then $S_j = S'_j$. If the function to be optimized is an error function defined such that it remains ≤ 0 , then the optimization program will operate on the variables utilizing gradient projection in such a manner as to reduce the function to zero. One of many ways to express an error function for this problem is shown below:

$$\mathcal{E}(\omega_{p_1}, \nu_1) = - \sum_{j=1}^3 \int_{\omega_1}^{\omega_2} a_j |S_j^{\nu} - S_j^{\mu}|^{b_j} d\omega \leq 0$$

$$\begin{aligned} m &> 0 \\ b_j &> 0 \\ a_j &\geq 0 \end{aligned}$$

If $\mathcal{E} = 0$ for particular ω_{p_1} and ν_1 , then $S_j = S_j^{\nu}$ between ω_1 and ω_2 and the resultant structure is a terminal equivalent model of the plasma distribution for $\omega_1 \leq \omega \leq \omega_2$. It is not the intent of this discussion to belabor the many facets of the optimization program and the techniques for establishing suitable error functions since these are explained in the references. It is sufficient to note that for a large number of elements and given accurate data, the results should be comparable with those obtained in the homogeneous multilayer designs.

To date this technique has not been applied to any plasma device for which there was experimentally derived data. However, specific models have been set up which have successfully demonstrated the application. One important conclusion can be drawn from the examples. Namely, as expected, it is important to have as accurate and complete a spectrum (i. e. numerous values of the reflection and transmission coefficients) as possible for a successful synthesis process.

The outlined procedures offer a highly systematized approach to the evaluation and synthesis of longitudinally inhomogeneous plasma-dielectric media. For plasma media, a piecewise continuous approximation to the electron density and a stepwise approximation to the collision term, may be accomplished simultaneously. For dielectric media, piecewise continuous approximations may be utilized for both the dielectric constant and conductivity. Since the technique allows the incorporation of both dielectric and plasma media within the same structure, it affords a means to obtain approximate results for problems encountered in shock tubes, discharge tubes, missile wakes and re-entry plasmas. Similarly, the technique can be applied to investigating and determining optimum designs in non-uniform-wall radomes and microwave absorbing materials. It is important to note that the optimization process is in essence operating on the parameters which define the overall scattering matrix. Once this generality is established, the individual scattering matrices may represent lumped or distributed parameter networks. From a programming standpoint at Grumman, the problem has been viewed as the general optimization of a system of cascaded two ports. The individual matrix coefficients are determined within specific subroutines in terms of a general array of parameters. An entire library of subroutines has been set up to cover such standard components as a length of waveguide, waveguide bends, various lumped parameter networks, and the plasma and dielectric slabs. The only programming necessary for any problem is that required to associate the optimization variables with the parameters under optimization. The choice of components and their order is accomplished by merely specifying and properly arranging input data.

III. C. CONTINUOUSLY DEFINED INHOMOGENEOUS MEDIA (NON-MULTILAYER)

Although the piecewise - continuous approximation of III B. can be applied to a variety of problems, there may arise instances when it is desirable to encompass both incidence polarizations in the design or synthesis problem. An example of this would be the problem of TM-wave propagation in waveguides utilizing inhomogeneous

components as loads or filters. The programming necessary to arrive at the transmission and reflection coefficients for this problem, by virtue of the iterative techniques used, is more involved than that for the formalism of III A. or the series in III B. However, once the program for general evaluation studies is made available it can be stripped of all the printed output and automatic plotting routines (inherent to programs produced for research studies) and packaged as a basic subroutine for use with the optimization programs.

Although the schematization of references 9 and 15 may be employed directly for purely dielectric or purely plasma media, the practical problem of generating a plasma discharge necessitates the inclusion of dielectric retaining walls in the analysis. This problem is solved by determining the scattering parameters for the inhomogeneous plasma portion separately and using the three-element sandwich equations or matrix multiplication to evaluate the overall structure.

The association of the optimization variables to the parameters of the structure is dependent upon the form of the function chosen to describe the inhomogeneity. For instance if the distribution of electron density (which is proportional to the square of the plasma frequency) and collision frequency are assumed to be of the form

$$\omega_p^2(z) = \sum_{n=1}^M a_n z^{n-1}; \quad \nu(z) = \sum_{n=m+1}^N a_n z^{n-m-2} \quad 0 \leq z \leq d$$

then the N optimization variables, x_n , are the unknowns a_n (i. e., $a_n = x_n$). An interesting application arises when the general form of the distributions are arrived at heuristically and only a few parameters need be determined. To illustrate more clearly assume that the electron density and the collision frequency are assumed to have the following form;

$$\omega_p^2(z) = a_1 e^{-a_2(z - \frac{d}{2})^2}; \quad \nu(z) = a_3 e^{-a_4(z - \frac{d}{2})^2},$$

where d is the confinement distance. This lends itself to a simple specification of the optimization variables, namely $a_n = x_n$. Since the gross form of the distribution is assumed known, only four parameters have to be determined - a circumstance for which the application of n-dimensional optimization is highly practical.

IV CONCLUSIONS

The use of a n-dimensional optimization as an engineering design tool is becoming more wide spread and, as the number of applications increases, the stockpile of available design data will grow. This will be essential to competently evaluate for future applications the relative merits of the various optimization methods and modifications thereof. The application to pure synthesis is a problem presently undergoing investigation at Grumman and will undoubtedly remain more of a laboratory or research tool than a practical design technique.

As a design technique it has proven successful in the design of radome walls, microwave absorbers, and antenna arrays and has certain distinct advantages. However, the total merit of any scheme must weigh factors such as cost along with less tenable entities as the loss in the intuitive reasoning behind the final design. As a

suggestion - it is advisable to take advantage of the sophisticated automation, presumably built into the computer programs, to keep the number of manhours spent handling cards and programs to a minimum. This allows the hard-core analytic design groups, which will never be eliminated, to work in conjunction with the computer towards the end goal of a better design.

V. REFERENCES:

1. R. B. Barrar and R. M. Redheffer, "On Non-uniform Dielectric Media," IRE Transactions, Vol. AP-3; (July, 1955).
2. R. Bellman, Dynamic Programming, Princeton University Press, Princeton, New Jersey; (1957).
3. M. C. Blyseth, "Computer Design and Optimization of Arbitrary Multilayer Dielectric Distributions and Planar Antenna Arrays," Grumman Advanced Development Report ADR-03-04-63.1; Proceedings of the ASD-OSU Electromagnetic Window Symposium; (June 1962).
4. M. C. Blyseth, "Scattering Matrix Formulation for Isotropic inhomogeneous Media with Application to Plasma Diagnostics," Grumman Advanced Development Report ADR-03-04-63.2 (June 1963).
5. M. C. Blyseth and G. B. Hummel, "Synthesis and Sidelobe Reduction of Electronically Scanned Arrays," to be presented at the 1964 PTGAP International Symposium, New York.
6. H. J. Carlin, "The Scattering Matrix in Network Theory," IRE Trans., PGCT, Vol. CT-3, No. 2; (June 1956).
7. J. F. Carpenter, "Reflection and Transmission of Plane Electromagnetic Waves by a Lossy Multi-Ply Sandwich," Proceedings of the OSU-WADC Radome Symposium, WADC-TR-57-314; (1957).
8. R. E. Collin, Field Theory of Guided Waves, McGraw-Hill Book Co., Inc., New York; (1960).
9. J. H. Richmond, "Transmission through Inhomogeneous Plane Layers," IRE Transactions, Vol. AP-10, No. 3, p. 300; (May 1962).
10. J. B. Rosen, "The Gradient Projection Method for Nonlinear Programming, Part I, Linear Constraints," J. Soc. Indus. Appl. Math., Vol. 8, No. 1, March, 1960
11. J. B. Rosen, "The Gradient Projection Method for Nonlinear Programming, Part II, Nonlinear Constraints," Shell Development Co., Emeryville, California, January, 1961.
12. L. J. Slater, Confluent Hypergeometric Functions, Cambridge University Press, Great Britain; (1960).
13. A. D. Smirnov, Tables of Airy Functions and Special Confluent Hypergeometric Functions, Pergamon Press, New York; (1960).
14. D. C. Stickler, "On the Propagation of Electromagnetic Waves in a Stratified Layer," OSURF, 786-22; (1959).

15. C. T. Swift and J. S. Evans, "Generalized Treatment of Plane Electromagnetic Waves Passing through an Isotropic Inhomogeneous Plasma Slab at Arbitrary Angles of Incidence," Langley Research Center, NASA Technical Report R-172; (1963).

An effort has been made to include references which are representative of the basic treatments and which contain numerous references for further study.

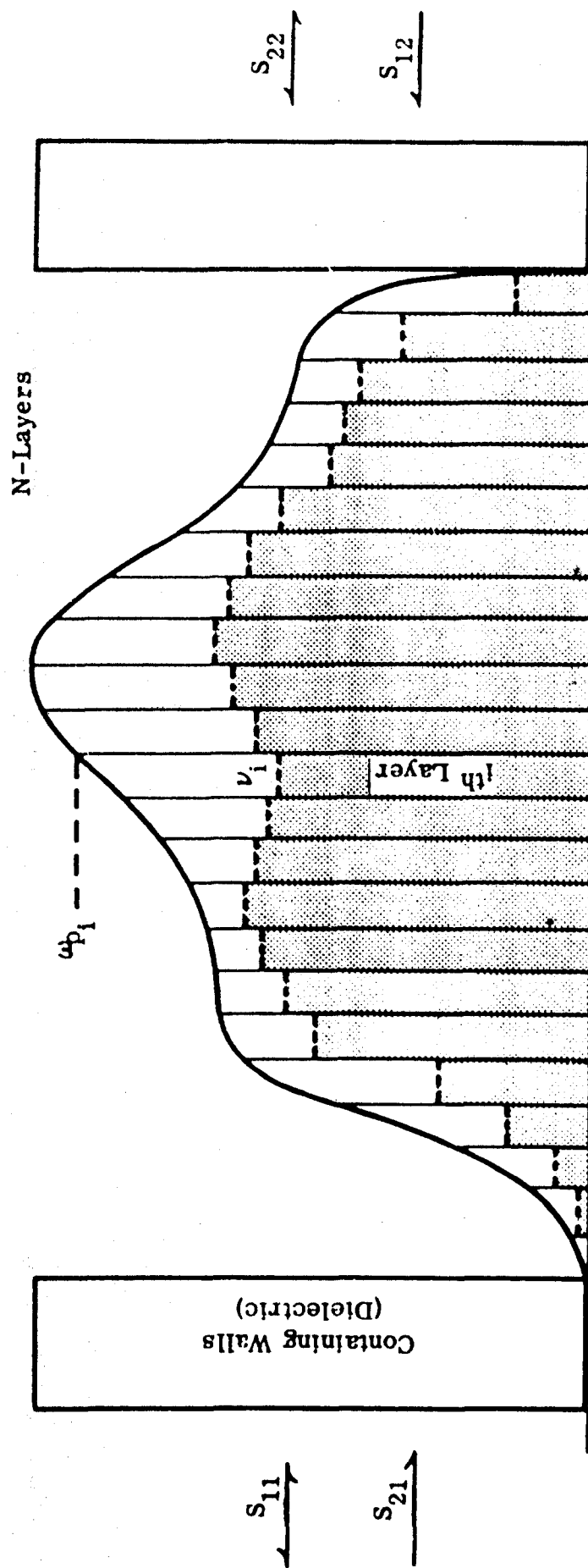


Figure 1 Piecewise Continuous Approximation for the Synthesis Problem

Type of Linear Inhomogeneity	Definition of Variation	P	Q	$D(d)$
Plasma Electron Density	$\omega_p^2(z) = \left(\frac{\omega_p^2(d) - \omega_p^2(o)}{d} \right) z + \omega_p^2(o)$	$1 - \left(\frac{1+j\nu}{1+\nu^2} \right) \omega_p^2(o)$	$-\left(\frac{1+j\nu}{1+\nu^2} \right) \left(\frac{\omega_p^2(d) - \omega_p^2(o)}{d} \right)$	$1 - \left(\frac{1+j\nu}{1+\nu^2} \right) \omega_p^2(d)$
Lossy Dielectric Dielectric Constant	$\epsilon_r(z) = \left(\frac{\epsilon_r(d) - \epsilon_r(o)}{d} \right) z + \epsilon_r(o)$	$\epsilon_r(o) - jr$	$\frac{\epsilon_r(d) - \epsilon_r(o)}{d}$	$\epsilon_r(d) - jr$
	$r(z) = \left(\frac{r(d) - r(o)}{d} \right) z + r(o)$	$\epsilon_r - jr(o)$	$-j \frac{(r(d) - r(o))}{d}$	$\epsilon_r - jr(d)$
	As Above	$\epsilon_r(o) - jr(o)$	$\frac{[\epsilon_r(d) - \epsilon_r(o)] - j[r(d) - r(o)]}{d}$	$\epsilon_r(d) - jr(d)$
Lossy Dielectric Conductivity				
Lossy Dielectric Dielectric Constant and Conductivity				

Figure 2 Coefficients for Equation 3.7

	Medium	\bar{P}	\bar{Q}	$t(z)$	$W(o)$	$W(d)$
CASE I	Plasma	$1 - \left(\frac{1 + j\nu}{1 + \nu^2} \right) \omega_p^2(o)$	$\left(\frac{1 + j\nu}{1 + \nu^2} \right) \left(\frac{\omega_p^2(d) - \omega_p^2(o)}{d^2} \right)$	$W = z$	0	d
	Dielectric	$\epsilon(o) - jr(o)$	$\frac{\epsilon(o) - \epsilon(d) + j(r(d) - r(o))}{d^2}$	$W = z$	0	d
CASE II	Plasma	$1 - \left(\frac{1 + j\nu}{1 + \nu^2} \right) \omega_p^2(d)$	$\left(\frac{1 + j\nu}{1 + \nu^2} \right) \left(\frac{\omega_p^2(o) - \omega_p^2(d)}{d^2} \right)$	$W = z - 1$	-d	0
	Dielectric	$\epsilon(d) - jr(d)$	$\frac{\epsilon(d) - \epsilon(o) + j(r(o) - r(d))}{d^2}$	$W = z - 1$	-d	0

Figure 3 Table of Coefficients for Equation 3.9

QUALITY CONTROL AND NON-DESTRUCTIVE TESTING
OF DIELECTRIC COMPONENTS

USING THE MICROWAVE THICKNESS GAUGE

By J. D. Leonard and G. T. Stropki

North American Aviation, Inc.
Columbus, Ohio

Introduction

In recent years many methods have been investigated and various techniques implemented to measure and control the wall thickness of radomes, antenna covers, printed circuit boards and other items utilizing dielectric materials. The more successful approaches have involved the use of electromagnetic energy in the microwave region. These include various interferometer techniques which make use of the relationships between reflected or transmitted energy and the physical parameters of interest.

Since the factors which enter into the design of radomes (physical thickness, incidence angle, relative dielectric constant and wavelength) are interrelated, it is convenient to consider them together in terms of "electrical thickness". It is principally this quantity which is observed in the various applications of interferometry to measurement and control problems.

A highly successful device was developed by North American Aviation, Inc., Columbus Division in the early phases of the A3J radome development as a result of the need for greater precision in electrical thickness control than was otherwise obtainable. Results obtained using the MTG (Microwave Thickness Gauge) were first reported in a paper presented at the OSU-WADD Symposium on Electromagnetic Windows in 1960. Since that time, its value in non-destructive testing and quality control of dielectric components has eliminated all correction by "patching" and has assured a high degree of uniformity and reproducibility. A variety of other applications, a few of which are described below, have further demonstrated its usefulness and versatility.

Theory of Operation

The MTG utilizes basic microwave components which are assembled as shown in Figure 1.

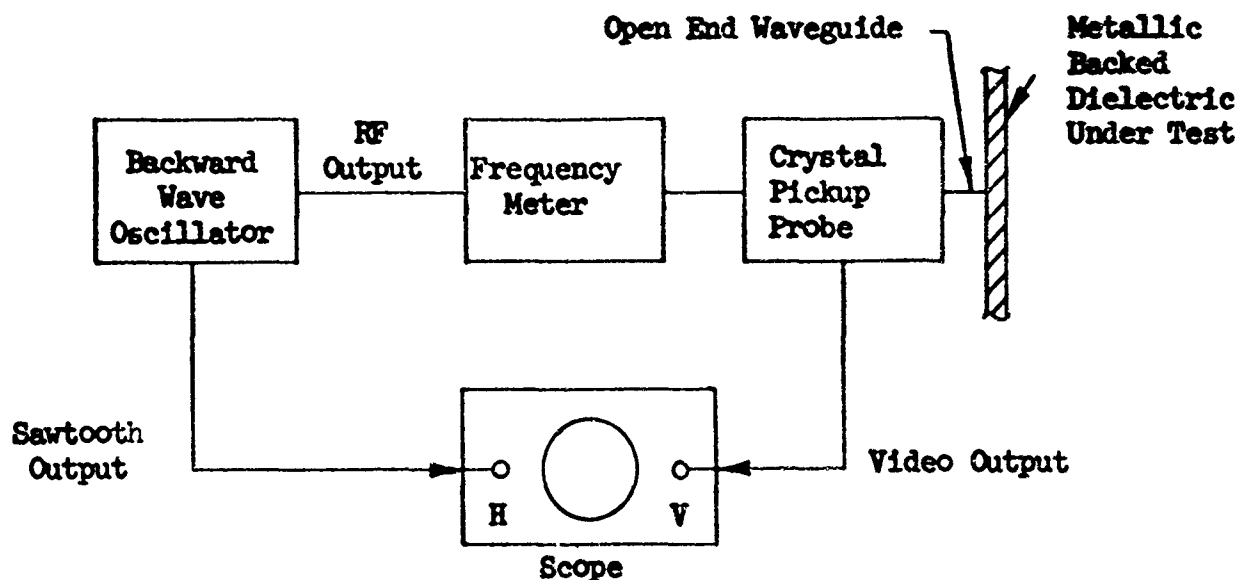


FIGURE 1 - MICROWAVE THICKNESS GAUGE BLOCK DIAGRAM

Operation of the Gauge is described with the aid of Figure 2. When the probe is properly positioned against the material to be measured, the reflecting surface produces a standing-wave in the probe assembly, advancing or retarding in relative position as the frequency is swept. The sweep voltage applied to the backward wave oscillator is also fed to the horizontal input of the oscilloscope, and the output of the probe detector is fed to the input of the vertical amplifier of the oscilloscope. In this manner a waveform representing the standing-wave amplitudes at the detector as a function of frequency is presented on the scope. Normally a single minimum is displayed in an inverted form as a peak. The marker frequency meter is a reaction cavity type and may be adjusted to the frequency at which the displayed peak occurs on the oscilloscope.

As the material thickness varies at the probe, the electrical length of the line changes between the reflecting surface and the detector coupling point, and the resultant standing-wave minimum (displayed as a peak) shifts its position horizontally on the scope. The marker pip, however, remains at the same point horizontally on the scope. Hence, the relative motion between the peak position and the marker pip on the oscilloscope is a measure of the electrical path length through the dielectric material, and calibration of this motion may be performed with a sample of known thickness.

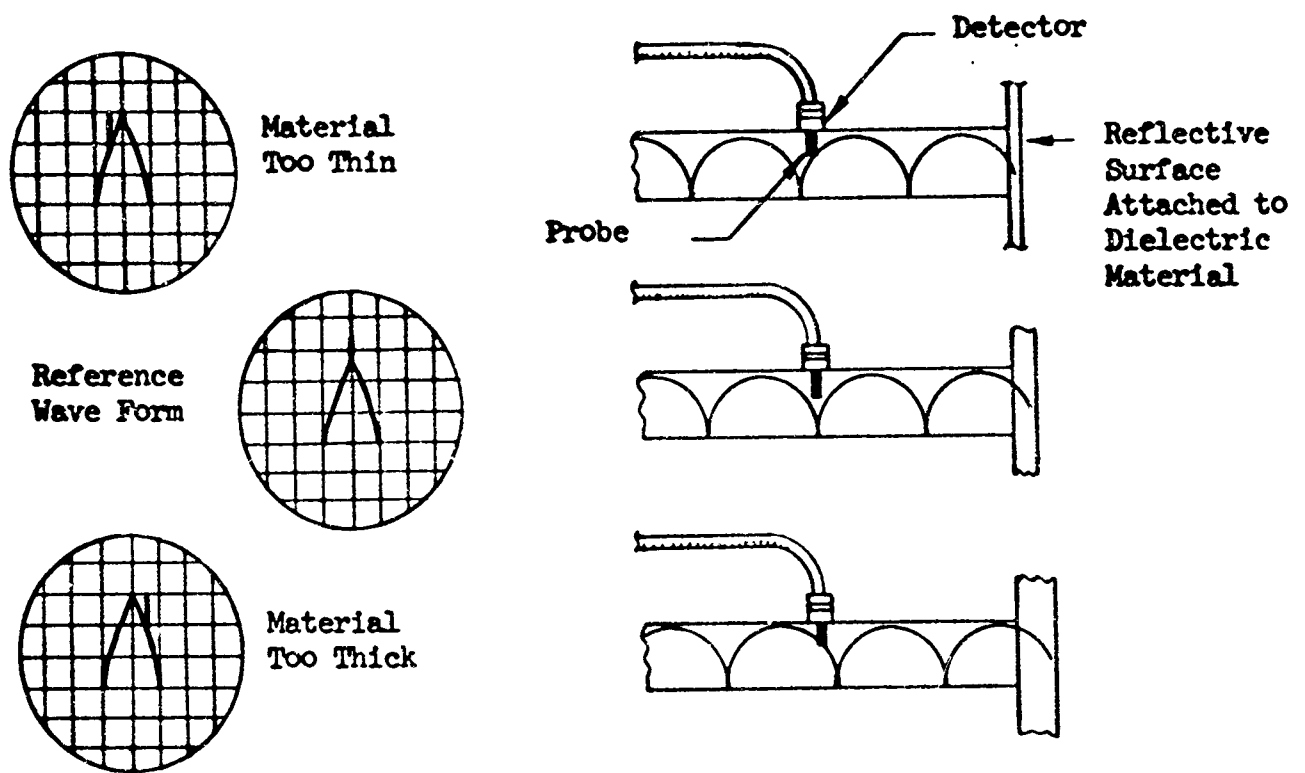


FIGURE 2 - SCOPE DISPLAY AND STANDING WAVE RELATIONSHIP

The rear surface of the material to be measured must be coated with a highly conductive reflective substance. A suitable substance for this purpose required development, since metallic material with adhesive backing is, in general, unsuitable. A plastic spray with imbedded silver particles was developed which can be applied to irregular shapes without wrinkling and is readily removable by stripping.

Variations in electrical thickness detected by the MTG are caused by non-uniformity of the dielectric material, voids, discontinuities such as delaminations, etc., as well as changes in physical thickness. The capability of the MTG to detect these variations was investigated.

Microwave Thickness Gauge Sensitivity

A series of tests to determine detection sensitivities were performed on a typical sample.

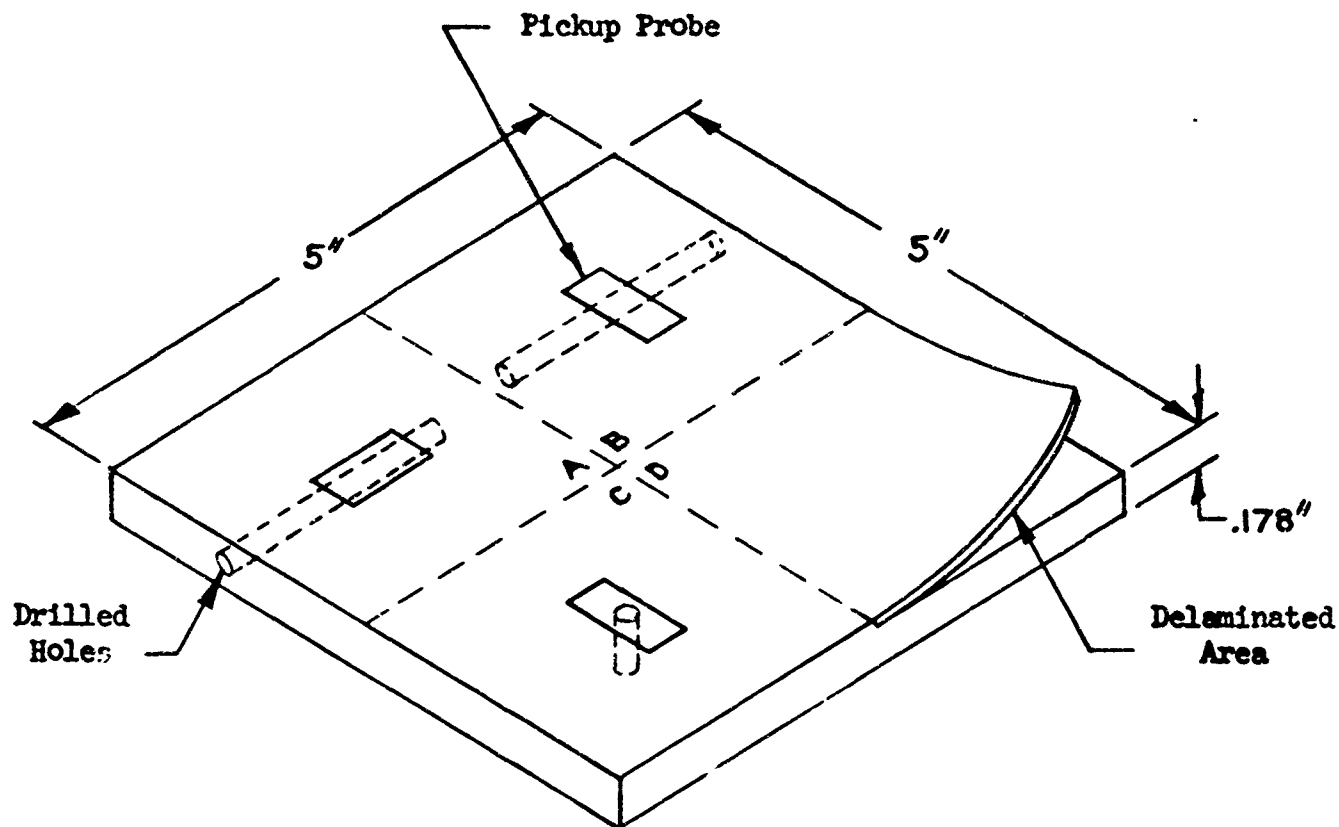


FIGURE 3 - FIBERGLASS LAMINATE TEST SAMPLE

The sample was divided into four areas - A, B, C and D, as shown in Figure 3. The instrument was calibrated and referenced in each area before modifications. In area A the thickness gauge indicated the material to be .002" thinner after a .027" diameter hole was drilled in the sample. Holes of larger size gave more marked indication of thickness change.

In area B the same size holes gave less indication than before due to difference in polarization. In area C the results were the same as those obtained in B.

In area D the instrument gave an indication of increased thickness after delamination of the top plys.

Tests performed on printed circuit material indicated results similar to those achieved in area D.

Applications

Radomes fabricated with the aid of the MTG have exhibited excellent electrical properties and repeatability from unit to unit without the need for individual tailoring. Additional experience has been gained in a variety of applications of interest.

One of the more interesting applications of the MTG has been in electrical thickness control of reactive wall radomes for special purpose ECM applications. The reactive element consists of a grid of etched conductors with inter-conductor spacing determined by operating frequency and other factors. In some cases the spacing is such that the indication obtained with the MTG depends on the position and orientation of the probe. In this application it is not practical to rely on mechanical means to give an accurate measure of electrical thickness. However, the MTG was successfully used following a probe modification which increased the aperture to encompass a greater area and reduced the interaction between the grid and the pickup probe.

The MTG was also used in an application involving spiral antennas fabricated using printed circuit techniques. The antennas were mounted in cavities and used in pairs in a phase comparison system. When completed, the active element of the antenna (spiral) was bonded between two layers of fiberglass laminate. In this case the MTG used the spiral itself as the reflective element to determine the electrical thickness of the laminate on each side of the spiral.

In a non-electrical application, failure of the fiberglass laminate used in a missile firewall had been experienced as a result of voids in the laminate material. The MTG was successfully applied to determine whether the voids were detectable by this means. As a part of this test, and unknown to the operator of the instrument, a 2.5 cm long, 4 mm diameter hollow pyrex rod was imbedded in one of the fiberglass samples. Not only was the MTG capable of detecting the perturbation caused by the rod, but the exact location and orientation was correctly determined.

Conclusion

Experience in using the Microwave Thickness Gauge in a variety of production applications has demonstrated the basic soundness of its design for non-destructive testing and quality control of dielectric components. Also, it has been a versatile and highly useful laboratory tool in both analytical and development work.

DUAL FREQUENCY RADOME FEASIBILITY

Grant M. Randall
and
Donald F. Zemke
Autonetics

A Division of North American Aviation, Inc.
Anaheim, California

Introduction

Based upon the needs of advanced weapon systems having multimode missions to perform, complex requirements are placed on the radar system. These multimode missions demand optimum radar performance for each mode of operation. Since the optimum radar performance requires different radar parameters for each mode, complex design requirements are placed upon the radar. Consideration must be given in the design of the radar to optimize the radar performance for each mode without too many compromises. One way in which the radar performance can be enhanced for the various mode requirements is to utilize a dual frequency radar concept. In this way, optimum radar performance for each mode can be obtained by using two different frequencies.

Dual frequency radar operation in a high performance aircraft has been considered in the past. The radome performance considerations are deemed of most importance to the dual frequency radar operation.

A dual frequency radome feasibility study has been initiated by the Armament Control Division of Autonetics. The results of this study have been completed and show that a dual frequency radar-radome combination is feasible. A dual frequency NASARR radar system has been developed and successfully demonstrated in actual flight test in an X-band radome. Very satisfactory operation at the Ka-band frequency in this radome was obtained.

Basic Radome Design

One of the basic concepts used in radome design is to use a dielectric material of specific thickness as a radome wall. The optimum thickness is a function of the frequency of operation, characteristics of the dielectric material and the radome shape. The proper thickness is chosen to provide optimum electromagnetic energy transmission through the radome. Figure 1 shows the

radome wall and a definition of the design equation parameters.

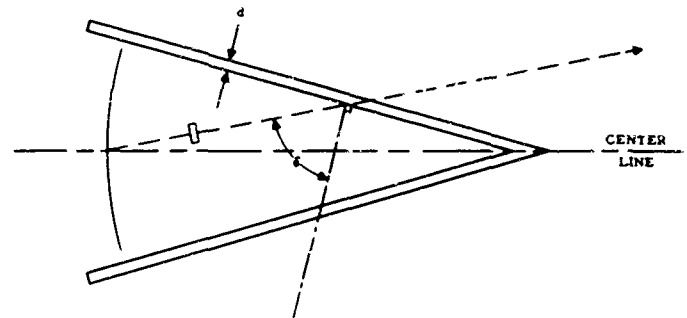


Figure 1. Radome Wall and Design Parameters

Optimum radome wall thickness for maximum transmission is given by the following equation.

$$d = \frac{n \lambda_0}{2 \sqrt{\epsilon - \sin^2 \theta}} \quad (1)$$

where d = thickness of dielectric sheet

n = any positive integer

λ_0 = free space wavelength

ϵ = relative dielectric constant

θ = angle of incidence

If (n) in Equation 1 is equal to 1, then the radome is called a half-wave radome. This value of (n) also is the minimum wall thickness. By making (n) equal to 2, 3, or 4, a higher order radome design is obtained.

Now consider the dual frequency radome design concept:

If $n = 1$ and
 $\lambda_0 = 1.36$ inches (X-band)

A specific value of d can be calculated.

If $n = 2$ and
 $\lambda_0 = 0.68$ inches (Ku-band)

then d would be equal to the same value obtained in the X-band case. Thus, multiples of the basic X-band frequency can be used in a dual frequency radar concept. See Table I.

Table I

Radar Band	Frequency Mc	Wavelength Inches	n	Radome Thickness d Inches
X	8,700	1.36	1	0.320
Ku	17,400	0.68	2	0.320
K	26,100	0.45	3	0.320
Ka	34,860	0.34	4	0.320

Figures 2 and 3 show the multiple peaks for optimum radome transmission at the various frequencies for two incident angles.

Evaluation of the radome transmission equations for various materials, for a high performance radome shape and at dual frequencies, requires considerable analysis. A radar study program was initiated to further investigate the dual frequency radome concept.

Radome Study Program

A. Purpose

The purposes of the dual frequency radome study program were as follows:

1. Determine the feasibility of dual frequency radar operation in the presence of a high performance aircraft radome.
2. Determine the effect of various radome materials on the radar performance characteristics.
3. Make an analytical radome study.
4. Fabricate dual frequency radome test panels from design information.
5. Measure dual frequency radome performance characteristics on the radome test panels.
6. Compare analytical and measured results.

7. Summarize dual frequency radome feasibility.

B. Study Program Phases

1. Analytical comparison of materials, radome construction methods and expected performance.
2. Fabrication
 - (a) Fabricate radome test panels.
3. Radome Test Panel Measurements
 - (a) Transmission
 - (b) Insertion phase
 - (c) Dielectric constant
 - (d) Temperature effects

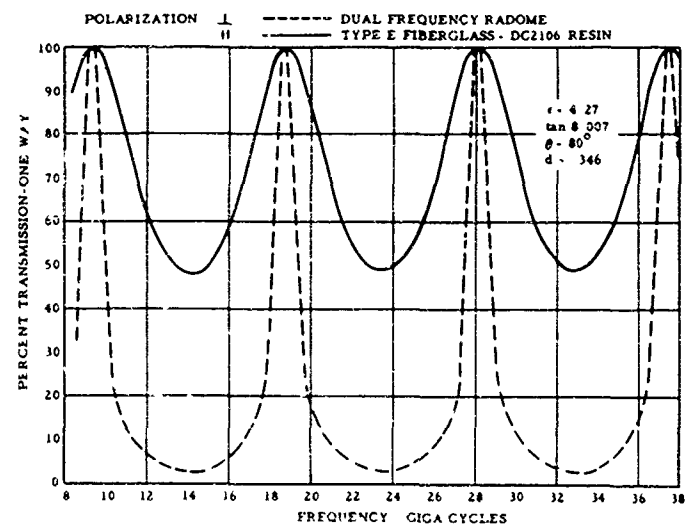


Figure 2. Dual Frequency Radome Type "E" Fiberglass DC-2106 Resin (80° angle)

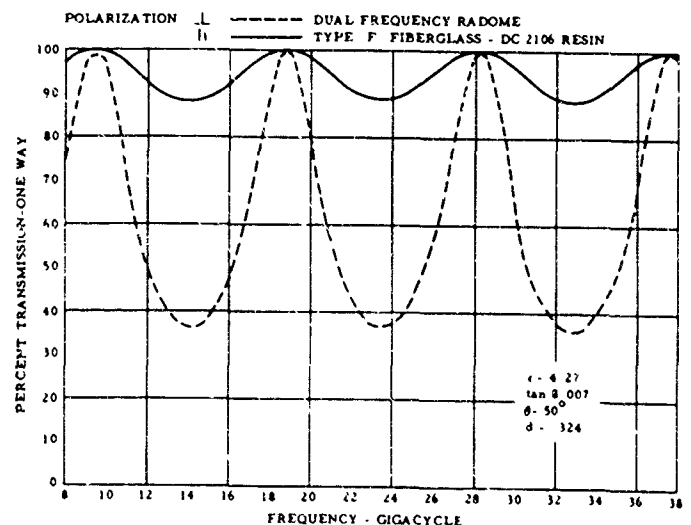


Figure 3. Dual Frequency Radome Type "E" Fiberglass DC-2106 Resin (55° angle)

4. Comparison and Conclusions

Results

The analytical study, fabrication of test panels, and measurements were conducted in conjunction with the radome department of the Los Angeles Division at North American Aviation, Inc.

A summary of the most significant analytical and measured data is shown in the appendix.

Conclusions

- A. The data presented in the report support the feasibility of designing and constructing a dual frequency radome.
- B. Two radome materials were analyzed and found that both were satisfactory.
- C. Superior high-temperature performance and better radome transmission can be obtained with the type II material (General Electric quartz fabric with Dow Corning DC2106 silicone resin).
- D. Non-multiples of the dual frequency can be used for radar operation. However, this requires specialized design techniques using a reactive wall concept. This method may give some slight degradation in electrical performance and would probably cost more for fabrication of production radomes.

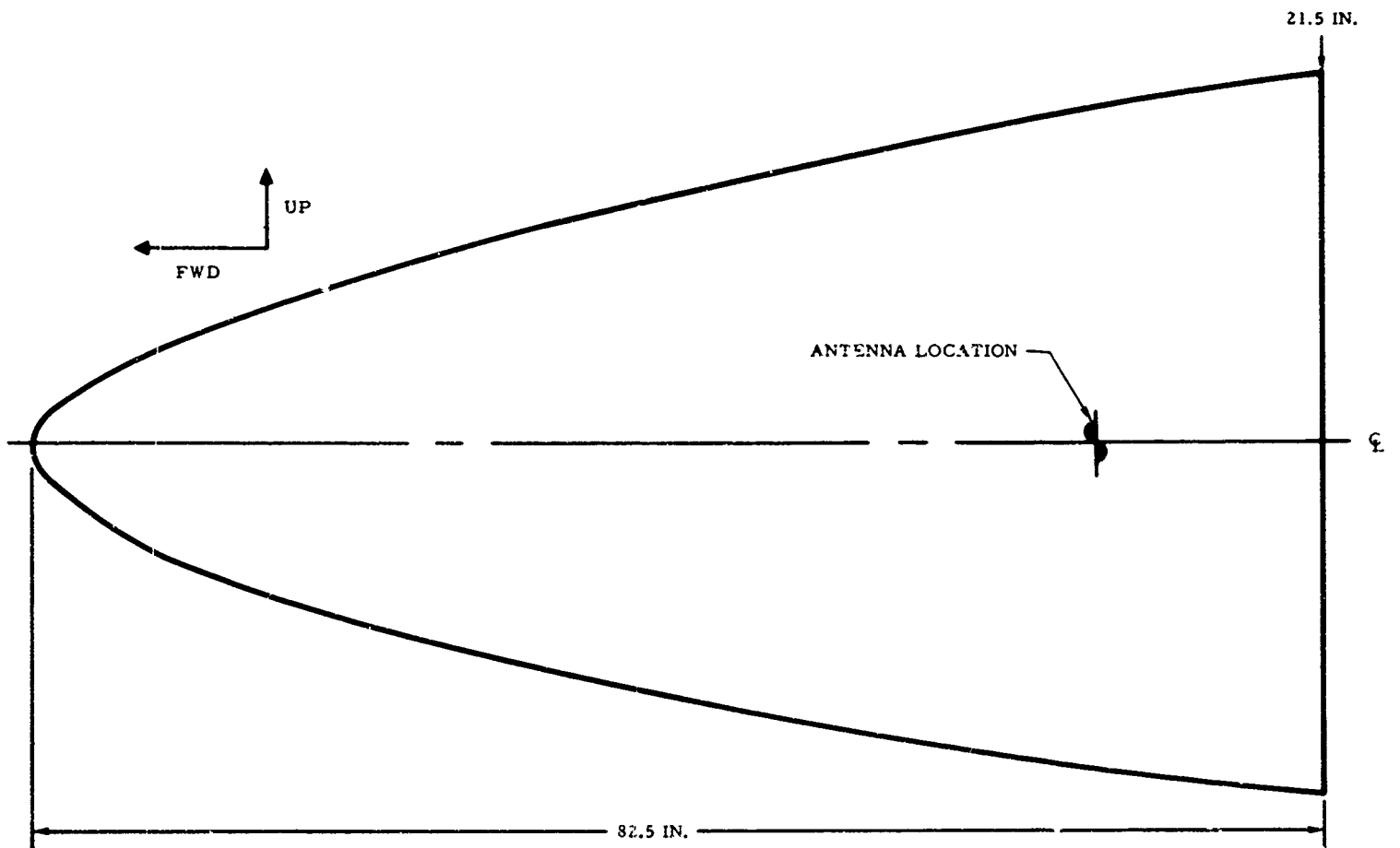


Figure A-1. Radome Shape Studied

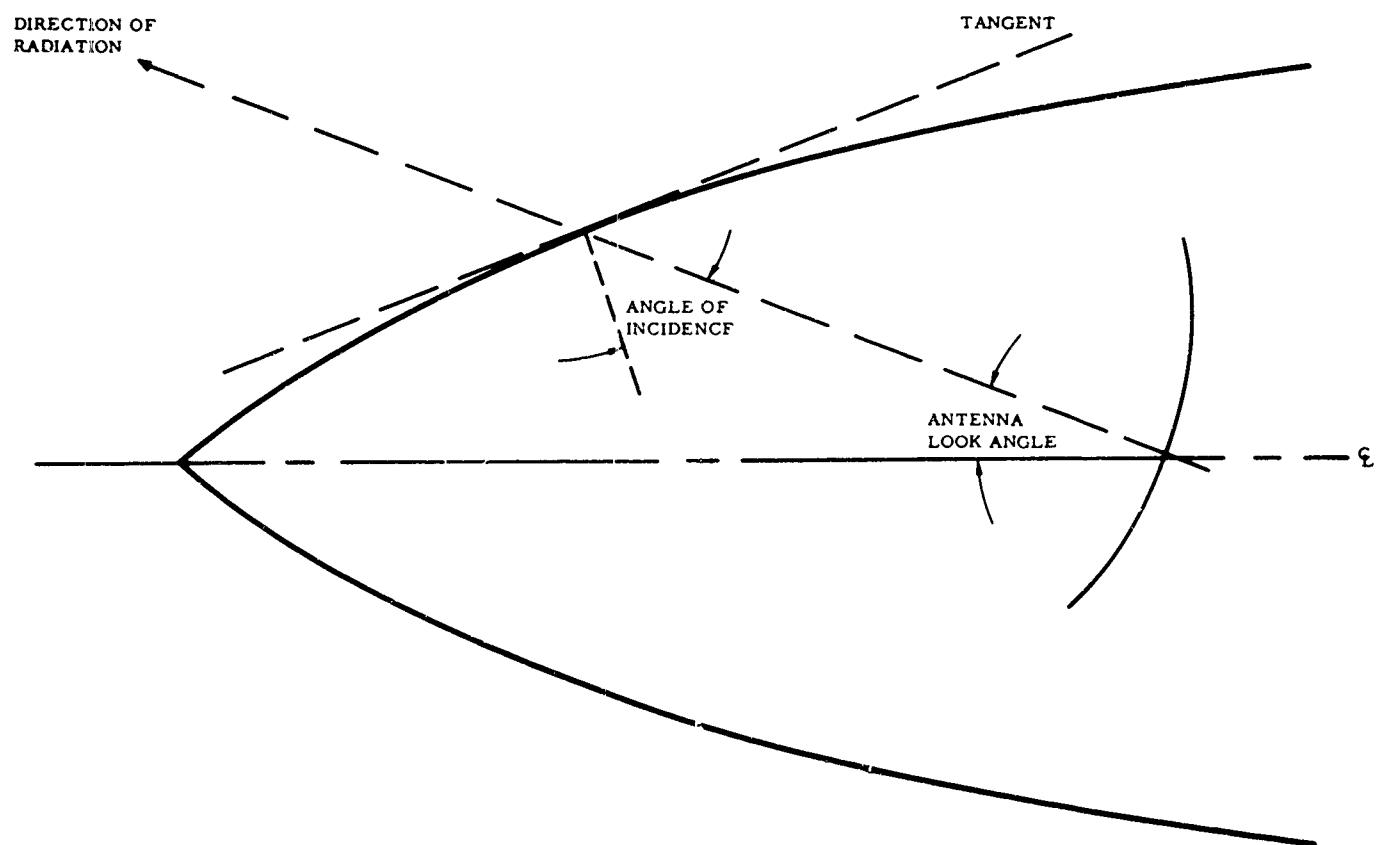


Figure A-2. Definition of Incidence Angle

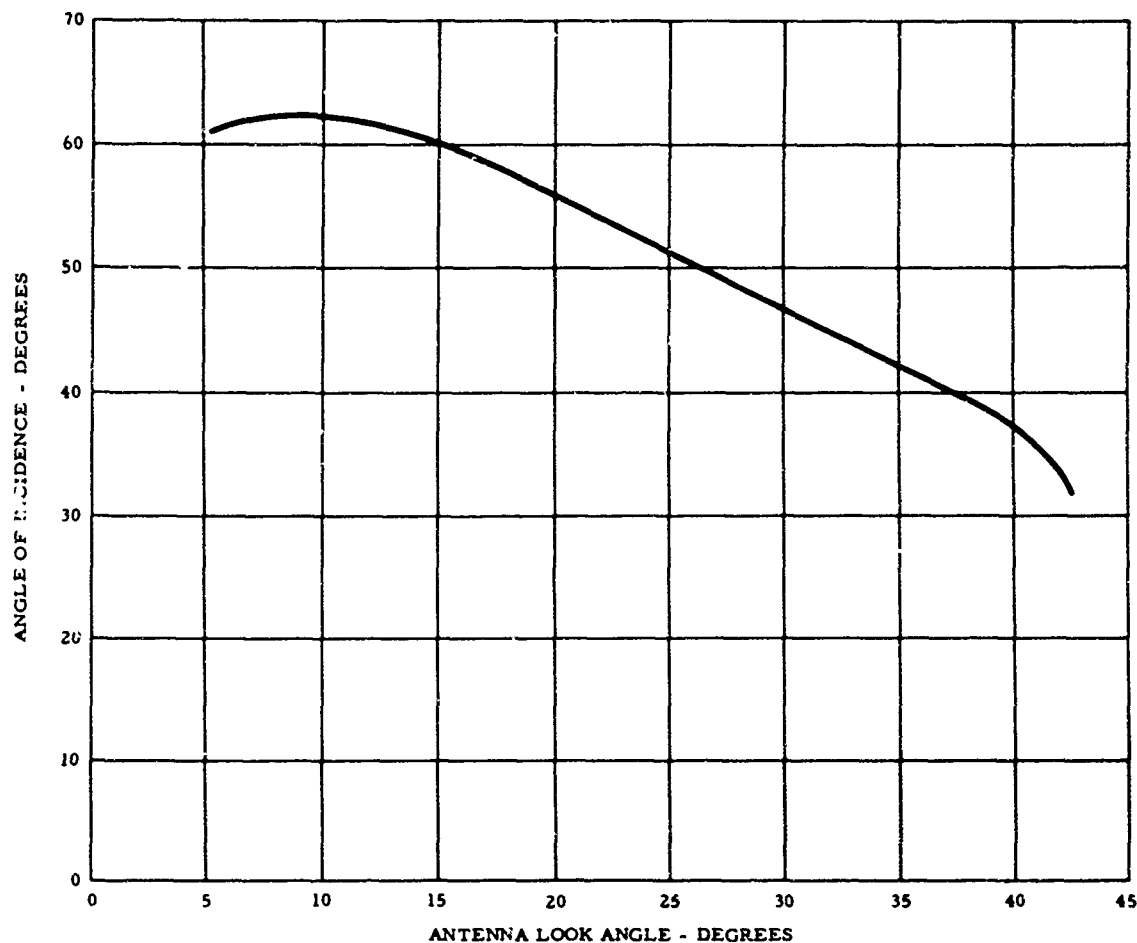


Figure A-3. Incidence Angle Versus Antenna Look Angle

1. CONSTRUCTION METHOD	- FILAMENT WOUND OR HAND LAY-UP-PRESS MOLDING TECHNIQUES		B. K. -BAND FREQUENCY	$\pm f_c \pm 0.150\text{KMC}$	
2. ELECTRICAL			TRANSMISSION (ONE WAY)	<u>PERCENT</u>	<u>ANTENNA LOOK ANGLES</u>
A. X-BAND FREQUENCY	$f_c \pm 0.125\text{KMC}$			60	± 45 DEG AZIMUTH ± 10 DEG ELEVATION -15 DEG ELEVATION ALL
TRANSMISSION (ONE WAY)	<u>PERCENT</u>	<u>ANTENNA LOOK ANGLES</u>	BORESIGHT SHIFT	55 MIN	
	85 AVG	± 15 DEG AZIMUTH ± 10 DEG ELEVATION -15 DEG ELEVATION		MILLI-RADIANS	<u>ANTENNA LOOK ANGLES</u>
	80 MIN	- ALL		6.3	± 45 DEG AZIMUTH ± 10 DEG ELEVATION -15 DEG ELEVATION
	90	- OUTSIDE ± 15 DEG CONE		6.3	OUTSIDE ABOVE ANGLES
BORESIGHT SHIFT	<u>MILLI-RADIANS</u>	<u>ANTENNA LOOK ANGLES</u>		12.3	
	3	± 15 DEG AZIMUTH ± 10 DEG ELEVATION -15 DEG ELEVATION			
	3	OUTSIDE ABOVE CONE			
	6.3				

Figure A-4. Dual Frequency Radome Requirements

TYPE I "E" TYPE FABRIC

PRE-IMPREGNATED WITH 38 \pm 2
PERCENT DOW CORNING DC 2106
SILICONE RESIN

DIELECTRIC CONSTANT - 4.27

LOSS TANGENT - 0.007

TYPE II GENERAL ELECTRIC QUARTZ
FABRIC

PRE-IMPREGNATED WITH 38 \pm 2
PERCENT DOW CORNING DC 2106
SILICONE RESIN

DIELECTRIC CONSTANT - 3.13

LOSS TANGENT - 0.0036

Figure A-5. Radome Material Electrical
Characteristics

θ	- 80°
ϵ	- 4.27
TAN δ	- 0.007

CURVE	FREQUENCY	POL.
1	8,715 MC	I
2	8,715 MC	II
3	34,860 MC	I
4	34,860 MC	II

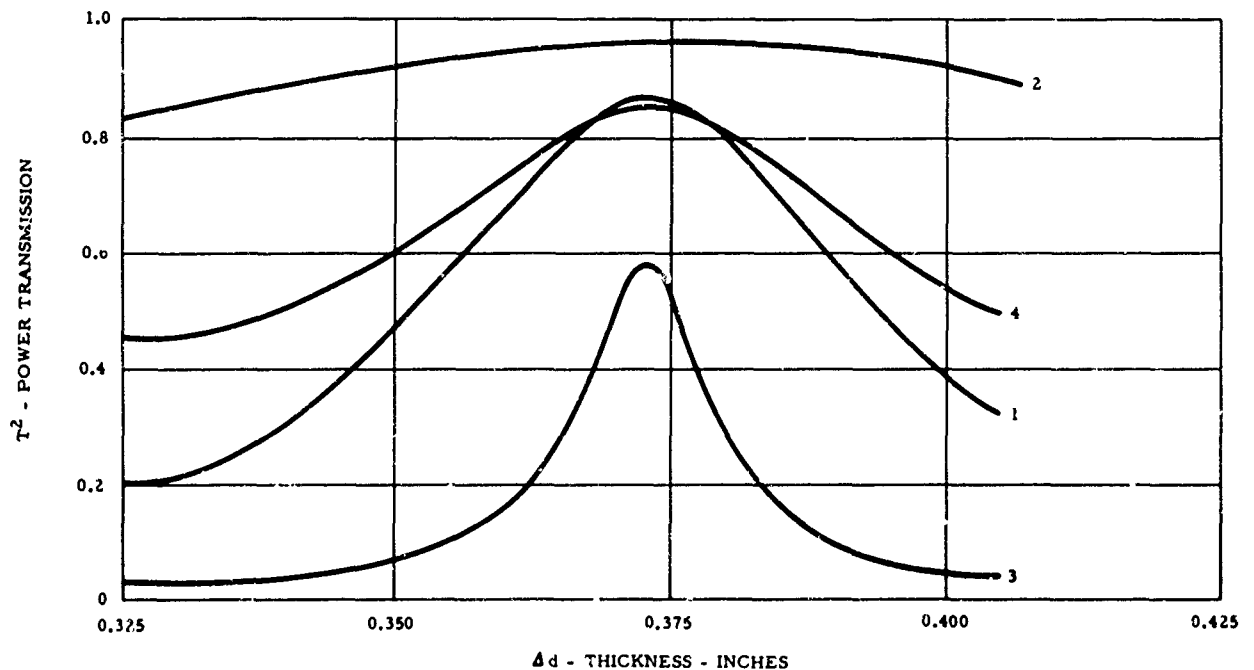


Figure A-6. Transmission Versus Thickness Type I Material

$\epsilon - 80^\circ$
 $\epsilon - 3.13$
 $\text{TAN } \delta - 0.0036$

CURVE	FREQUENCY	POL.
1	8,715 MC	I
2	8,715 MC	II
3	34,860 MC	I
4	34,860 MC	II

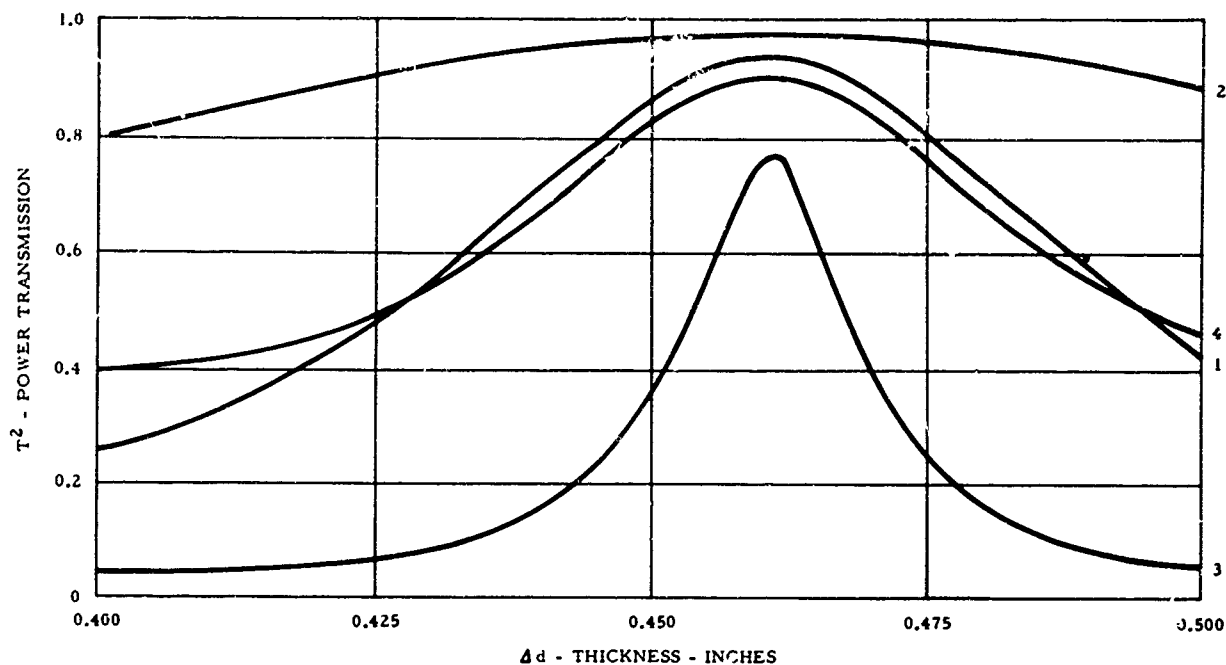
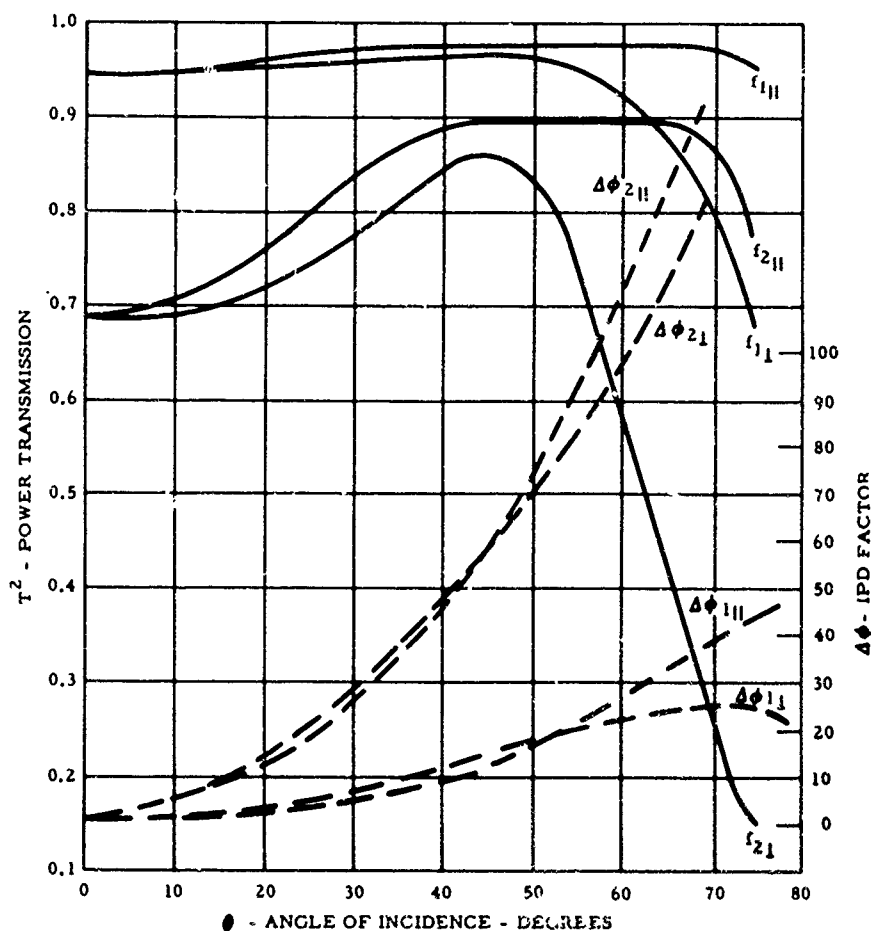


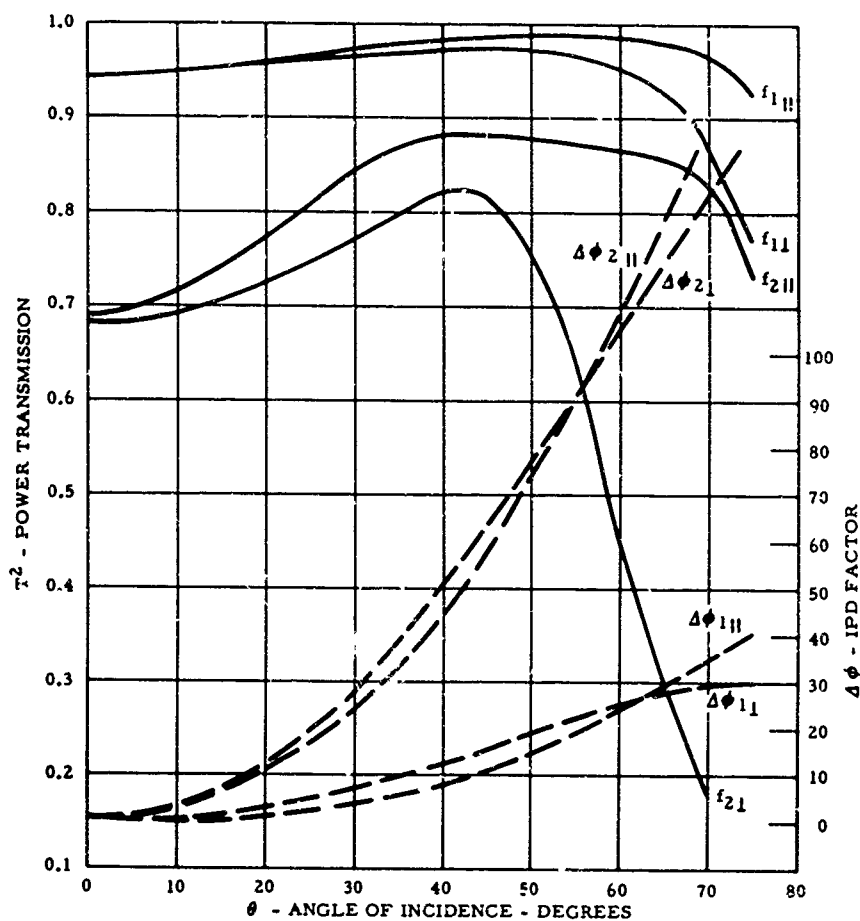
Figure A-7. Transmission Versus Thickness Type II Material



T ² - AVE.	FREQUENCY
94.7	f ₁ - 8715 MC
74.4	f ₂ - 34860 MC

$\epsilon - 3.85$
 $\text{TAN } \delta - 0.007$
 $d - 0.371 \text{ IN.}$

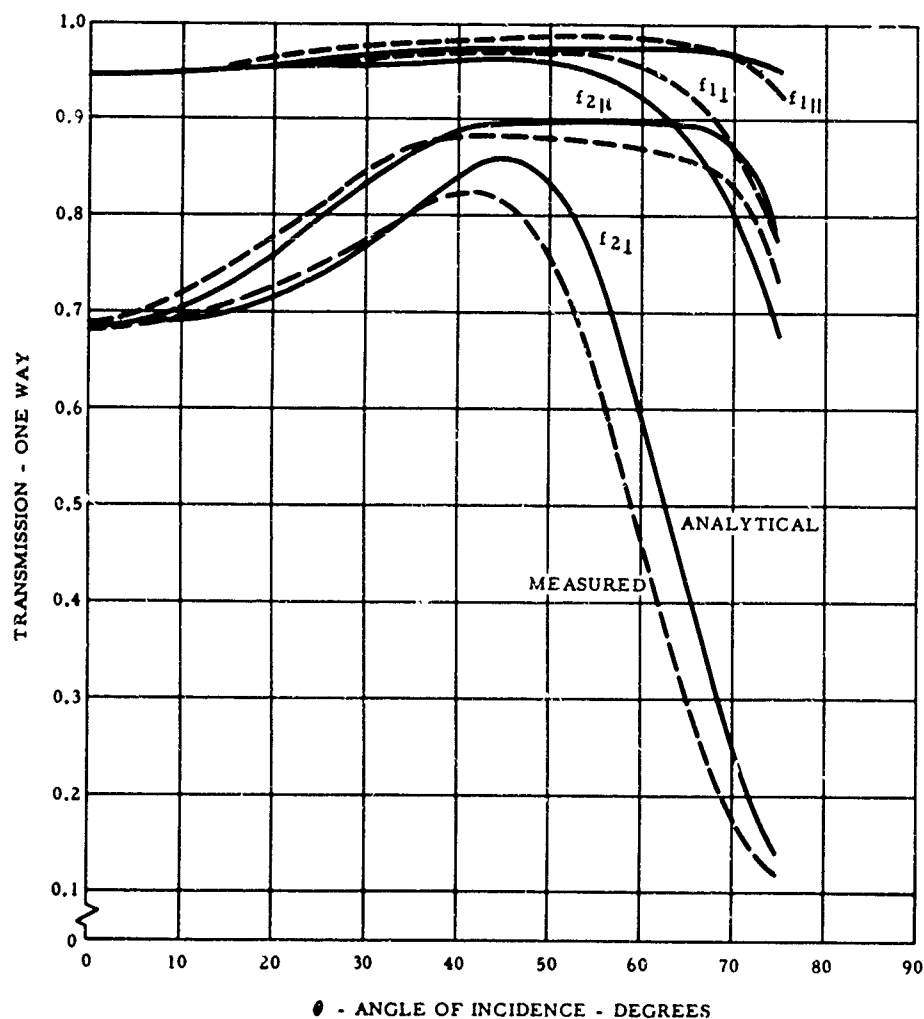
Figure A-8. Transmission Versus Incidence Angle; Analytical; Type I Material



$\epsilon - 3.87$
$TAN \delta - 0.007$
$d - 0.371 \text{ IN.}$

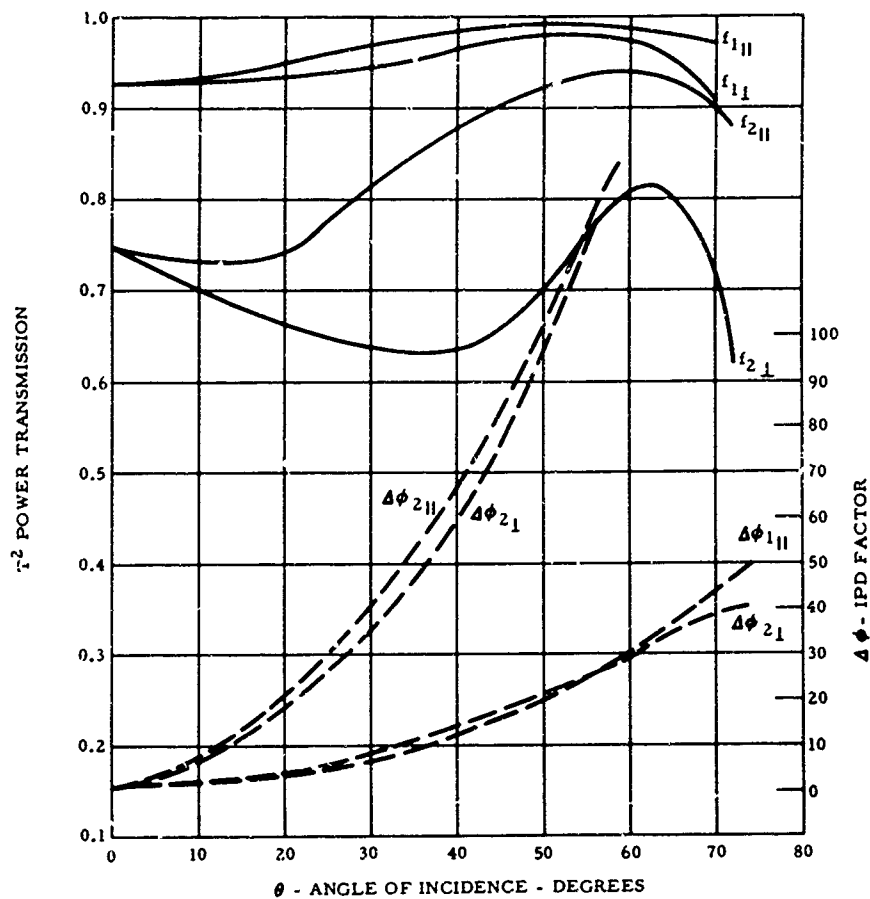
T^2_{AVE}	FREQUENCY
95.9	$f_1 - 8715 \text{ MC}$
72.4	$f_2 - 34860 \text{ MC}$

Figure A-9. Transmission Versus Incidence Angle; Measured; Type I Material



$f_1 - 8,715 \text{ MC}$
$f_2 - 34,860 \text{ MC}$
$\epsilon - 3.85$
$TAN \delta - 0.007$
$d - 0.371 \text{ IN.}$

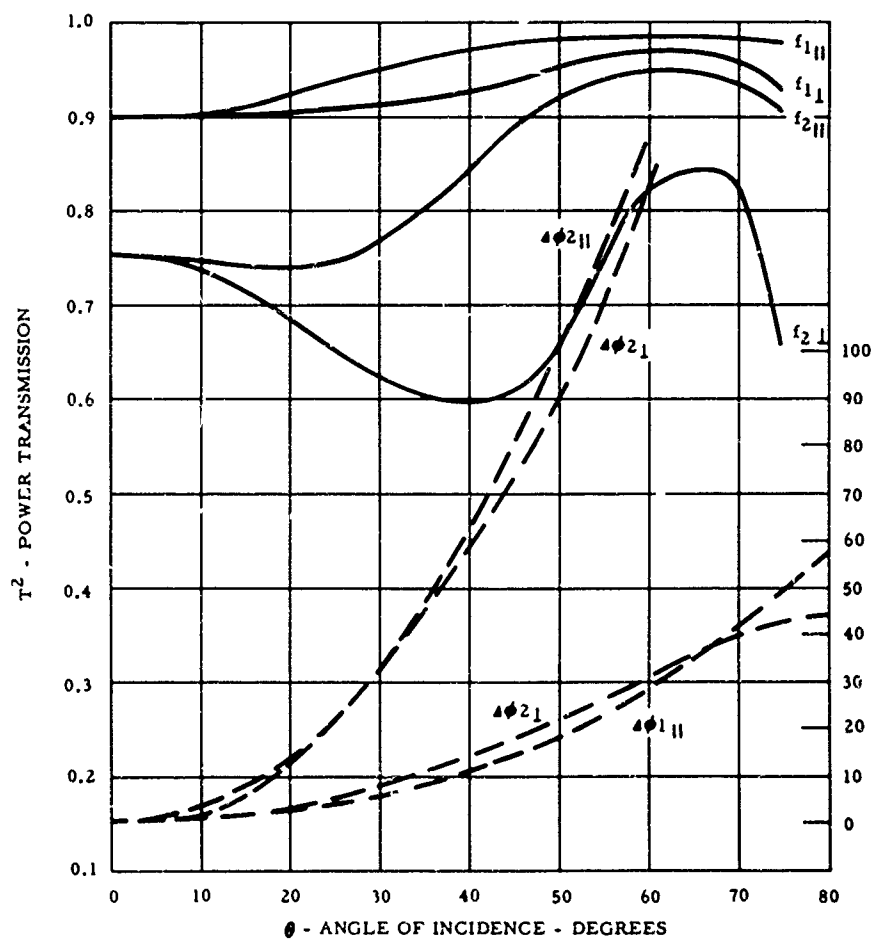
Figure A-10. Comparison of Analytical and Measured Data, Type I Material



ϵ	- 3.13
TAN	- 0.0036
d	- 0.448 IN.
TEMP	- 70 F

T ² AVE	FREQUENCY
95.0	f_1 - 8715 MC
76.3	f_2 - 34860 MC

Figure A-11. Transmission Versus Incidence Angle; Analytical; Type II Material



ϵ	- 3.13
TAN ϵ	- 0.0036
d	- 0.448 IN.
O	- 65°

T ² AVE	FREQUENCY
94.22	f_1 - 8715 MC
77.12	f_2 - 34860 MC

Figure A-12. Transmission Versus Incidence Angle; Measured Data; Type II Material

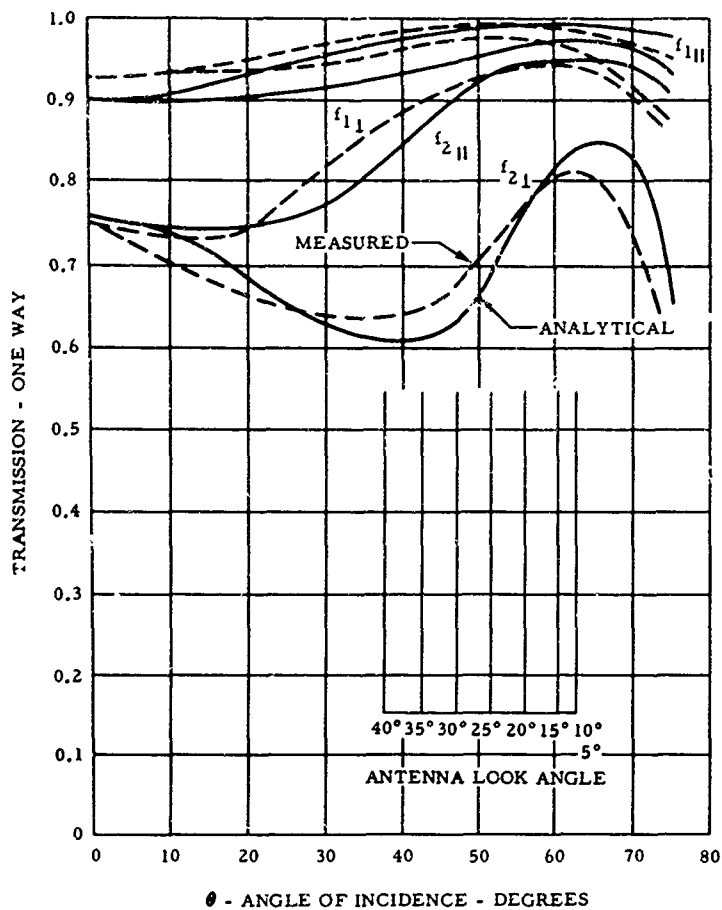


Figure A-13. Comparison of Analytical and Measured Data, Type II Material

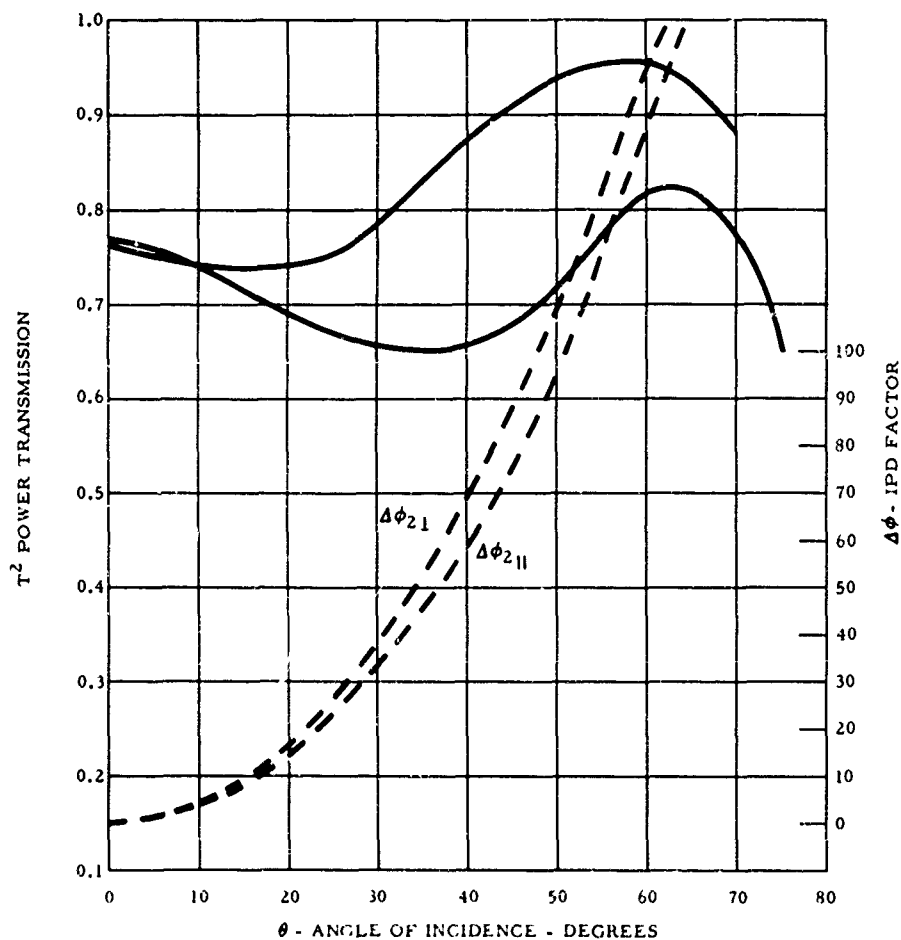


Figure A-14. Transmission Versus Incidence Angle; Measured Data at Elevated Temperature; Type II Material

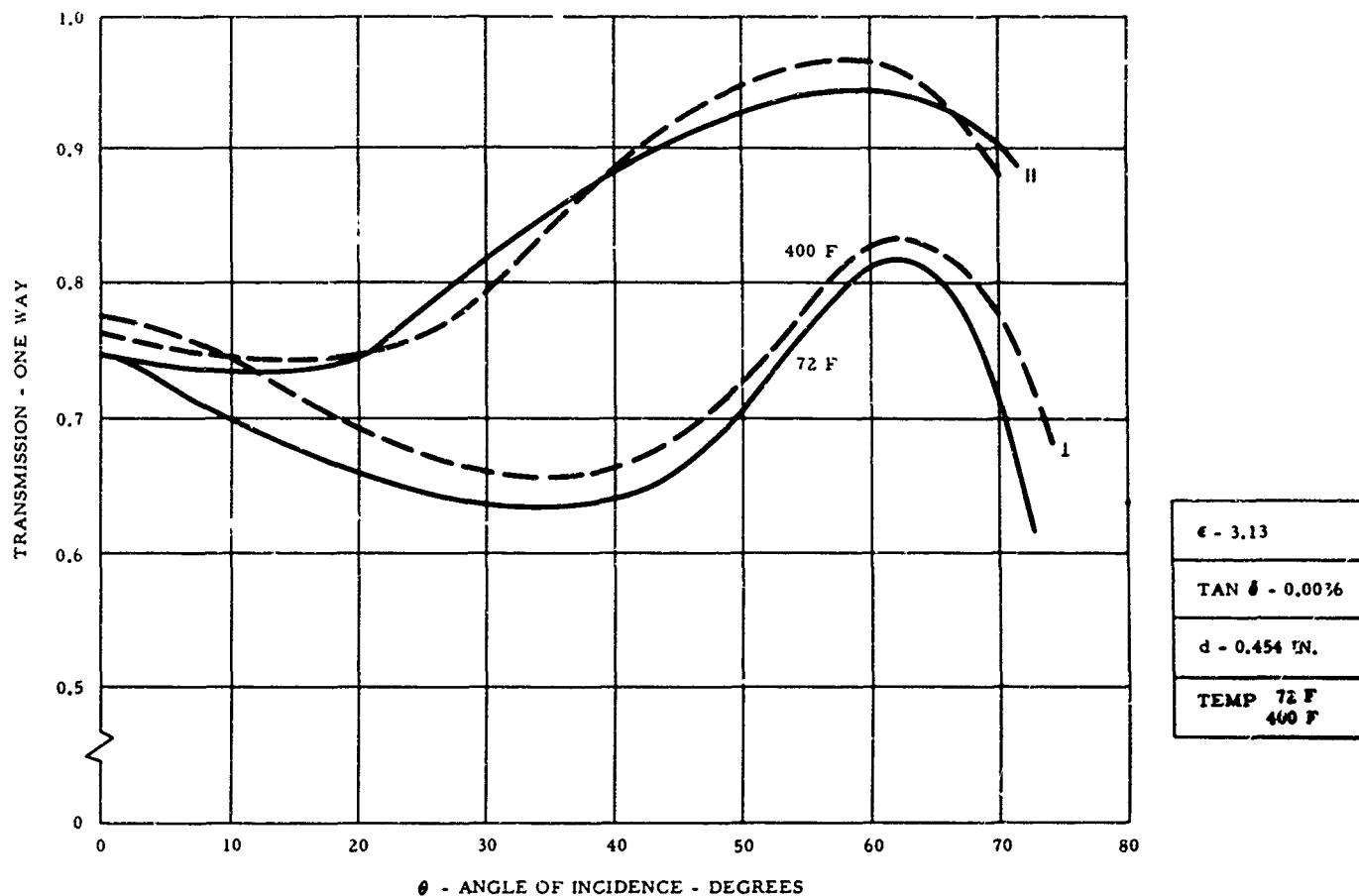


Figure A-15. Comparison of Measured Data, K-Band, Type II Material, Elevated Temperature^a

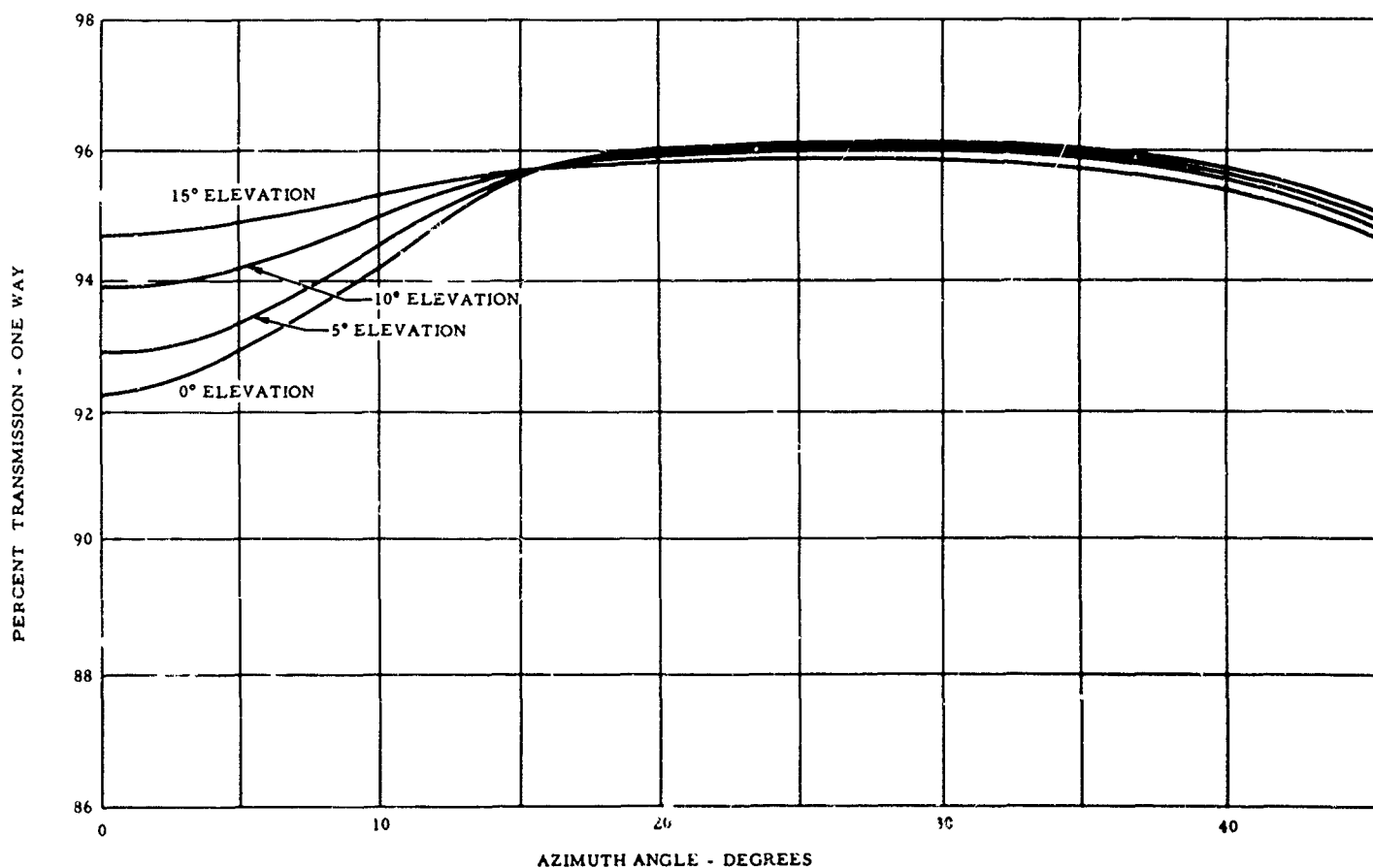


Figure A-16. Transmission Versus Azimuth Antenna Look Angle for Various Elevation Angles; Type I Material; X-Band

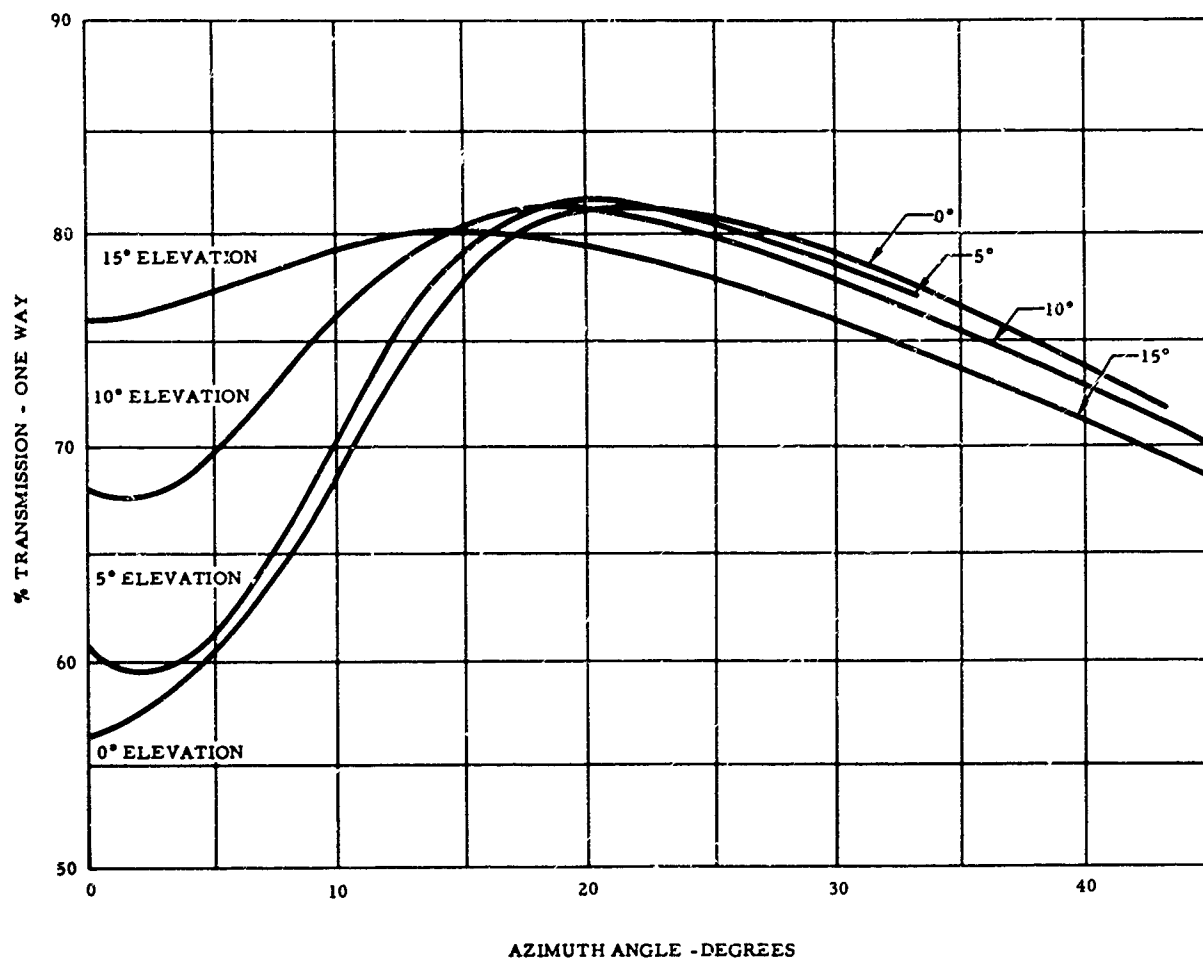


Figure A-17. Transmission Versus Azimuth Antenna Look Angle for Various Elevation Angles; Type I Material; K_a -Band

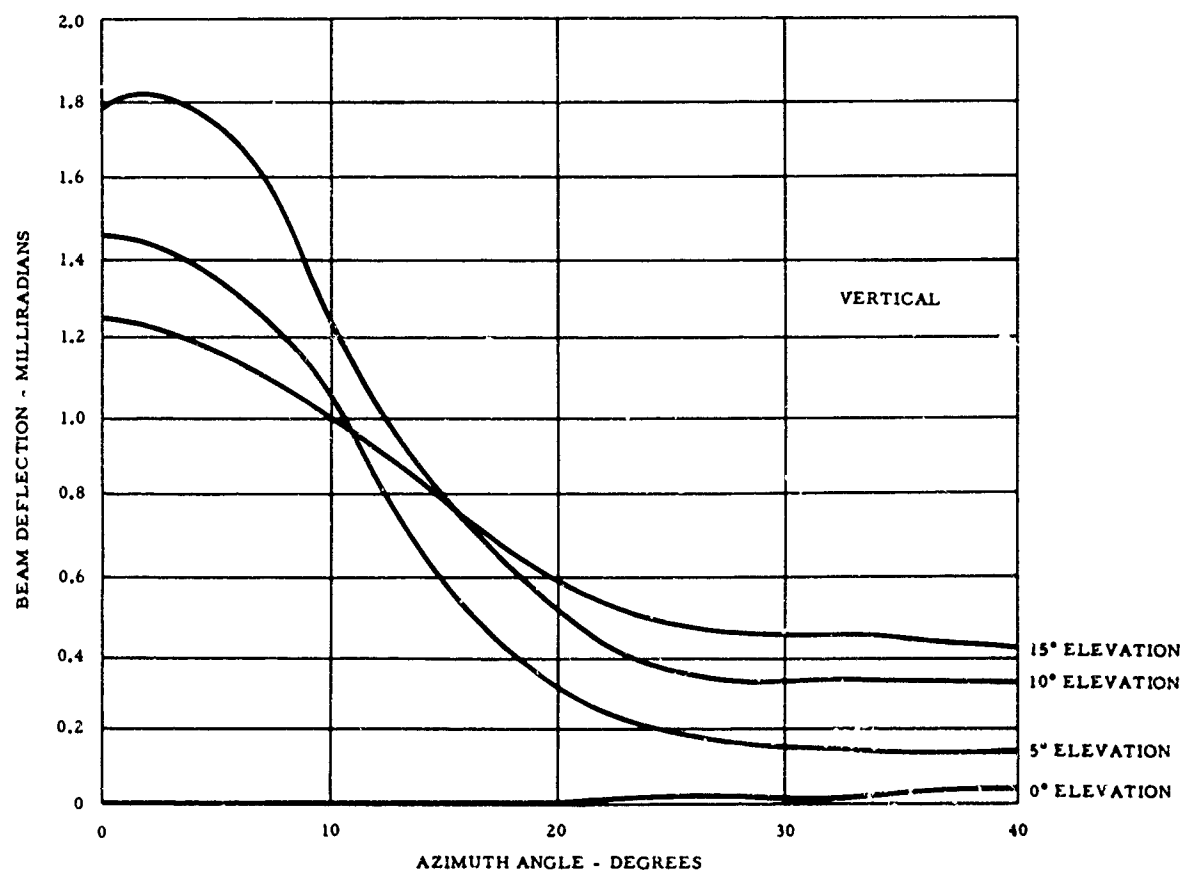
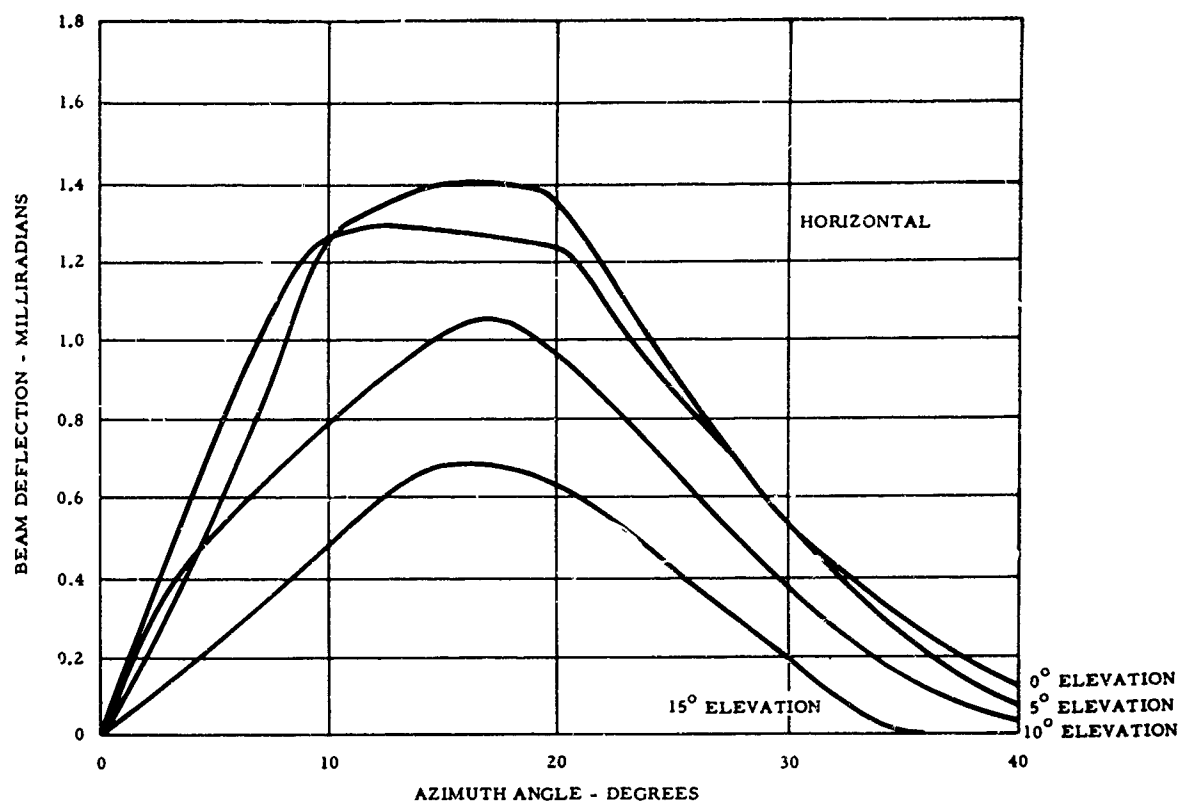


Figure A-18. Boresight Shift Versus Azimuth Antenna Look Angle for Various Elevations Angles; Type I Material X-Band

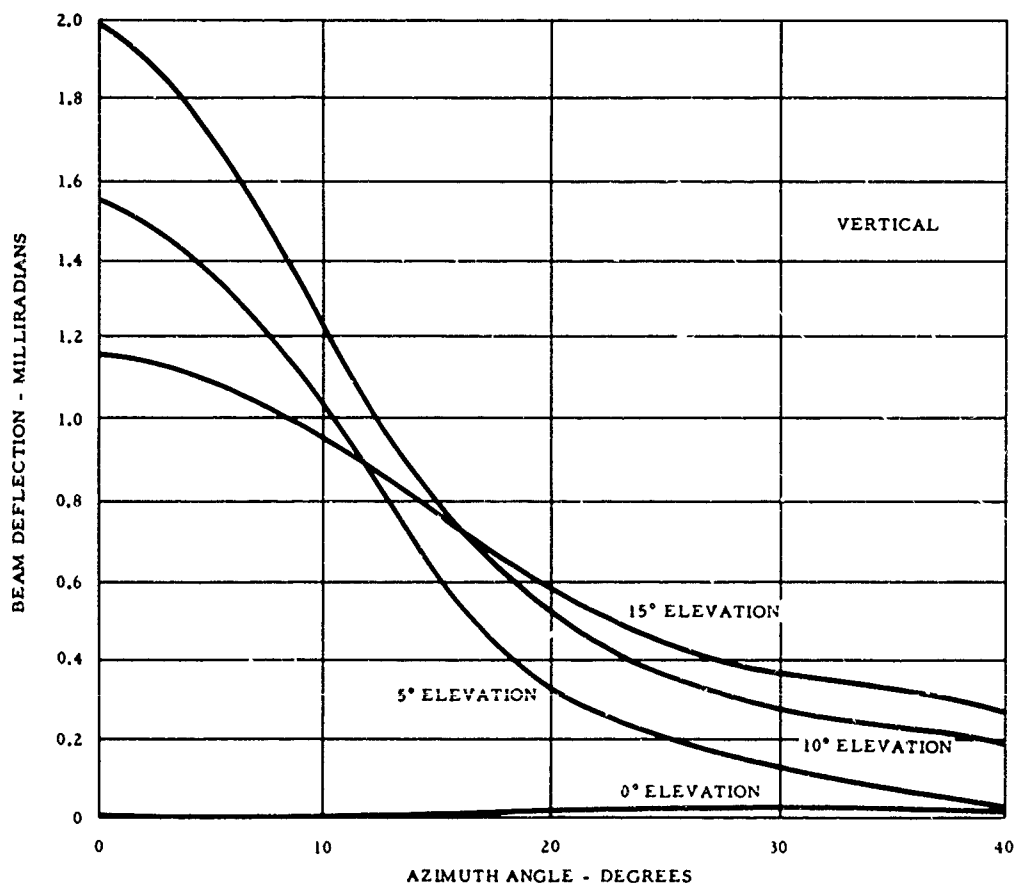
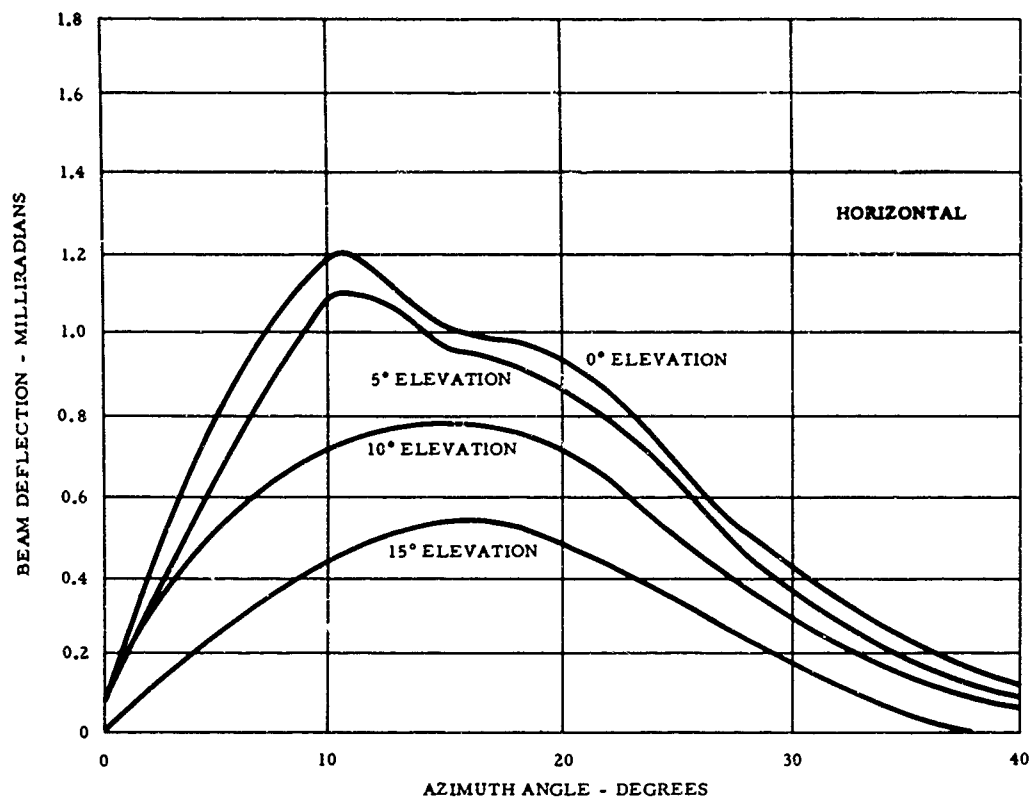


Figure A-19. Boresight Shift Versus Azimuth Antenna Look Angle for Various Elevation Angles; Type I Material; K_a - Band

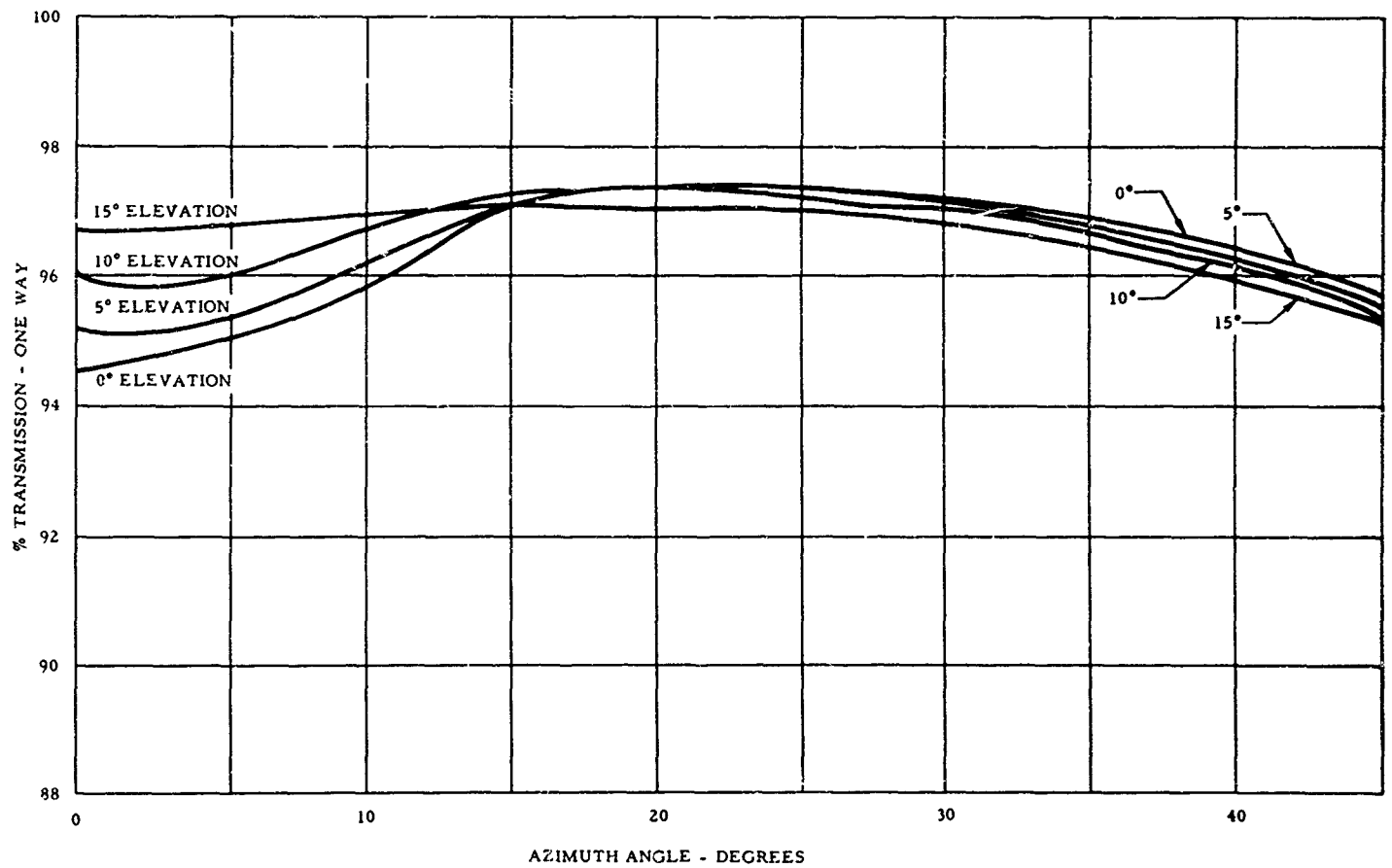


Figure A-20. Transmission Versus Azimuth Antenna Look Angle for Various Elevation Angles; Type II Material; X-Band

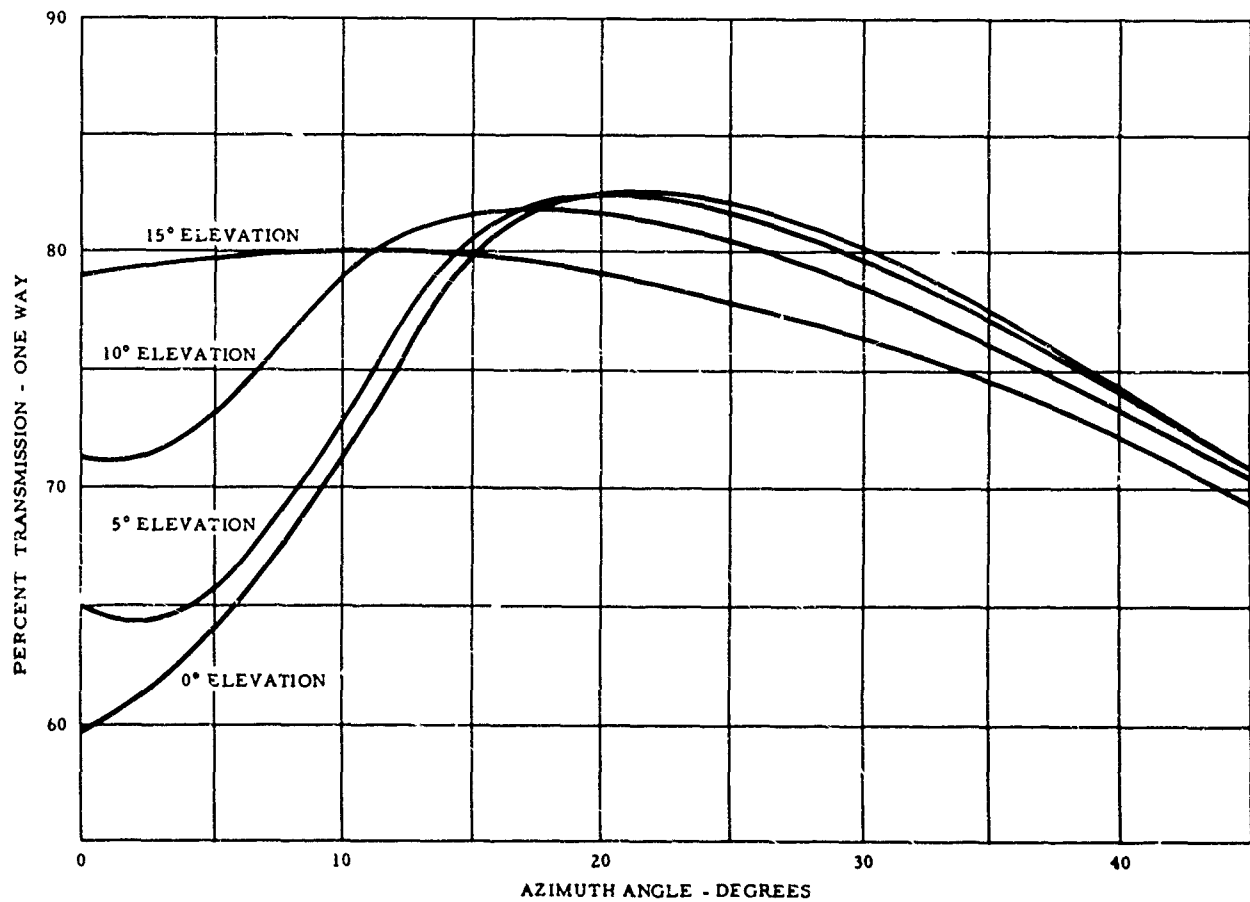


Figure A-21. Transmission Versus Azimuth Antenna Look Angle for Various Elevation Angles; Type II Material; K_a - Band

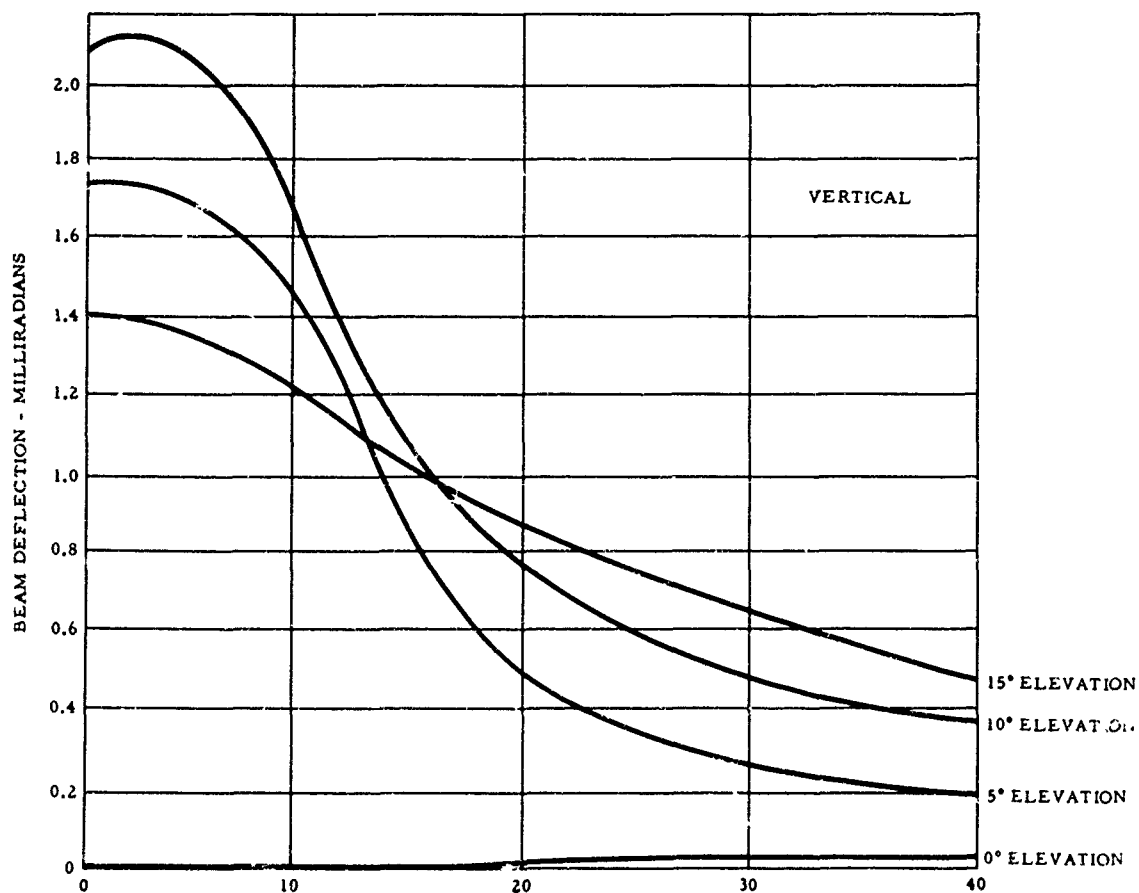
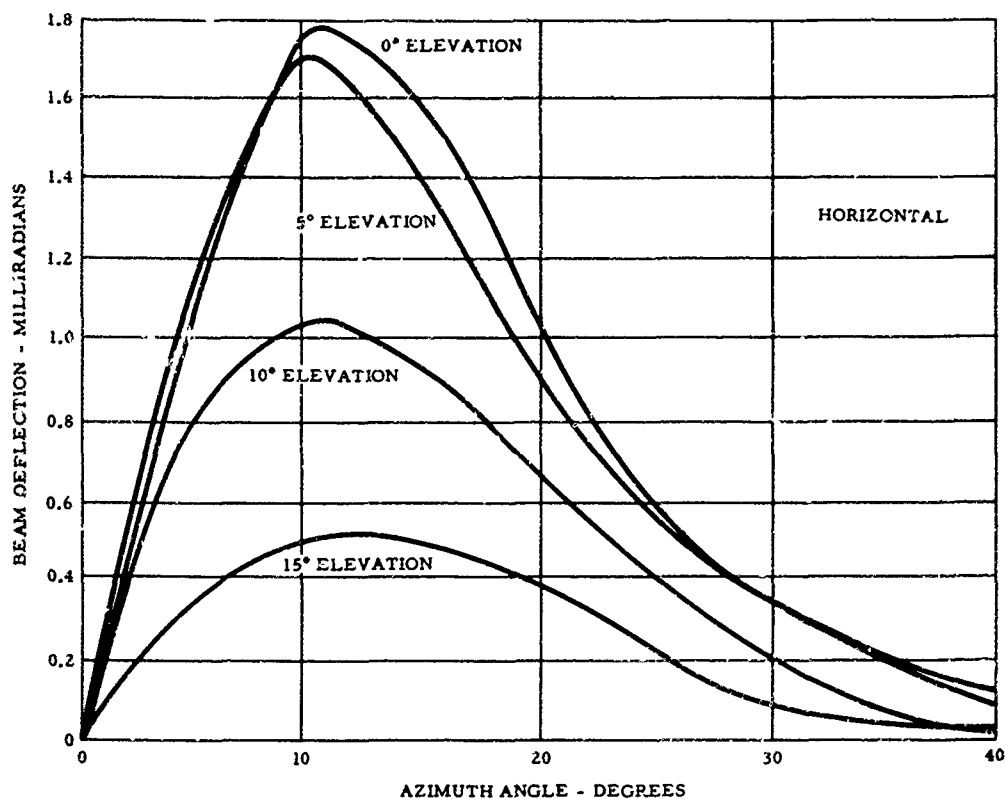


Figure A-22. Boresight Shift Versus Azimuth Antenna Look Angle for Various Elevation Angles; Type II Material; X-Band

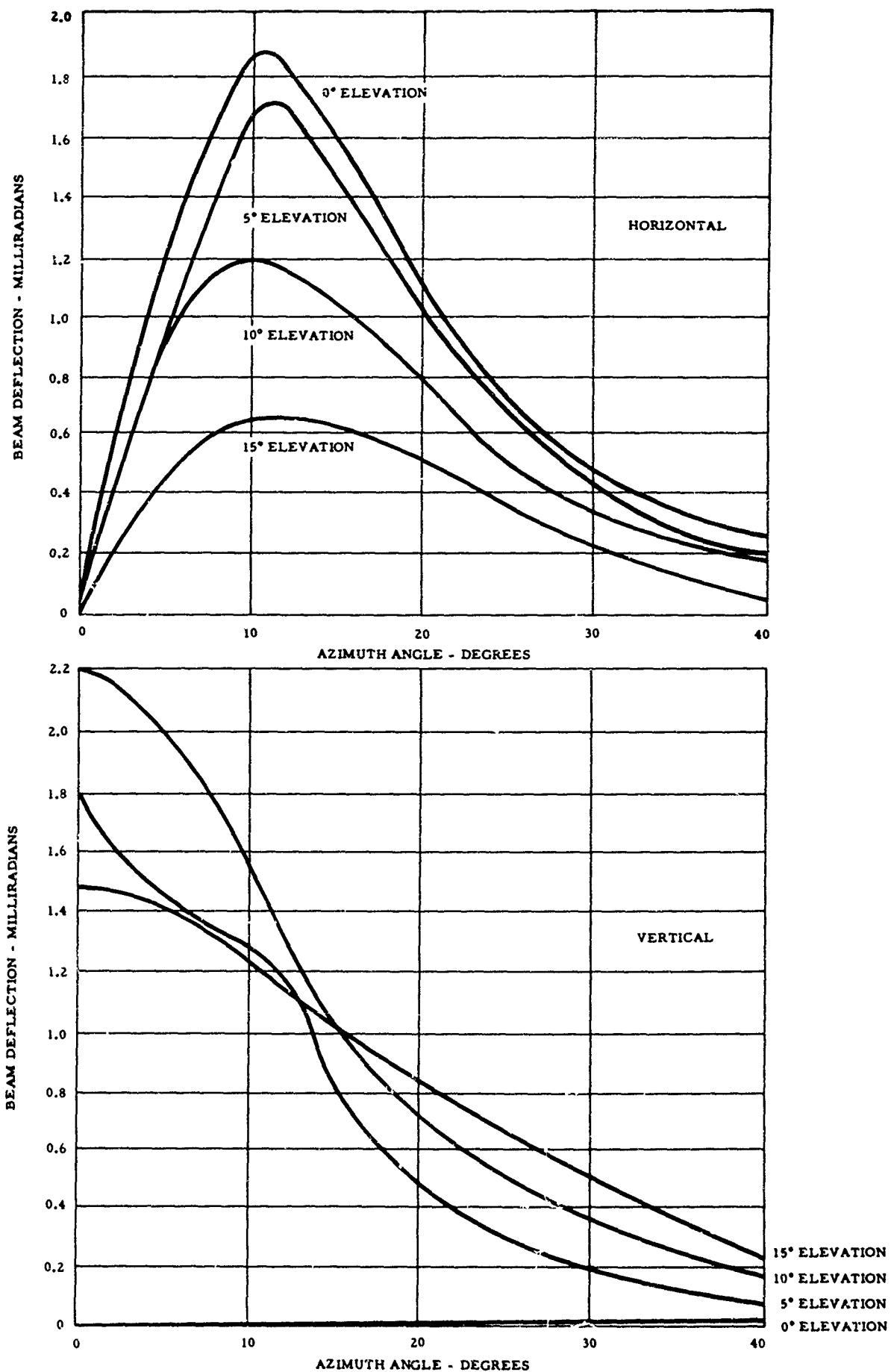


Figure A-23. Boresight Shift Versus Azimuth Antenna Look Angle for Various Elevation Angles; Type II Material; K_a-Band

LARGE AIR SUPPORTED RADOMES

FOR

SATELLITE COMMUNICATIONS GROUND STATION.

Walter W. Bird, President
BIRDAIR Structures, Inc.
Buffalo, New York

INTRODUCTION

The success of the large air supported radomes used to house and protect the Telstar Earth Stations in Andover, Maine and in Fleumer Bodou, France has once again demonstrated the superiority of the air supported radome where high performance is required. Developed by BIRDAIR for the Bell Telephone Laboratories, these radomes have been in use for approximately two years. Service experience has been excellent and the electrical performance has more than met the expectations of the BTL engineers.

A similar radome, though slightly smaller in size, was installed in the Bavarian Alps at Raisting, Germany last October and this station is expected to be in operation this summer. Another radome is now being fabricated by BIRDAIR for the Canadian Government under an R.C.A. Victor Company, Ltd. subcontract and will be installed in Nova Scotia next fall.

The manufacture of these radomes required development of new materials, fabrication techniques, and equipment. Uniquely new installation procedures also had to be devised in order to erect these radomes which weigh up to 30 ton. The success of these radomes is especially significant as it was made possible as a result of development work carried out by BIRDAIR with the cooperation of a few textile concerns and coaters willing to work with BIRDAIR to provide the improvements required to make large radomes practical. The support provided by the Bell Telephone Laboratories in developing the 210 ft. diameter Telstar radomes made it possible to prove the feasibility of our designs.

BACKGROUND

The air supported radome, developed at the Cornell Aeronautical Laboratory in 1946-47 under the direction of the author, was the first successful large radome. Because of the urgent need for radome protection for the large search radar stations being built as a protective line throughout the United States and Canada, this radome was put in service with a minimum of field testing and no real service experience. However, except for minor service problems, mostly traceable to malfunctioning of associated equipment, these radomes had a good service record from the start.

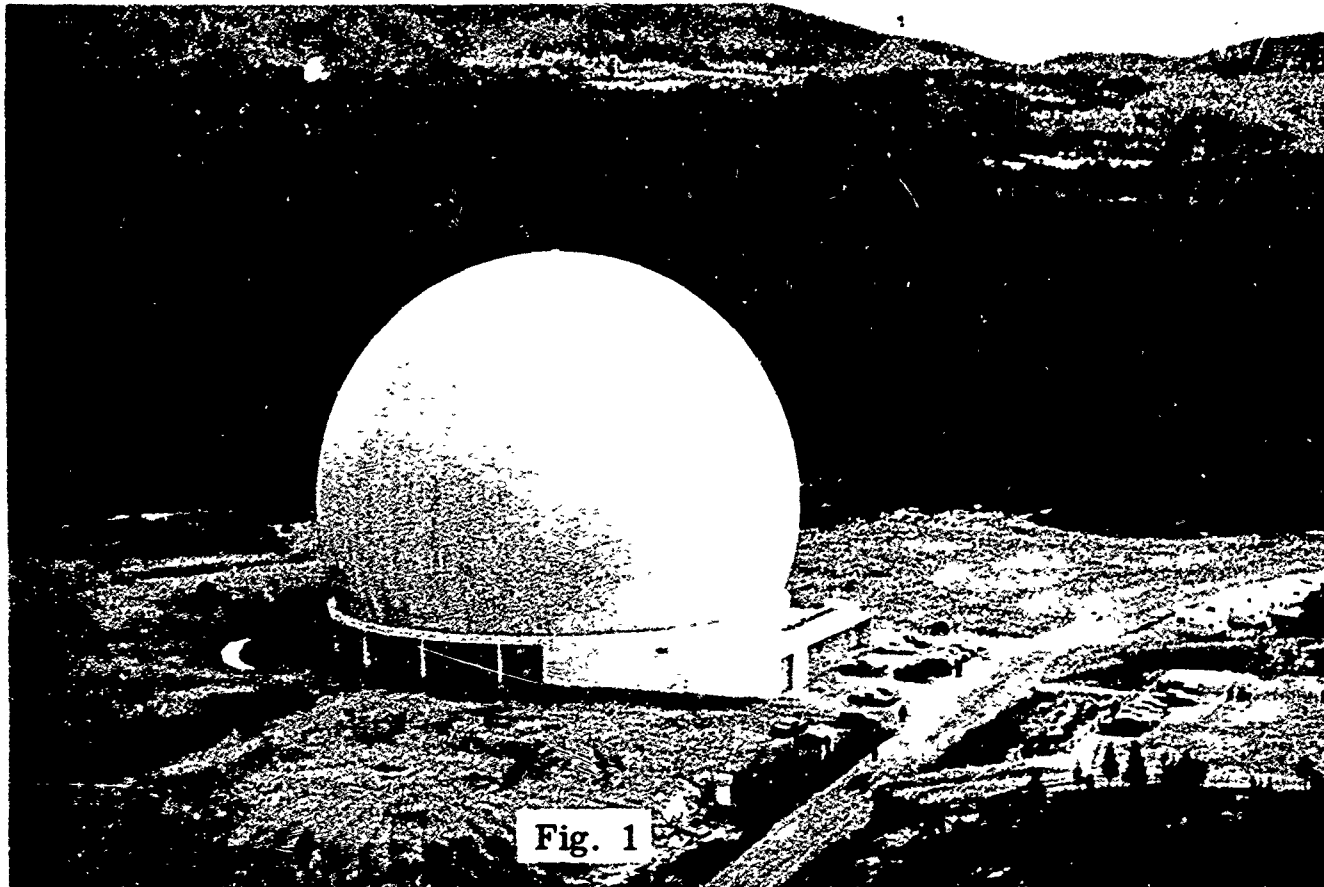


Fig. 1

"TELSTAR" RADOME

210 ft. in diameter, 160 ft. high, this is the largest radome currently in use.

Fig. 2

CONSTRUCTION SHELTER

The same size as the radome, this construction shelter provided low cost all-weather protection during construction of the antenna.

cat
qui
its
rad
Alt
as
the
int
wei
the
equ
cur

tha
ist
fie
1.

2.

3.

The air supported radome was originally developed to meet specifications requiring maximum portability. The portable concept was abandoned quite early, due to the fact that the radar equipment tower and antenna itself did not possess the desired portability in design. However, these radomes were used for many years on a large number of fixed sites. Although rigid antennas were specified on many of the new "fixed" sites, as the air supported radome often provided the only practical solution to the requirements of light weight and transportability, it was incorporated into many portable radar systems. To meet the need for other types of light weight portable equipment, the air supported principle was also applied by the author to the development of inflatable antennas, inflatable towers, equipment shelters, and the low pressure dual-wall cellular radome now currently in use on a number of portable radar systems.

Although remarkably successful from the start, field experience indicated that in order to provide improved service life, better electrical characteristics, and maximum reliability, improvements were required in the following fields:

1. Materials

Structural and electrical requirements of radomes of 50-60 ft. in diameter were taxing the capabilities of materials which were then available. Improvement in strength, electrical properties, and in weatherability, were required if larger radomes of improved characteristics were to be provided.

2. Fabrication Techniques

As even the best of materials would be of little value unless they could be joined together to provide a unit of uniformly high quality, improvements in fabrication techniques and in sectionalizing methods were needed.

3. Auxiliary Equipment

The air supported radome requires maintenance of a small differential pressure in the unit to provide stability and resistance to wind and weather. Field experience had shown that most of the service difficulties which developed were due to malfunctioning of equipment, not due to any deficiency in the basic envelope. The development of equipment with improved reliability and of better operating procedures was therefore required.

The Air Force, through RADC, sponsored some early research programs with CAL and a few other companies. At CAL, programs under the direction of the author led to the development of a Hypalon paint which was used to protect and provide improved weathering resistance to the radome envelope, and to the development of techniques of treating Dacron fibers to provide higher strength and lower elongation. However, interest in research programs related to air supported radomes appeared to lag as attention was shifted to other, newer, radome developments and no effective sponsorship was continued. In contrast, good financial support was provided for the development of rigid radomes of various types and a number of large experimental rigid radomes were constructed.

The rigid radomes also did not prove to be entirely free of service problems. While they did not require maintenance of pressure and thus an uninterrupted source of power (normally judged the most serious drawback to air supported radomes), many design and material problems were encountered. Leakage, vulnerability to winds during the comparatively long period required for erection, weatherability of the material, and icing, were among the problems which developed. Because of the need for thicker materials and/or metallic frames, RF properties were generally poorer than for air supported radomes. As BIRDAIR was convinced of the superiority of air supported radomes where high performance, portability, or low cost were important factors, and as we believed the service difficulties which had been encountered could be overcome with improved designs, a continuing program of applied research and development of materials and equipment was continued by BIRDAIR. Considerable progress had therefore been made when we were advised of the requirement for the 210 ft. diameter Telstar radomes. BTL had decided that satisfactory electrical characteristics would be achieved only with a lightweight material such as Hypalon-coated Dacron. An air supported radome was therefore desired. Even though additional development work was required to meet the stringent requirements of this program, as a result of our experience we were able to demonstrate new techniques and the feasibility of our design approach to the BTL engineers. With the support of BTL, BIRDAIR was able to develop the new materials, equipment, and techniques of both fabrication and assembly, which led to the successful development of the Telstar radomes.

DESIGN AND DEVELOPMENT OF TELSTAR RADOMES

The Telstar radome, Figure 1, is 210 ft. in diameter and stands approximately 160 ft. high. It is designed to resist winds of up to 100 mph and the snow loading associated with the Maine environment. In order to meet these requirements, a material stronger than any previously developed for radomes was required and this material would need to have far better RF characteristics and a greater service life than that associated with materials currently in general use. Because of the enormous size of this unit, it would also be

necessary to develop new fabrication techniques and methods of handling the material while assembling the envelope. Because of the need to maintain precise pressure control with maximum reliability, in order to assure maintenance of the proper pressure under all conditions of operation, a fully reliable inflation system was needed. One of the most critical problems was, however, to develop techniques to install this 30 ton radome envelope over the horn antenna without allowing the weight or forces involved in erection to apply loads to the antenna which might result in distortion or deflection. Solutions to these problems had to be found in order to make this radome application feasible. The approach used to solve many of these problems is briefly discussed below:

1. Material Development

In order to meet the load requirements, it was determined that a fabric having a strip tensile strength of 1000# per inch, biased combined to provide a two ply, 45° construction, would be needed in order to assure a satisfactory distribution of load and uniform thickness of material over the full surface of the radome. Tests and experiments previously carried out by BIRDAIR indicated that, in order to join materials of this strength, a lap joint of extremely high efficiency would be required.

The efficiency of a lap joint depends on the uniform distribution of shear load across the joint. This in turn depends on the elastic characteristics of the materials being joined. With materials having a high modulus of elasticity, like metals working in the elastic range, uniform shear distribution can be provided in a lap joint as the deflection or stretch of the material is small; thus, the difference in stretch at the interface between the materials at the edge of a lap joint (the edge of one panel having zero load in it and the other panel to which full load has been transferred), is small. Relatively uniform shear stresses are thus developed at the interface, resulting in a high efficiency joint. However, with coated fabrics the modulus of elasticity is relatively low, and due to a considerable variation in stretch of the materials, distribution of shear across the joint varies from a very high stress at the edge to a relatively low stress at the center of the lap. This condition results in edge peel and eventual failure of the joint. It is traditionally compensated for in radome construction by double taping the joint in order to help distribute the high stress. This approach, however, results in an excessive buildup of material in the joint area and a wider joint, which reduces the RF transmission efficiency of the radome.

This problem on the Telstar radome was approached from the point of view of basic concepts. As the concentration of stress at the edge of the lap is due to high elasticity of the material, it could be best overcome by providing a material with low stretch and by using a joint

construction which took into account the varying stretch across the joint. Based on experience gained in previous work, the solution used was to develop a fabric construction employing a basket weave to minimize crimp, yet allow us to pack in enough yarn to provide the required strength without developing too bulky a fabric. A Dacron yarn, hot stretched and heat stabilized to increase strength and reduce elongation, was employed, and a special finishing technique was developed to control the fill elongation of the fabric in order to maintain relatively uniform crimp in both warp and fill yarns.

In selecting a protective coating, consideration had to be given to both the physical and electrical properties of the material. The electrical properties of neoprene are not good enough to be considered for use at the frequencies and in the material weights required for the Telstar unit. Also, water absorption of neoprene is relatively high and results in a serious loss in RF transmissibility after periods of exposure to rain. Other compounds which offer good electrical properties, such as the silicones, do not provide the required high physical properties. Laminates employing films, such as Tedlar, have not been developed to an extent providing the required properties. Those available could not be biased combined and presented serious fabrication problems. Laminates on fabric also have extremely high water absorption if the surface film is punctured or penetrated in any way.

Hypalon was selected as offering the best combination of properties, as it provided both good mechanical strength, high abrasion and weathering resistance, and good electrical properties. Hypalon-coated Dacron material had been developed having a dielectric constant of less than three and with water absorption so low that no significant difference could be distinguished in RF tests made at 5000 megacycles on samples soaked for 24 hours. Coating techniques had been developed which could provide the required high adhesion and BIRDAIR had developed techniques of bonding Hypalon-coated materials to provide high strength joints.

A two ply, 45° bias constructed, Hypalon-coated Dacron was therefore selected for use. In order to insure the desired properties, it was necessary that it be fabricated under close specification control, starting with the basic yarn and following through to the final assembly of the joints.

The general properties of this material are as follows:

Construction: 2 ply, 45° bias combined, Hypalon-coated Dacron fabric

Physical Properties:	Thickness	- .070 inch
	Weight	- 70 oz./sq. yd.
	Strip Tensile	- 1000#/inch
	Trapezoidal Tear	- over 400 lbs.
	Water Absorption	- approx. 1%

Electrical Properties*: Reflective Coefficient - δ = .18-.21
Dissipative Loss - .03-.04 db

*C-band waveguide tests at 5000 MC

In addition to conventional material tests, the strength of the material and special joint configuration were proven in a pressure log test with joints arranged in configurations representative of actual radome conditions. These tests proved that the joints could support the maximum design loads for the radome with a good factor of safety and provide a construction which would result in approximately simultaneous failure of joint and material. As this construction resulted in only a single lap joint with only the outer edge weather sealed with a thin, gum Hypalon tape, maximum uniformity of electrical characteristics was assured.

In order to minimize any variation in electrical characteristics due to variation in panel widths, a step-down construction was used in the crown to maintain the ratio of seam-to-panel width as uniform as possible throughout the dome. Although other techniques have now been developed by BIRDAIR to assure even more uniform electrical thickness when conditions require, the relatively low thickness of the basic envelope (.070" for a 210 ft. diameter radome), combined with good electrical characteristics, did not require these techniques to be employed on the Telstar radome.

2. Fabrication Techniques

Assembly of the heavy radome material also presented an unusual problem. Techniques used to assemble large coated fabric envelopes such as airships have, in the past, been to assemble these units on the floor, joining and taping the joints in the flat. This technique, although used on some of the early radomes, was found to result in joints of relatively poor quality, particularly where heavier materials were used. Use of curved fixtures, as employed by BIRDAIR in the fabrication of the first prototype 50 ft. radome, was therefore almost universally adopted for assembling large radomes.

However, the weight and stiffness of the material used for the Telstar radomes and the relative inflexibility of this material necessitated the development of new techniques. The problem was aggravated by the fact that the Hypalon cements proved to be much more difficult to work with. Thus, it was necessary to develop a new type of fixture which could properly position and hold this heavy fabric, yet require a minimum of handling and folding. Special equipment for applying the cement and for joining the panels, which would insure a uniformly high strength bond, free of air pockets, voids, or wrinkles, and capable of developing the full strength of the material, was also developed.

While accelerated tests on this material indicated good retention of properties with long exposure to weather, it is recognized that accelerated tests are only an indication of expected results and final proof must be in actual service life. As the materials and techniques employed in this radome are new, a test program has been set up to periodically check samples exposed at each radome site. It is expected that through this program we will be able to detect any differences in conditions of exposure at the different sites and also to detect any signs of deterioration, in order to permit corrective action to be taken to assure maximum service life. Preliminary tests made on samples taken from the Andover and Fleumer Bodou sites reveal little change in properties and expectations of a long service life with minimum maintenance.

3. Equipment Reliability

The inflation equipment is the heart of the air supported radome system. The radome envelope depends upon the inflation pressure for the pretensioning which provides its support and stability. The inflation system must therefore be completely reliable at all times. As with any mechanical system, the performance achieved is a function of the quality of the design. What is required to assure a reliable pressurization system is reliance on good engineering design practice, quality components, and recognition of the advantages of certain system approaches. Although pressurization systems can vary to wide ranges of complexity as a function of the radome system requirements, over a period of years BIRDAIR has established certain basic principles which, if adhered to, will provide a reliable pressurization system. These are noted as follows:

- (a) Continuous blower operation is advised. In contrast with the cyclic operation utilized in early systems, it has been demonstrated that continuous blower operation provides greater reliability than a stop-start system. Powered by inductive-type motors, the motor and blower bearings are the only wear points. Normal maintenance (lubrication) is all that is required to provide reliable service.
- (b) Size blower motors to be non-overloading under all conditions of operation. Maximum power is thus only utilized during initial inflation or emergency conditions of excessive air leakage. During the vast majority of the time the motor is then operating at approximately one-third of its rated power.
- (c) Select blowers which provide a maximum pressure equal to the desired inflation pressure and a flat performance curve. At the low differential pressures and widely varying flow rates desired for radome inflation, a blower provides a simple and an extremely accurate means of pressure control and prevents any possibility of over pressurization of the envelope.

- (d) Provide multiple blowers, parallel-installed, equipped with reverse flow check valves. This provides a fail-safe system in that it insures against mechanical failure of an individual blower. Individual blowers should be sized to maintain full inflation pressure with normal ventilation and leakage.
- (e) Provide a reliable source of power to the inflation system. In general, this requires a primary power source plus either a fully automatic emergency power generator or a gasoline driven standby blower.
- (f) Provide a system which will furnish several pressure levels for large radomes and/or radomes having severe wind requirements. This permits the radome to operate at low pressures (lightly stressed) during the majority of the time, yet have full stabilizing pressure during periods of high wind loads.
- (g) Provide a source of inflation air to the blowers which will closely correspond to ambient free stream pressure. This can be done by providing an air pickup, remote from the radome, away from major aerodynamic influence, or from a plenum fed from ducts providing controlled flow of air into the plenum to insure minimum variation with wind direction and velocity.

Because of the extremely large size and relatively high wind loading on the Telstar radome, a three level system is used. A different blower or pair of blowers is used for each level of pressure. The type of blowers selected develop essentially constant pressure over a wide range of flow conditions. In Stage 1, one or both of two blowers operate with wind velocities of 0 to 45 mph. In Stage 2, a third blower operates with wind speeds of 45-75 mph, and in Stage 3, two additional blowers are used for winds up to 70-100 mph. Under normal conditions the radome pressure is maintained at approximately 1 1/2" of water, resulting in a stable structure without undue continuous stresses. The higher pressure levels are actuated by an anemometer to assure a stable structure without excessive distortion in winds up to 100 mph.

Pressure switches detect any loss of pressure below established minimum levels and automatically put the second and third stage blowers into operation, as required to supply additional air. This would normally only occur in case of severe leakage due to excess ventilation or accidental damage. Each blower is equipped with a shutter-type check valve to prevent backflow. All blowers discharge into a common plenum chamber. The air intake is located at a distance greater than one diameter from the radome. The function of this intake is to provide air to the blowers at ambient static pressure, undisturbed by turbulence or blockage effects of the radome. The intake pipe is of sufficient size to result in insignificant pressure losses at normal flow rates. A reference ambient pressure tap is located near the inlet of the intake

pipe as this area is least affected by turbulent wind conditions and resultant variable pressures in the room at the base of the radome. The switching point for the two upper pressure stages has been selected to precede the calculated wind level by approximately 10%. This is to reduce any lag and insure that the structure reaches a minimum distortion condition as rapidly as possible.

As it is absolutely essential that power be available at all times for the pressurization system, a special emergency 30 KVA engine alternator has been provided for this service only. In order to avoid imposing a high motor starting load on the engine alternator, a sequential start system is included in the control circuit. This system provides time delays between the starting of the individual blower motors. The control also includes safe or low pressure indication for each stage as a function of wind level. Indication is also provided for unsafe high pressure.

The controlled pressure, multiple blower operation, in combination with low pressure controls and emergency power provisions, is believed to assure a continuous source of inflation pressure under any emergency conditions which could develop. With proper maintenance, a safe, trouble-free radome installation is thus assured.

ERECTION OF LARGE RADOMES

As the Telstar radomes weighed close to 30 ton and were fabricated as one-piece units with no sectionalizing, in order to assure maximum uniformity of electrical characteristics, handling and erection of these radomes required the development of new techniques. For packaging and transport the envelope was accordian-folded along the gore panels to provide a long slender strip, eight to nine foot wide and 200 foot long. This, in turn, was laid up in folds on a special shipping pallet, 10 foot wide and 40 foot long, providing a folded package 9 x 40 x 6. The transport container was built with a special steel truss construction so that when bolted together the whole unit could be lifted and handled by crane. Shipment was made on flat bed trailers and by boat to France.

As the original program schedule called for completion of the antenna before erection of the radome, and as it was desired to plan for eventual replacement of the radome, the Bell specification required that the radome be erected over the antenna and that weight and loads imposed on the antenna be kept to a minimum. One of the early concepts considered was that of using the antenna itself to position the envelope ready for attachment to the base. A method of spreading out the antenna, and of making attachment to the horn antenna frame so that it could be rotated about its horizontal axis to lift and position the envelope, with weight distributed over the full length and width of the horn, was therefore considered. However, in scheduling the program, Bell engineers decided that if work on the radome

was to continue through the winter months, weather protection would be required. As the lead time required to develop the special materials to assemble the radome would not permit the radome schedule to be moved up, and as there was at that time some concern that the radome envelope might be damaged by cranes or equipment working within it, if it were installed first, BIRDAIR was asked if a construction shelter could be provided to enclose the entire base while the antenna and all equipment was installed.

Because of limitations in availability of materials suitable for construction of a unit of the size needed and because of early delivery requirements, BIRDAIR recommended a construction shelter the same size as the radome, but fabricated from a heavy vinyl-coated material. Although such a unit would not fully meet the environmental conditions required by the specification, the unit was intended for use only during the winter months and weather data for the area indicated that a unit designed for somewhat lower windloads would give satisfactory service.

As the construction shelter would be in place when the radome was ready for erection, a study was made to determine whether a simplified erection procedure could be worked out. The result of this study was a recommendation that the construction shelter be sectionalized to facilitate installation and removal, and that a means of attaching it in a position which would permit the radome to be pulled over it, be developed. To accomplish this, a catenary skirt was added at a point approximately half way up the side (see Figure 2). With the construction shelter attached at this point, a lower silhouette unit resulted which still provided adequate clearance on the antenna, except for the equipment room at the end of the horn. A 45 ft. diameter "bubble" was therefore built into the construction shelter at this point to provide necessary clearance.

Using the construction shelter, the erection procedure was to first stow the antenna and then drop the construction shelter and reattach it at the catenary. The attachment was made inside of the radome base angle so as to leave it free for attachment of the radome. The radome was then spread out at the side of the base using cranes and special handling gear developed by BIRDAIR. It was then pulled over the construction shelter using cranes with a special harness and air pressure to facilitate movement. Although some difficulties were encountered in developing this procedure, with a number of improvements worked out as a result of experience gained at the Andover site, we were able to pull the 30 ton radome unit over the antenna with little difficulty.

After pulling the radome into position over the construction shelter, and attaching it at the base, it was inflated. The construction shelter was then allowed to deflate and drop down to lay over the antenna. The sections of the construction shelter were disconnected, dropped to the floor of the radome, and stored away for later use. One of the advantages of having a construction shelter is that it is available as a piece of equipment ready to be used again in case of eventual replacement of the radome, thus providing a means of replacement which would assure that tolerances on the antenna were not disturbed.

Both the German and Canadian programs were set up to provide for installation of the radome before building the antenna. In both cases the radome was scheduled for erection in the early fall so that assembly of the antenna could proceed without interference from the weather during the winter months. If the radome can be installed before the antenna is erected, the erection is, of course, much simpler. The procedure used so successfully in Germany was to spread out the envelope at the side of the base, using specially developed equipment, and then to lift the envelope and drape it over the base and pedestal so that it could be attached to the base angle and inflated. Installation by this method, using the special equipment and procedures developed by BIRDAIR, went smoothly. A separate procedure was developed and proposed for use in installing the radome over the antenna in case of eventual replacement of the envelope.

CONCLUSIONS

Three large air supported radomes, two with a diameter of 210 ft. and one with a diameter of 160 ft., have been put in service for periods ranging up to two years. These radomes, having generally higher RF performance and costing but a fraction of the cost of comparable size rigid radomes, prove the practicality of air supported radomes of this large size where superior performance is required. The superior properties being provided in the Telstar radome are possible only because of the combination of material properties, design, and fabrication techniques which have been developed by BIRDAIR with the assistance and cooperation of our suppliers. Extremely close controls have been established and must be maintained throughout the preparation of the material and assembly of the radome, starting with the basic yarn treatment and compounding of the coating and cement.

We at BIRDAIR are convinced that the possibilities of air supported structures, not only for radome use but for other military and commercial structures as well, are almost unlimited. However, if this full potential is to be developed and made available to the military services within a reasonable period of time, additional financial support is required. As the Government has provided little financial support of research and development activities for air supported structures for many years, the developments which led to the successful fabrication of the Telstar radomes were supported almost entirely by private industry. The volume of material or equipment used in this field is, however, still too small to encourage major investments by industry. However, with adequate Government support for a well coordinated program of research and development, it is believed that great strides could be made.

EFFECTS OF APERTURE OBSTRUCTIONS AND
RADOME FINISHES UPON RADOME
ELECTRICAL CHARACTERISTICS

by

J. R. Rogers
Electronics Engineer
Aircraft Engineering Division
MCDONNELL AIRCRAFT CORPORATION
ST. LOUIS, MISSOURI

ABSTRACT

Radar performance is degraded by the installation of hardware in the window area of the radome. Rain erosion coatings and protective finishes also affect radome electrical characteristics. Effects of installations such as pitot static booms, fairings or pods attached to the radome to house electronic systems, paint and other protective finishes are discussed in the following report.

INTRODUCTION

The radome design engineer computes an optimum radome wall by using standard design techniques. Once the analytical design is complete the designer is reasonably sure that the radome electrical characteristics will be approximately as calculated. However, installation on the radome of contrivances such as pitot static booms, ports, pods, fairings, etc., that have a degrading effect on the electrical design performance of the radome can not be accurately calculated and must be measured.

The purpose of this paper is to present experimental data measured on various radome/antenna configurations with known obstructions placed in the window area of the radome. The effect on power transmission, beam deflection and antenna pattern distortion is shown. It is felt that this data is typical and that similar installations on other radomes will react much in the same manner.

DISCUSSION

Nose Boom Installations

The first radome to be considered is an X-band foamed core A-sandwich ogive in shape. The radome is 50 inches long with a 35 inch base diameter. The electrical characteristics of this radome met all specification requirements which were average one-way power transmission of 96 percent with a maximum beam deflection of 5.8 milliradians; typical data on this radome is shown in Figures 1 and 2.

This radome was later modified for use on another aircraft employing a different X-band radar system. There were slight modifications to the radome base to mate the new aircraft fuselage, however, the basic radome wall design remained the same. Figure 3 shows the transmission to be slightly lower than the original radome. Maximum beam deflection was 4.8 milliradians.

The reduction of the transmission may be attributed to the two different antenna systems. These differences did not warrant electrical redesign of the radome since the electrical characteristics were adequate for satisfactory radar system operation.

Later modification required the addition of a pitot static nose boom on the radome with the associated pitot heater wires and static and pressure tubes. Tests were made to determine the degradation that might be expected with the nose boom installed. It was determined that for structural reasons the base mounting of the boom would be 3.2 inches in diameter. In order to determine the effect of an aperture block of this size, a metal cylinder 3.2 inches in diameter and 6 inches long was located in free space at various distances in front of the radar antenna. The metal cylinder was first located with the aft end at the same distance from the antenna as the radome apex. The cylinder to antenna spacing was varied from this position to plus $\frac{3}{8}$ of an inch in $\frac{1}{16}$ inch increments. One-way power transmission was recorded at each position for low, mid and high frequencies and is shown in Figure 4.

The cylinder to antenna spacing was then increased beyond the apex by 0.5, 1.0 and 1.5 feet and moved toward the antenna $\frac{3}{8}$ of an inch in $\frac{1}{16}$ inch increments at each position. One-way power transmission was recorded at mid frequency and is shown in Figure 5.

The one-way power transmission varied by 1 to 29% depending upon the frequency and the position of the cylinder.

The results of the free space tests discussed above provided sufficient information to say that a pitot boom installation was feasible from an electrical standpoint. A test was then conducted on a radome with a mock-up of the nose boom installed.

Results of the beam deflection and one-way power transmission measurements are as follows: Without the nose boom the radome had a maximum beam deflection in azimuth of 4.9 milliradians and a maximum elevation error of 2.95 milliradians. The minimum one-way transmission was 91.0% at 0° antenna look angle. With the nose boom installed maximum beam deflection was 10.85 milliradians. The maximum error in elevation was greater than 10.0 milliradians. Two readings for elevation error were beyond the measureable capability of the equipment. The minimum one-way power transmission was 51.0% at 0° elevation angle.

Figure 6 shows transmission and beam deflection at 5° antenna down look angle for radomes with and without nose boom. Figures 7 and 8 show antenna patterns with and without the nose boom. An extensive electrical correction program was required on the production installation.

The optimum nose boom configuration was determined to be two 1/4 inch OD aluminum tubes mounted on each side of the centerline of the radome and 20° up in the radome with respect to the waterline as shown in Figure 9. The heater wires were mounted on the top centerline of the radome. Minimum one-way power transmission of the radome without the nose boom was 79% as compared to 67% with the boom and compensation for beam deflection. This is a substantial improvement over the 51% minimum one-way power transmission measured with the radome before correction. Figures 10 and 11 show the transmission and beam deflection of the radome with the nose boom before and after correction.

EFFECTS OF VARIOUS SIZE METAL OBSTRUCTIONS IN THE TIP OF THE RADOME ON RADOME PERFORMANCE

Cone and Dome Shaped Obstructions

A study was made to determine the effects of large aperture blocks in the nose of an X-band radome. Three different size mock-ups with dome and cone shaped tips were tested separately in the radome. A 23" diameter parabolic antenna with a conical scan feed system was used for these tests.

Transmission and beam deflection was measured at scan angles of + 50 degrees for various elevation angles. Figure 12 is a tabulation of transmission for various elevation angles through the basic radome with cone and dome shaped cylinders of 4", 6" and 8.5" diameter in the nose of the radome.

Minimum transmission and maximum azimuth and elevation errors are shown in Figure 13. The ratio of the size of the antenna dish to the aperture block will determine the degradation to radar performance. The larger the dish, the less effect there is on transmission for a given aperture block. Frequency is also a factor to be considered when considering the effects of an aperture obstruction.

Cylinder Installation in Fairing on Radome

A metal cylinder approximately 6" by 20" was mounted in a fiberglass fairing on two X-band radomes 53" long with a 35" base and 74" long with a 42" base. The smaller radome housed a 24" diameter antenna and the larger radome housed a 32" diameter antenna.

Figure 14 shows minimum one-way power transmission measured on these two radomes to be 12% for the small radome and 31% for the large radome. Figure 15 shows transmission minimum of 31% with the 6" x 20" cylinder. This was reduced to 23% by the addition of 5" x 12" long cylinder aft of the larger cylinder.

It is apparent that an obstruction of this size would seriously affect the antenna pattern. Figure 16 shows the antenna pattern with and without the radome for an antenna look angle of -40° which would be a cut through the fairing. The shaded area of the antenna dish was covered with absorber material and the antenna pattern measured. This pattern duplicates very closely the pattern measured through the radome with the cylinder and fairing as may be seen in Figure 17.

One-way power transmission of the small radome with and without the fairing and cylinder installed is shown in Figure 18. A photo of the small radome with the cylinder and fairing in place is presented as Figure 19.

ELECTRICAL DEGRADATION CAUSED BY RAIN EROSION RESISTANT AND EPOXY FINISHES

Rain Erosion Shoes

One-way power transmission and beam deflection tests were made on an X-band solid wall radome with a 14" long preformed neoprene rubber and dacron fabric reinforced rain erosion shoe. The following radome configurations were tested:

- (A) Production Radome (A) with GAC23-56 rain erosion coating.
- (B) Radome (A) with the erosion shoe placed directly over the 23-56 rain erosion coating as shown in Figure 20.
- (C) Radome (A) with the 23-56 rain erosion coating removed from the forward 14 inches of the tip with the erosion shoe installed over this area. (Refer to Figure 21.)
- (D) Radome (B) finished with an epoxy white finish (MMS 405 No. 17875) without the erosion shoe. (Refer to Figure 22.)
- (E) Radome (B) with the epoxy finish and the erosion shoe in place. (Refer to Figure 23.)
- (F) Radome (B) with epoxy finish, erosion shoe and antiglare flat black (MIL-L-6805) on the top of the radome. (See Figure 24.)

The erosion shoe installed over the 23-56 erosion coating Radome (A) decreased one-way power transmission by 2% at the low frequency and 5% at the high frequency. Beam deflection was increased by 2.3 milliradians from 2.5 due to the erosion shoe with an average increase of 1.5 milliradians in the 20° cone off the nose with only one scan exceeding the 4.0 milliradian specification limit by .8 milliradian. Electrical characteristics of the radome with the 23-56 erosion coating removed from the first 14" of the nose and the shoe replacing the 23-56 material in this area were about the same. A slight reduction was noted in beam deflection.

Performance through Radome (B) with the white epoxy finish was degraded slightly more than Radome (A) when the erosion shoe was placed over the tip. The beam deflection was increased by 2.5 milliradians from 3.3 milliradians and there were 7 areas that exceeded the 4.0 milliradian specification. Two areas were noted with a maximum of 5.8 milliradians.

The additional degradation experienced through the radome with the erosion shoe installed over the white epoxy finish can be attributed to the fact that the radome is electrically thinner since the radome wall design takes into account the .010 inch thickness of the 23-56 rain erosion coating over the complete radome. The flat black antiglare paint MIL-L-6805 over the top of the white epoxy radome had very little effect upon one-way power transmission and beam deflection. Figures 25 and 26 show transmission and beam deflection measured with and without the erosion boot installed over the 23-56 erosion coating on Radome (A).

Figures 27 and 28 show transmission and beam deflection through Radome (B) without any finish, with white epoxy finish, and with the erosion shoe installed over the epoxy finish. Data shown are for worst case conditions noted.

The installation of the rain erosion shoe on both radomes definitely affected the electrical characteristics of each radome. However, the degradation is not of such a magnitude to prevent satisfactory radar system operation when the shoe is installed on radomes presently being finished with other materials and techniques.

Although the data with white epoxy finish shows more degradation it must be remembered that the discontinuity on the radome surface caused by the erosion shoe edge may be compensated. On a new design, the wall could be tapered to eliminate this discontinuity.

Figure 27 shows a 1 to 6% reduction in transmission at the low frequency. The validity of the reduction in transmission is questioned since the test without the finish was made 18 months prior to the test with the epoxy finish. This data was measured through the upper half of the radome only. A structural change that had been made to the fairing on the bottom of the radome during this time may have contributed to the loss. Also the 23-56 coatings had been stripped from the radome several times. The solvent used to soften the coatings for stripping may have also effected electrical characteristics.

White Epoxy Finish

The white epoxy finish has a titanium dioxide pigment which has a dielectric constant of 100. The manufacturer of the white epoxy finish could not supply the dielectric constant or the loss tangent of the epoxy paint. The major problem in measuring the dielectric constant and/or loss tangent of the finish was in getting a sample large enough to measure. A hardened sample taken from a can left open to dry would not be representative of a sprayed finish coating and would therefore give erroneous results.

One way to obtain a sample was to build one up in the same manner that the finish would be applied to the radome in the paint shop. A simple solution devised by the Materials Department was to spray a finish on an 8" x 12" aluminum panel each day as production aircraft were being painted. Not more than 10 coats were applied each day so that the drying characteristics of the sample and the finish on the aircraft would be the same. After several weeks a thickness was attained that would allow X-band electrical test samples to be cut from it.

Preliminary dielectric constant and loss tangent measurements made at room temperatures show the dielectric constant to be 4.8 and the loss tangent to be .06 at X-band. Tests are in progress at this time to measure dielectric constant and loss tangent of the white epoxy samples for X and K_u-band frequencies at temperatures up to 350°F.

Tests made on a radome with the erosion boot installed and finished with white epoxy were conclusive enough to allow the use of this process on the nose and side looking radomes of an aircraft currently in production. Figure 29 shows the nose radome being tested on a radome test range. Electrical characteristics of this radome are good and met the specification requirements.

The nose boom attach area was held to a maximum diameter of 1.5 inches. The tubes and wires were installed to give minimum degradation. The dielectric constant of the erosion shoe is approximately the same as the radome glass, and the radome tip was tapered to give the desired wall thickness for a near flush installation. The white epoxy finish is applied without primer and does not exceed a thickness of .002 inch.

One problem area which will be experienced when employing an epoxy finish is that of accumulation of an excessive thickness when refinishing is required. If the radome is to be refinished, the old finish should be sanded off. Care should be taken so that the finish is removed evenly from the radome. Up to .006 of an inch of buildup is allowable before sanding is required.

Epoxy stripper should not be used to remove the finish from the radome because the stripper will also attack the basic radome material and destroy or damage the radome.

CONICAL SCAN FEED SYSTEMS VS MONOPULSE FEED SYSTEMS WITH NOSE BOOM INSTALLATIONS

The situation may arise where it may be desirable to use a different antenna dish and feed system in a radome that has been designed and electrically compensated for a antenna system in the same frequency range but having a different type of feed system.

Figures 30 and 31 show the one-way power transmission and in-plane error of the same radome/nose boom combination with two different antennas. One-way power transmission was essentially the same for both antenna systems except for a few discrete angles. However the in-plane error was increased from 3.6 milliradians with the conical scan feed system to 7.34 milliradians with the fixed monopulse feed system. The 7.34 milliradian in-plane error was the maximum measured throughout the radome and occurred at the low frequency.

The in-plane component of the error was affected more than the cross-talk component therefore, only the in-plane error is shown. In-plane error at the high frequency was 3.5 milliradians with the four horn monopulse antenna as compared to 2.3 milliradians at mid-frequency with the conical scan antenna. Total boresight error with the conical scan antenna on this radome was 4.25 milliradians as compared to 8.6 milliradians with the four horn fixed feed monopulse antenna.

The substantial increase in beam deflection with the monopulse system is typical of monopulse feed systems, however, the radome can be corrected to reduce the error.

It is the writers experience that a monopulse antenna system is more sensitive to aperture blocks than the conical scan feed system.

Generally nose boom installations will reduce the transmission through the nose area below the 75% level. By keeping the nose boom attach area in the radome apex small with respect to the wave length and antenna size these problems may be minimized.

A monopulse antenna in a radome with a minimum transmission below 75% will increase the existing side lobes to a level that may interfere with radar operation especially in a terrain avoidance mode. In every case (to the writers knowledge) where a nose boom has been incorporated an extensive correction program has been necessary and in some cases without success. All radomes manufactured with nose booms require some degree of individual correction for production units.

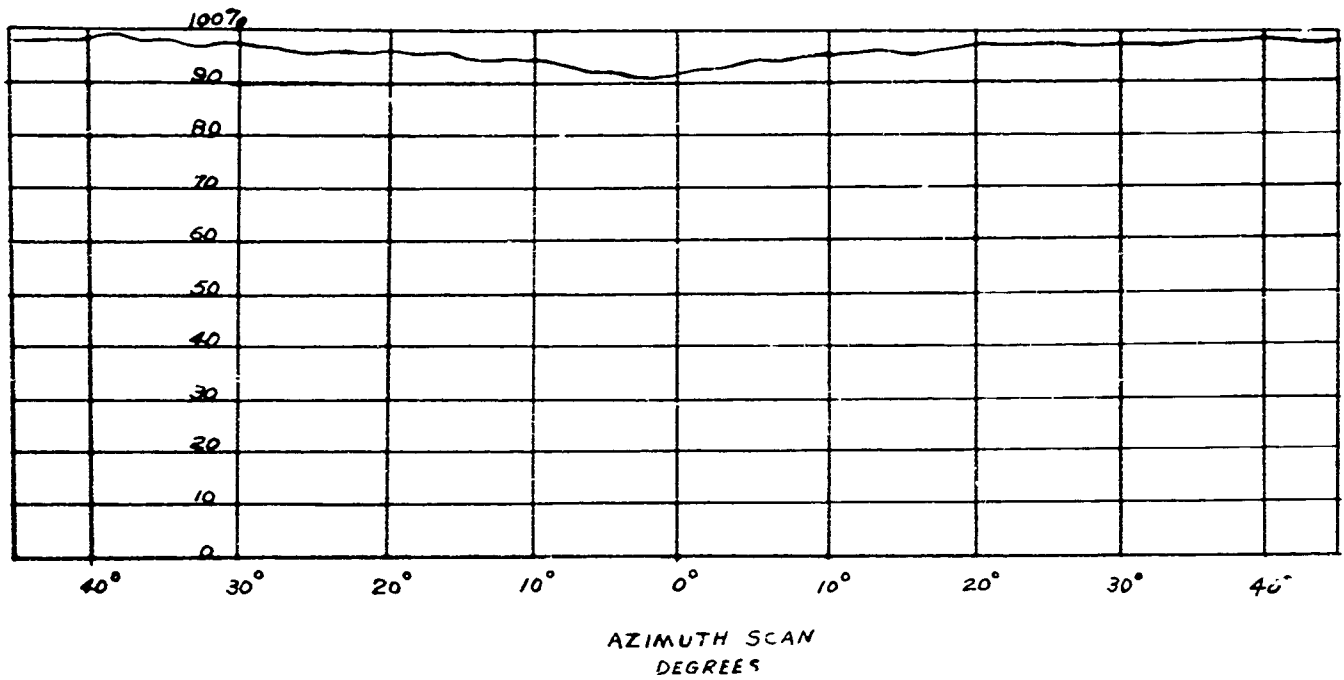


FIGURE 1 ONE-WAY POWER TRANSMISSION
X-BAND RADOME

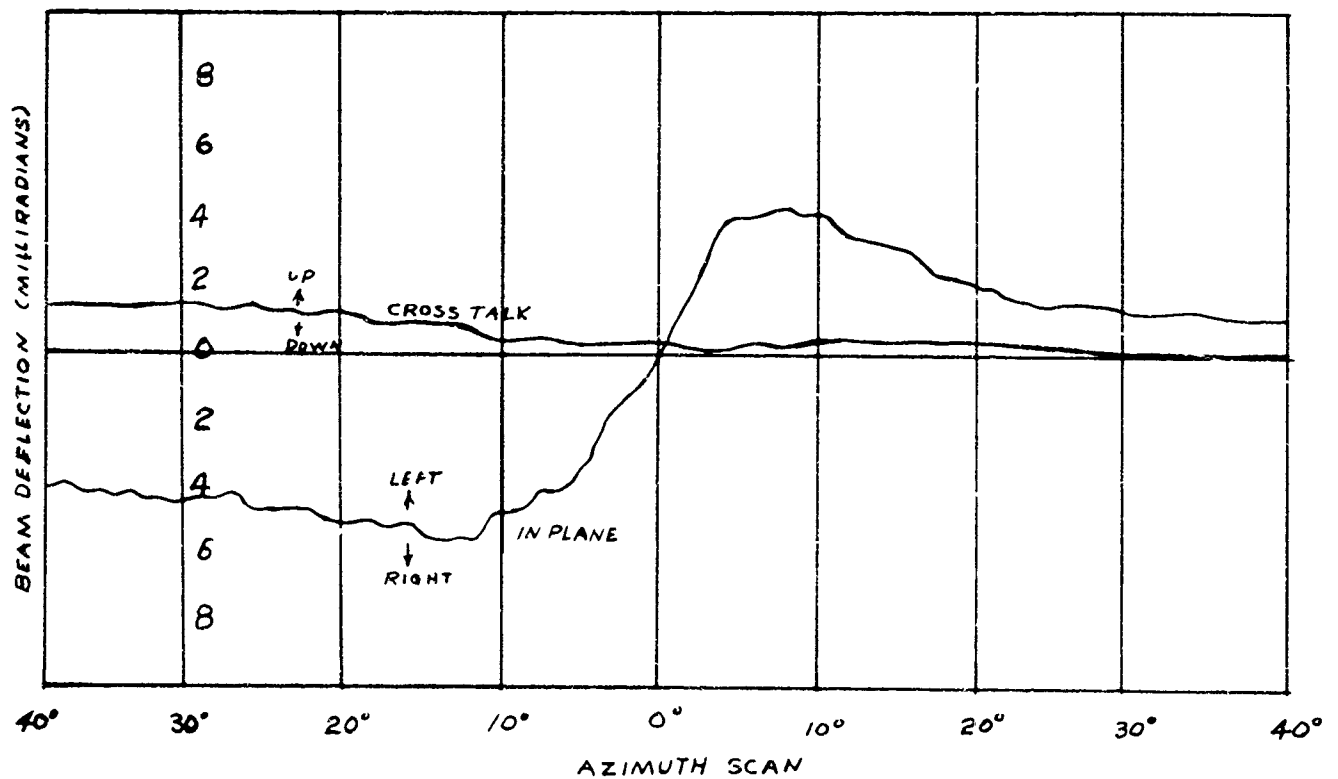


FIGURE 2 BEAM DEFLECTION
IN-PLANE AND CROSS TALK ERROR

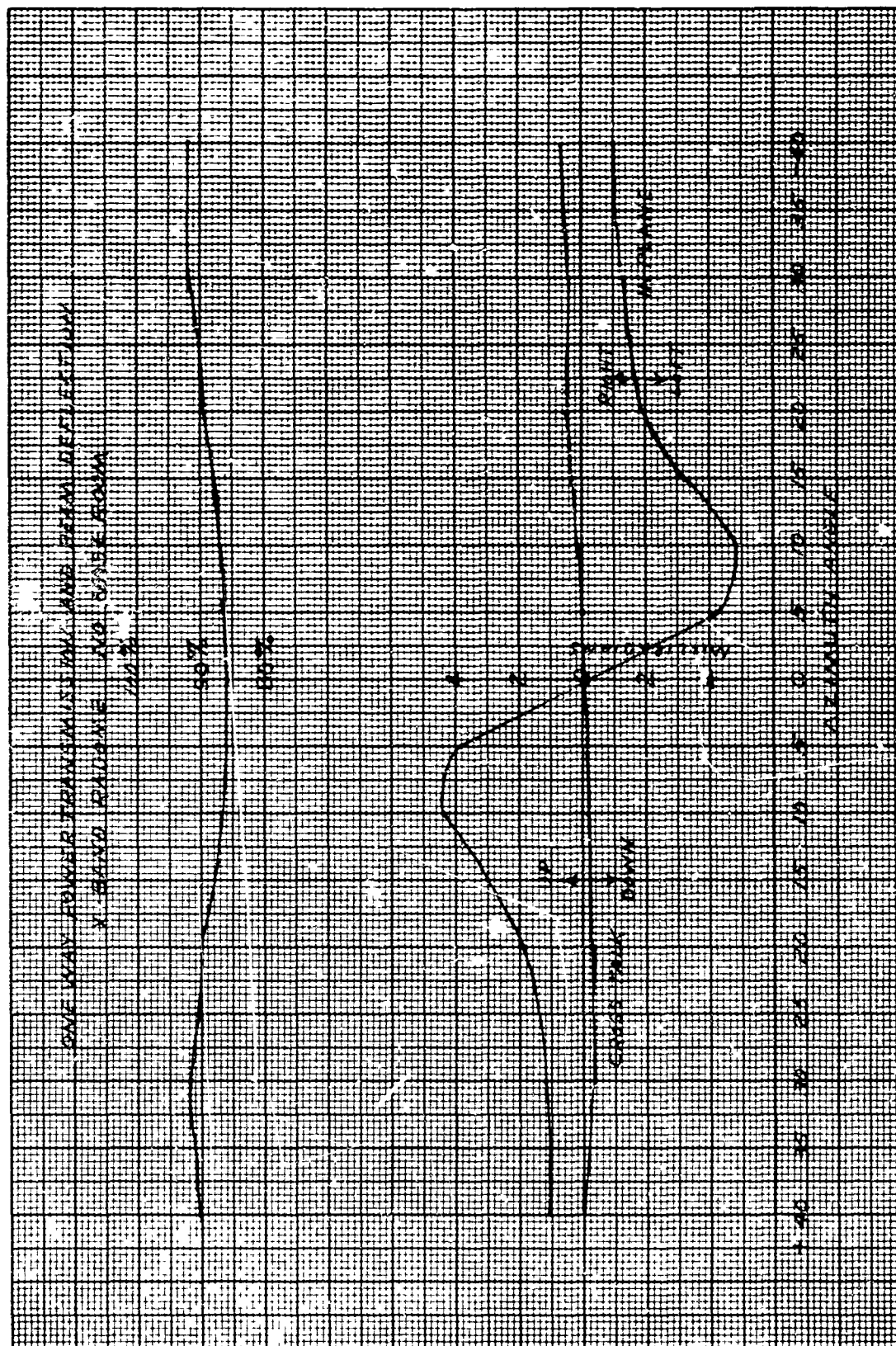


FIGURE 3 TRANSMISSION AND BEAM DEFLECTION OF
MODIFIED X-BAND RADOME WITHOUT NOSE BOOM

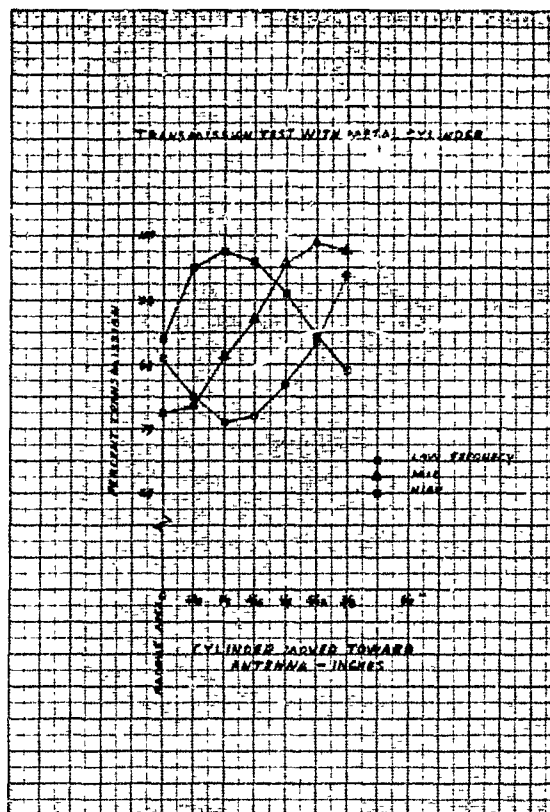


FIGURE 4 TRANSMISSION WITH METAL CYLINDERS
LOW, MID AND HIGH FREQUENCIES

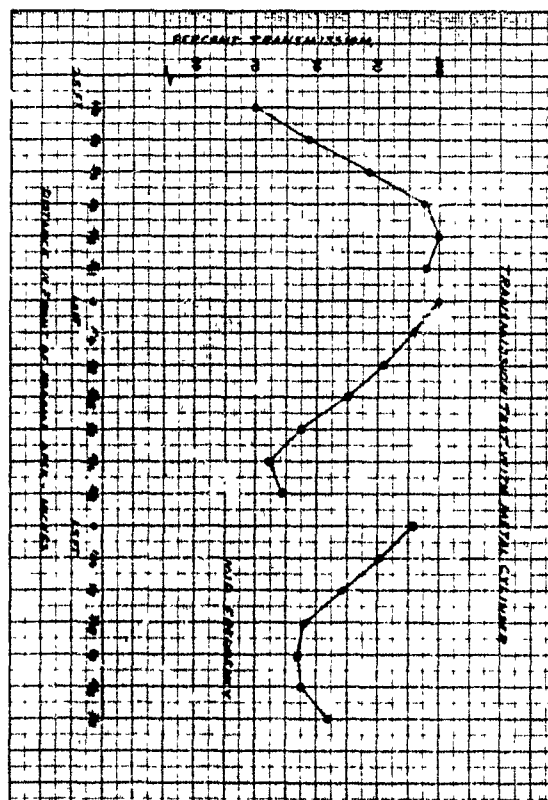


FIGURE 5 TRANSMISSION WITH METAL CYLINDERS
MID FREQUENCY

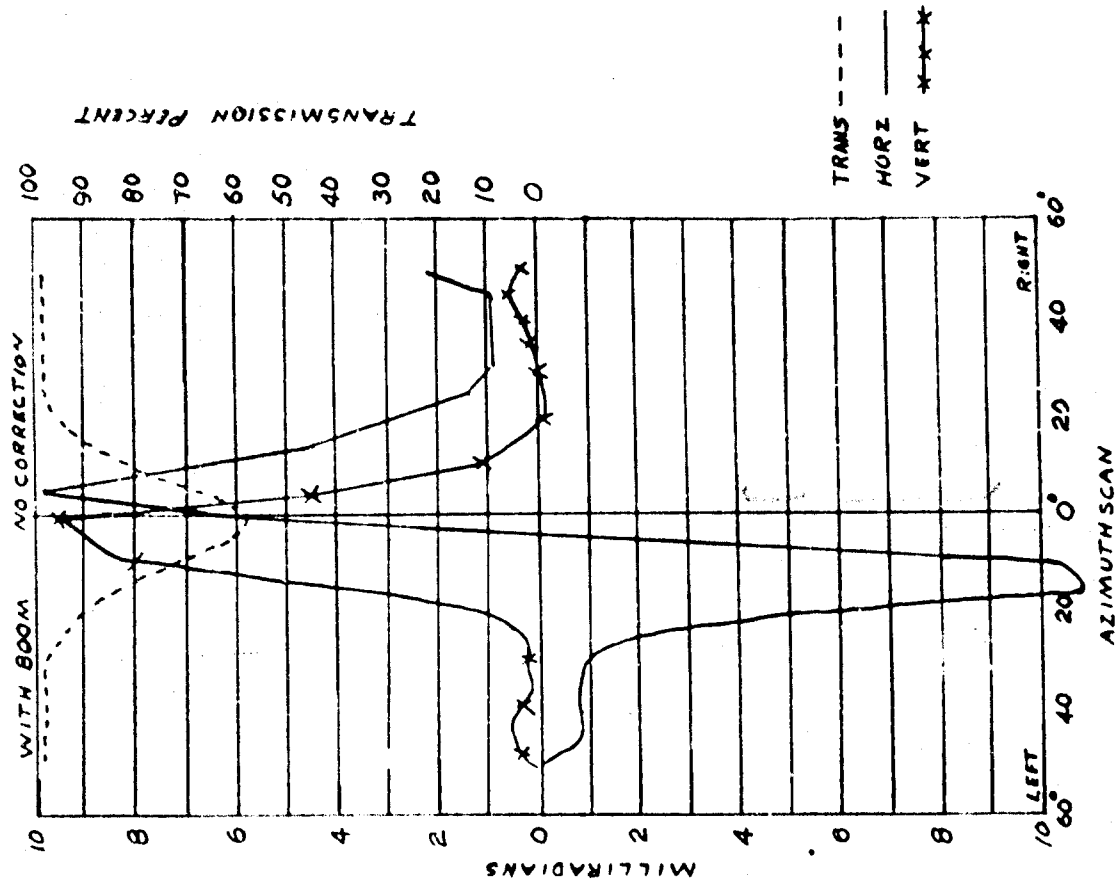
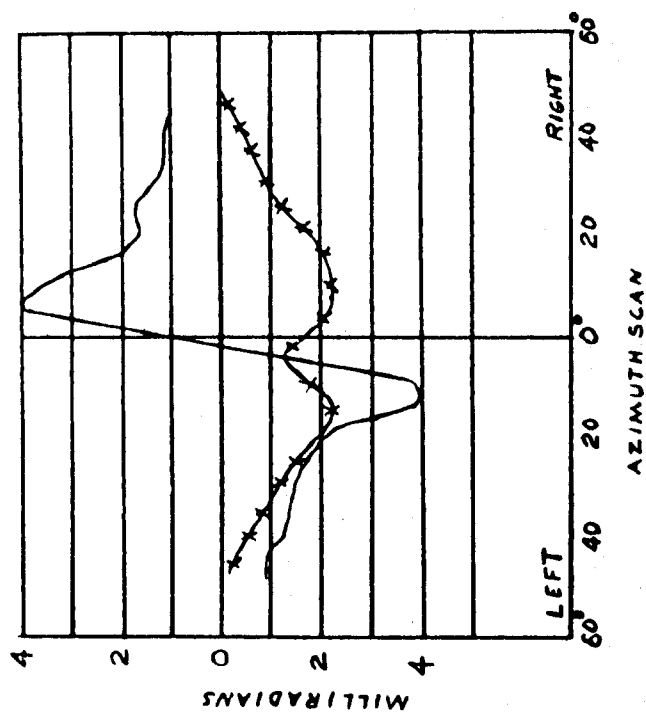
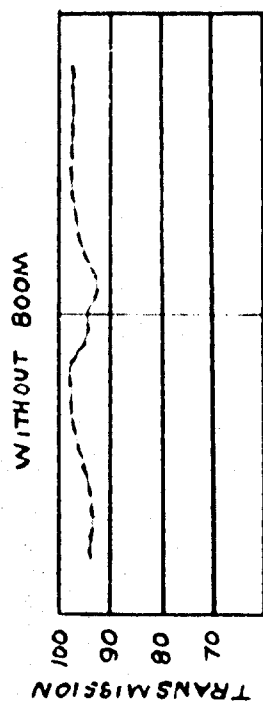
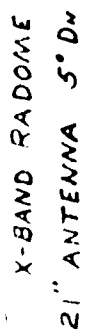


FIGURE 6 TRANSMISSION AND BEAM DEFLECTION WITHOUT NOSE BOOM AND WITH NOSE BOOM BUT NOT CORRECTED

X-BAND RADOME
21' ANTENNA
HORIZ. POL.

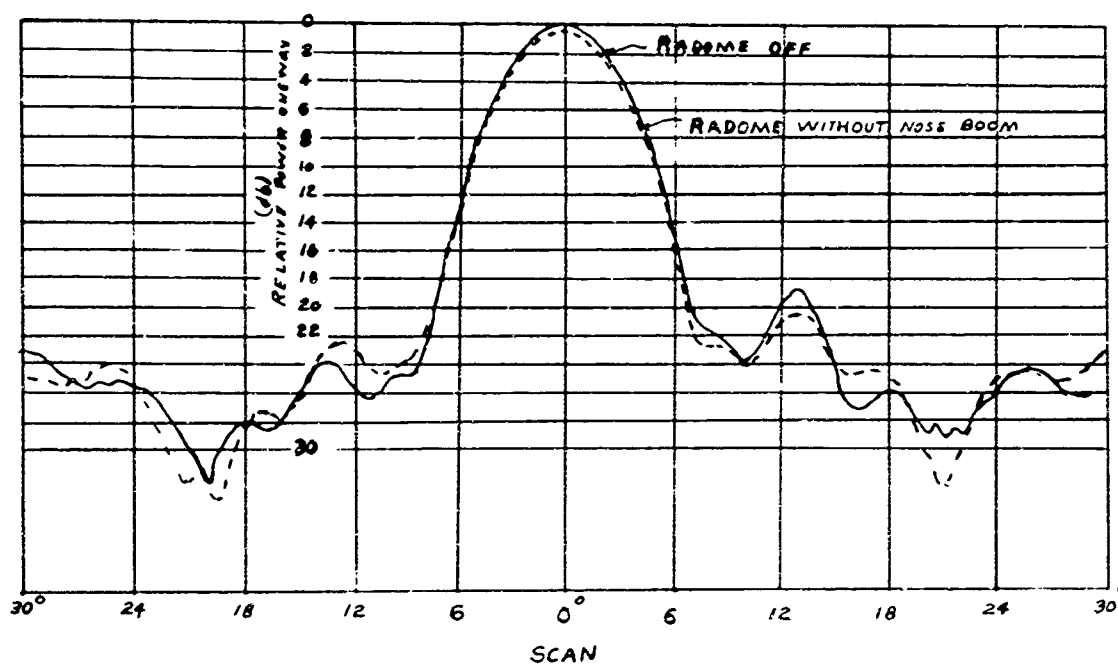


FIGURE 7 ANTENNA PATTERN RADOME
WITHOUT NOSE BOOM

X-BAND RADOME WITH PROTOTYPE
NOSE BOOM 21" ANTENNA HORIZ POL.

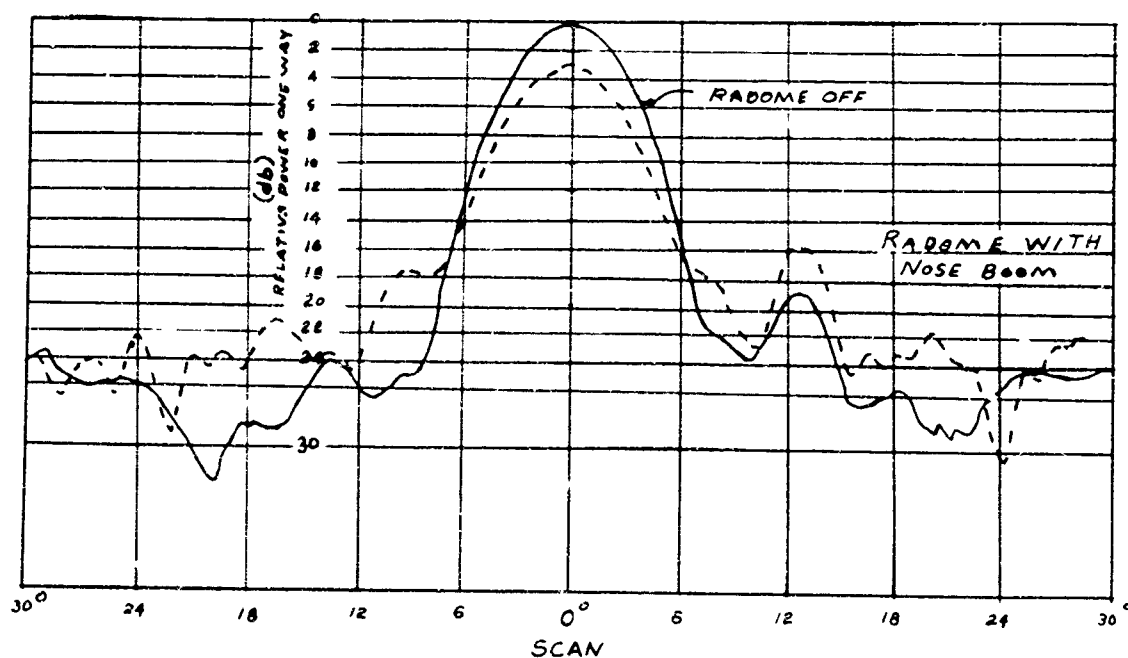
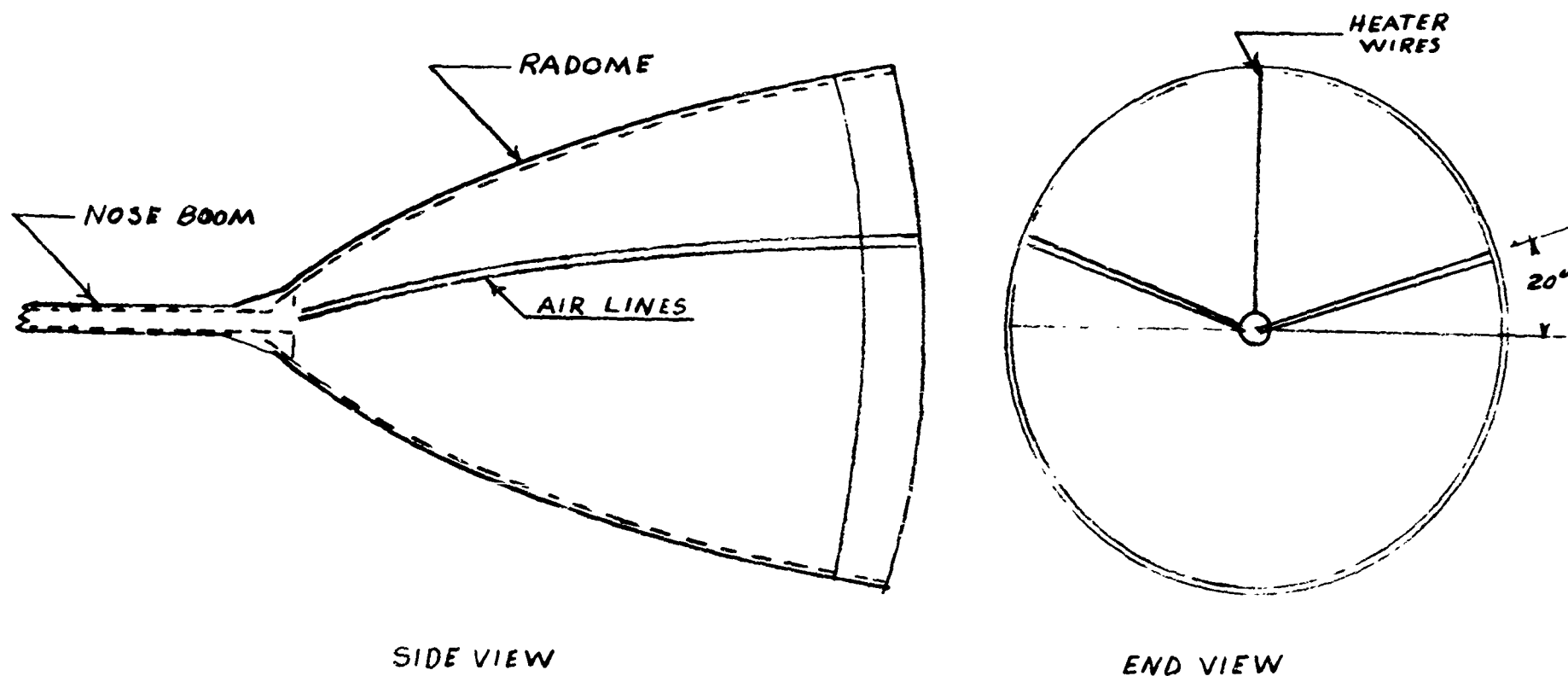


FIGURE 8 ANTENNA PATTERN RADOME
WITH NOSE BOOM



NOSE BOOM INSTALLATION WITH
PITOT TUBE STATIC LINES AND HEATER
WIRES LOCATED FOR OPTIMUM BEAM
DEFLECTION AND ONE-WAY TRANSMISSION

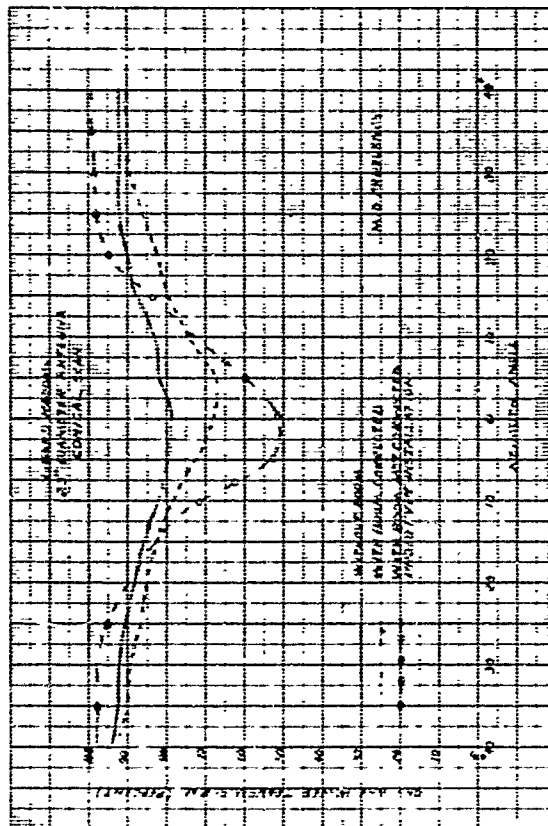


FIGURE 10 TRANSMISSION WITH AND WITHOUT NOSE BOOM AND PROTOTYPE NOSE BOOM INSTALLATION

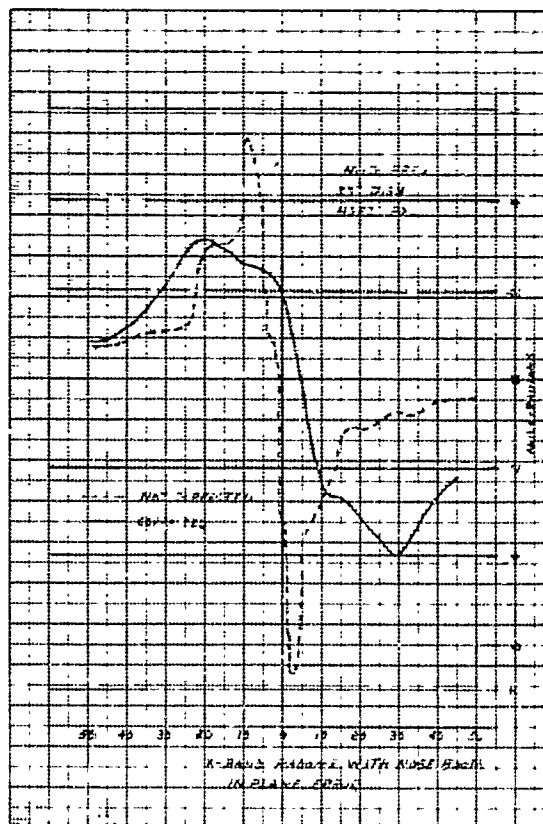


FIGURE 11 IN-PLANE ERROR OF CORRECTED AND UNCORRECTED RADOME

X-BAND RADOME WITH 23" CONICAL SCAN ANTENNA

	Minimum Transmission	Maximum Azimuth Error	Maximum Elevation Error
Radome Clean	86%	2.3 mils	6.0 mils
4" Dia. Can (Cone Shape)	64%	2.7 mils	7.0 mils
6" Dia. Can (Cone Shape)	52%	3.5 mils	9.3 mils
8.5" Dia. Can (Cone Shape)	38.7%	4.3 mils	10.3 mils
4" Dia. Can (Dome Shape)	61.5%	2.6 mils	7.2 mils
6" Dia. Can (Dome Shape)	54%	3.45 mils	8.5 mils
8.5" Dia. Can (Dome Shape)	36.5%	4.6 mils	9.2 mils

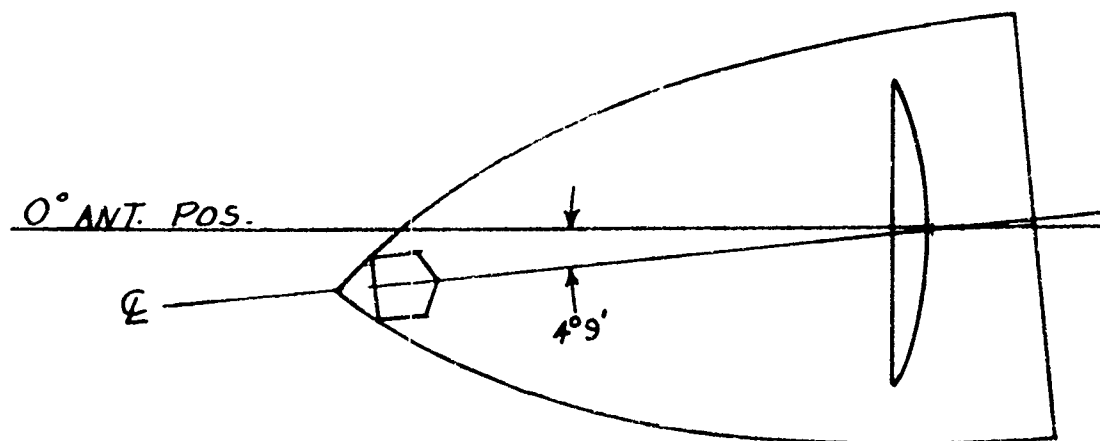


FIGURE 13

X-BAND RADOME TRANSMISSION DATA WITH
23" CONICAL SCAN ANTENNA

Antenna Position	Radome Clean	Radome With 4" Dia. Can (Cone)	Radome With 6" Dia. Can (Cone)	Radome With 8-1/2" Dia. Can (Cone)	Radome With 4" Dia. Can (Dome)	Radome With 6" Dia. Can (Dome)	Radome With 8-1/2" Dia. Can (Dome)
20° Up	90%	90%	88%	87%			
15° Up	91%	87.5%	82%	77%		82%	
10° Up	90%	80%	76%	65%	81%	74%	63%
5° Up	88%	75%	67%	55%	74%	68%	54%
0	85%	62.5%	56%	43%	62%	54%	40%
5° DN	84%	55%	50%	34%	58%	45%	34%
10° DN	86%	60%	51%	40%	62%	47%	38%
15° DN	87.5%	69.5%	62%	48%		60%	
20° DN	90%	78%	73%	60%			
25° DN	91%	86%	83%	70%			

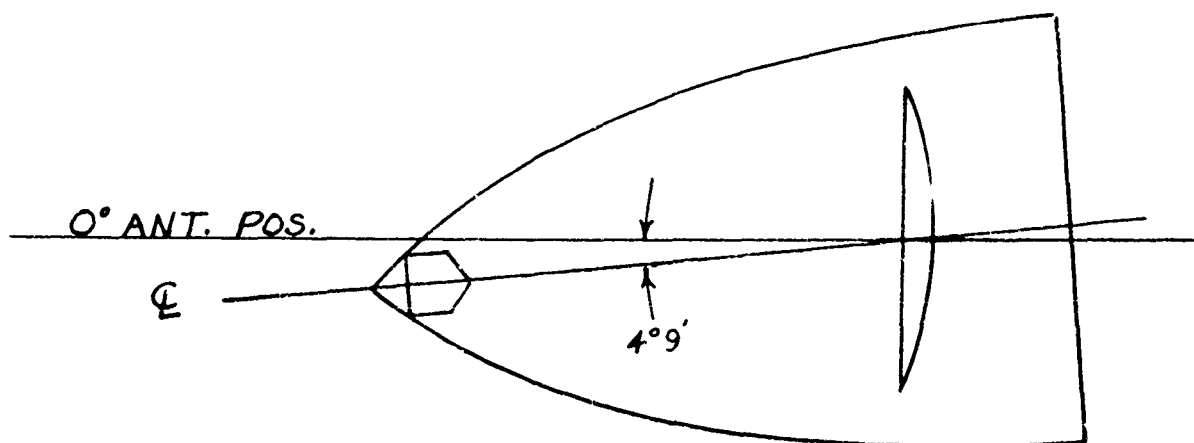


FIGURE 12

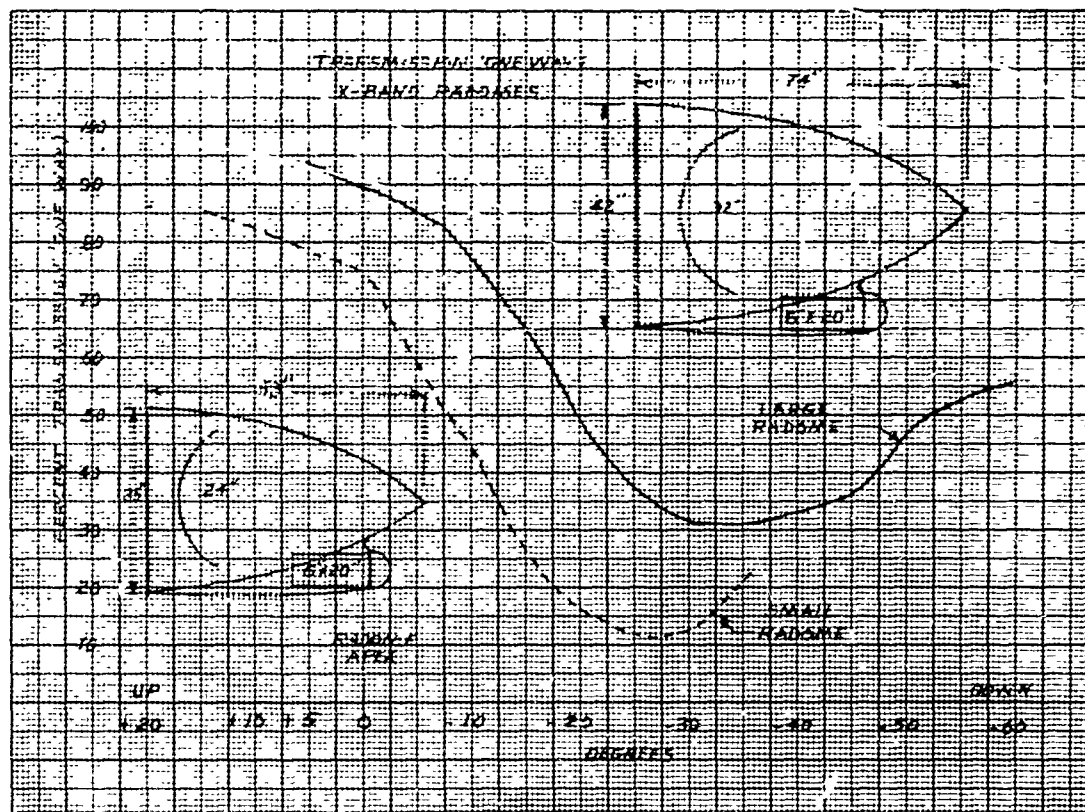


FIGURE 14 TRANSMISSION DATA THROUGH
LARGE AND SMALL RADOME WITH CYLINDER AND FAIRING

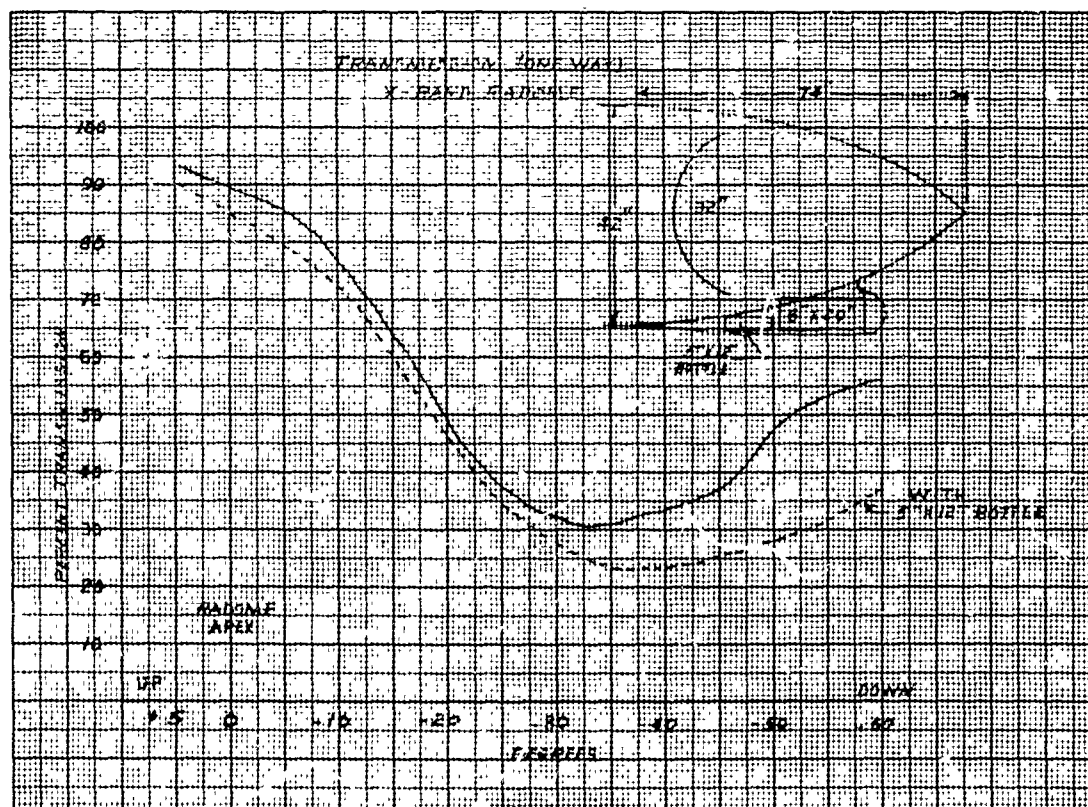


FIGURE 15 TRANSMISSION DATA WITH LARGE RADOME
WITH ADDITIONAL 5" x 12" CYLINDER IN FAIRING

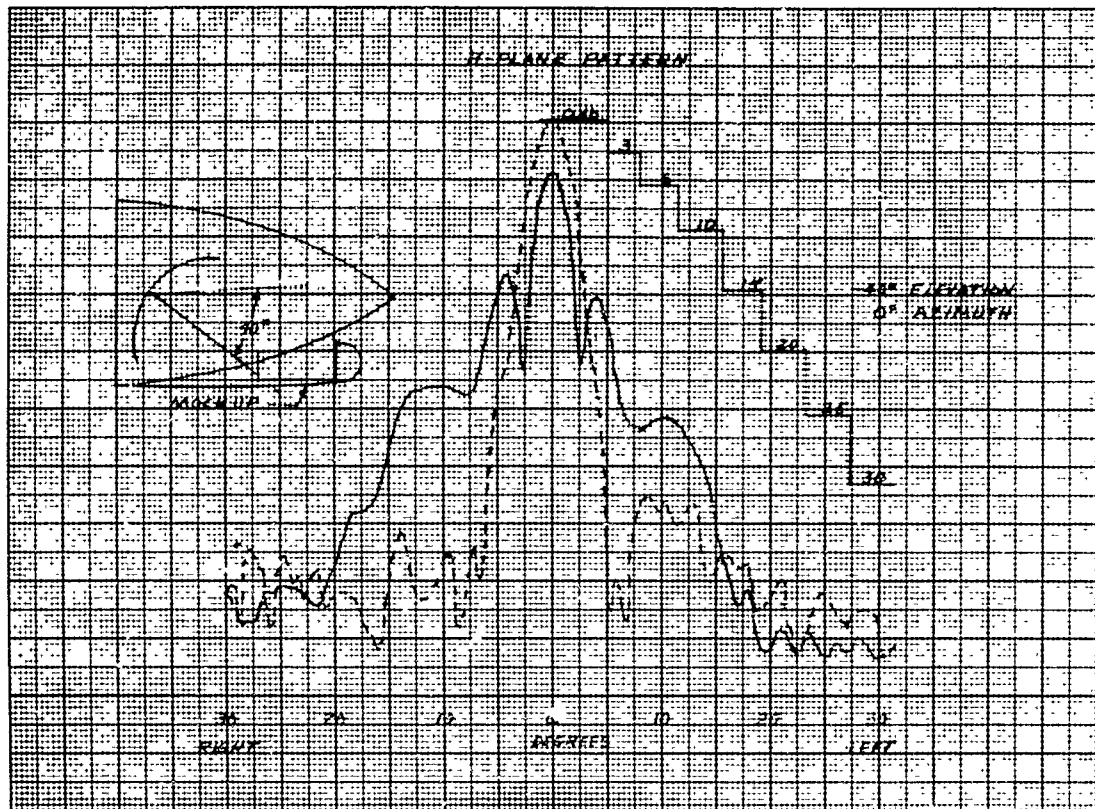


FIGURE 16 H-PLANE PATTERN WITH
RADOME AND FAIRING

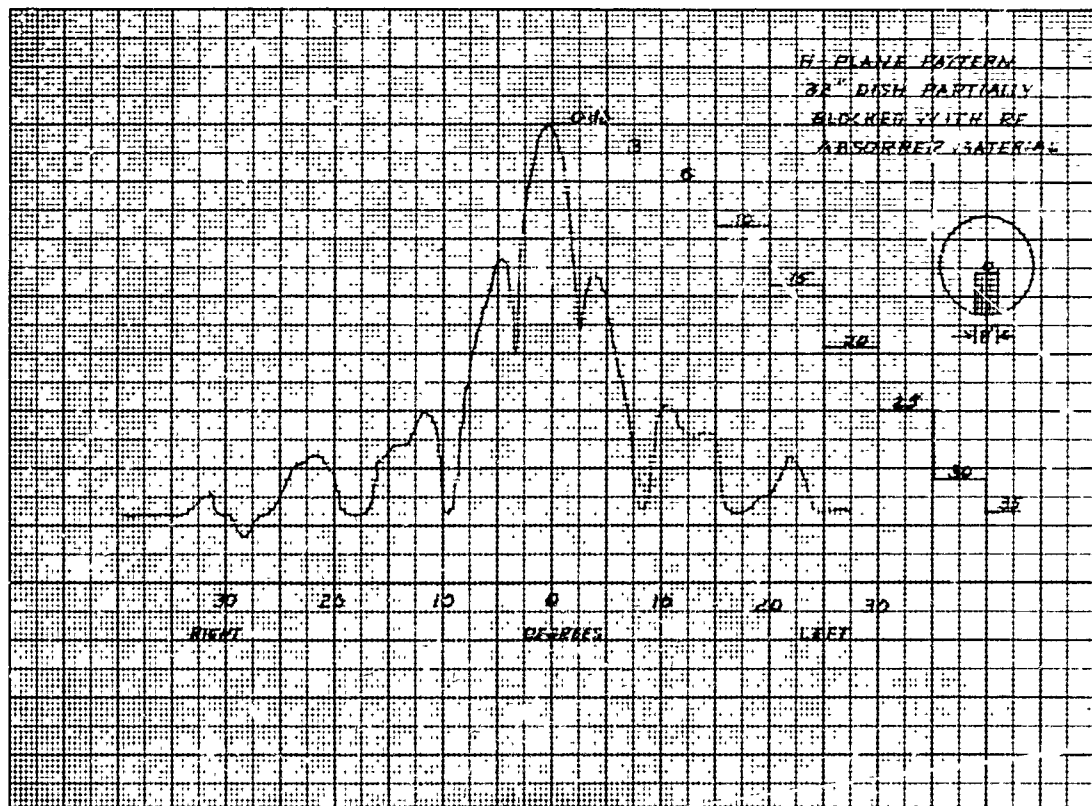
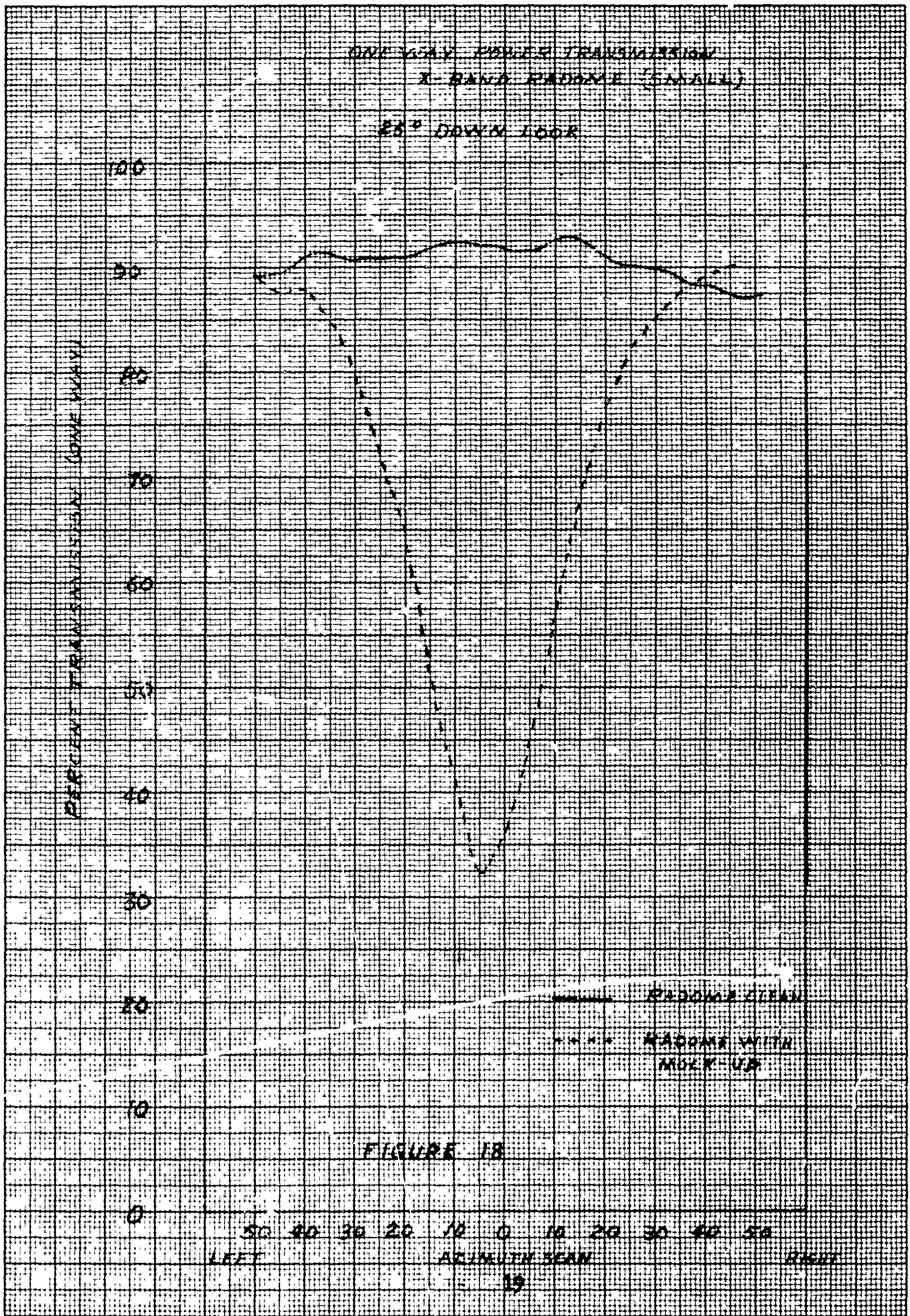


FIGURE 17 H-PLANE PATTERN WITH
RF ABSORBER MATERIAL OVER ANTENNA DISH



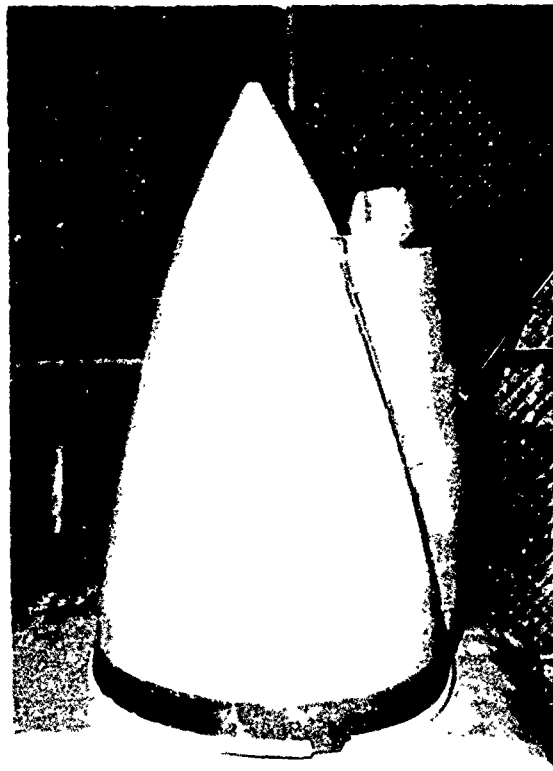


FIGURE 19 SMALL RADOME WITH CYLINDER
MOCK-UP AND WITH FAIRING IN PLACE

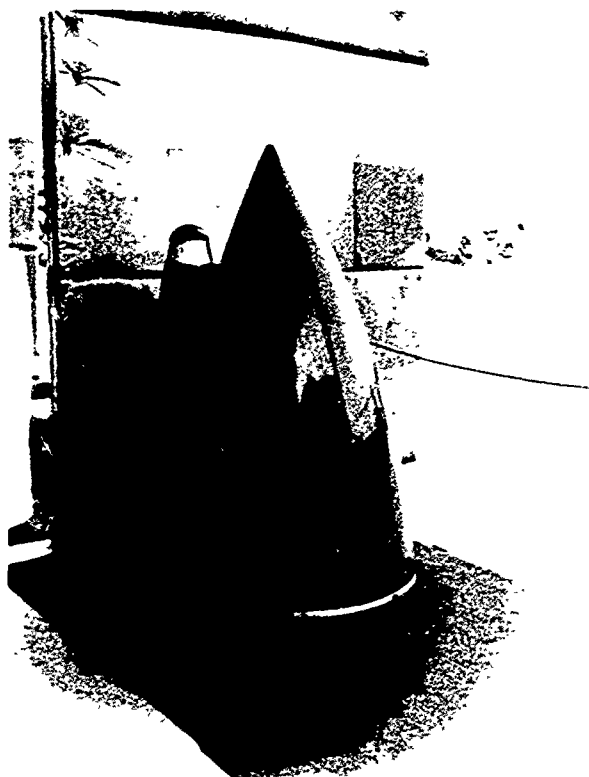


FIGURE 20 RADOME WITH EROSION SHOE OVER
SPRAYED NEOPRENE COATING

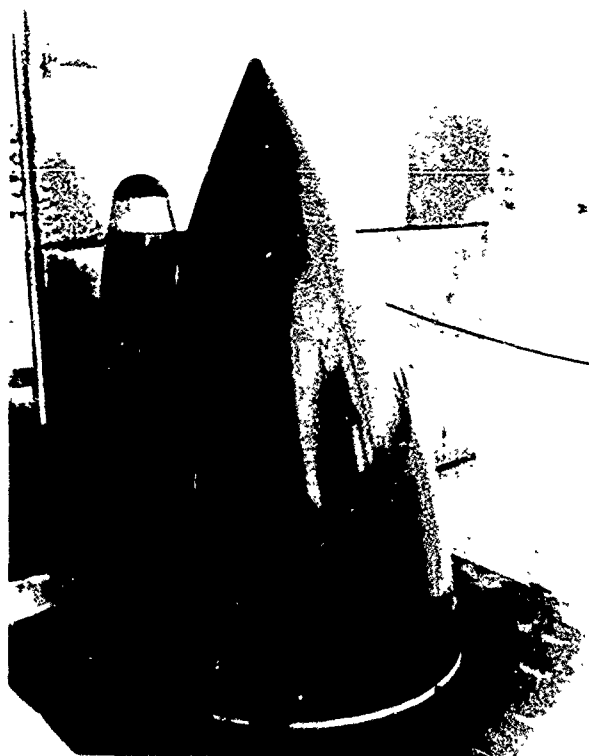


FIGURE 21 RADOME WITH EROSION SHOE
REPLACING THE SPRAYED NEOPRENE COATING

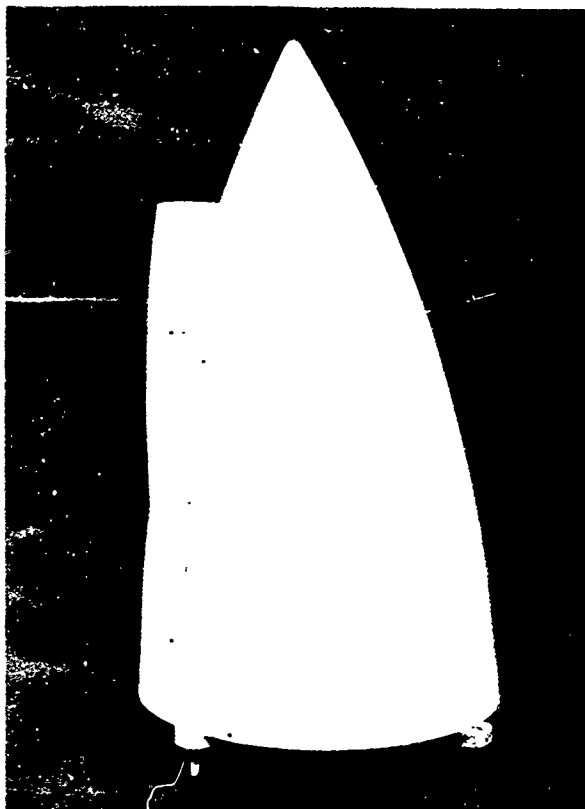


FIGURE 22 RADOME FINISHED WITH
EPOXY WHITE PAINT

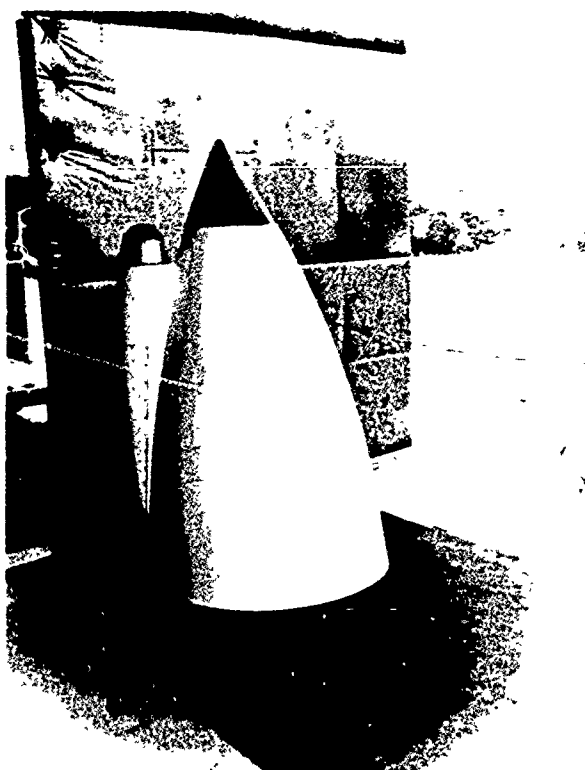


FIGURE 23 RADOME FINISH WITH EPOXY WHITE
PAINT WITH EROSION SHOE IN PLACE

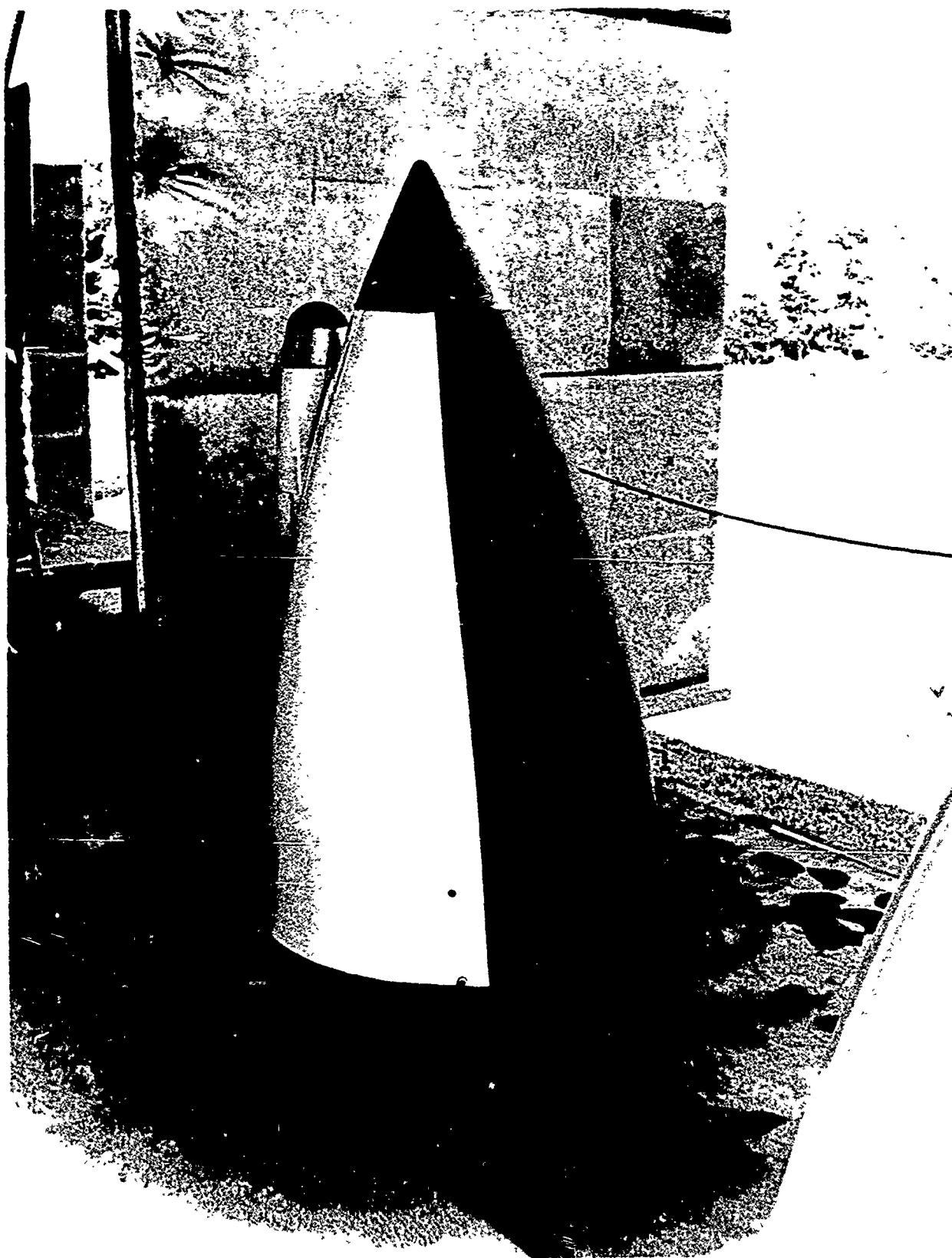


FIGURE 24 RADOME FINISHED WITH EPOXY WHITE PAINT
WITH FLAT BLACK ANTI-GLARE PAINT AND EROSION SHOE INSTALLED

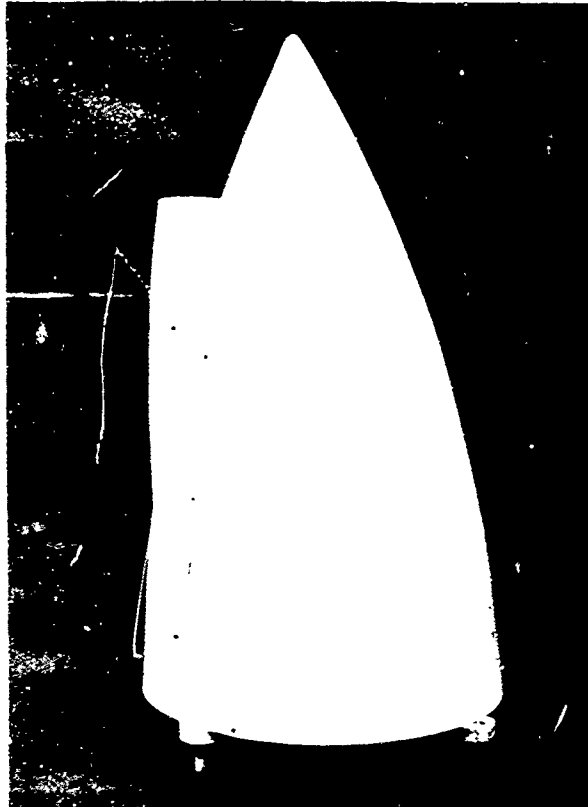


FIGURE 22 RADOME FINISHED WITH
EPOXY WHITE PAINT

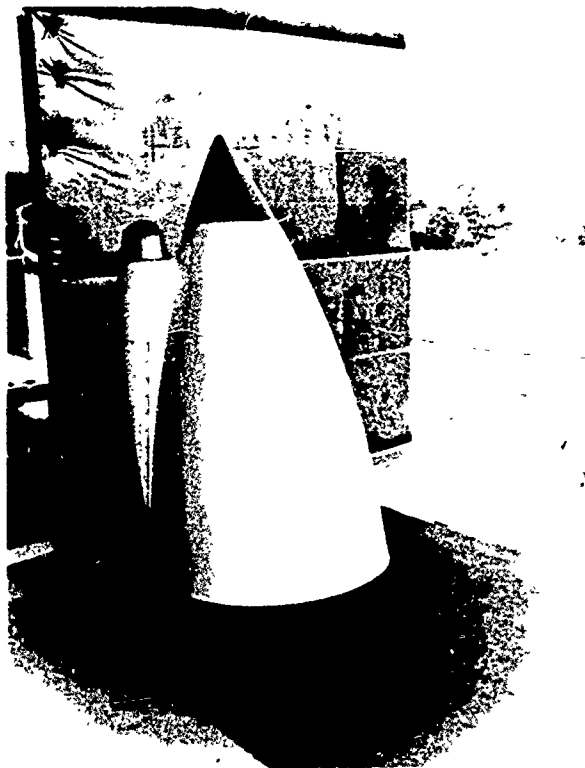


FIGURE 23 RADOME FINISH WITH EPOXY WHITE
PAINT WITH EROSION SHOE IN PLACE

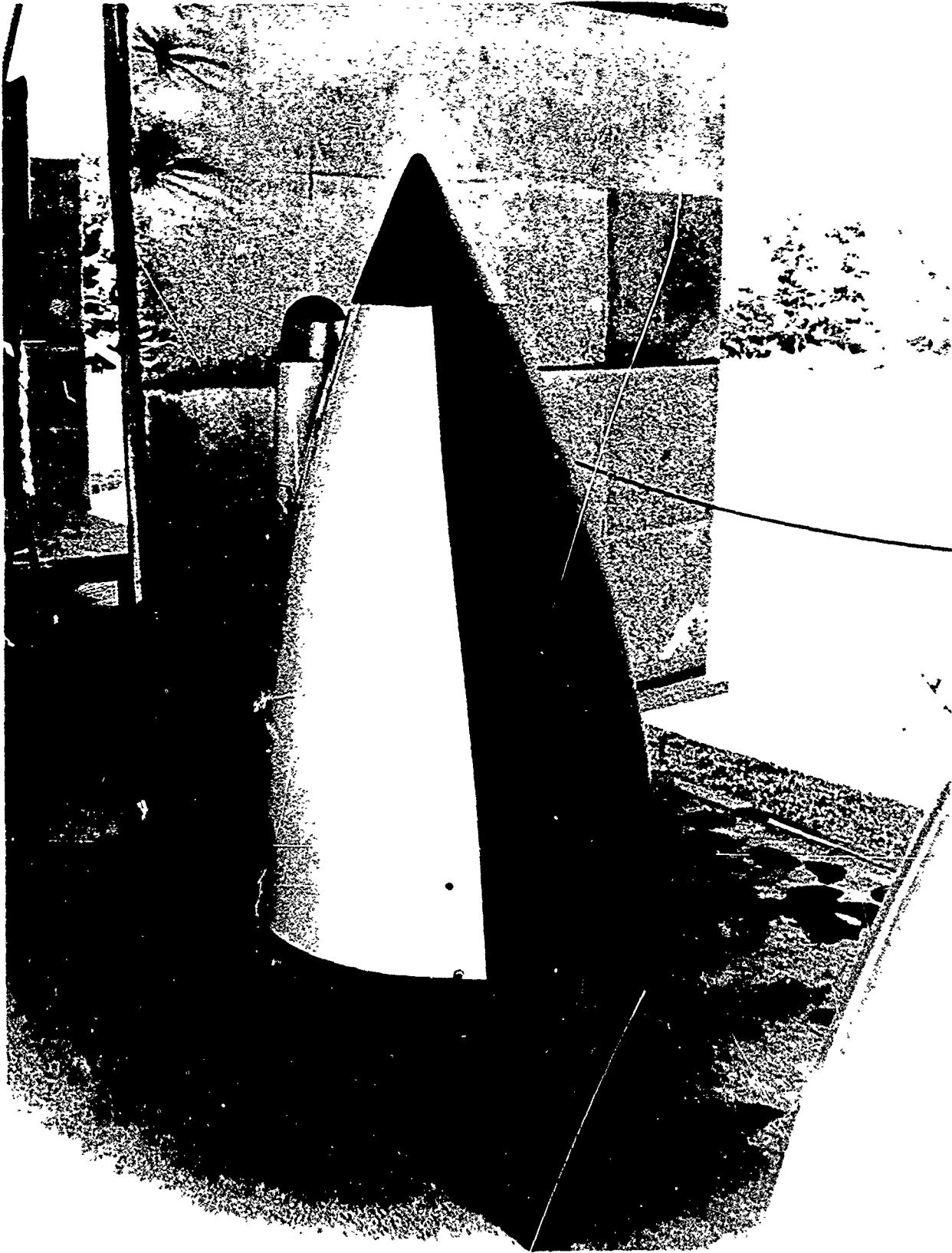


FIGURE 24 RADOME FINISHED WITH EPOXY WHITE PAINT
WITH FLAT BLACK ANTI-GLARE PAINT AND EROSION SHOE INSTALLED

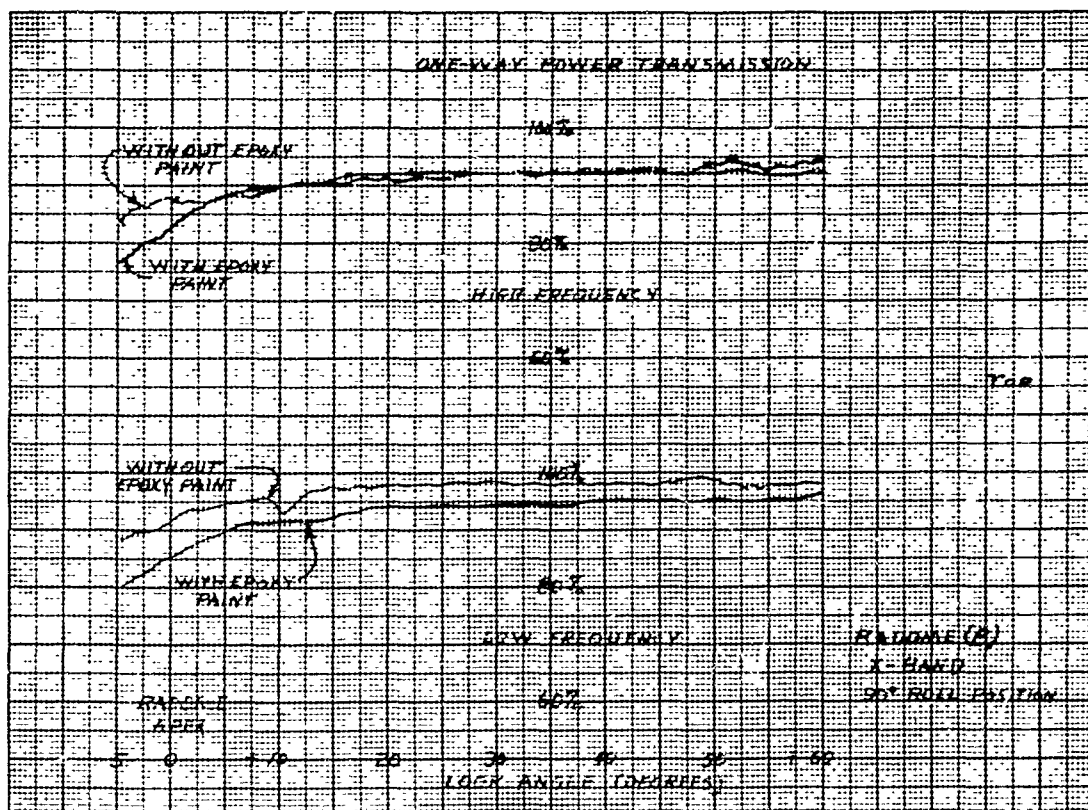


FIGURE 27 TRANSMISSION WITH AND WITHOUT EPOXY PAINT

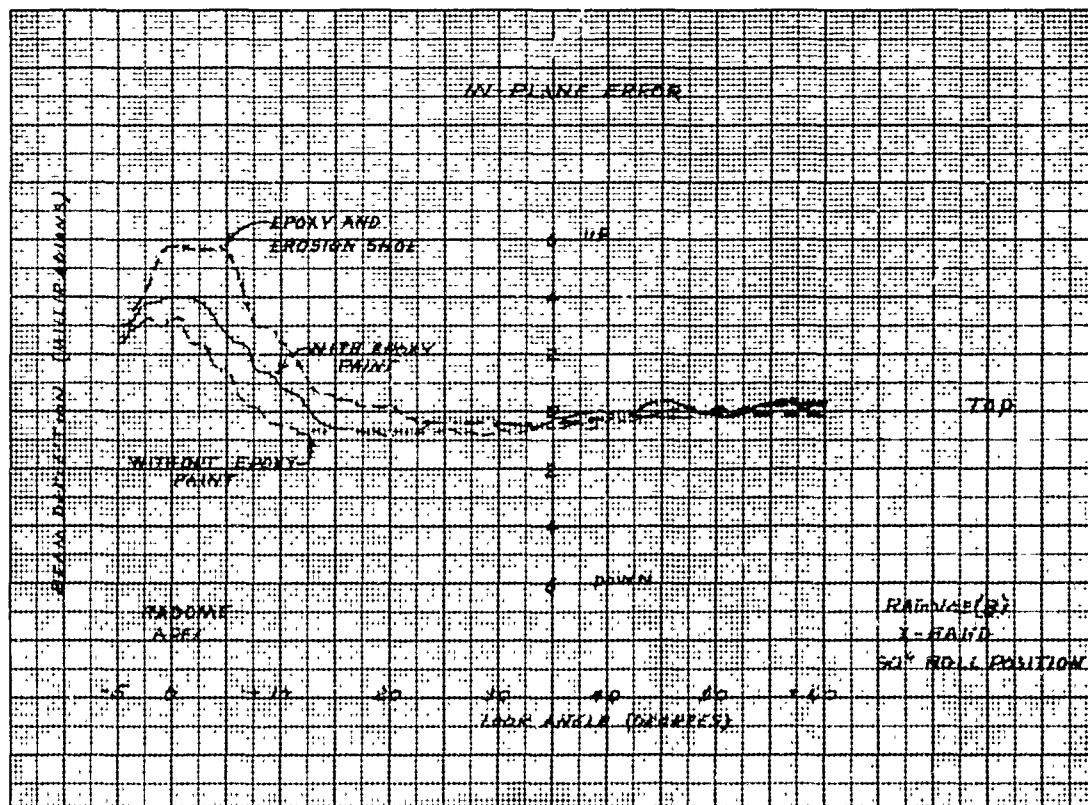


FIGURE 28 IN-PLANE ERROR WITH AND WITHOUT EPOXY PAINT AND WITH EPOXY PAINT WITH EROSION SHOE IN PLACE

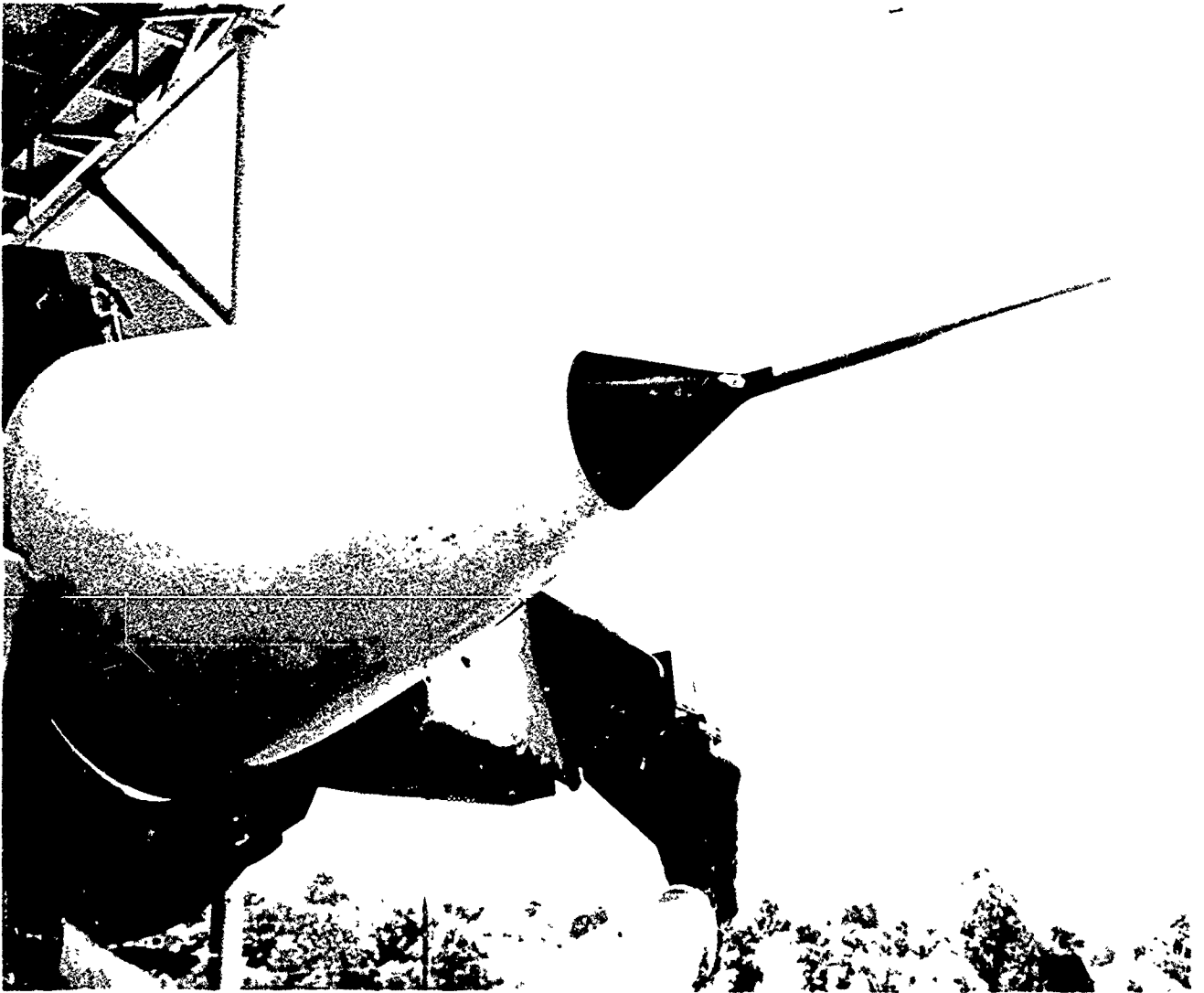


FIGURE 29 RADOME WITH EPOXY WHITE PAINT,
NOSE BOOM AND RAIN EROSION SHOE

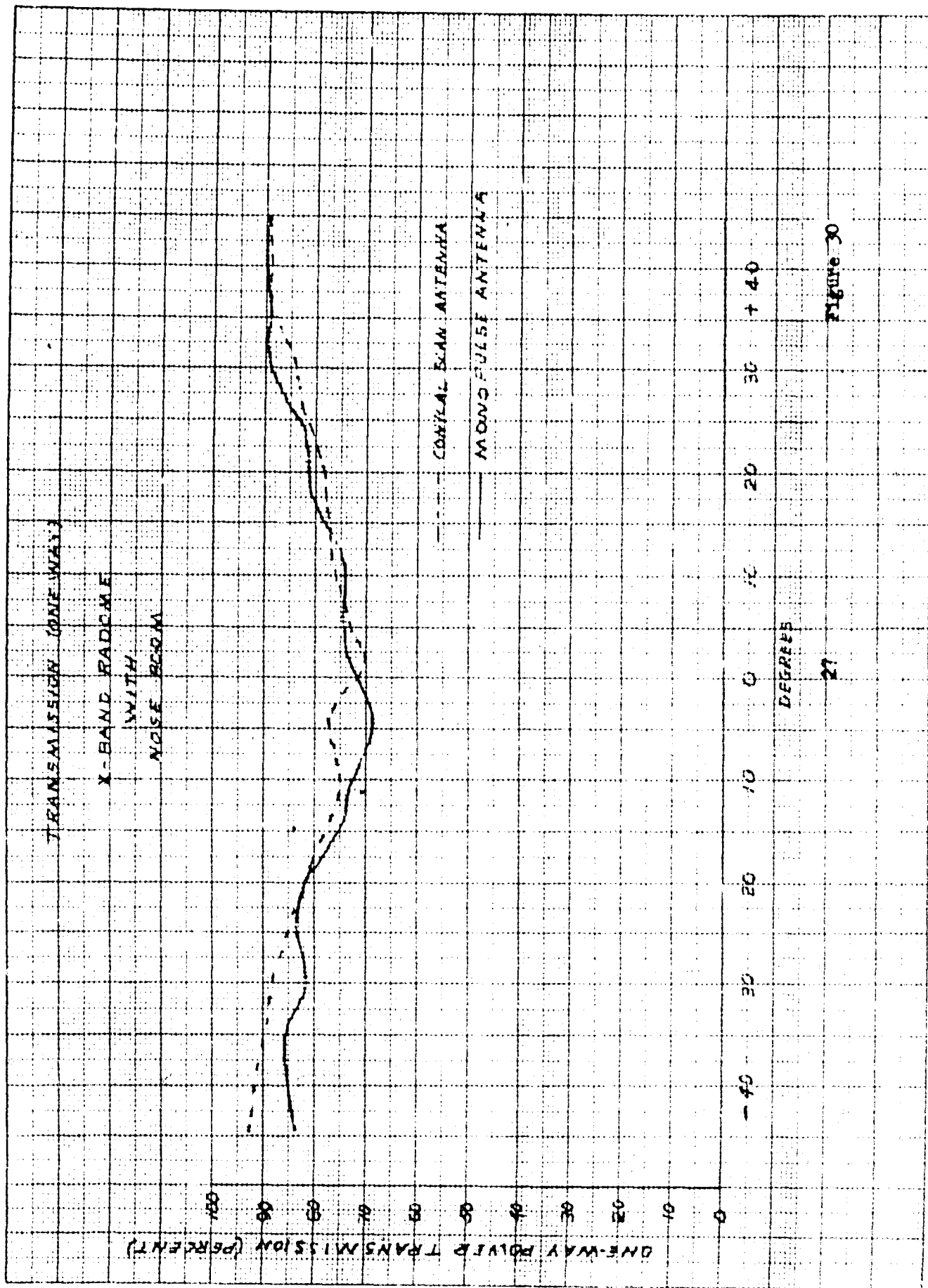
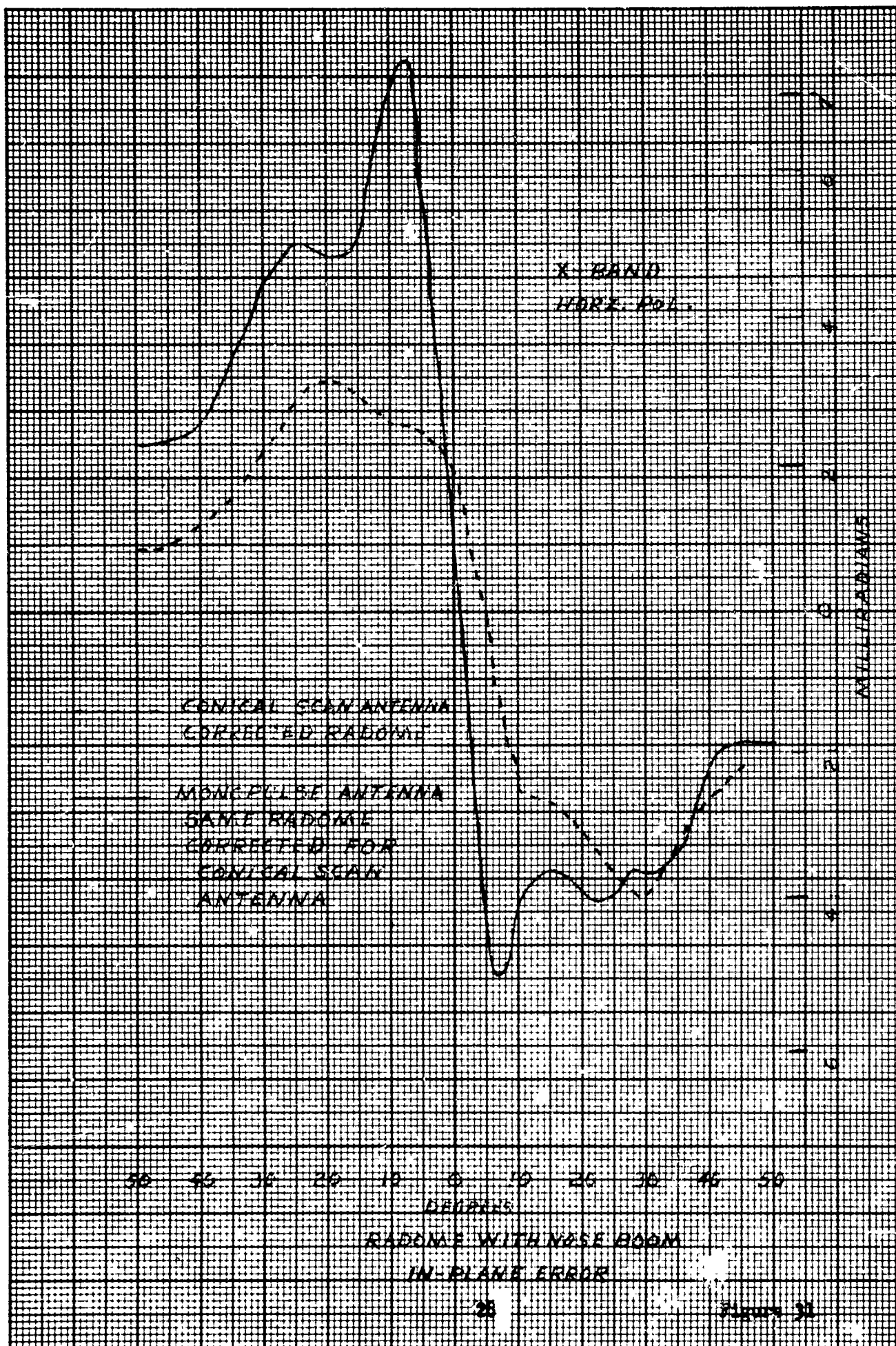


Figure 30



MEASUREMENTS OF DYNAMIC COLLIMATION ERROR

by

D. L. Loyet and J. R. Maurer

Infrared Systems and Guidance Heads Laboratory
HUGHES AIRCRAFT COMPANY
CULVER CITY, CALIFORNIA

INTRODUCTION

The dynamic collimation error test facility developed by Hughes Aircraft Company is used to measure collimation error derivatives and to evaluate the electrical characteristics of sealed guidance units and individual radomes when combined with different microwave systems. Thus, not only radome errors but also those due to the antenna, to the antenna support structure, and to components aft of the antenna can be evaluated.

The test equipment, which is housed in a specially designed anechoic chamber, consists of a mounting fixture for the guidance unit and a movable target. This target can provide linearly, circularly, or elliptically polarized energy and can also move in a linear and/or circular manner while maintaining a constant or variable angle of polarization. The mounting fixture for the guidance unit allows for controlled sweeps in azimuth and/or elevation when the guidance unit is fixed or rolling. The guidance unit and target move in such a way that collimation error derivatives and other electrical characteristics can be evaluated for all typical missile motions.

DEFINITION OF COLLIMATION ERROR

Before discussing the various techniques that have been devised to measure collimation error, we must define the parameters to be determined. Consider a microwave system that has been designed to track a moving target and

provide information on the position and/or rate of change of position of this target. Figure 1 is a vector diagram of such a system consisting of an antenna supported by a gimballed pedestal attached to a base. This base in turn is attached to the aircraft or missile. The mechanical axis of the missile, A, remains fixed at all times as do the axes, C and B, of the orthogonal torquing mechanisms. These three vectors (A, B, and C) define an orthogonal set of axes fixed in the missile that are related to a non-moving coordinate set X, Y, and Z by specified angles. Although the gimballed antenna is attached to the missile, it can scan a prescribed solid angle and track the target. If no electrical or mechanical perturbations are present, the antenna points in the direction defined as LOS, line of sight. However, if any such perturbations are present, the antenna points in the direction of the apparent line of sight, ALOS. The angular separation between LOS and ALOS is the error angle η_r that can be broken into two orthogonal components η_{rc} and η_{ro} . If the LOS azimuth and elevation angles are defined as β_o and β_c , respectively, four error derivatives, k_{oo} , k_{oc} , k_{co} , and k_{cc} can be defined as follows:

$$k_{oo} = \frac{\partial \eta_{ro}}{\partial \beta_o}$$

$$k_{co} = \frac{\partial \eta_{rc}}{\partial \beta_o}$$

$$k_{oc} = \frac{\partial \eta_{ro}}{\partial \beta_c}$$

$$k_{cc} = \frac{\partial \eta_{rc}}{\partial \beta_c}$$

Note that k_{oo} and k_{co} are the derivatives that are usually called "inplane" and "crosstalk" slope, respectively. A more descriptive terminology is

k_{oo} = collimation error derivative

k_{oc} = collimation error cross derivative

k_{co} = collimation crosstalk error derivative

k_{cc} = collimation crosstalk error cross derivative .

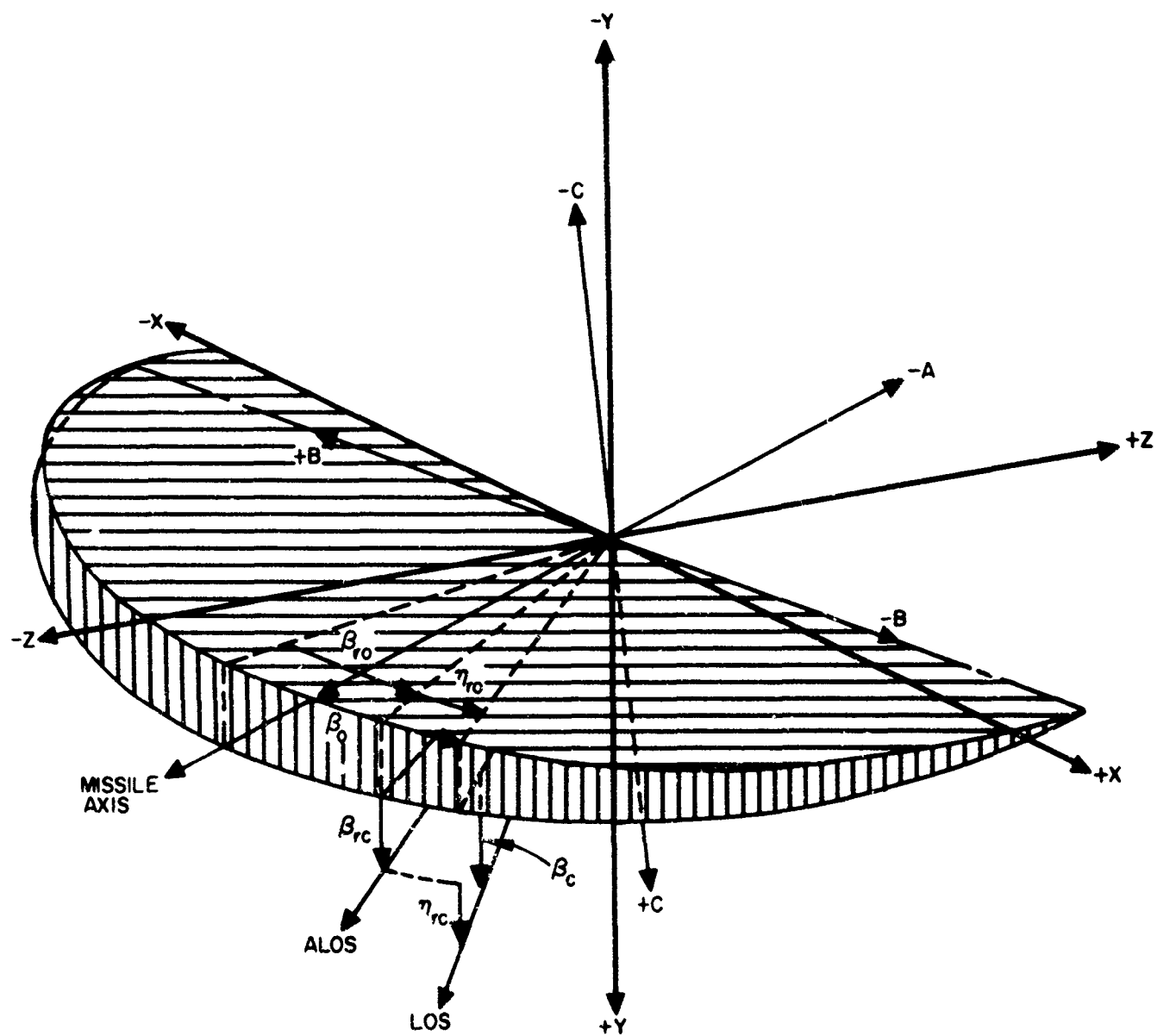


Figure 1. Angles used in describing radome error

FACILITIES FOR MEASURING BORESIGHT ERROR

The measurement of boresight error is based on the assumption that the previously discussed derivatives and error angles are due to reflections within the radome and to refraction through it. Since the radome is thus considered to be the source of boresight error, a facility has been built for determining and, when possible, for reducing the magnitude of this error. A review of the Proceedings of the Electromagnetic Window Symposia reveals that many facilities have been designed for this purpose. Since all of them are essentially similar, a representative facility of this type will be described. The primary requirement is to simulate the environment in which the missile is to operate. Such simulation is usually accomplished by enclosing the target horn and missile mount within an anechoic chamber designed to minimize reflections. However, large antenna systems are usually not evaluated in such a chamber but in out-door facilities designed to reduce reflections to a minimum.

The boresight facility designed and operated at Hughes Aircraft Company consists of an enclosure in the form of a distorted parallelepiped. Each wall is in the form of a pyramid rather than a plane sheet. The dimensions of the chamber are such that any energy that strikes the microwave-absorber lined surfaces is reflected at least three times before it reaches the receiver. An exploded view of this facility is shown in Figure 2. The radome, which is mounted on a pedestal, covers an antenna that simulates the actual unit. The antenna is mounted in such a way that its position remains fixed and is independent of that of the radome. The mount can be used only for azimuth scan. Since the principle of reciprocity is assumed, the antenna can also be operated as a transmitter even if it is designed to be used as a receiver. This particular facility used a transmitting antenna that was tracked by a four-horn null-seeking mechanism moved by a servo system. This null seeker is designed to follow the null and maintain itself on the null. The displacement of the null seeker in both azimuth and elevation is automatically recorded as a function of radome offset angle from the dead-ahead position. This graph gives the inplane (azimuth) and crosstalk (elevation) boresight error angles. With a system such as this, antennas with different polarizations can be evaluated by replacing the tracking antennas.

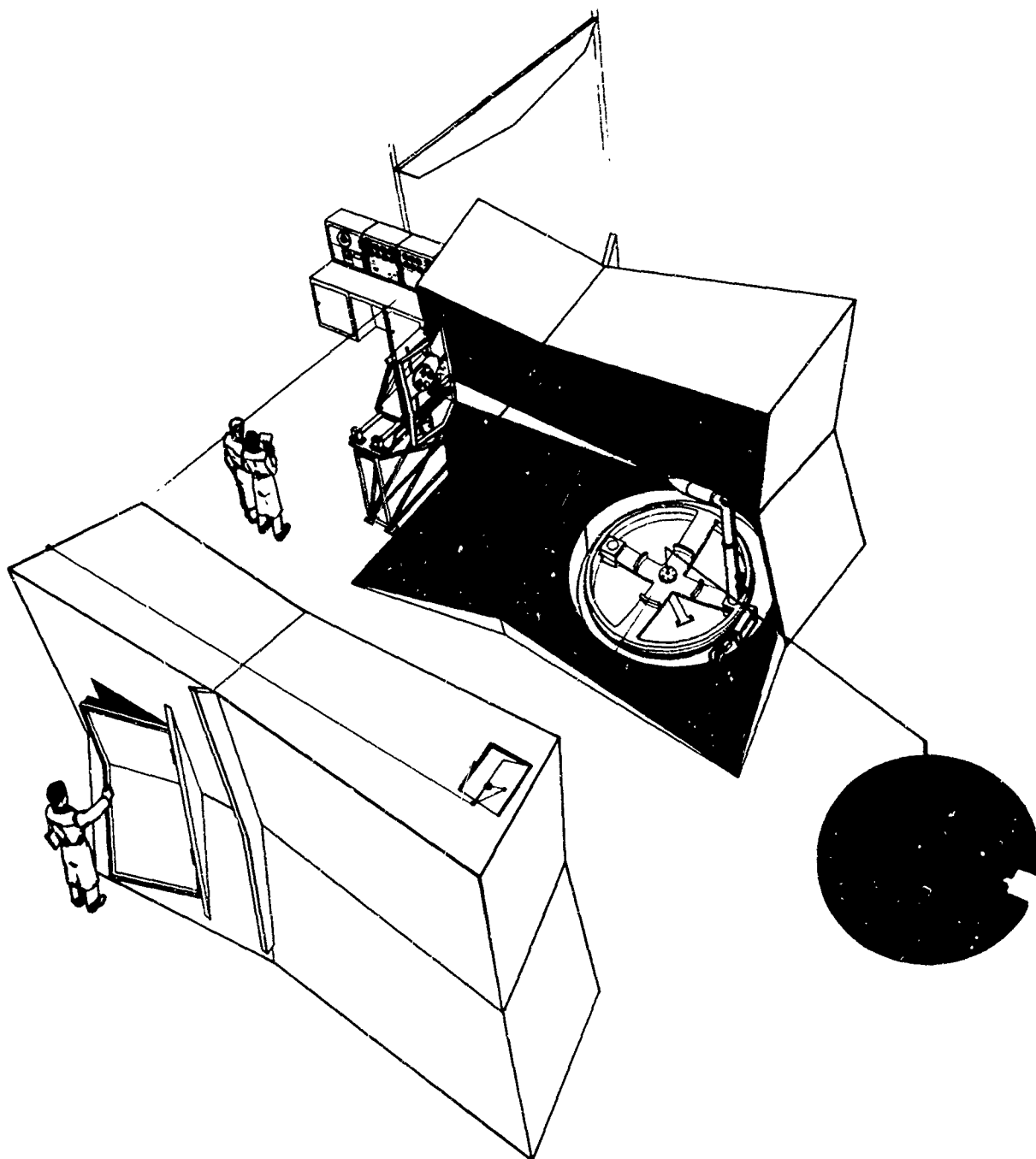


Figure 2. Precision boresight error measuring facility

FACILITY FOR MEASURING COLLIMATION ERROR

Although the boresight error measurement facilities can be used to obtain a quantitative measurement of the angular errors associated with various radomes when tested with a specific antenna, they do not provide data based on these radomes with the actual guidance system. Measurements of the boresight error of the radome alone provide a graphical record of error angles from which the slopes can be determined. Although a boresight system allows the design and quality control of radomes as individual components, equivalent errors introduced by the combination of antenna and missile body in the absence of a radome may be comparable in magnitude to the total error allowable for the complete system, including the radome. Thus a better method must be devised for measuring the errors introduced into the guidance system by the radome, its mounting structure, the antenna, and the components within the radome cavity.

The dynamic collimation error measurement facility at Hughes Aircraft Company is used to evaluate these interacting phenomena with actual guidance systems. The basic equipment, which consists of a mount for the forward missile section, a simulated missile receiver, and a movable target horn, is housed in an anechoic chamber suitable for use at X-band frequencies.

The principal unit in this test facility (shown schematically in Figure 3) is the mount for the forward missile section, which includes the guidance unit under test. This mount allows the forward missile section to be swept in azimuth about the gimbal center of the guidance unit and to be rolled about the longitudinal axis of the missile. The rates of sweep and roll can be controlled independently and continuously over the range of look angles of interest. This mount also allows the missile to be swept in elevation. These independently controlled motions make it possible to conduct several different types of tests. For example, azimuth sweep with the guidance unit at any desired roll and elevation angle, roll sweep with the guidance unit at any azimuth and elevation angle, elevation sweep with the guidance unit at any roll and azimuth angle, and tests in which two or all of these motions take place simultaneously. All typical missile motions can be simulated in this way and the collimation error associated with each kind of motion can be measured.

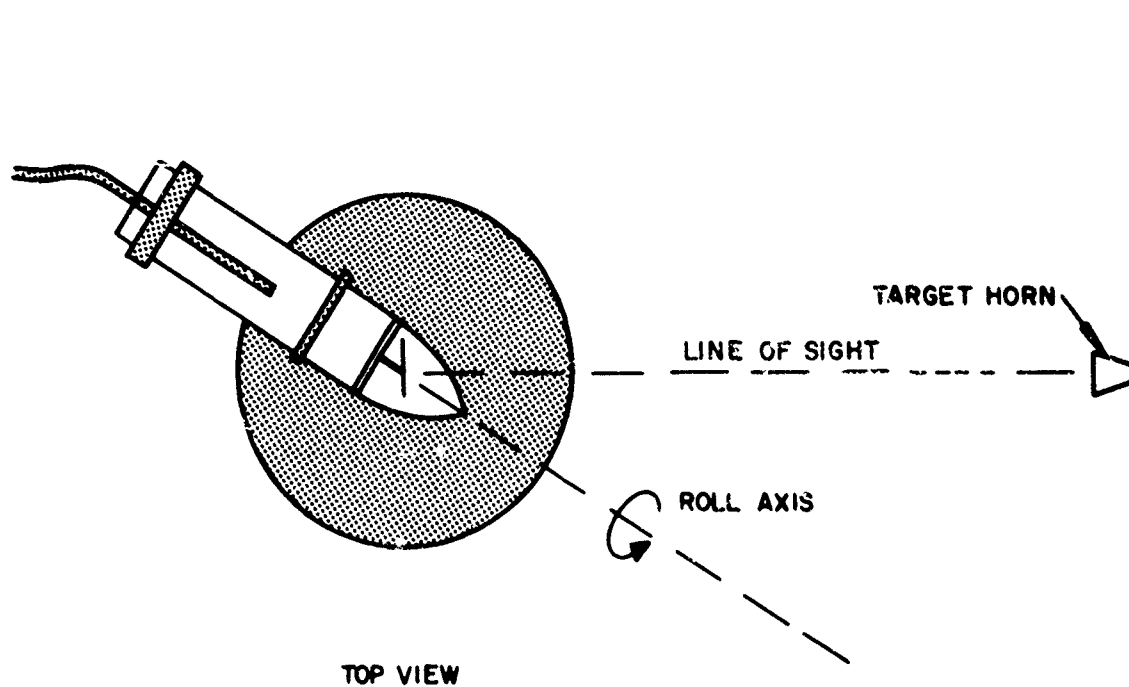
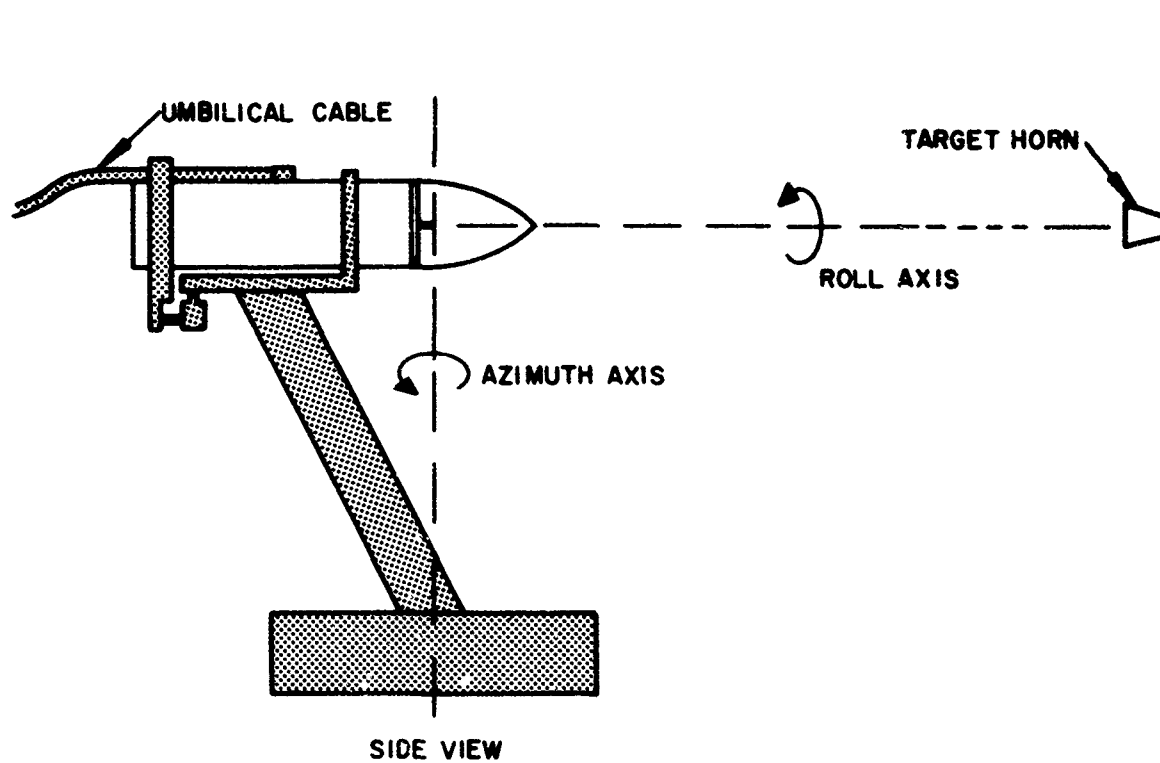


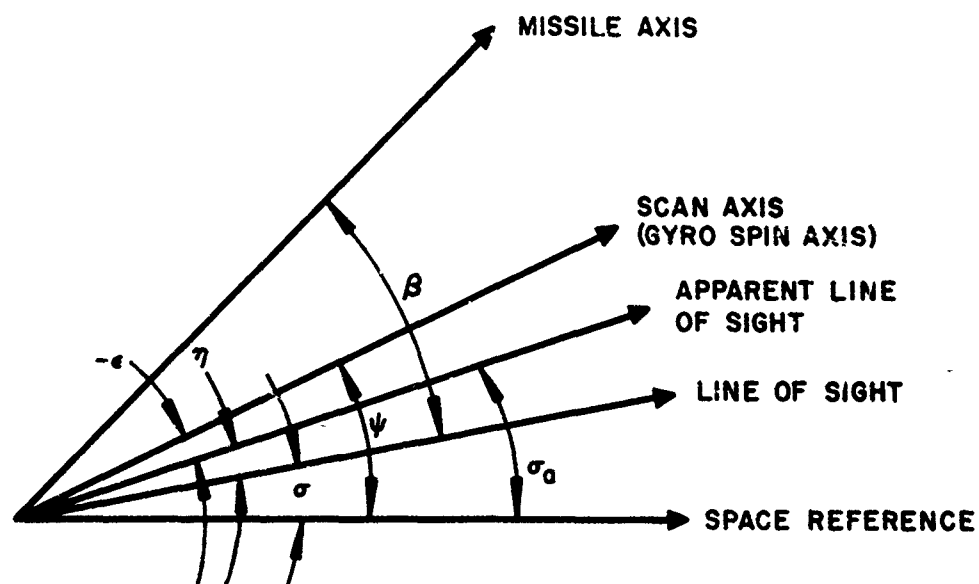
Figure 3. Diagram of mount for forward missile section

The target horn can transmit linearly, circularly, or elliptically polarized energy. The angle of polarization can be controlled by rotating the horn about its axis and by means of a servo it can be made to rotate as the missile rolls. Therefore, during any test the angle of polarization can be either varied or maintained constant. The mount for the target horn also makes it possible for the horn to simultaneously rotate radially or circularly within a ± 1 -degree look angle. In this way additional types of missile motion can be simulated by the motion of the target horn and many of the guidance unit parameters that are usually measured at a facility specifically designed for antennas can be evaluated.

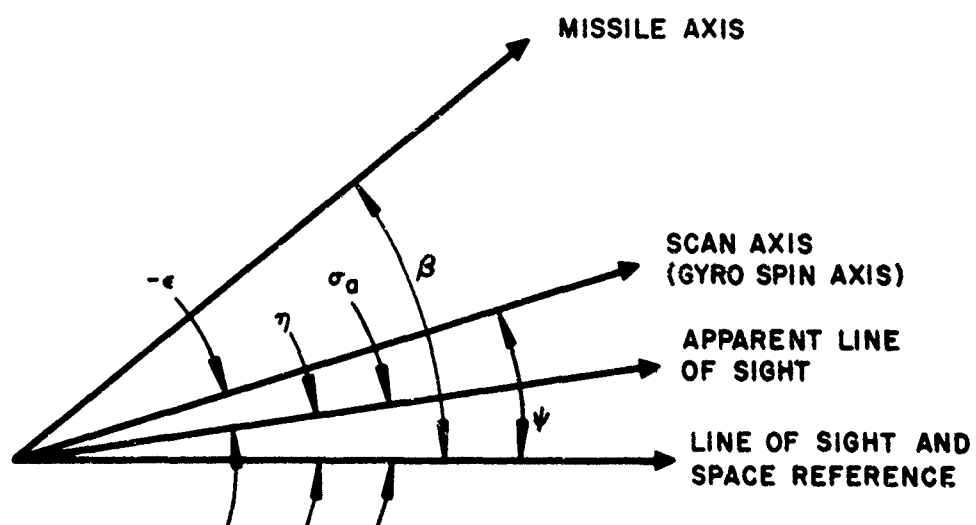
MEASUREMENT OF COLLIMATION ERROR

In measuring collimation error, the parameter of greatest significance is the collimation error derivatives from which the error angle can be derived. These derivatives are the rate of change of the collimation error angle with respect to the angle between the missile axis and the line of sight to the target. The missile angles are identified in Figure 4. The significance of these derivatives is that a large error derivative appears to the guidance unit as an abrupt shift in the position of the target. Large error derivatives will impair the tracking ability of the missile and may cause the missile to become unstable. These derivatives can be computed directly from measurements made at the collimation error facility.

In the basic collimation error test the missile forward section is swept about the guidance unit gimbal center or rolled about its longitudinal axis while the transmitting target horn remains stationary. The tracking loop is in operation during this test and the resulting steering voltages from the pitch and yaw channels are recorded as a function of the azimuth or roll angle. These voltages are recorded as a function of the displacement angle on a magnetic tape that can be fed directly into a digital computer. The computer calculates the collimation error derivatives and the collimation error angle as a function of look or roll angle. The data for the azimuthal sweep are similar to those for inplane and crosstalk errors obtained at the boresight facilities.



STANDARD SYMBOLS



SYSTEM USED IN COLLIMATION ERROR TEST

Figure 4. Definition of terms

The steering voltages result from an apparent rotation of the line of sight. In the collimation facility, the line-of-sight rotation is identical to the apparent line-of-sight rotation produced by the total collimation error due to the combined effects of the radome, antenna, bulkhead, and miscellaneous missile hardware. The steering voltage is a function of the following parameters:

1. Target motion
2. Collimation error
3. Gyro drift
4. Cable torque
5. Bearing friction
6. Torquer unbalance
7. Windage
8. Inertial effects .

Since the target horn remains stationary during the test, the steering voltages are caused by Items 2 through 8 listed above. To determine collimation error, the effects of Items 3 through 8 must be eliminated. Fortunately, since these effects are essentially independent of the rate of motion of the missile, they can be eliminated by recording the steering voltages at two different sweep speeds or roll rates and by finding the difference in the values indicated by the two curves showing steering voltage as a function of look angle. This difference is due to the apparent rotation of the line of sight caused by the collimation errors.

The collimation errors are in turn a function of the following parameters:

1. Look angle
2. Roll reference angle
3. Polarization angle
4. Type of polarization
5. Frequency
6. Signal level
7. Temperature of guidance unit.

The variation in signal level and temperature are negligible at the test facility and the other parameters can be controlled independently. Therefore the effect of each parameter can be investigated separately by keeping the other parameters constant during a given test.

On the basis of the considerations discussed above, an expression for the collimation error derivative can be obtained from the differential equation for

the r-f tracking loop. This derivation is given in Appendix I for the case in which the missile is swept in azimuth at a fixed roll orientation. The resulting expression for this error derivative is Eq. (I-7). The terms on the right-hand side of this equation have been evaluated separately and compared to determine their relative magnitudes.

Typical curves showing the sum of the collimation error derivatives and curves for each of the four separate terms are given in Figures 5 through 9. The data used in preparing these curves were obtained in tests of a 3/4-power-shaped radome having a fineness ratio of two. These data were taken at 0.3-degree increments in the look angle β . They show that the term involving the third derivative of V_s is negligible, and that the second derivative term is also of little importance in most cases. Therefore, an analysis that includes only the first two terms of Eq. (I-6) is all that is needed to determine collimation error derivatives for most systems.

The variation in peak collimation error and boresight error derivative over a narrow frequency band is shown in Figure 10. Although boresight error derivatives are relatively constant, the collimation error derivative varies appreciably because of the various interactions between the components of the guidance unit. An evaluation of system performance based on boresight error derivatives will not provide data that is representative of that for the actual system.

The collimation error cross derivatives (change in error angles in both elevation and azimuth with respect to a change in elevation angle for a fixed offset angle) and the collimation error cross angles can be determined by orienting the missile at a fixed azimuth offset angle and rotating it about its longitudinal axis. This information can also be integrated to determine the magnitude of the components that cause a variation in apparent line of sight that occurs at the missile roll frequency. Another method of evaluating the cross derivatives involves the use of measured data for azimuth sweeps at various elevation angles; conversely, azimuth angle can be varied in discrete steps and sweeps in elevation angle can be evaluated.

The other parameters listed above can be evaluated by keeping all but one parameter fixed and varying the one that is to be determined. For example,

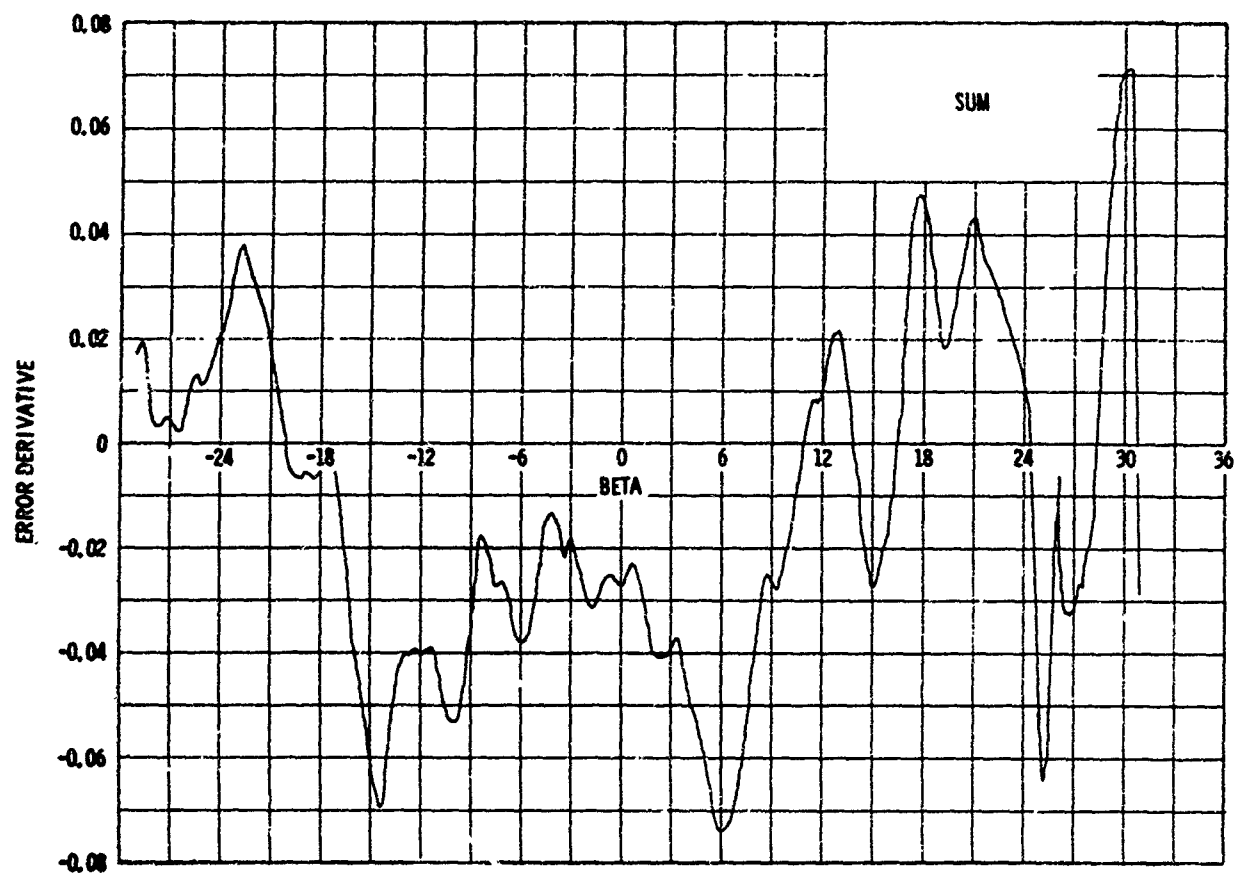


Figure 5. Sum of collimation error derivative terms

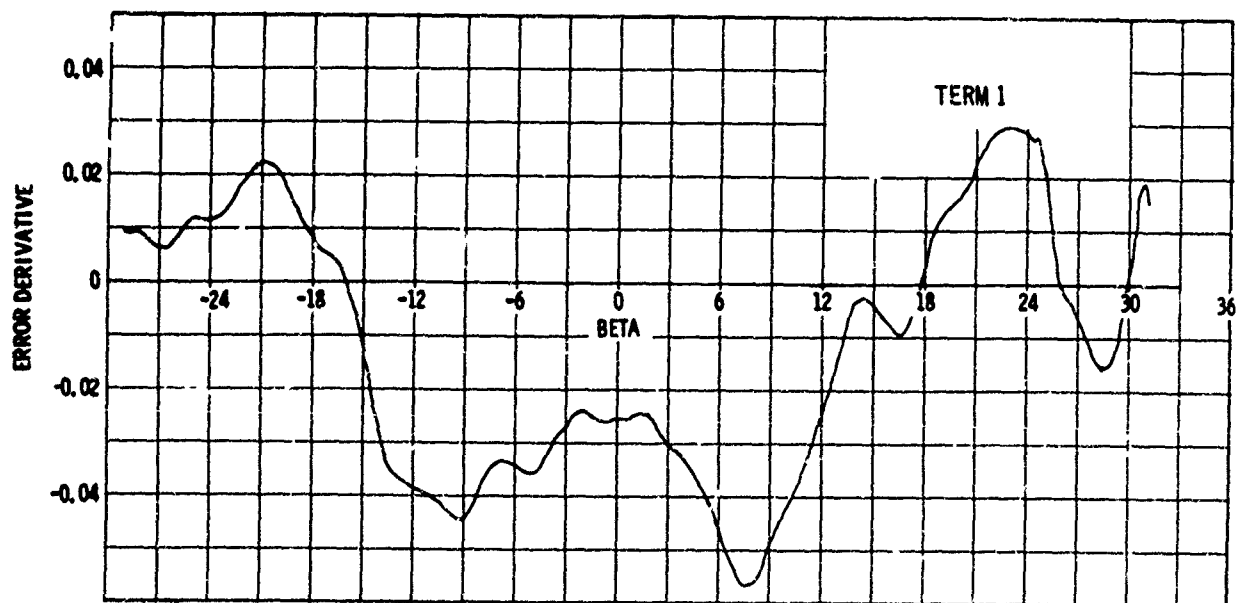


Figure 6. Term 1 of collimation error derivative

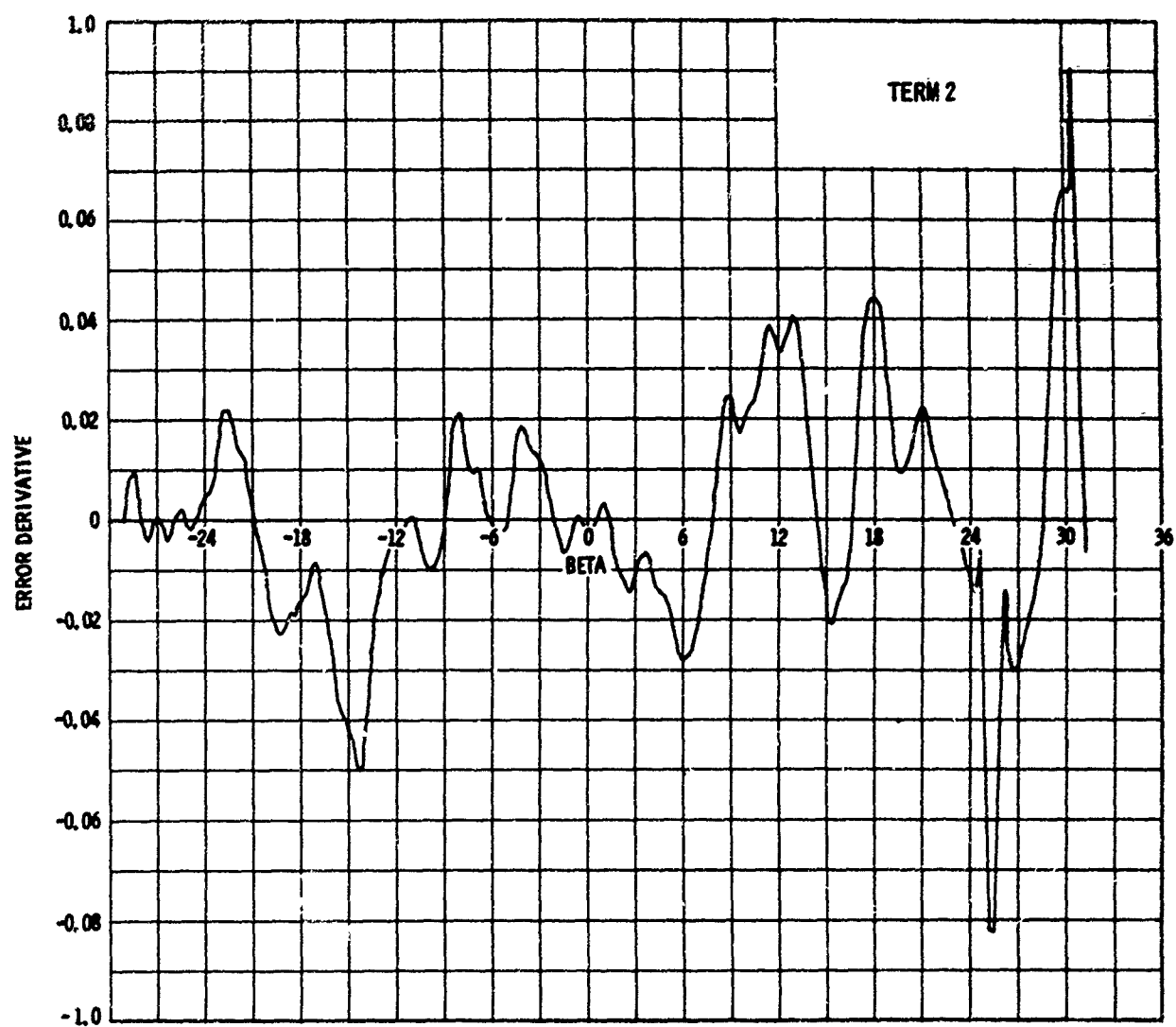


Figure 7. Term 2 of collimation error derivative

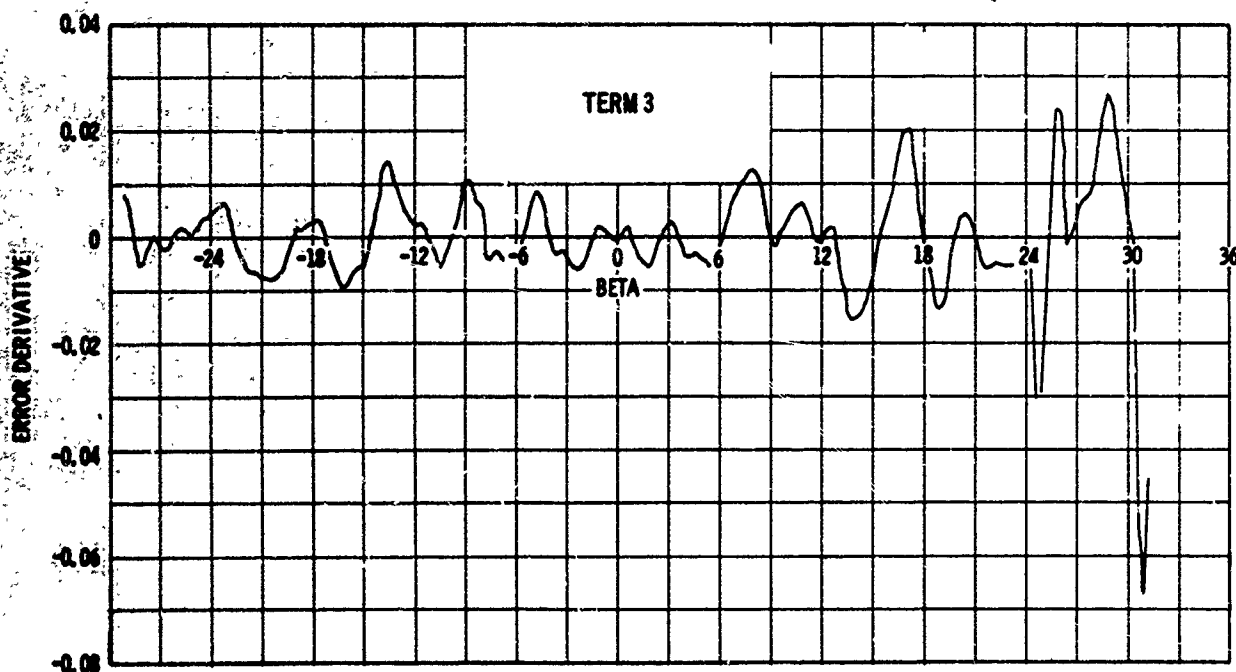


Figure 8. Term 3 of collimation error derivative

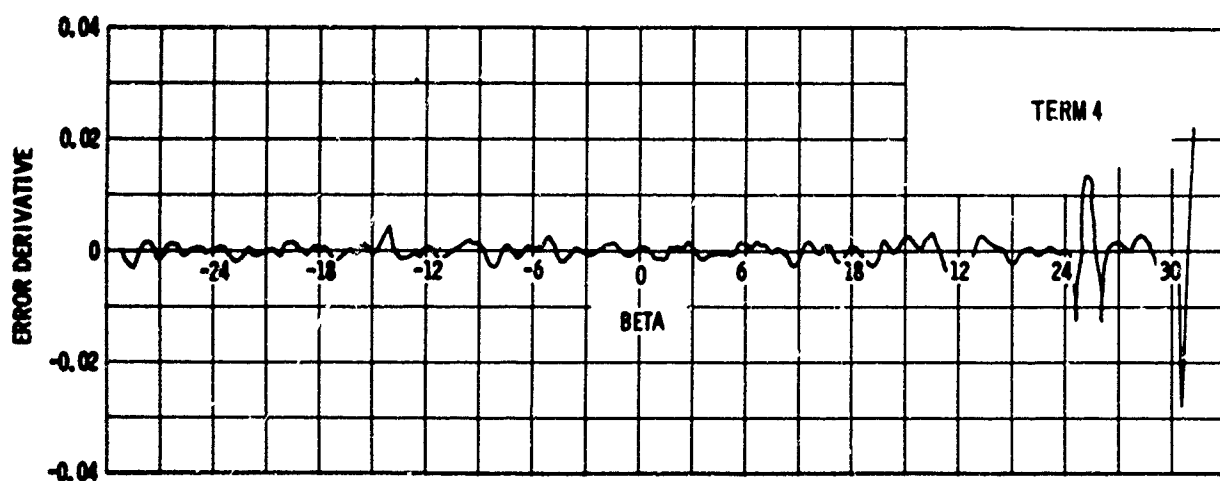


Figure 9. Term 4 of collimation error derivative

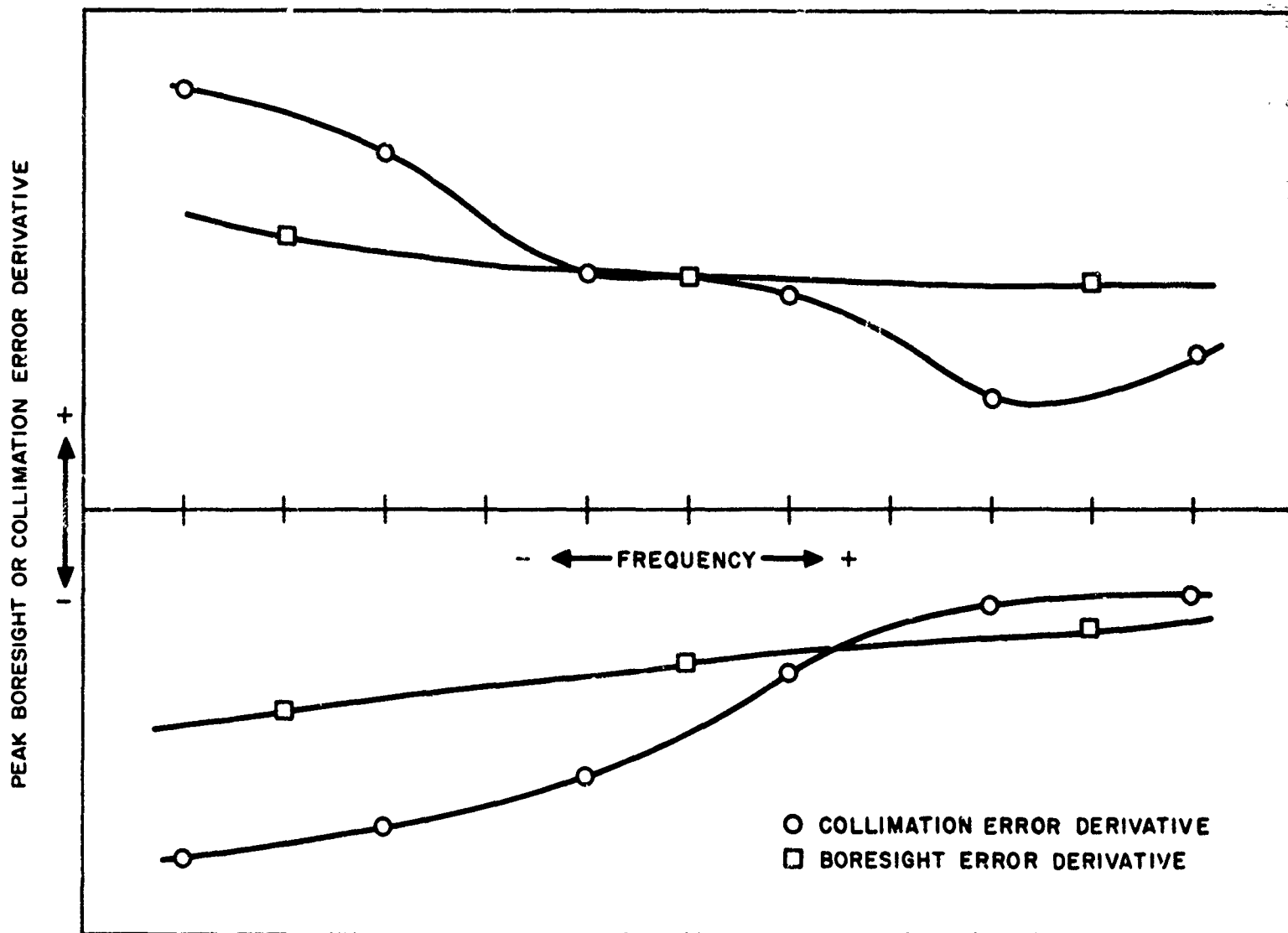


Figure 10. Maximum boresight and collimation errors as a function of missile frequency

the variation in the apparent line-of-sight angle resulting from a change in the angle of incidence of the polarized energy can be measured by rotating the target horn with the missile at any fixed location.

This facility can also be used in measuring antenna patterns and determining the tracking error gain of a monopulse antenna system. Since such a system utilizes the complete guidance unit and a simulated missile receiver, the signal-to-noise ratio can be measured. Radome transmission characteristics can be determined by operating the antenna for which it was designed in the prescribed environment. This facility can also be used for antenna boresighting and for aligning sensing devices such as potentiometers.

CONCLUSIONS

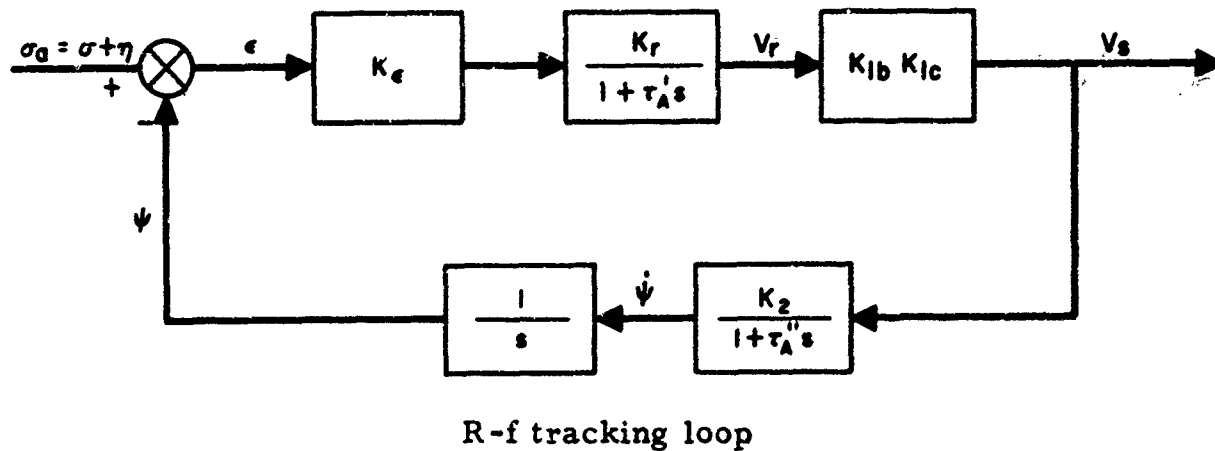
The dynamic collimation error facility provides a means of evaluating the electrical performance of a completely assembled guidance unit and for optimizing the characteristics of the microwave system. This is an essential feature since reliable acceptance criteria must be based on the interactions of radome, antenna, and missile components, not just on the radome itself. In summary, the equipment has the following desirable characteristics.

1. Collimation error derivatives (rather than error angles) are plotted or tabulated directly as a continuous function of line-of-sight orientation.
2. The operation is automatic and requires no precise measurement of small angles.
3. The errors can be averaged automatically over any specified range of offset angle.
4. The equipment can be used to evaluate cross derivatives.
5. Antenna characteristics can be determined in the same facility used in evaluating the guidance unit.
6. This facility is available for assembly operations that usually require outdoor ranges or precision fixtures such as those for antenna boresighting.

APPENDIX I

COLLIMATION ERROR DERIVATIVE

The collimation error derivative is expressed in terms of the steering voltage and the parameters of the r-f tracking loop by the following derivation for the case in which the look angle β is varied.



In the closed-loop transfer function

$$\frac{V_s(s)}{\sigma_a(s)} = \frac{K_1 s(1 + \tau_A'' s)}{s(1 + \tau_A' s)(1 + \tau_A'' s) + K_1 K_2} \quad (I-1)$$

where

V_r = receiver output voltage

V_s = steering signal voltage

K_e = tracking error gain

- K_r = receiver gain
 K_{1b} = torquer control amplifier gain
 K_{1c} = sampling resistor responsivity
 K_2 = tracking system responsivity
 $\tau_A = 1/K_1 K_2$ = tracking system time constant
 τ'_A = receiver output filter time constant
 τ''_A = hysteresis clutch time constant
 $K_i = K_e K_r K_{1b} K_{1c}$ = open-loop gain .

Solving for $\sigma_a(s)$, we obtain

$$\sigma_a(s) = \frac{s(1 + \tau'_A s)(1 + \tau''_A s) + K_1 K_2}{K_1 s(1 + \tau''_A s)} V_s(s) . \quad (I-2)$$

The corresponding differential equation is

$$\dot{\sigma}_a + \tau''_A \ddot{\sigma}_a = K_2 V_s + \frac{1}{K_1} \dot{V}_s + \frac{\tau'_A + \tau''_A}{K_1} \ddot{V}_s + \frac{\tau'_A \tau''_A}{K_1} \dddot{V}_s . \quad (I-3)$$

In the collimation error test, the target is stationary at the space reference. Therefore the value of sigma is zero and the input to the tracking loop is $\sigma_a = \eta$.

Also, since β is the only parameter that is varied in this test,

$$\dot{\eta} = \frac{\partial \eta}{\partial \beta} \dot{\beta} .$$

Making these substitutions yields

$$\dot{\beta} \frac{\partial \eta}{\partial \beta} + \tau''_A \ddot{\eta} = K_2 V_s + \frac{1}{K_1} \dot{V}_s + \frac{\tau'_A \tau''_A}{K_1} \ddot{V}_s + \frac{\tau'_A \tau''_A}{K_1} \dddot{V}_s + C . \quad (I-4)$$

The constant term is added in order to account for gyro drift and other static effects. This term is eliminated by using two different sweep speeds, $\dot{\beta}_1$ and $\dot{\beta}_2$, and taking the difference between these equations on the assumption that

$$\frac{\partial \eta}{\partial \beta} = \left(\frac{\partial \eta}{\partial \beta} \right)_1 = \left(\frac{\partial \eta}{\partial \beta} \right)_2 \quad (I-5)$$

The resulting equation is

$$\begin{aligned} \frac{\partial \eta}{\partial \beta} + \frac{\tau_A'}{\dot{\beta}_2 - \dot{\beta}_1} (\ddot{\eta}_2 - \ddot{\eta}_1) = \frac{1}{\dot{\beta}_2 - \dot{\beta}_1} \left[K_2(V_{s2} - V_{s1}) + \frac{1}{K_1} (\dot{V}_{s2} - \dot{V}_{s1}) \right. \\ \left. + \frac{\tau_A' + \tau_A''}{K_1} (\ddot{V}_{s2} - \ddot{V}_{s1}) + \frac{\tau_A' \tau_A''}{K_1} (\ddot{V}_{s2} - \ddot{V}_{s1}) \right] \quad (I-6) \end{aligned}$$

In the second term on the left of Eq. (I-6), typical values for the parameters are $\tau_A'' = 0.02$ sec, $\dot{\beta}_2 = 5$ deg/sec, and $\dot{\beta}_1 = 2$ deg/sec. Therefore

$$\frac{\tau_A''}{\dot{\beta}_2 - \dot{\beta}_1} (\ddot{\eta}_2 - \ddot{\eta}_1) = 0.0066 (\ddot{\eta}_2 - \ddot{\eta}_1) .$$

It has also been shown from boresight error data that in general $\ddot{\eta}$ is less than $0.1\dot{\eta}$. Therefore this term is less than 0.066 percent of the collimation error derivative and can be neglected. We therefore obtain the following expression for the collimation error derivative.

$$\frac{\partial \eta}{\partial \beta} = \frac{K_2}{\dot{\beta}_2 - \dot{\beta}_1} (V_{s2} - V_{s1}) \quad (I-7)$$

$$+ \frac{1}{K_1 (\dot{\beta}_2 - \dot{\beta}_1)} (\dot{V}_{s2} - \dot{V}_{s1})$$

$$+ \frac{\tau'_A + \tau''_A}{K_1 (\dot{\beta}_2 - \dot{\beta}_1)} (\ddot{V}_{s2} - \ddot{V}_{s1})$$

$$+ \frac{\tau'_A \tau''_A}{K_1 (\dot{\beta}_2 - \dot{\beta}_1)} (\ddot{\ddot{V}}_{s2} - \ddot{\ddot{V}}_{s1}) \quad .$$

A Technique for Electrical Evaluation of Electromagnetic Window and Radome Shapes

MAY 1964

Prepared by:
FORREST L. COLING
Consulting Engineer

To be presented at
OSU-RTD Electromagnetic Window Symposium
in Columbus, Ohio
3-5 June, 1964

TECHNIQUES FOR ELECTRICAL EVALUATION OF ELECTROMAGNETIC WINDOW AND RADOME SHAPES

by
Forrest L. Coling
Budco Engineering Company
Torrance, California

I. SUMMARY

This paper presents the electrical evaluation of electromagnetic window and radome shapes including shape definition, cross section, and intersection parameters. Computer studies can be made that will determine electrical design and electrical performance data when such techniques are available that can handle general symmetrical and non-symmetrical shapes.

II. INTRODUCTION

The technique for electrical evaluation of electromagnetic windows and radome shapes used by some radome designers involves the use of radial planes as shown in figure 1 for defining three-dimensional general radome shapes. This technique handles all types of symmetrical and unsymmetrical radome shapes. In order to make electrical design and performance studies on the computer, a technique is required that will define the electromagnetic window or radome shape. A variety of shapes have been studied by radome designers in the past. The aerodynamicist prefers a .75 power series shape because of minimum pressure drag at high supersonic speeds. The structural designer prefers a cylindrical shape because of superior mechanical properties. The thermodynamicist prefers a spherical shape because of superior thermal properties. The electrical designer prefers the hemisphere shape because of its superior electrical properties. It is obvious that compromise must be made in the shape in order to design a radome. It is also obvious that performance studies should be made on a variety of shapes in order to select a shape for a specified vehicle.

III. Typical Shapes

The purpose of this section is to describe techniques for use in electrical evaluation of shapes on digital computers.

A number of different shapes have been investigated for radome use. Some of the classes of shapes have been: elliptical, ogive, hemispherical, logarithmic and equiangular spirals, power series, parabolic, and others. These classes of shapes are defined in other literature, and some of them are shown in figure 2. A symmetrical or circle of revolution radome can be described by one radial plane equation. Some examples of this type of shapes are: hemisphere, ogive, cone, and other power shapes. These specific type of shapes simplify the amount of time required to prepare a computer study and also reduces the computer time considerably.

IV. Shape Definition

A technique used to describe a general radome shape for computer studies employs the radial plane definition as shown in figure 3. This type of definition uses at least 4 radial planes per quadrant at any arbitrary cross sectional cut. Each radial plane is equally spaced and emanates from the center line of the radome. It starts at the point of intersection of the radome center line and the radome nose, and extends aft to a point of shape discontinuity or to the end of the radome. A typical cross section is shown in figure 3C with 9 radial planes. The figure shows a radome cross section where upper and lower halves are non-symmetrical, while the right and left halves are symmetrical. Such a radome could be studied on the right side saving half of the computations. A symmetrical radome would have all radial planes equal and thus could be described by one equation. Each radial plane (r) will be described by a form of the general shape equation:

$$(1) \quad r = Jy + K \pm \sqrt{Ly^2 + My + N}$$

Other electromagnetic windows in this general class are defined similar to the one just described. Flat windows can be described in two dimension as a special case.

VII. CONCLUSIONS

Electrical evaluation of radome shapes will provide data that can be used to influence preliminary design approaches, estimates of design time required to study alternate shapes, provide data for inputs to proposal programs, provide a method for obtaining data on alternate design approaches for a vehicle, provide a means for obtaining design and performance data for many design studies, save design time by studying many shapes on the computer as opposed to empirical (test) approach on fabricated prototype parts. Comparing data for one radome shape with another primarily shows a change in the magnitude of the incidence angle discontinuity across the radome. Large incidence angles are common to sharp pointed shapes such as cones. Large incidence angles cause high losses in electrical performance. This results in a decrease in transmission and an increase in reflection and discontinuity in the phase front.

This general shape equation is developed from the general expression for a second degree curve:

$$(2) \quad Ay^2 + Byr + Cr^2 + Dy + Er = 0$$

Solving (2) by the quadratic equation and by substitution of coefficients you can obtain each term of (1). It is desirable to employ a method that will handle all types of three-dimensional shapes to minimize design and development time and simplify computer studies.

One technique that is employed by some radome designers when using the general shape equation (1) is by specifying the radome shape with three points and two slopes as shown in figure 1. This technique requires a detailed drawing of the radome shape, as shown in figure 2. Points and slopes are developed from a drawing of the shape and calculations are made to determine the equation (1) that describes the shape. It would take one equation or radial plane (1) to describe a radome shape that has properties of symmetry, and a continuous contour from nose to base. A non-symmetrical radome with a continuous contour from nose to base would require nine equations to describe the nine radial planes as shown in figure 3A. The radome in figure 3B, for a non-symmetrical type, would require 18 equations to describe each radial plane. A non-symmetrical radome with four sections to each radial plane would require 36 equations to describe. A computer program with the capacity for 36 equations would seem to be quite adequate for analyzing most radome shapes.

V. Computer Use

Setting up a computer program to electrically evaluate radome shapes requires other component parts in addition to a shape definition method. Other components of a geometry program include intersection of ray and radome; calculations of incidence angle, polarizing angle, and surface normal; and an iteration procedure. Data obtained from such a geometry program can be used for a radome design or performance study. A typical computer program is shown in figure 4. The design or performance program may be for a boresight error or a transmission study.

VI. Electromagnetic Window Shapes

It is also desirable to make electrical design and performance studies of electromagnetic window shapes on computers. This requires a shape definition program for electromagnetic windows. It is not easy to develop a technique for defining all possible electromagnetic window shapes. The electromagnetic windows might be located on an ogive, cone, cylinder, frustrum, hemisphere, or other shapes. An example of an electromagnetic window shape would be one as shown in figure 5 where it is located on an ogive. To illustrate a method for describing electromagnetic windows, let's consider the two types illustrated in figure 5. In order to describe analytically the geometrical shape of these electromagnetic windows, we define the ogive shape as previously described and the window by means of a set of points P (X, Y, Z) such that $F(X, Y, Z) = 0$. Where

$$0 \leq z_1 \leq z \leq z_2 \leq C$$

$$\rho = \sqrt{x^2 + y^2}$$

$$0 \leq \rho_1 \leq \rho \leq \rho_2$$

$$\theta_1 \leq \theta \leq \theta_2$$

$$0 \leq \theta_1$$

$$\theta_2 \leq 2\pi$$

Window B in figure 5 can be defined as the set of points P (X, Y, Z) such that $F(X, Y, Z) = 0$

Where:

$$0 \leq z_1 \leq z \leq z_2 \leq C$$

$$B \leq y_1 \leq y \leq y_2 \leq B$$

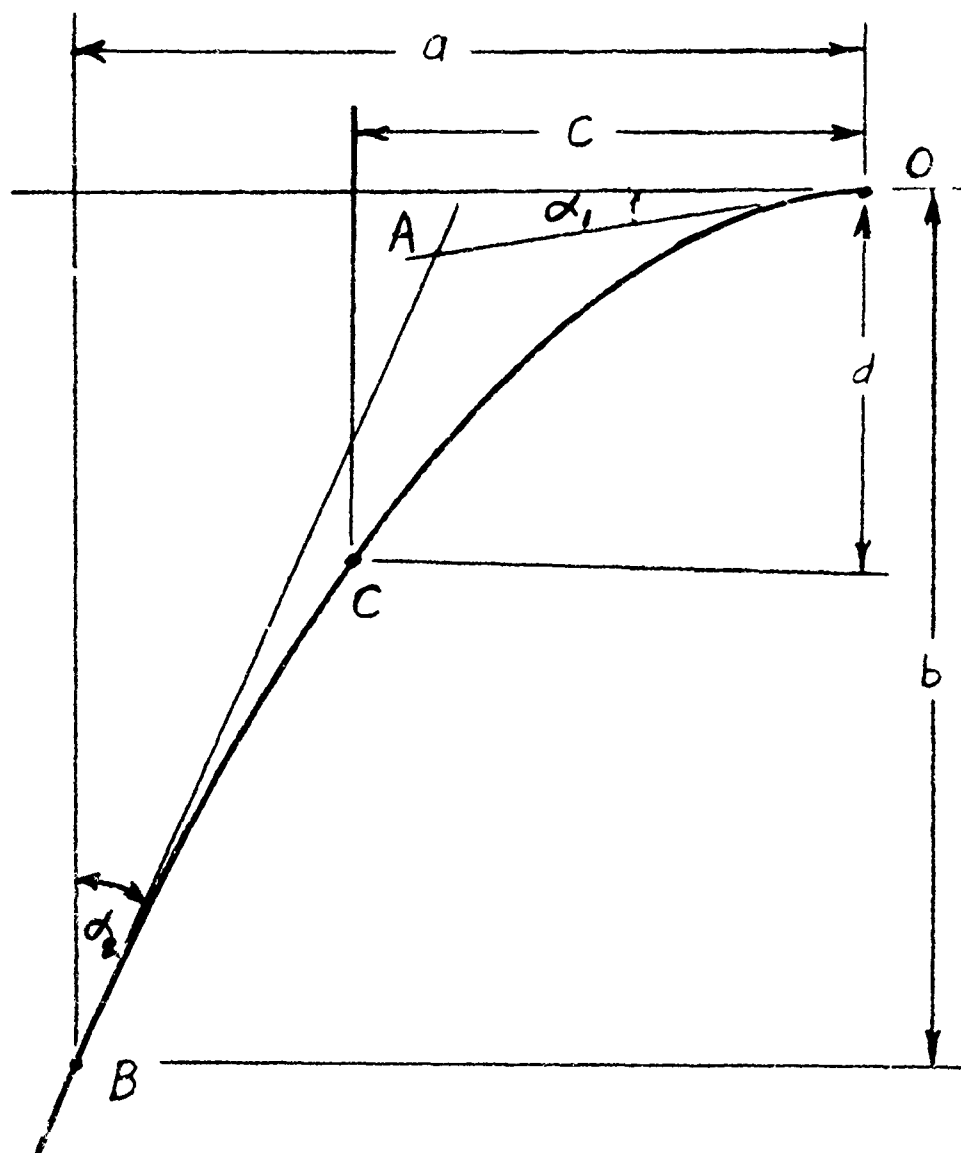
P (X, Y, Z) are in quadrant I, Points B and C are in the ogive definition.

Other electromagnetic windows in this general class are defined similar to the one just described. Flat windows can be described in two dimension as a special case.

VII. CONCLUSIONS

Electrical evaluation of radome shapes will provide data that can be used to influence preliminary design approaches, estimates of design time required to study alternate shapes, provide data for inputs to proposal programs, provide a method for obtaining data on alternate design approaches for a vehicle, provide a means for obtaining design and performance data for many design studies, save design time by studying many shapes on the computer as opposed to empirical (test) approach on fabricated prototype parts. Comparing data for one radome shape with another primarily shows a change in the magnitude of the incidence angle discontinuity across the radome. Large incidence angles are common to sharp pointed shapes such as cones. Large incidence angles cause high losses in electrical performance. This results in a decrease in transmission and an increase in reflection and discontinuity in the phase front.

Figure 1 Analytic Determination of A Conic By 3 Points and 2 Slopes

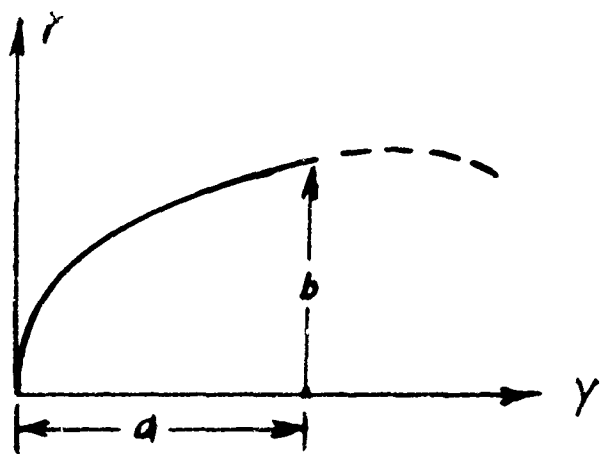


Given Points: $O (0,0)$, $B (a,b)$, $C (c,d)$

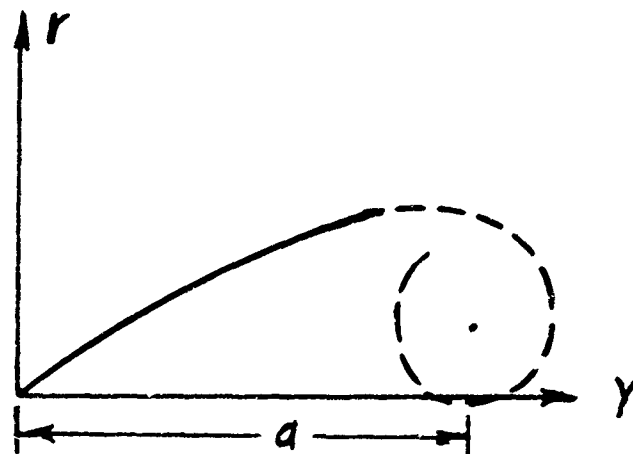
Given Slopes: $\tan \alpha_1 = m_1$, $\tan \alpha_2 = m_2$

Figure 2

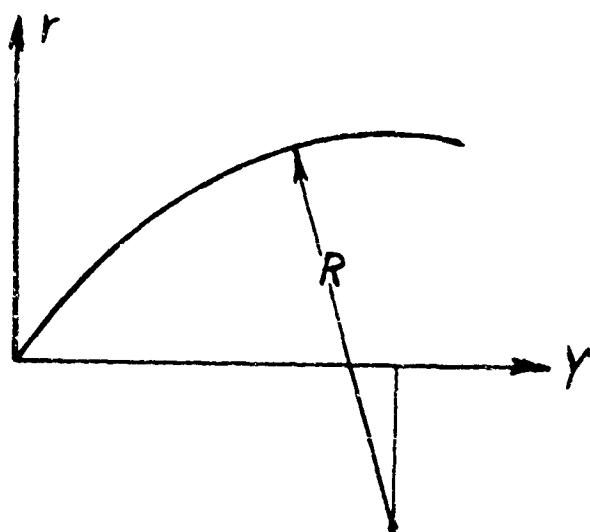
TYPICAL RADOME SHAPES



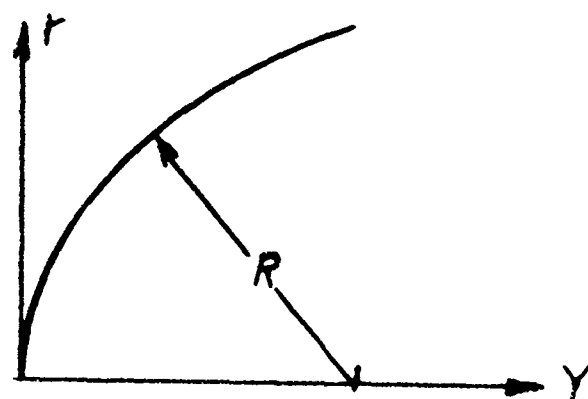
ELLIPSOID



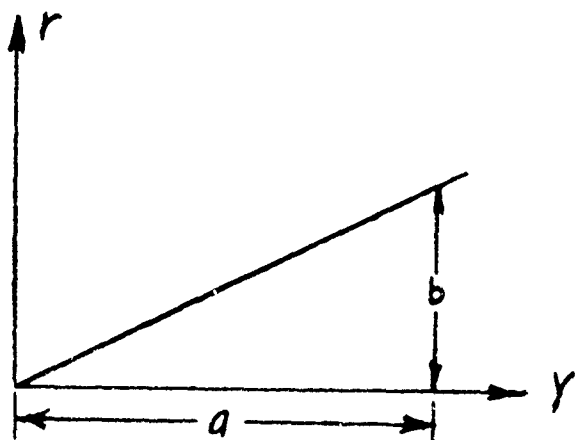
LOG SPIRAL



OGIVE

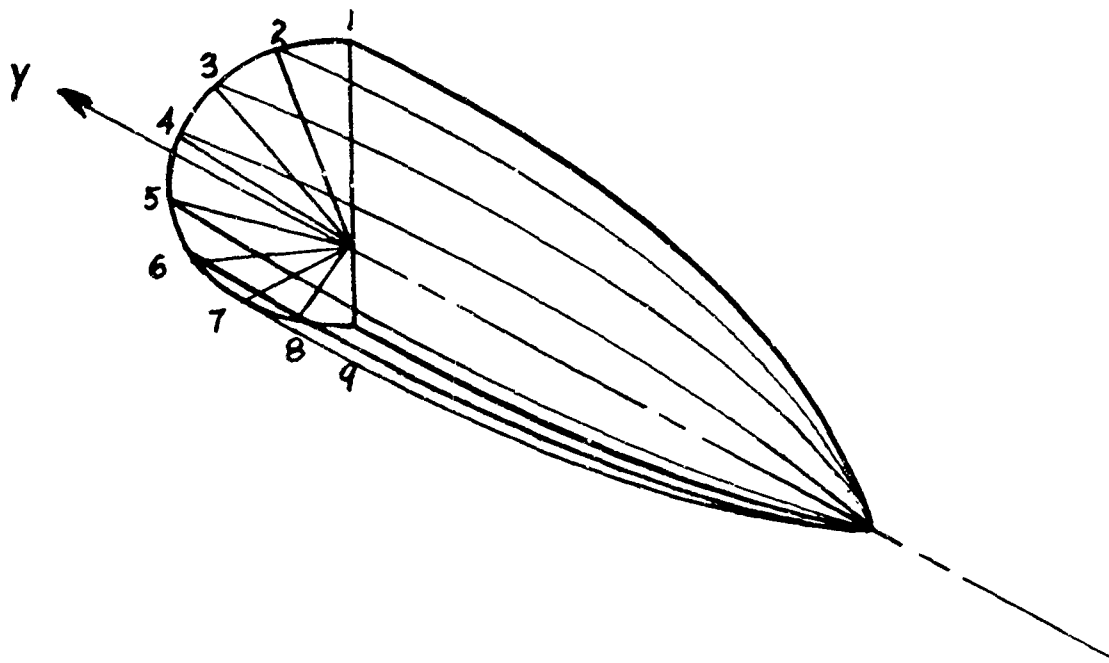


HEMISPHERE

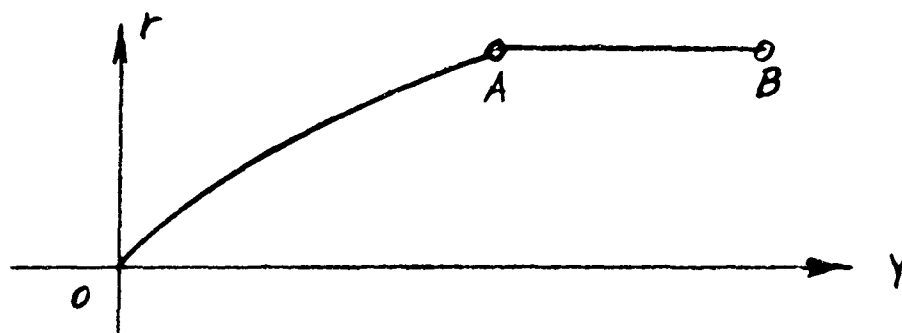


CONE

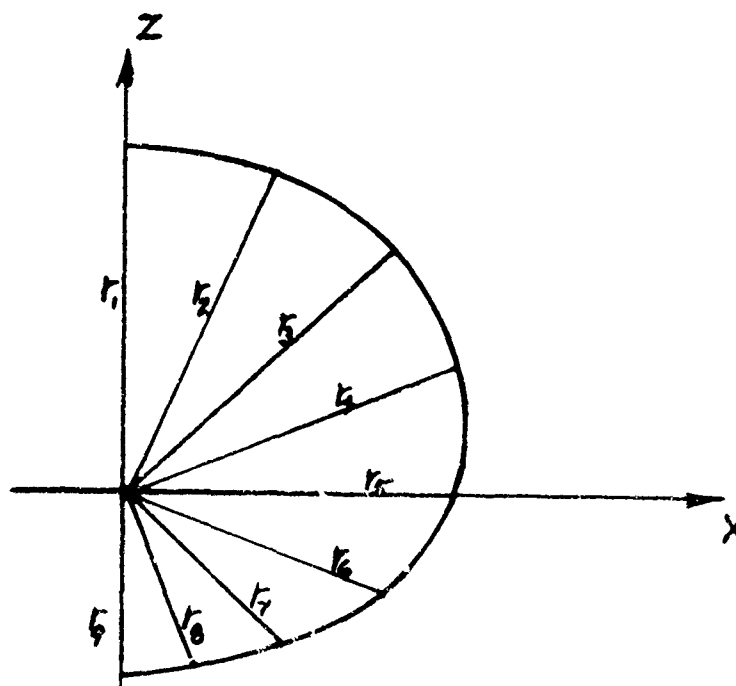
Figure 3 TYPICAL RADIAL PLANE DEFINITION



3A Radial Planes



3B Typical Radial Plane



3C Cross Section At Typical Radome Station (Y)

Figure 4

COMPUTER PROGRAM

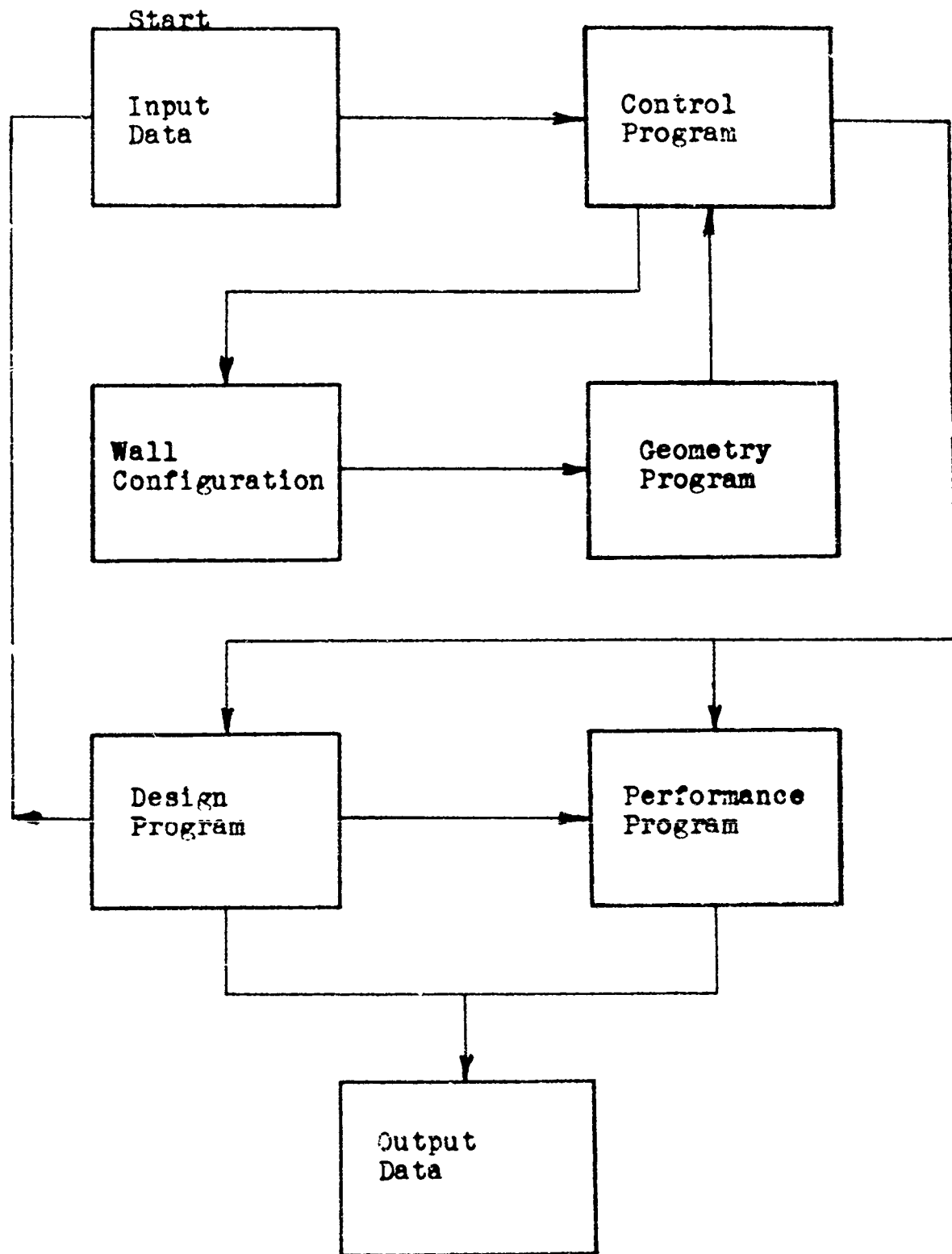


Figure 5 TYPICAL ELECTROMAGNETIC WINDOW DEFINITION

